



The
University
Of
Sheffield.

Defining the perivascular niche in the early stages of breast cancer bone metastasis

A thesis submitted in partial fulfilment of the requirements for
the degree of
Doctor of Philosophy by

Gloria Allocca

Supervised by

Prof. Ingunn Holen and Prof. Nicola J. Brown

The University of Sheffield
Faculty of Medicine, Dentistry and Health
Department of Oncology and Metabolism

August 2018

Acknowledgements

Firstly, I would like to thank my supervisors Prof. Ingunn Holen and Prof. Nicola J. Brown for their encouragement, support, help, and guidance during my last years. Thank you, thank you, thank you!

I would like to thank all the people that in these years taught me so many techniques, in particular Dr. Hannah Brown, Dr. Penelope Ottewell, Dr. Ning Wang and Alyson Evans. A big thank you also to Matthew Fisher for helping me with some of my *in vivo* work and taking care of the cryostat.

A big thank you goes to all the members of the Holen team and the Ottewell team for all the support I received in this years, Penny, Diane, Lewis, Claudia thank you! A special thank you goes to Dr. Victoria Cookson and Dr. Russell Hughes, thank you to keep me (semi) sane, for all your help and moral support, for listening to all my complains, for keeping me well fed (Vicky and Alex finding the croissant on my desk was the highlight of most of the days in the last few months, and Russ the Bounty you gave me after I was almost crying at the confocal was the best I ever had!). I would never have managed without you guys.

Also, thank you to all of the lovely people I met here in Sheffield, Paris, Ameera, Jess, Jack, Nicky Hi, Ifi, Caroline, Faith, Gareth, Karan, Shelly, Allie and all 'my dancing family'.

The most important thank you goes to my family for their never-ending support. Sì, ho finalmente finito la tesi!!! Grazie per avermi supportato (e sopportato) in tutti questi anni. Spero di avervi reso orgogliosi.

Last but not least to my 'Ohana', Ila, Andre, Hannah, Silvietta, Ryan and Francesco, I cannot thank you enough for always been there for me and sharing with me my sad and happy moments. Love you all so much!

Funding bodies

My PhD studies were funded by Breast Cancer Now, UK.



Further funding was kindly provided by:



The
University
Of
Sheffield.

Declaration

I hereby declare that this thesis is an original report of my research work under the guidance of my supervisors Prof Ingunn Holen and Prof Nicola Brown. The experimental work was performed by myself and any contribution by others is explicitly indicated in the corresponding methodologies section. References have been provided on all supporting literatures and resources.

Consent to reproduce work published prior to presentation in this thesis has been obtained from all authors and permission of reproduction is granted for the following manuscripts:

Allocca G, Wang N. Tracking cancer cells colonisation in the bone of mouse xenografts using two-photon microscopy. Bone Research Protocols (In press)

Allocca G, Kusumbe AP, Ramasamy SK, Wang N. Confocal/two-photon microscopy in studying colonisation of cancer cells in bone using xenograft mouse models. Bonekey Rep. 2016 Dec 7; 5:851

Publications and abstracts arising from this thesis

A. Publications

Allocca G, Wang N. Tracking cancer cells colonisation in the bone of mouse xenografts using two-photon microscopy. Bone Research Protocols 2018 (In press)

Ubellacker JM, Haider MT, DeCristo MJ, **Allocca G**, Brown NJ, Silver DP, Holen I and McAllister SS. Zoledronic acid alters hematopoiesis and generates breast tumor-suppressive bone marrow cells. Breast Cancer Research 2017, 19:23

Allocca G, Kusumbe AP, Ramasamy SK, Wang N. Confocal/two-photon microscopy in studying colonisation of cancer cells in bone using xenograft mouse models. Bonekey Rep. 2016 Dec 7; 5:851

B. National and International Presentations

Oral presentations:

Allocca G, Brown HK, Brown NJ, Holen I. Therapeutic modification of the bone: overlap between endosteal and microvascular niches. White Rose Workshop, 09.06.2017, York, UK.

Allocca G, Brown HK, Holen I, Brown NJ. The importance of the perivascular niche in the early stage of breast cancer bone colonisation. 10th World Congress for Microcirculation, 25-27.09.2015, Kyoto, Japan. In: Microcirculation (2015), Abstracts from the 10th World Congress for Microcirculation, HS6-5, DOI:10.1111/micc.12246

Allocca G, Brown HK, Wang N, Eaton CL, Holen I. Breast cancer cells compete for the space in the bone metastatic niche. 4th Joint Meeting of European Calcified Tissue Society and International Bone and Mineral Society, 25-28.04.2015, Rotterdam, The Netherlands. In: IBMS BoneKEy 13, Article number: 685 (2015), CABS OC1.2, DOI:10.1038/bonekey.2015.53

Allocca G, Brown HK, Brown NJ, Holen I. Visualisation of tumour cells in the perivascular niche in models of breast cancer bone metastasis. British Microcirculation Society Meeting, 16-17.04.2015 Manchester, UK. In: Microcirculation (2015), Volume 22, Issue 8, pages 757-758, O12, DOI:10.1111/micc.12212

Poster presentations:

Allocca G, Brown HK, Hughes RO, Fisher M, Ottewell PD, Brown NJ, Holen I. Overlap between osteoblastic and perivascular niches: fertile soil for breast cancer cells. UK Interdisciplinary Breast Cancer Symposium, 15-16.01.2018, Manchester, UK.

Allocca G, Brown HK, Hughes RO, Brown NJ, Holen I. Age matters – therapeutic targeting of the bone microenvironment to modify disseminated breast cancer cells. BACR Tumour Microenvironment – Basic Science to Novel Therapies, 14-16.06.2017, Nottingham, UK.

Allocca G, Brown HK, Holen I, Brown NJ. Young and mature animal models: differences in the early stages of breast cancer bone colonization. SEARCHBreast in vivo models of breast cancer workshop, 03-04.03.2016, Glasgow, UK.

Allocca G, Brown HK, Holen I, Brown NJ. The importance of the perivascular niche in the early stage of breast cancer bone colonisation. 10th World Congress for Microcirculation, 25-27.09.2015, Kyoto, Japan. In: Microcirculation (2015), Abstracts from the 10th World Congress for Microcirculation, P37, DOI:10.1111/micc.12246

Summary

Advanced breast cancer is frequently associated with skeletal metastases. During dissemination to bone, breast cancer cells locate in a putative 'metastatic niche'. Its components are not fully elucidated, however there is evidence of at least partial overlap between the hematopoietic stem cell (HSC), endosteal, metastatic and perivascular niches in bone.

Two-photon microscopy was used to detect single tumour cells and map their location within the bone microenvironment. Irrespective of ER status, route of injection and animal age, breast cancer cells preferentially located in the trabecular region of the bone adjacent to the bone surface. Animals pre-treated with AMD3100 to mobilise HSCs prior injection of tumour cells displayed a higher number of breast cancer cells homing to bone, indicating that HSCs and breast cancer cells compete for space within the niche.

The microenvironment of tumour growth-promoting (6-week old) and dormancy-supporting (12-week old) animal models were investigated. In mature animals, bone volume, length and number of H-vessels and expression of CD31⁺ and CD34⁺ vasculature were reduced, while TSP-1 expression was increased, compared to the young model.

To investigate the effect of Zoledronic acid (ZOL) on the bone microvasculature, young and mature animal model were treated with a single dose of ZOL and changes in the vasculature visualised with immunofluorescent protocols. In young animals ZOL did not change the microvasculature, while mature animals showed shorter and more numerous vessels.

Alteration of microvascular activity, decreased with cediranib and increased with Deferoxamine mesylate, was investigated. Preliminary data did not show substantial changes in either the bone or the microvasculature structure and further studies are required.

Overall, my work supports that the bone metastatic niche consists of several overlapping and interconnected niches. My data suggest that new approaches for

treatment of bone metastasis should evaluate the effect on several components of the bone microenvironment.

List of abbreviations

Abbreviation	Meaning
°C	Degree Celsius
ATCC	American Type Culture Collection
ATP	Adenosine Triphosphate
BM	Bone Marrow
BPs	Bisphosphonates
BV/TV	Bone Volume Per Tissue Volume
Ca²⁺	Calcium
CD31 (or PECAM-1)	Cluster Of Differentiation 31 (Or Platelet Endothelial Cell Adhesion Molecule)
CD34	Cluster Of Differentiation 34
CO₂	Carbon Dioxide
CRUK	Cancer Research UK
CTCs	Circulating Tumour Cells
CXCL12 (or SDF-1)	C-X-C Motif Chemokine 12 (Or Stromal Cell-Derived Factor-1)
CXCR4	C-X-C Chemokine Receptor Type 4
DAPI	4',6-Diamidino-2-Phenylindole
DFM	Deferoxamine Mesylate
dH₂O	Deionized Water
Dkk1	Dickkopf1
DMEM	Dulbecco Modified Eagle Medium
DMSO	Dimethyl Sulfoxide
DOX	Doxorubicin
DPX	Distyrene, Plasticizer (Tricresyl Phosphate) And Xylene
DTCs	Disseminated Tumour Cells
EBCTCG	Early Breast Cancer Trials Collaborative Group
EDTA	Ethylenediaminetetraacetic Acid
EGF	Epidermal Growth Factor
EMT	Epithelial-Mesenchymal Transition
EPC	Endothelial Progenitor Cells
FBS	Foetal Bovine Serum
FDA	Food And Drug Administration
G-CSF	Granulocyte Colony-Stimulating Factor
GFP	Green Fluorescent Protein

GM-CSF	Granulocyte Macrophage Colony-Stimulating Factor
GP	Growth Plate
H₂O	Water
HCl	Hydrochloric Acid
HeNe	Helium-Neon
HIF-1α	Hypoxia Inducible Factor-1 α
hr	Hour
HSCs	Hematopoietic Stem Cells
i.c	Intracardiac
i.p.	Intraperitoneal
i.v.	Intravenous
IC₅₀	Half-Maximal Inhibitory Concentration
IgG	Immunoglobulin G
IL-6	Interleukin-6
iRNA	Ribonucleic Acid Interference
Kg	Kilogram
kV	Kilovolt
LOX	Lysyl Oxidase
M	Molar
mA	Milli Ampere
mg	Milligram
min	Minute
miRNA	Micro Ribonucleic Acid
ml	Milliliter
mm	Millimeter
MMP-9	Matrix Metalloproteinase-9
MMPs	Matrix Metalloproteinase
nm	Nanometer
OBs	Osteoblasts
OCs	Osteoclasts
PBS	Phosphate Buffered Saline
PCR	Polymerase Chain Reaction
PDGF	Platelet-Derived Growth Factor
PECAM1	Platelet Endothelial Cell Adhesion Marker
PF4	Platelet Factor 4

PFA	Paraformaldehyde
PTH	Parathyroid Hormone
PVP	Polyvinylpyrrolidone
qPCR	Real-Time Polymerase Chain Reaction
ROI	Region Of Interest
RPM	Rounds Per Minute
s.c.	Subcutaneous
sec	Second
Tb. N.	Trabecular Number
Tb. Th.	Trabecular Thickness
TKI	Tyrosine Kinase Inhibitor
TRAP	Tartrate-Resistant Acid Phosphatase
TSP-1	Thrombospondin-1
VEGF	Vascular-Endothelial Growth Factor
w/v	Weight Per Volume
Wnt	Wingless
ZOL	Zoledronic Acid
α-SMA	Alpha-Smooth Muscle Actin
μCT	Micro Computed Tomography
μg	Microgram
μl	Microliter
μm	Micrometer
μm³	Micrometer Cubic

Table of contents

Chapter 1	22
Introduction	22
1.1 Metastatic breast cancer	23
1.1.1 The early steps of the metastatic process.....	23
1.1.2 Dormant cells	25
1.2 The Metastatic niche(s)	26
1.2.1 The HSC niche	28
1.2.1.1 How is access to the HSCs niche regulated?.....	29
1.2.1.2 Competition for the limited space in the HSCs niche	31
1.2.2 The osteoblastic niche	32
1.2.2.1 Osteoblasts and their interaction with cancer cells	33
1.2.3 The perivascular niche	35
1.2.3.1 Regulation of dormancy	38
1.3 Therapeutic modification of the metastatic niche	39
1.3.1 Targeting the bone cell population of the niche	41
1.3.1.1 Bisphosphonates	41
1.3.1.1.1 Anti-tumour effects of BPs	42
1.3.1.1.2 Clinical use of BPs.....	44
1.3.2 Targeting the microvasculature	46
1.3.2.1 Cediranib	47
1.3.2.1.1 Anti-tumour effects of Cediranib	49
1.3.2.1.2 Clinical use of Cediranib	50
1.3.3.1 Deferroxamine mesylate	53
1.4 Summary, conclusion and outstanding questions	55
1.5 Aims of the thesis	56
Chapter 2	57
Materials and Methods	57
Materials	58
Methods	60
<i>In vitro</i> experiments	60
2.1 Cell Lines	60
2.1.1 MDA-MB-231-GFP-IV bone homing	60
2.1.2 MDA-MB-231-B02	61
2.1.3 MDA-MB-231-NW1-Luc2	61
2.1.4 MCF-7	61
2.1.5 T47D	62
2.2 Cell line subculture	62
2.2.1 Counting cell number by haemocytometer	63
2.2.2 Storage and thawing of cells.....	63
2.3 Staining of cells with lipophilic membrane dyes	64
<i>In vivo</i> work	65
2.4 Home Office approval	65
2.5 Animals	65

2.6 Tumour cell injection	65
2.6.1 Intravenous injection.....	65
2.6.2 Intracardiac injection.....	66
2.6.3 Intraarterial injection	66
2.7 Administration of drugs and other solutions	67
2.7.1 Preparation of drugs.....	67
2.7.1.1 Luciferin	67
2.7.1.2 AMD3100 octahydrochloride hydrate	67
2.7.1.3 Zoledronic acid (ZOL)	67
2.7.1.4 Cediranib (AZD2171).....	67
2.7.1.5 Deferoxamine mesylate (DFM).....	68
2.7.1.6 Phosphate buffered saline	68
2.7.2 Route of administration	68
2.7.2.1 Subcutaneous injection.....	68
2.7.2.2 Intraperitoneal injection	68
2.7.2.3 Oral gavage	68
2.8 <i>In vivo</i> detection of tumour growth	69
<i>Ex vivo</i> work	69
2.9 Collection of bone samples	69
2.9.1 Preparation of bone samples for histological analysis	69
2.9.2 Preparation of bones for fluorescent immunohistochemistry	70
2.10 Two-photon microscopy	70
2.10.1 Preparation of the bone specimen.....	70
2.10.2 Imaging the bone.....	71
2.10.3 3D reconstruction and analysis of the location of tumour cells within bone.....	73
2.11 Micro computed tomography (μCT)	75
2.12 Staining of bone components.....	77
2.12.1 Dewaxing and dehydrating of paraffin embedded bones	77
2.12.2 Haematoxylin and Eosin (H&E) staining	77
2.12.3 Masson-Goldner trichrome staining.....	77
2.12.4 Toluidine Blue staining	78
2.13 Immunofluorescence.....	80
2.13.1 Visualization of bone microvasculature on gelatin embedded sections	80
2.14 Scoring of histological slides.....	82
2.14.1 Quantification of extracellular matrix composition	82
2.14.2 Quantification of Endomucin positive vessels.....	83
2.14.3 Quantification of CD31 and CD34 positive vessels	84
2.14.4 Quantification of α -SMA, TSP-1 and Osterix expression in the bone microenvironment.....	86
2.15 Statistical analysis.....	86
Chapter 3	87
Homing of breast cancer cells in the bone microenvironment	87
3.1 Summary	88
3.2 Introduction	89
3.3 Aims	92

3.4 Materials and Methods	93
3.4.1 Breast cancer cell-lines	93
3.4.2 <i>In vivo</i> studies.....	93
3.4.2.1 Homing of breast cancer cells in mature animal models	93
3.4.2.2 Hematopoietic stem cell (HSCs) niche modification.....	96
3.4.2.3 Comparison between young and mature animal models	96
3.4.2.4 Collection and preparation of the samples	97
3.4.3 Two-photon microscopy	98
3.4.3.1 Mapping the location of breast cancer cells.....	98
3.4.4 Statistical analysis	98
3.5 Results	99
3.5.1 The MDA-MB-231-GFP-IV cell-line homes to the trabecular region of bone.....	100
3.5.1.1 MDA-MB-231-GFP-IV cells locate close to the bone surface	103
3.5.2 Comparison between the pattern of homing of MDA-MB-231-GFP-IV and MDA-MB-231/B02-GFP cells	105
3.5.3 The route of injection does not affect the homing of MDA-MB-231-GFP-IV cells to the bone microenvironment.....	107
3.5.4 ER+ve breast cancer cell-lines display the same pattern of seeding as triple negative cell-lines	109
3.5.5 Modification of the HSCs niche changes the homing of breast cancer cells.....	111
3.5.6 Breast cancer cells show no difference in the colonisation of young or mature animals.....	112
3.6 Discussion	116
Chapter 4	120
Characterisation of the metastatic niche in young and mature mice ...	120
4.1 Summary	121
4.2 Introduction	122
4.3 Aims	124
4.4 Materials and Methods	125
4.4.1 Breast cancer cell lines.....	125
4.4.2 <i>In vivo</i> study	125
4.4.2.1 Collection and preparation of the bones for two-photon microscopy.....	126
4.4.2.2 Collection and preparation of the bones for micro computed tomography (μ CT) and fluorescent immunohistochemistry	127
4.4.3 Two-photon microscopy and location of cancer cells within the bone structure....	127
4.4.4 Micro computed tomography (μ CT)	128
4.4.5 Immunofluorescence protocols for the staining of the perivascular niche components	128
4.4.5.1 Visualisation of Endomucin positive vessels.....	128
4.4.5.2 Staining of CD31 or CD34 and Endomucin positive vessels.....	128
4.4.5.3 Visualisation of Osterix, α -SMA or Thrombospondin	129
4.4.6 Scoring of immunofluorescence stainings	129
4.4.6.1 Quantification of Endomucin positive vessels.....	129
4.4.6.2 Quantification of vessels positive for both Endomucin and CD31 or CD34.....	130
4.4.6.3 Quantification of Osterix, α -SMA or Thrombospondin expression	130

4.4.7 Statistical analysis.....	130
4.5 Results.....	131
4.5.1 Breast cancer cell bone colonisation in young and mature animal models	132
4.5.2 Trabecular bone of young animals is more dense than bone of mature animals ...	134
4.5.3 Differences in the metastatic niche between young and mature mice	138
4.5.3.1 Young animals have more osteoprogenitors cells than mature animals.....	138
4.5.3.2 Endomucin expression is higher in mature mice than in young mice.....	141
4.5.3.2.1 Area occupied by different vessels sub-types	143
4.5.3.2.2 Reorganisation of the vascular bed with aging.....	146
4.5.3.3 Ageing results in decreased CD31 expression.....	150
4.5.3.4 Aged animals have less expression of CD34	154
4.5.3.5 Arterial component of the bone microenvironment does not change with age	158
4.5.3.6 Dormancy-supporting Thrombospondin-1 levels are increased in the microenvironment of mature animals.....	161
4.5.4 DTC in bone marrow locate next to components of the perivascular niche	164
4.5.5 Reorganisation of the microvasculature and TSP-1 expression in presence of tumours	166
4.6 Discussion.....	170
Chapter 5	176
Effect of ZOL on the bone microvasculature structure	176
5.1 Summary	177
5.2 Introduction	178
5.3 Aims	181
5.4 Materials and Methods.....	182
5.4.1 Breast cancer cell line.....	182
5.4.2 <i>In vivo</i> studies	182
5.4.2.1 Preparation of long bones for ex vivo analysis	182
5.4.3 Two-photon microscopy.....	184
5.4.4 Micro Computed tomography.....	184
5.4.5 Toluidine Blue staining	184
5.4.5 Immunofluorescent staining of the components of the metastatic niche	185
5.4.6 Statistical analyses.....	187
5.5 Results.....	188
5.5.1. ZOL changes the bone structure.....	188
5.5.1.1. ZOL causes an expansion of the proteoglycan-rich area of the growth plate	192
5.5.1.2 Alteration of the bone structure is reflected in the osteoprogenitor population	194
5.5.2 ZOL treatment affects the bone microvasculature	199
5.5.2.1 Effect of ZOL on Endomucin positive vessels of young and mature animals.....	199
5.5.2.2 ZOL treatment does not cause alteration in CD31 vessels	207
5.5.2.3 Newly formed CD34 ⁺ vessels are not influenced by the ZOL treatment.....	212
5.5.3 ZOL treatment and the homing of breast cancer cells in the bone microenvironment	216
5.5.4 ZOL modification of expression of TSP-1	218
5.6 Discussion.....	221

Chapter 6	227
Therapeutic modification of the microvasculature and its effect on the bone metastatic niche	227
6.1 Summary	228
6.2 Introduction	229
6.3 Aims	231
6.4 Materials and methods	232
6.4.1 <i>In vivo</i> studies.....	233
6.4.2 Processing of bone samples	235
6.4.3 Two-photon microscopy	235
6.4.4 μ CT	235
6.4.5 Toluidine Blue staining	236
6.4.6 Immunofluorescent staining	236
6.4.7 Statistical analysis	236
6.5 Results	237
6.5.1 Cediranib treatment to decrease the microvascular activity	237
6.5.1.1 Effect of Cediranib on bone structure	237
6.5.1.1.1 Changes in the extracellular matrix	239
6.5.1.1.2 Effect of Cediranib on the osteoprogenitor population.....	240
6.5.1.2 Effect of Cediranib treatment on bone microvasculature.....	242
6.5.1.2.1 Endomucin ⁺ vessels.....	242
6.5.1.2.2 CD31 ⁺ vessels	247
6.5.1.2.3 CD34 ⁺ vessels	251
6.5.1.3 Effect of Cediranib treatment on TSP-1 expression	255
6.5.1.4 Effect of Cediranib treatment on breast cancer cell homing to bone.....	257
6.5.2 Deferoxamine mesylate treatment to increase the microvascular activity	259
6.5.2.1 Effect of DFM on bone structure.....	259
6.5.2.1.1 Changes in the extracellular matrix	262
6.5.2.1.2 Effect of DFM on the osteoprogenitor population	263
6.5.2.2 Effect of DFM treatment on bone microvasculature.....	265
6.5.2.2.1 Endomucin ⁺ vessels.....	265
6.5.2.2.2 CD31 ⁺ vessels	270
6.5.2.2.3 CD34 ⁺ vessels	274
6.5.2.3 Effect of DFM treatment on TSP-1 expression	278
6.5.2.4 Effect of DFM treatment on breast cancer cell homing to bone.....	280
6.6 Discussion	282
Chapter 7	287
Discussion	287
References	301

Table of Figures

Figure 1.1 Schematic illustration of the metastatic colonisation of bone.....	25
Figure 1.2 Schematic models of competition for the space in the niche	30
Figure 1.3 Schematic illustration of the vessel architecture in bone	36
Figure 1.4 Regulation of dormancy by the perivascular niche	39
Figure 1.5 Benefits of targeting both cancer cells and microenvironment.....	40
Figure 1.6 Chemical structure and anti-tumour effects of nitrogen-containing bisphosphonates	42
Figure 1.7 Chemical structure and mechanism of action of Cediranib	48
Figure 2.1 Schematic illustration of Haemocytometer.....	63
Figure 2.2 Preparation of the specimen for two-photon microscopy.....	72
Figure 2.3 Schematic illustration of the analysis of the location of tumour cells within the bone marrow	74
Figure 2.4 Illustration of the μ CT reference point.....	76
Figure 2.5 Histological sections showing tibial structures.....	79
Figure 2.6 Area of interest quantified with Toluidine Blue staining.....	82
Figure 2.7 Endomucin positive vessel quantification	83
Figure 2.8 Schematic illustration of quantification of CD31/CD34 positive vessels	85
Figure 3.1 Outline for the <i>in vivo</i> studies evaluating homing of bone-seeking MDA-MB-231 cell- lines	94
Figure 3.2 Homing after different routes of injection and both ER+ve and ER-ve cell-lines	95
Figure 3.3 Modification of HSCs niche and comparison between young and mature mice.....	97
Figure 3.4 <i>In vivo</i> tumour model	99
Figure 3.5 Homing of MDA-MD-231-GFP-IV cells.....	102
Figure 3.6 Location of MDA-MB-231-GFP-IV cells in the bone microenvironment.....	104
Figure 3.7 Comparison between homing of MDA-MB-231-GFP-IV cells and MDA-MB-231/B02- GFP cells	106
Figure 3.8 Comparison between different routes of injection.....	108
Figure 3.9 T47D and MCF7 cell-lines colonisation of bone	110
Figure 3.10 Modification of the HSCs niche	112
Figure 3.11 Homing of breast cancer cells in the young (6-week old) vs mature (12-week old) animal model.....	114
Figure 4.1 Outline of the <i>in vivo</i> studies evaluating homing of bone-seeking MDA-MB-231 cell- lines	126
Figure 4.2 <i>In vivo</i> tumour model	131
Figure 4.3 Homing of MDA-MD-231-GFP-IV cells in young and mature animals	133
Figure 4.4 Quantification of trabecular bone volume, thickness and number.....	135
Figure 4.5 Representative mCT analysis and reconstruction of bone of young animals.....	136
Figure 4.6 Representative mCT analysis and reconstruction of bone of mature animals.....	137
Figure 4.7 Representative images of immunofluorescent staining against Osterix	139
Figure 4.8 Quantification of immunofluorescent staining against Osterix.....	140
Figure 4.9 Immunofluorescent staining against Endomucin	142
Figure 4.10 Quantification of area of bones occupied by H- and L-vessels.....	144
Figure 4.11 Percentage of bone marrow occupied by H- and L-vessels.....	145
Figure 4.12 Number of H- and L-vessels quantified in the total area of bone marrow.....	147
Figure 4.13 Quantification of the number of H- and L-vessels.....	148
Figure 4.14 Average length of the two vessels sub-types	149
Figure 4.15 Representative images of immunofluorescent staining against CD31	151
Figure 4.16 Quantification of immunofluorescent staining against CD31	152
Figure 4.17 Quantification of CD31+ vessels.....	153

Figure 4.18 Representative images of immunofluorescent staining against CD34	155
Figure 4.19 Quantification of immunofluorescent staining against CD34	156
Figure 4.20 Quantification of CD34+ vessels	157
Figure 4.21 Representative images of immunofluorescent staining against α -SMA	159
Figure 4.22 Quantification of immunofluorescent staining against α -SMA.....	160
Figure 4.23 Representative images of immunofluorescent staining against Thrombospondin-1 (TSP-1).....	162
Figure 4.24 Quantification of immunofluorescent staining against Thrombospondin-1.....	163
Figure 4.25 Representative images of the location DTC in bone microenvironment	165
Figure 4.26 Endomucin+CD31+ microvessels in presence of bone metastasis.....	167
Figure 4.27 Endomucin+CD34+ microvessels in presence of bone metastasis.....	168
Figure 4.28 Expression of TSP-1 in bones with and without tumour	169
Figure 5.1 Outline for the <i>in vivo</i> studies evaluating the effect of ZOL on the bone microenvironment	189
Figure 5.2 Representative images of reconstructed bone after mCT analysis.....	190
Figure 5.3 Effect of a single dose of ZOL on bone structure of young and mature animal models	191
Figure 5.4 Quantification of the proteoglycan-rich area of bone	193
Figure 5.5 Representative image of the effect of ZOL treatment on Osterix expression in 6- week old animals	195
Figure 5.6 Quantification of the effect of ZOL treatment on Osterix expression in 6-week old animals.....	196
Figure 5.7 Representative image of the effect of treatment on Osterix expression in 12-week old animals.....	197
Figure 5.8 Quantification of the effect of ZOL treatment on Osterix expression in 12-week old animals.....	198
Figure 5.9 Quantification of immunofluorescent staining against Endomucin.....	200
Figure 5.10 Area of bone marrow occupied by H- and L-vessels	201
Figure 5.11 Percentage of bone marrow occupied by H- and L-vessels	202
Figure 5.12 Number of vessels quantified in the total area of bone marrow.....	204
Figure 5.13 Number of H- and L-vessels quantified in the area of bone they occupy	205
Figure 5.14 Average length of the H- and L-vessels sub-types	206
Figure 5.15 Representative image of the effect of ZOL treatment on CD31+ vessels	208
Figure 5.16 Quantification of immunofluorescent staining against CD31	209
Figure 5.17 Number and average length of CD31+ vessels measured with Aperio ImageScope	211
Figure 5.18 Effect of ZOL treatment on CD34+ vessels of young animals	213
Figure 5.19 Effect of ZOL treatment on CD34+ vessels of mature animals.....	214
Figure 5.20 Number and average length of CD34+ vessels.....	215
Figure 5.21 Homing of MDA-MD-231-NW1-Luc2 cells to bone in young and mature animals after the treatment with ZOL.....	217
Figure 5.22 Effect of ZOL treatment on TSP-1 expression in 6-week old animal	219
Figure 5.23 Effect of ZOL treatment on TSP-1 expression in 12-week old animal	220
Figure 6.1 Outline of the <i>in vivo</i> studies evaluating the effect of Cediranib and DFM on the bone microenvironment	234
Figure 6.2 Effect of a Cediranib treatment on bone structure.....	238
Figure 6.3 Visualisation of the proteoglycan-rich area of bone	239
Figure 6.4 Representative image of the effect of Cediranib treatment on Osterix+ cells	240
Figure 6.5 Quantifications of the effect of Cediranib treatment on Osterix expression.....	241
Figure 6.6 Quantification of immunofluorescent staining against Endomucin.....	243
Figure 6.7 Number of vessels quantified in bone marrow.....	245

Figure 6.8 Number of H- and L-vessels in different groups and their length	246
Figure 6.9 Representative image of the effect of Cediranib treatment on CD31+ vessels	247
Figure 6.10 Quantification of immunofluorescent staining against CD31	249
Figure 6.11 Number and average length of CD31+ vessels	250
Figure 6.12 Representative image of the effect of Cediranib treatment on CD34+ vessels	251
Figure 6. 13 Quantification of immunofluorescent staining against CD34.....	253
Figure 6.14 Number and average length of CD34+ vessels	254
Figure 6.15 Representative image of the effect of Cediranib treatment on TSP-1 expression	255
Figure 6.16 Quantification of the effect of Cediranib treatment on TSP-1 expression	256
Figure 6.17 Homing of breast cancer cells in animals treated with Cediranib	258
Figure 6.18 Effect of 3 weeks of DFM treatment on bone structure	260
Figure 6.19 Effect of 6 weeks of DFM treatment on bone structure	261
Figure 6.20 Visualisation of the proteoglycan-rich area of bone	262
Figure 6.21 Effect of DFM treatment on Osterix+ cells	264
Figure 6.22 Quantification of immunofluorescent staining against Endomucin after treatment with DFM	266
Figure 6.23 Number of vessels quantified in bone marrow after DFM treatment	268
Figure 6.24 Number of H- and L-vessels in different groups and their length	269
Figure 6.25 Representative image of the effect of DFM treatment on CD31+ vessels	270
Figure 6.26 Quantification of immunofluorescent staining against CD31	272
Figure 6.27 Number and average length of CD31+ vessels after treatment with DFM	273
Figure 6.28 Representative image of the effect of DFM treatment on CD34+ vessels	274
Figure 6.29 Quantification of immunofluorescent staining against CD34	275
Figure 6.30 Number and average length of CD34+ vessels after treatment with DFM	277
Figure 6.31 Effect of DFM treatment on TSP-1 expression	278
Figure 6.32 Quantification of the effect of DFM treatment on TSP-1 expression	279
Figure 6.33 Homing of breast cancer cells in animals treated with DFM	281

Table of Tables

Table 1.1 Common molecules involved in pathways of interaction between osteoblasts and cancer cells.....	34
Table 1.2 Currently ongoing and completed clinical trials using cediranib for the treatment of breast cancer	51
Table 2. 1 Laboratory reagents or kits	58
Table 2.2 Plastic and disposable equipment.....	59
Table 2.3 Software used for data analysis	59
Table 2.4 Laboratory equipment	59
Table 2.5 Molecular classification of breast cancer cell lines used in this thesis.....	60
Table 2.6 Primary antibodies used for staining components of the perivascular niche	81
Table 2.7 Secondary antibodies used used for staining components of the perivascular niche	81
Table 4.1 Summary of μ CT analysis	134
Table 5.1 Summary of the bone sample preparations for the different analyses performed. .	183
Table 5.2. Summary of immunofluorescent protocols used to visualise components of the metastatic niche.....	186
Table 6.1 Summary of material and methods of Chapter 6.....	232

Chapter 1

Introduction

1.1 Metastatic breast cancer

Breast cancer is the most common cancer worldwide in females and the second commonest cancer overall. In the UK, 1 in 8 women will be diagnosed with breast cancer during their life time, Cancer Research UK (CRUK) reports almost 55000 new cases of breast cancer every year, with a 20% increase of the incidences rates in the UK since the early 1990 and a 4% increase in the past decade (cruk.org/cancerstats). Improvement of the screening and diagnosis allow an early detection of the malignancy with 79-87% of breast cancer diagnosed at stage I-II. Unfortunately, 6-7% of patients are diagnosed at stage IV and already have metastatic disease. Secondary disease, particularly skeletal metastasis, can develop decades after the detection and treatment of the primary tumour. Recent studies show that the risk of distant recurrence progress at a steady rate for at least 20 years [1]. The organs that are most frequently colonised by breast cancer cells are bone, lungs and brain and post-mortem exams of patients with advanced breast cancer shown evidence of metastasis in bone in the majority ($\approx 70\%$) of cases [2]–[4]. Even though the bone metastases can be asymptomatic, pain, hypercalcemia, pathological fractures and spinal instability with compression of the spinal cord may occur [5]. One of the major issues of treating the metastatic disease is that it is not known which patient will develop secondary cancer or when this will happen. The lack of available biopsies hamper the investigation of the disease in humans, therefore pre-clinical models play a big role in the search for new therapeutic targets.

1.1.1 The early steps of the metastatic process

The development of the malignancy in a secondary organ is a multistep process that begins with the detachment of the tumour cells from the primary site. The mechanism(s) that trigger cancer cells to alter their interaction with the matrix surrounding the tumour and enter in the lymphatic or blood stream is not fully understood. It known that tumour cells undergo an epithelial-mesenchymal transition (EMT) that allows cells to increase their migration, invasion and resistance to apoptosis due to biochemical changes towards the mesenchymal phenotype [6]. After this transformation, the EMT cells with their enhanced tumourogenity, enter the blood

stream and travel through the circulation to reach the secondary organ. However, only a small proportion of the cells detached from the primary sites will successfully colonise a distant organ as the majority of circulating tumour cells (CTCs) are recognised and eliminated by the immune system, undergo spontaneous apoptosis or re-enter the blood stream and potentially colonise other organ(s) [7]–[10]. The few CTCs that survive in the circulation and reach the bone can remain dormant for long periods of time. At the end of the 19th century, Paget formulated the theory of the ‘seed and soil’, stating that the interaction between disseminated tumour cells (DTCs) and microenvironment is necessary for the survival of cancer cells in distant organs and fundamental for the progression of the secondary disease [11]. The cross-talk between breast cancer cells and the components of the bone microenvironment determine the fate of the tumour cells. As the metastatic foci develop, interactions between the tumour cells and bone cell populations create a cascade of events, known as the ‘vicious cycle’. Cancer cells that locate in the bone microenvironment interact in particular with the bone resorbing cells (osteoclasts, OCs), resulting in release of cytokines and growth factors that stimulate the growth of the secondary tumour [9], [12]–[16] (Figure 1.1).

While the interaction between cancer cells and the surrounding microenvironment that promotes tumour growth when metastases are already established has been extensively investigated [14]–[16], the mechanism(s) that initiates this process, triggering the DTCs to escape the quiescent state and start proliferating, have been less well studied.

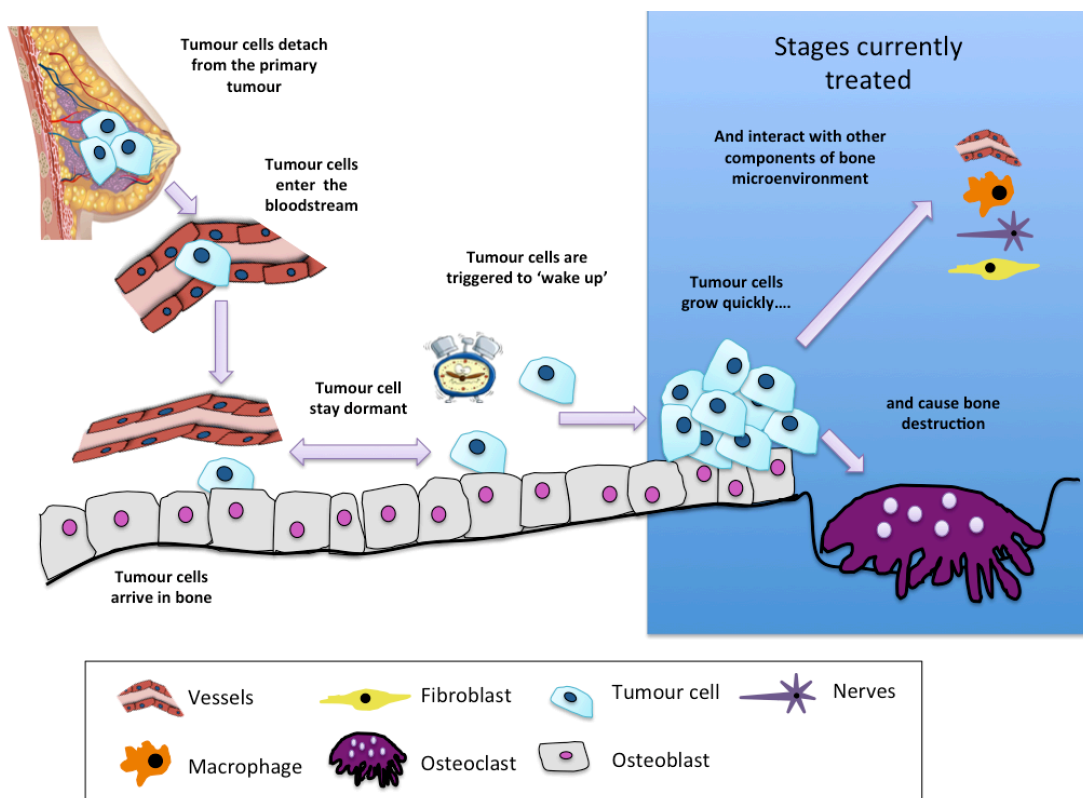


Figure 1.1 Schematic illustration of the metastatic colonisation of bone

The development of breast cancer bone metastasis is a multistep process in which the principal steps are: detachment from the primary tumour, entry in the circulation, colonisation of the bone microenvironment, dormant state of the cells, proliferation and destruction of the bone.

1.1.2 Dormant cells

Malignancies such as prostate and breast cancer are able to develop secondary tumours long after the initial diagnosis and treatment due to the presence of DTCs that stay dormant in the secondary site [7]. The mechanism(s) that allows tumour cells to acquire the dormant phenotype is still unclear, likewise a comprehensive characterisation of the quiescent state has not been clarified yet, is the focus of many investigations. DTCs presents stem cells (e.g. $CD44^{high}CD24^{low}$) and EMT (e.g. EpCAM and cytokeratins) phenotypes [17], [18]. Current anti-cancer treatments usually target cells with high proliferation rate and therefore they are not efficient against dormant cells which, due to their quiescent phenotypes, do not undergo proliferation or apoptosis [19]–[21]. Being in a non-proliferative state, dormant cells are negative for proliferation markers such as Ki67 and they have a high capability to retain membrane

dyes that would be lost during cellular division [22]–[24]. This ability to retain membrane dyes has been used to track single tumour cells in the bone microenvironment in the early stages of bone colonization [24]–[26]. The mechanism(s) that dormant cells use to maintain a quiescent state have not been fully clarified, but it has been suggested that these are similar to the ones used by hematopoietic stem cells (HSCs) in the bone marrow, such as CXCR4/CXCL12 and angiopoietin-1/Tie-2 interactions [10], [27]–[33]. Moreover, to acquire their quiescent state and to gain self-renewal ability, HSCs have to engage with components of the bone microenvironment [34]. Data from model systems have suggested that dormant prostate cancer cells locate in the same region(s) occupied by the HSCs, highlighting the importance of the microenvironment in the maintenance of the quiescent state for both of these non-proliferating cells [16], [28], [35], [36], however this has not been shown yet for breast cancer.

1.2 The Metastatic niche(s)

Bone is a particular organ in that it supports both active cell proliferation, e.g. haematopoiesis, as well as supporting the quiescent state of the HSCs. Bone is also subject to a constant remodelling process with the action of osteoblasts forming new bone and osteoclasts resorbing it, in particular during physiological bone growth and in order to repair microdamage [37]. The balance of these dynamic processes is obtained due to an intricate network of signalling between the many different cell populations of the bone marrow, a balance that can be altered by the action of tumour cells [38]. It has been suggested that dormant tumour cells, in particular prostate and breast cancer cells, colonise specialized region of bone in which the microenvironment supports their quiescent state: the metastatic niche(s) [16]. In these areas of bone, the dormant cells interact with the surrounding microenvironment and this cross-talk supports either tumour cell dormancy or promotes the proliferation of the cancer cells, resulting in the development of bone metastasis. The exact composition of the metastatic niche has not yet been elucidated, but there are evidences indicating that tumour cells locate in regions of bone where the HSCs niche, endosteal niche and perivascular niche overlap [34], [39]–[41]. This region of bone is characterized by a complex microenvironment, the presence of cytokines, hormones and soluble factors

produced by all the different components of the surrounding niches, creating a particularly rich soil for the seeding of the tumour cells reaching the bone marrow and influencing their fate towards dormancy or proliferation [31].

Besides osteoblasts (OBs) and osteoclasts (OCs), various components of the bone marrow affect the growth of metastatic disease, for example an emerging player in the bone colonization is the adipose tissue. It has been shown both *in vitro* and *in vivo* that adipose tissue promotes the colonisation of bone and tumour growth of both breast cancer and myeloma [29], [42], [43]. *In vitro* co-culture of MDA-MB-231 and MCF-7 breast cancer cell lines with human femoral head discs indicated an infiltration of the cancer cells in the bone marrow and displayed extensive contact with adipocytes, moreover it has been suggested that the recruitment of tumour cells towards the adipose niche was mediated by secretion of leptin and IL-1 β [42]. The bone marrow also contains several components of the immune system, monocytes and macrophages in particular, that have been shown to be involved in initiation and development of secondary disease by secreting chemokines and Matrix metalloproteinases (MMPs) [44], [45]. As well as the immune system, mesenchymal derived cells, like fibroblasts, have been recognised to play a role in tumourigenesis promoting the expression of inflammatory cytokines, recruiting macrophages and stimulating angiogenesis [46]. Overall, the complexity of the bone microenvironment with its numerous interacting cellular and molecular components makes it difficult to pinpoint the precise role of each individual cell type in regulating tumour cell homing.

As well as the fertile soil produced by resident cell populations of the metastatic niche, Kaplan and colleagues stated that hematopoietic progenitor cells derived from the bone marrow are implicated in the creation of a pre-metastatic niche [38]. Cox and colleagues have also investigated the concept of pre-metastatic niche, demonstrating that the homing of breast cancer cells to bone is influenced by factors secreted by the primary tumour. High levels of lysyl oxidase (LOX) in the primary tumour in particular, alter the microenvironment of bone resulting in the creation of a pre-metastatic niche which attracts the homing of CTCs [47].

It is not fully understood whether the metastatic niche(s) is a precisely defined, size limited physical area of the bone marrow that can be saturated or whether there are multiple distinct niches available for colonization by tumour cells. What it is known is that the altered balance between the activities of the cellular components of the overlapping niches (osteoblastic, hematopoietic stem cells and perivascular niches) influence the development of bone metastasis in *in vivo* models [30], [48].

1.2.1 The HSC niche

The presence of the HSCs niche, located in the endosteal region of the bone marrow, was defined in the 1970's by Trentin and Schofield as a region of bone where the microenvironment signals regulate the balance between quiescent state and proliferation of the HSCs [49], [50]. The mechanism(s) involved in the attraction of HSCs to the niche(s), the maintenance of the quiescent phenotype and the signals promoting proliferation and differentiation have not been fully elucidated. Likewise the metastatic niche, the region of bone hosting HSCs is a complex heterogeneous microenvironment composed by different cell populations. It is well established that the HSC niche is composed by two different regions: an endosteal (or osteoblastic) and a perivascular niche [51]. The close association between OBs and HSCs has been extensively studied and it has been shown that OBs or osteoblastic cell lines support HSCs in *in vitro* and *ex vivo* culture producing cytokines that regulate haematopoiesis [52]–[54]. Moreover, it has been shown *in vivo* that OBs can regulate the HSCs number through production of Notch ligand Jagged-1 [55], [56], molecules that are also overexpressed in several cancer types and thought to be implicated in cell proliferation and metastasis [57]. OBs can also influence the quiescent state and self-renewal properties of HSCs through thrombopoietin signalling [58], [59], the inhibition of the Wnt signalling through expression of Dkk1 [60] and the production of osteopontin [61]. CXCL12/CXCR4 is another important interaction between HSCs and OBs, known to be implicated in recruitment and preservation of HSCs in the bone marrow [62]–[64]. Inhibition of the interaction between the CXCR4 expressed by the HSCs and its ligand CXCL12 (abundantly expressed by the OBs) results in an increase level of circulating HSCs [64], [65]. CXCR4/CXCL12 has been particularly useful in target therapies and it is

of interest to researchers focusing investigating the metastatic processes, as it also influences the homing of prostate cancer cells in the bone marrow [66].

In addition to OBs, other cell types also influence the HSCs regulation in the bone marrow. Several studies reported that the osteoblastic and the perivascular compartments are not to be considered as distinct, but rather as overlapping areas, and the HSCs niche is therefore most commonly described as a vascularized endosteal region [67]. In support of the theory of an overlap between osteoblastic and perivascular niches, extensive cross-talk between the two different cell populations has been demonstrated. An example of the interaction between OBs and endothelial cells is the support of the quiescent state and enhanced survival of HSCs in the niche and the increase in angiogenesis due to the activation of Tie-2 on endothelial cells by angiopoietin-1, produced by the OBs [34], [68]–[72]. Likewise, OBs secrete vascular endothelial growth factor (VEGF) that is known to regulate vascularization and bone morphogenesis [73]–[75].

It is clear that multiple cell populations are involved in the HSCs recruitment and maintenance in the niche(s), but it has not yet been established whether the bone marrow holds distinct, topologically separated, highly specialised niches and how exactly the HSCs gain space in these regions of bone.

1.2.1.1 How is access to the HSCs niche regulated?

The involvement of the microenvironment in the regulation of the HSCs function has been widely investigated, however the mechanism(s) required to regulate the foothold of HSCs in the niche(s) remain to be identified. Experiments using transplantation and modification of the cellular composition of the HSCs niche showed that the space within it is limited and can therefore only host a certain number of HSCs [39], [51]. To explain the recruitment of HSCs in the niche(s), different theories have been proposed [41] (figure 1.2). The first theory describes the niche as ‘specialized’, suggesting that the bone marrow presents several distinct niches and that each of them is specialized to hold a specific type of HSCs. The distinction between niches for quiescent and activated HSCs suggest that the cellular composition of these areas is different depending on the function of the niche [76], [77]. The regions holding quiescent HSCs

have been proposed to be rich in OBs, the interaction of the bone cells with the HSCs via N-cadherin, Angiopoietin-1 and thrombopoietin sustain the quiescent state of the HSC, while the activated HSCs are thought to be in close association with the perivascular niche [71].

The alternative model assumes the presence of an ‘equivalent’ niche, able to host both quiescent HSCs and their proliferating progenitors [41]. This theory introduces the concept of competition for limited sites available in the niche, since the HSCs have to compete with other cells that are compatible with this microenvironment to gain access. The concept of an equivalent niche is consistent with the effect of therapies such as chemotherapy or irradiation have on the cells located in the niche. These treatments affect the highly proliferating HSCs progenitors but do not disturb the quiescent HSCs population [41]. Moreover, this model suggests that when HSCs are mobilized into the circulation they leave vacant space in the niche that can be occupied by other type of cells, including tumour cells [16], [26], [36], [78], [79].

It is not clear whether the ‘specialised’ or the ‘equivalent’ niche model is correct, but the second theory has been used in several studies to explain the competitive process that tumour cells undergo to home in areas of the bone marrow supposed to hold HSCs.

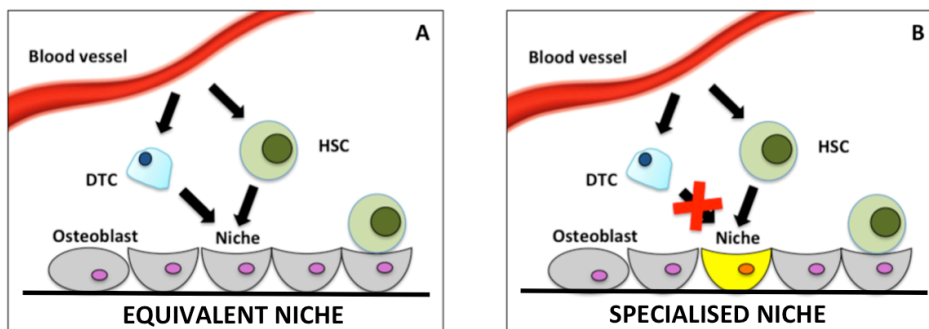


Figure 1.2 Schematic models of competition for the space in the niche

(A) In this model the niche can hold different type of cells. This ‘equivalent niche’ supports the hypothesis of competition between DTC and HSC for gaining the space in the niche. (B) The ‘specialized niche’ (indicated with yellow OB) theory suggests that HSC have their own niche that cannot be occupied by other type of cells.

1.2.1.2 Competition for the limited space in the HSCs niche

It is evident that the HSCs niche represents a fertile soil for the early stage of bone colonization of tumour cells, particularly breast and prostate cancer cells. Furthermore, it has been shown that these are the same areas of bone that have the capability to keep cells in a quiescent state. Tumour cells may therefore use utilise the same signalling pathways in used by the HSCs for the homing to bone, maintenance of the dormant state and switch to active proliferation. One of the most studied is the interaction between CXCR4 expressed by stem cells and CXCL12 expressed in the bone marrow, thought to be crucial in the homing to bone [76], [80]. Several competition studies demonstrate that tumour cells and HSCs not only home to the same niche(s) but they also compete to establish foothold in the bone marrow. Using *in vivo* models of prostate cancer, Shiozawa and colleagues elegantly showed how the mobilization of HSC from their niche created more space available for the subsequent homing of prostate cancer cells [28], [36]. In this study, an antagonist of CXCR4 (AMD3100) was used to mobilise the HSC from the niche. AMD3100 disrupts the interaction between the ligand (CXCR4) and the receptor (CXCL12), resulting in the detachment of the HSCs from the bone marrow niche making them re-enter the circulation. The recruitment of the HSCs in the circulation therefore modified the cellular composition in the niche, making the site available for other cells to colonise. This alteration of the cellular population in the niche resulted in an increase of the number of prostate cancer cells (detected by qPCR) that were able to home and locate in this region of the bone marrow, confirming that the tumour cell co-locate with the HSCs in particular niche situated in the highly vascularised endosteal surface of the bone. Moreover, confocal microscopy was used to localise labelled prostate cancer cells and HSCs after transplant showing that these cells locate in close proximity to each other [36].

It has been reported that breast cancer cell lines express high level of CXCR4, while in normal mammary gland tissue this receptor was not detected [81], [82]. It has been shown *in vivo* that limited expression of CXCR4 reduced the growth of orthotropic breast cancer cells and prevented the development of metastasis from primary tumour to lungs [82]. Moreover, the migratory response to condition media derived from organs commonly colonised by breast cancer cells, such as lungs, liver and bone

marrow, was significantly reduced after blocking the CXCR4 cascade using AMD3100 or CXCR4 RNAi [81]. CXCR4 has been suggested to promote the growth of primary breast cancer by increasing angiogenesis in the primary site, stimulate proliferation and recruiting immune cells that suppress anti-tumour immunity [83]. Due to the involvement of CXCR4 in multiple processes associated with tumour progression and metastatic spread, this marker has been considered as a potential molecule of prognosis and therapeutic target for breast cancer [83]–[85].

1.2.2 The osteoblastic niche

The endosteal surface of the bone is a dynamic region in which bone remodelling is taking place, due to the action of osteoblasts and osteoclasts, and this area also acts as a reservoir of HSCs. The principal components of this niche are the osteoblasts and their main function is bone deposition. This population of cells can be divided in two distinct categories: 1) the active osteoblasts; cuboidal cells that are positive for markers of bone formation (alkaline phosphatase, ALP, and collagen-1, Col-1), and 2) the inactive bone lining cells; flattened cells that stretch over the bone surface forming a protection layer for the metabolically inert bone [34]. As previously mentioned, these bone cells play a key role in the attraction, retention and function of the HSCs. Osteoblasts express several adhesion molecules that form adherent junctions with the HSCs through the surface molecules N-cadherin (N-cad)/ β -catenin (β -cat) and Tie-2/angiopoietin-1 [39], [86], [87]. Once the contact with the osteoblastic cells is interrupted, HSC lose their self-renewal ability and start to differentiate, highlighting the importance on the interaction between these cell types to keep the HSC in a quiescent state [39].

This region of bone has a characteristic plasticity due to the continuous remodelling mediated by actions of the bone-forming osteoblasts and bone-resorbing osteoclasts. Osteoblasts activity lasts as long as the bone apposition is required to replace resorbed bone, after which this type of cells face two types of destiny: to die or turn into cells not functionally active in the bone deposition, like osteocytes or bone-lining cells. Because of this transient aspect of the osteoblasts it is not likely that this type of cells are the only ones implicated in the HSC osteoblastic niche [55], [88]. In addition to the

cell types mentioned above, other components of the bone microenvironment of also play a role in the maintenance of the HSC; for example megakaryocytes secrete factors, including TGF- β , that increase the population of osteoblasts and therefore the size of the niche. Likewise, macrophages are important for niche maintenance as their depletion causes the release of the HSC from their niche [89], [90]. The number and function of osteoblasts can also be modulated by the endocrine system, one striking example is the interaction of parathyroid hormone (PTH) with its receptor (PPR) expressed on osteoblastic cells or mesenchymal stem cells. This interaction causes an increase in the pool of the bone-forming cells and it also enhances their function *in vitro* and *in vivo* [55]. PTH treatment increases the number of HSC niches and thereby the number of HSCs recruited in the bone marrow [36]. Moreover, unpublished data of our lab showed that pre-treatment with PTH results in increased number of breast cancer skeletal metastasis, associating once again osteoblastic action with tumour growth in bone.

1.2.2.1 Osteoblasts and their interaction with cancer cells

In addition to their function in retaining HSC in the niche, osteoblasts may have a role in the attraction and interaction with cancer cells that colonise the bone marrow. As mentioned above, breast cancer cells act in a way similar to the HSC when they gain access in the metastatic niche, due to the similarity of the molecules expressed on both types of cells. Osteoblast and cancer cells interact through several pathways stimulated by secreted factors or direct cell-cell interactions (table 1.1).

Table 1.1 Common molecules involved in pathways of interaction between osteoblasts and cancer cells

Molecules	Function	References
IL-6/ IL-8	Modulation of the osteoblasts differentiation; regulation of angiogenesis	[91], [92]
TGF- β	Regulation of proliferation	[93]
CXCR4/CXCL12	Chemotaxis towards bone; retention in the niche	[36]
E-/N-Cadherin	Cell-cell adhesion	[87]
VEGF	Stimulation of angiogenesis	[73]
IGFs	Cell proliferation	[94]
ET-1	Osteoblast proliferation	[94]
RANK/ RANKL	Bone remodelling	[91]

IL-6/IL-8=interleukin-6/8; TGF- β =transforming growth factor beta; CXCR4=C-X-C chemokine receptor type 4; CXCL12=C-X-C motif chemokine 12 (also know as stromal cell-derived factor 1, SDF-1); VEGF=vascular endothelial growth factor; IGFs=insulin-like growth factors; ET-1=endothelin 1; RANK/RANKL=receptor activator of nuclear factor kappa-B/ligand.

The interleukin-6 (IL-6) pathway is one of the most studied in HSC-osteoblast interactions that is also commonly used by breast cancer cells. IL-6 is an inflammatory cytokine secreted by osteoblasts and macrophages during the remodelling of bone and it is involved in the regulation of cell proliferation, apoptosis angiogenesis and positive modulation of the osteoblasts differentiation [95]. This cytokine is needed for the engraftment of the HSC and these cells in turn modulate its secretion from the osteoblasts. The group of Mundy et al. elegantly described the function of the ‘vicious cycle’ or rather the complex interconnection between the metastatic cells and the bone microenvironment in the late stage of disease [9], and IL-6 is known to have an active role in this process. The cytokine increases the expression of RANKL by osteoblastic cells that binds to RANK on osteoclasts, stimulating bone resorption. The destruction of the bone matrix allows the release of matrix-bound growth factors that stimulate further tumour cell growth. Moreover, it has been demonstrated both *in vitro* and *in vivo* that RANKL stimulates IL-6 expression in breast cancer cells, which in

turn stimulates the expression of RANK on cancer cells themselves to make them more sensitive to RANKL [91], [96]. Furthermore, Rajsiki and colleagues reported that the IL-6 pathway mediates interactions between breast cancer cells and osteoblasts *in vitro*. In their study, several breast cancer cell lines were co-cultured with bone-forming osteoblasts (NHOst) and analysis of the gene expression of both type of cells in the co-culture were performed. Interestingly, the gene expression pattern in the two cell lines was modified in the co-culture compared with the pattern in the single cultures. In particular, two sets of genes were highly increased, the first was genes involved in the DNA replication while the second was the IL-6 signature genes [93].

The ultimate effect of the 'vicious cycle' and the changes in the gene expression is the stimulation of tumour growth, and high levels of serum IL-6 are linked with a poor prognosis in breast cancer patients [93].

It has been proposed that direct contact between osteoblasts and cancer cells is needed for the proliferation of the malignant cells in the bone microenvironment in the early stages of the metastatic colonization. To investigate this hypothesis, Wang *et al.* studied the interactions between breast cancer cells and osteoblasts, with particular focus on the formation of adherent junctions between these cells [87]. Cancer cells were shown to express E-cadherin (E-cad) and this transmembrane protein binds through adherent junctions with N-cadherin (N-cad), expressed on osteoblasts, resulting in activation of the mTOR pathway that is associated with cancer progression.

The importance of interactions between osteoblasts and tumour cells suggest that combining agents that interfere with these could be a potential approach in anti-cancer treatment.

1.2.3 The perivascular niche

The area of bone marrow where the HSCs niche and the osteoblastic niche are located is a highly vascularised region of red-marrow-containing long bone. The organisation of the bone microvasculature has not yet been fully elucidated due to technical difficulties in the visualisation of the three-dimensional structure of the vasculature.

Arteries enter the bone marrow cavity through the cortical bone and a few unbranched arteries are found in the bone diaphysis, while towards the growth plate these vessels are highly branched and arterioles connecting with capillaries in the bone metaphysis. In the bone diaphysis the capillary network is joined to the venular component that is located in the central part of the bone and this exits the bone marrow cavity through the cortical bone [97](figure 1.3). Therefore, because the majority of blood vessels within the bone marrow are in fact capillaries these will be referred to as bone vessels in all subsequent sections of this thesis.

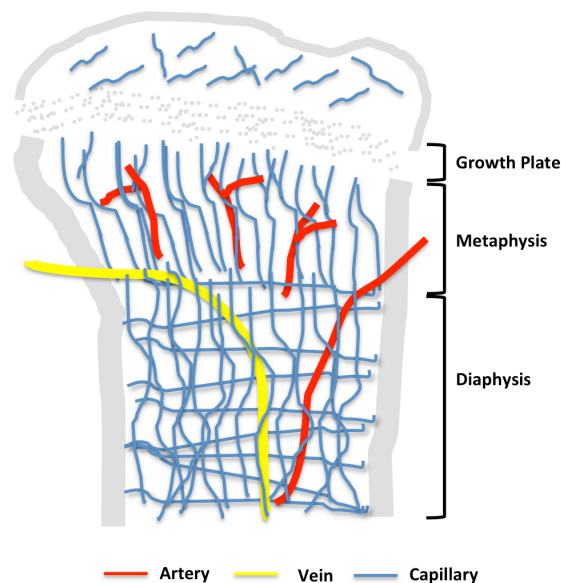


Figure 1.3 Schematic illustration of the vessel architecture in bone

Schematic illustration of the bone microvasculature. A small number of arteries enter the bone marrow cavity through the cortical bone, in the bone diaphysis this structure are unbranched while in the metaphysis they branch and subsequently connect with an extensive capillary network that occupies the majority of the bone marrow. This capillary network typically drains into a large central vein that exits the bone cavity through the cortical bone. Grey=bone, blue=capillary, yellow=vein and red=artery.

The principal role of the microvasculature is the transport of oxygen and nutrients as well as waste products, it also plays a key role in the homing of HSCs and DTCs. *In vivo* studies reported that transplanted hematopoietic stem cells progenitors locate in the trabecular region of bone, where vasculature and endosteal niches are overlapping [98], [99].

As has been described above for bone, the vasculature is a dynamic structure that is balanced between growth and regression and the main factors that control these

processes are vascular endothelial growth factor (VEGF) and pigment epithelial derived factor (PEDF) [100]. Intriguingly, the inhibitor of angiogenesis PEDF and the proangiogenic VEGF are expressed in area of active bone remodelling. Expression of PEDF was detected by immunohistochemistry and real time PCR in cultured murine osteoblasts and marginally in murine osteoclasts, moreover Western Blot analyses on condition media from osteoblasts indicated that they secrete high levels of PEDF. Furthermore, both osteoblasts and osteoclasts cultures expressed high levels of VEGF-A and its receptor VEGF-R1 and -R2 [74]. This data indicate that the inhibitory and stimulating signals for the angiogenic process in bone are tightly coupled with active bone remodelling.

The theory of an overlap between perivascular and endosteal niches, including cross-talk between the components of these niches, is supported by the discovery of new vessel sub-type that couple angiogenesis and osteogenesis. Using an innovative technique for the visualisation of the bone microvasculature, Kusumbe and colleagues detect this novel capillary (H-vessel, CD31^{hi}Endomucin^{hi}) that express high levels of both the endothelial markers Endomucin and platelet endothelial cell adhesion marker (PECAM1) or cluster of differentiation 31 (CD31). The H-vessel sub-type have a specific column-like shape and it is located in the metaphysis region, while another sub-type of vessels expressing low level of the endothelial markers (L-vessel, CD31^{low}Endomucin^{low}) presents a highly branched sinusoidal structure and is localized in the diaphysis [97]. H-vessels have been shown to be surrounded by osteoprogenitors in young murine models. In aged mice, where bone turnover is reduced the presence of this vessel sub-type was limited and only few osteoprogenitors were detected in the surrounding microenvironment [97]. Using transgenic murine system or a pharmacological approach, alterations of the microvascular component were demonstrated to reflect changes in the bone structure and cell populations, indicating a close relationship between these two compartments of the mice [97]. The bone microvasculature is a highly changeable component that stabilises in adulthood, similar to what is seen for bone remodelling. The alteration of both these niches could be therefore an explanation on the reduced level of tumour uptake in mature animal models compared with young animals [101].

1.2.3.1 Regulation of dormancy

As previously stated, breast cancer cells behave like the HSCs and their progenitors in many aspects of process of homing to bone. It is known that microenvironmental signals determine the fate of HSCs by supporting the quiescent state or promoting proliferation and differentiation [102]. Rafii and colleagues observed that human endothelial cells from the bone marrow co-cultured *in vitro* with HSCs progenitors promoted their proliferation and differentiation by production of interleukin-6 (IL-6), Kit-ligand, granulocyte colony-stimulating factor (G-CSF), and granulocyte macrophage colony-stimulating factor (GM-CSF) [103]. The importance of the chemokine signalling between vasculature and HSCs has also been studied using *in vivo* models. Heissig *et al.* demonstrated that the mobilisation of HSCs from a niche supporting the quiescent state to an active vascular niche in the bone marrow where proliferation and differentiation was taken place was influenced by expression of matrix metalloproteinase-9 (MMP-9) and release of soluble c-kit ligand [104]. Furthermore, *in vivo* studies have demonstrated that the regeneration of the bone marrow vasculature after chemotherapy is necessary to re-establish thrombopoiesis [105].

As well as HSCs, disseminated tumour cells (DTCs) require environmental signals to maintain their dormancy or start the proliferation process that result in overt metastasis. Even though the precise mechanism(s) determining the fate of DTCs is not fully elucidated, it has been shown that the vasculature has a key role in the regulation of the growth stimulating or inhibiting signals [78], [106]. Recently, it has been reported that the microvasculature has a key role in the maintenance of tumour cell dormancy via expression of Thrombospondin-1 (TSP-1) [35], [107]. Ghajar and colleagues observed that *in vivo* breast cancer cells, when colonising secondary organs such as lungs and bone, locate in close proximity to microvasculature. Furthermore, in these studies the researchers co-cultured HUVEC cells with mesenchymal cells or fibroblasts and several breast cancer cell lines and noticed that tumour cells seeded in proximity of sprouting vasculature had a higher rate of growth than tumour cells located next to established quiescent microvasculature. These observations led to proteomic and mass spectrometry analyses that revealed that different states of microvasculature development influence the expression of inhibitory (TSP-1) or growth promoting (periostin and TGF- β 1) molecules [35] (figure 1.4). Interestingly, as well as

being soluble in the bone microenvironment, high level of TSP-1 are expressed by myeloid cells and in particular by megakaryocytes. This particular cell population has been shown to maintain HSCs population in a quiescent state *in vivo* [108]. Furthermore, *in vivo* studies underlined the importance of megakaryocytes in the inhibition of metastasis development in both prostate [109] and breast cancer [109], [110] through expression of TSP-1.

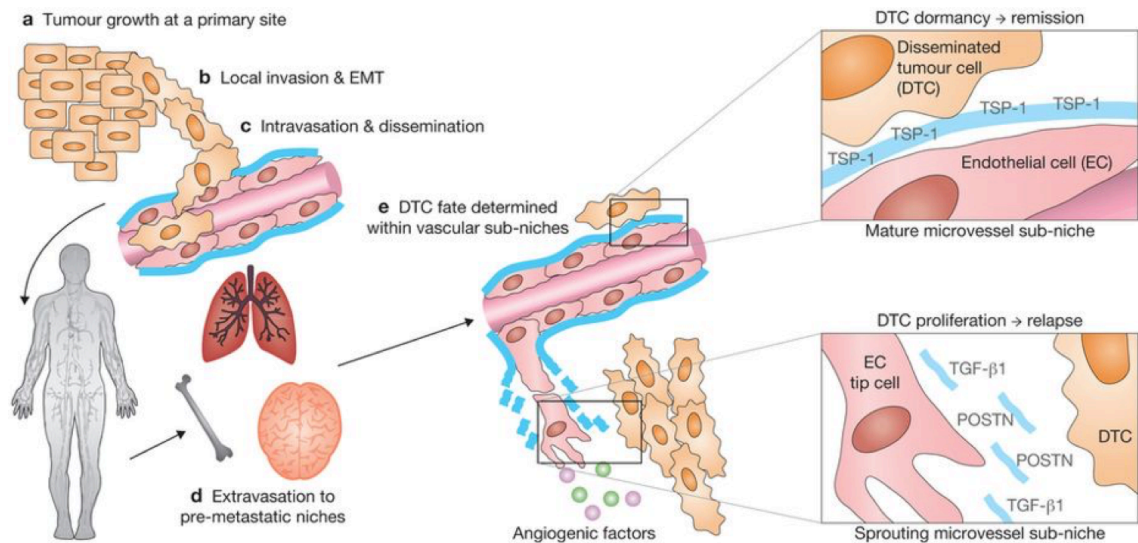


Figure 1.4 Regulation of dormancy by the perivascular niche

Metastatic process steps are illustrated in (a-e). Once the DTC reach the secondary organ, their fate is regulated by the vascular niche; expression of TSP-1 by established vasculature maintain the DTC dormant while production of TGF-1 and periostin (POSTN) by sprouting vessels stimulate the DTC to proliferate. Reprinted by permission from SpringerNature: Nature Cell Biology [107].

1.3 Therapeutic modification of the metastatic niche

As previously discussed, the interaction between cancer cells and bone microenvironment are required from the early stages of the metastatic process. These interactions in turn influence the homing of tumour cells in the secondary organ, the maintenance of dormancy, the initiation of the proliferative state and later the tumour growth progression and consequent osteoclast-mediated bone destruction. Unfortunately, the treatments currently available for bone metastasis are palliative rather than curative, aiming in improving the quality of life of the patients, and the disease-free and overall survival in combination with surgery, radiotherapy or

chemotherapy [30], [111]. The microenvironment plays a key role in the progression of the metastatic disease and therefore it is essential to not only target the tumour cells but also the components of the bone that promote tumour development [111] (figure 1.5).

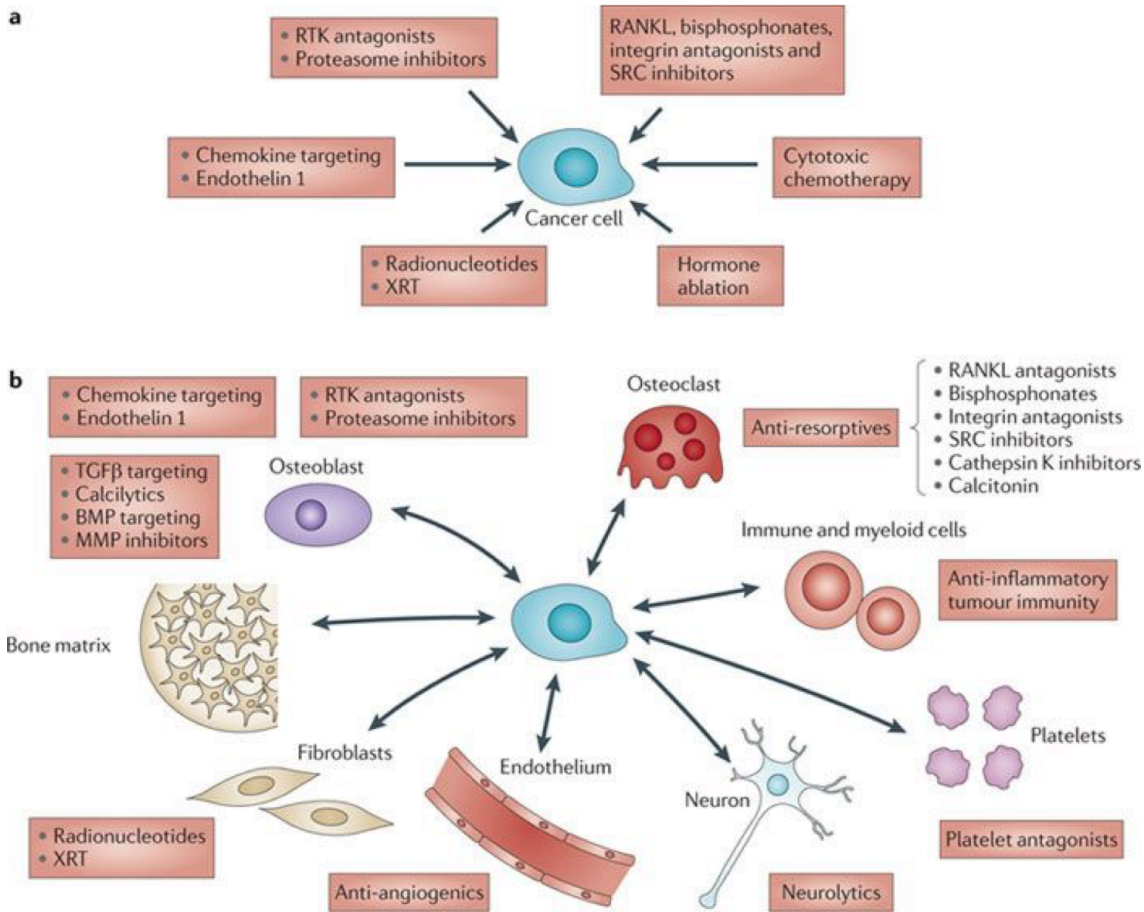


Figure 1.5 Benefits of targeting both cancer cells and microenvironment

Several treatment approaches targeting the cancer cells (a) can also affect the components of the bone microenvironment (b) enhancing the anti-tumour effect. MMP= matrix metalloproteinase; XRT= radiotherapy; RTK=receptor tyrosine kinase; TGFβ=transforming growth factor-β; BMPs=bone morphogenetic proteins. Reprinted by permission from SpringerNature: Nature Reviews Cancer [32].

1.3.1 Targeting the bone cell population of the niche

Once tumour cells are seeded in the bone microenvironment they promote the activation and differentiation of bone-resorbing osteoclasts, this leads to the starting of a vicious cycle in which osteoclasts resorb bone releasing growth factors embedded in the bone matrix which stimulate tumour growth that increase osteoclast activity and inhibit osteoblasts causing bone destruction [15]. To limit the skeletal lesions caused by the bone metastasis, current therapies are focused in the inhibition of osteoclast activity using different approaches, such as cathepsin K, mTOR or c-Scr inhibitors, the standard of care anti-resorptive drugs (bisphosphonates) or anti-RANKL antibody (Denosumab) [111]. The use of bisphosphonates, in particular Zoledronic acid, will be discussed in greater detail as it was used for the in vivo experiment of Chapter 5 of this thesis.

1.3.1.1 Bisphosphonates

Bisphosphonates (BPs) are the standard of care for skeletal disorders, such as osteoporosis and cancer-induced bone disease, and their anti-resorptive activity results in pain relief and reduction of bone lesion incidence [112], [113]. BPs have high affinity for the bone matrix due to their stable P-C-P motif that bind to divalent cations such as Ca^{2+} , Mg^{2+} and Fe^{2+} [114]. The anti-resorptive activity and potency of the BPs is determined by their chemical structure, dividing this class of drugs in two groups: simple BPs and nitrogen-containing BPs. With its complex structure containing a ring structure with nitrogen, Zoledronic acid (ZOL) is the most potent of the BPs presenting a 10,000 fold higher anti-resorptive activity than the simpler BPs [115]. Nitrogen containing BPs, such as ZOL, inhibit the mevalonate pathway which is responsible for the production of isoprenoid and cholesterol required for cell proliferation. In more detail, the inhibitory action of BPs is carried out on the key enzyme farnesyl diphosphate (FPP) synthase, which is responsible for conversion of isopentenyl diphosphate (IPP) to FPP. This results in a lack of prenylation of GTPases, such as Ras, Rab, Rho and Rac that are essential for osteoclast activity and viability [116], [117]. BPs bind to the bone surface in regions of active bone remodeling and this could explain the high selectivity on osteoclasts, however it has been shown that repeated administration of BPs results in the internalization of the drugs by other cells, such as

macrophages, osteoblasts, vascular endothelial cells and tumour cells [44], [117]–[119].

1.3.1.1.1 Anti-tumour effects of BPs

In addition to their anti-resorption action, the anti-tumour effect of BPs has been extensively studied *in vitro* and *in vivo*. As indicated in figure 1.6, this anti-tumour effect is both direct to tumour cells and indirect acting on the microenvironment in which the tumour develops.

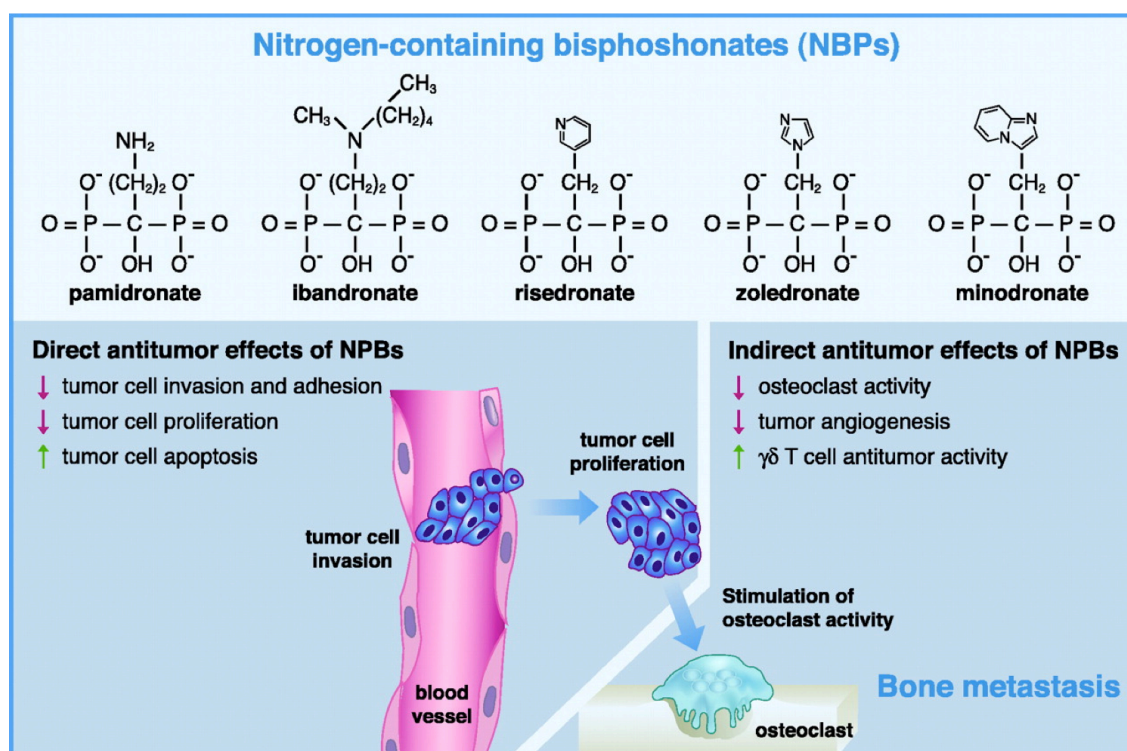


Figure 1.6 Chemical structure and anti-tumour effects of nitrogen-containing bisphosphonates

Nitrogen-containing BPs (chemical structure on the top panel) can have a direct anti-tumour effect interfering with cell adhesion, invasion, proliferation and survival and an indirect one, inhibiting bone resorption, angiogenesis and stimulating T cells. Reprinted by permission from American Association for Cancer Research: Cancer Research [120].

In vitro studies performed on several cancer cell lines, including breast cancer, indicate that BPs induce apoptosis, inhibition of proliferation, invasion and adhesion [121]–[123]. However, these *in vitro* studies used prolonged exposure and/or high doses of BPs that are not achievable *in vivo*. In clinical settings ZOL is administered at a dose of 4mg infusion every 3-4weeks and it has been shown to have a short serum half-life (approximately 1 hour), however in bone ZOL is stored for years and bone resorption caused by osteoclasts releases the drug stored in the matrix and that could in theory induce cytotoxic effects in DTC in bone [124], [125]. In addition to the cytotoxic effect of ZOL on tumour cells, BPs also have an indirect anti-tumour effect via disruption of the vicious cycle of bone metastasis. The majority of the preclinical studies performed *in vivo* identify the inhibition of the osteoclast-mediated bone resorption as the major cause for the reduction of tumour burden in animal models treated with ZOL [30], [32], [126]–[128] and reduction of the tumour relapse incidence in animal models [129], [130]. Even though treatment with ZOL caused a change in the bone microenvironment resulting in reduced development of overt metastasis, a combination therapy with repeated dosing of cytotoxic drug such as doxorubicin (DOX) and ZOL had a more potent anti-tumour effect in tumour bearing mice [120], [126], [127], [131], [132]. Furthermore, it has been shown that in mice, a single administration of ZOL affects the metastatic process from the early steps, altering the pattern of homing of breast cancer cells in the bone microenvironment, probably due to the modification of the bone resident cells number and activity [118]. The bone microenvironment is complex, with multiple components that interact to regulate of each others functions, it is therefore surprising that the information on the effect of ZOL on other cell type residing in bones is limited. In the literature there are reports indicating that ZOL increases level of apoptosis in macrophages both *in vivo* and *in vitro* [44], [133]. Additionally, ZOL has been shown to have an effect on haematopoiesis and on the generation of tumour-suppressing bone marrow cells. A single dose of ZOL (100µg/kg) administered to both immunocompromised and immunocompetent mice increased the number of progenitors of HSCs, myeloid cells, megakaryocytes and macrophages in the bone marrow. Moreover, when bone marrow cells isolated from animals treated with ZOL were added to MDA-MD-231 cells that

were subsequently injected subcutaneously in recipient mice, researchers observed that tumour incidence in animals injected with bone marrow cells deriving from mice treated with ZOL was reduced, indicating that ZOL contributed to the generation of tumour-suppressing bone marrow cells [134].

Furthermore, emerging data indicated that anti-tumour effect of ZOL is partially mediated by its anti-angiogenic properties. *In vitro* and *in vivo* studies reported a reduction of angiogenesis and proliferation, migration and tubule formation of HUVEC cells (0.31-160 μ M ZOL for 24, 48 or 72h)[135], [136]. Moreover, it has been shown that ZOL inhibits proliferation of endothelial progenitors and causes their apoptosis in a dose-dependent manner [137]. In agreement with this, cancer patients treated with BPs show a reduced level of the angiogenic factor VEGF after intermittent treatment with low-doses of ZOL [138].

1.3.1.1.2 Clinical use of BPs

Bone metastasis can cause hypercalcemia, bone pain, pathological fractures and spinal cord compression and usually bisphosphonates are used to treat these skeletal morbidities in metastatic breast and prostate cancer and advanced multiple myeloma [139]. The efficacy of BPs in treating the skeletal disease suggested that BPs could potentially be used in adjuvant setting to prevent bone metastasis. Early clinical studies reported improved disease-free survival as well as overall survival of patient presenting breast cancer (stage I-III) following treatment with clodronate [140]. These promising results obtained with one of the weakest BPs, led to several clinical investigations on the potential of more potent BPs, such as ZOL. Clinical trials, including the ABSCSG-12, AZURE and ZO-FAST, investigated the beneficial effect of ZOL in the adjuvant setting in combination with endocrine therapy, aromatase inhibitors and chemotherapy [139], [141]–[144]. In the ABSCSG-12 trial, premenopausal patients who had received ovarian function suppression (and thus should be considered postmenopausal, n=1,803), with endocrine responsive breast cancer were treated with the aromatase inhibitor anastrozole +/- ZOL. The addition of the BP to the endocrine treatment resulted in an increase in disease-free survival. Furthermore, the administration of ZOL decreased the development of metastases both inside and

outside bone, as well as regional recurrence and eliminated the cancer-treatment induced bone loss [144]. Comparable studies were performed in the ZO-FAST trial, in which postmenopausal women with hormone-receptor positive breast cancer (n=1,065) were treated with the aromatase inhibitor letrozole +/- ZOL [144]. Patients treated with ZOL had an increase in the bone mineral density and, in agreement with the ABSCSG-12 trial, they had a prolonged disease-free survival and reduction of distant disease both inside and outside bone [143], [144]. The design of the AZURE trial was slightly different from the studies discussed above, in this trial women with both hormone-receptor positive and negative breast cancer were included regardless their menopausal status (n=3,360); patients were treated with standard therapy +/- ZOL [142]. In contrast with the previous studies, the AZURE trial did not show a difference in the overall disease-free survival between the treatment groups. However, subgroup analyses demonstrated that postmenopausal patients had a beneficial effect with the adjuvant ZOL by preventing or delaying cancer recurrence and development of skeletal metastases [141], [142].

The Early Breast Cancer Trial Collaborative Group (EBCTCG) performed a meta-analysis of results from 26 randomised trials on treatment with BPs involving 18,766 women describing that clinical outcomes, such as the time till the first overall recurrence, recurrence in bone, distant recurrence in any site and breast cancer mortality, was improved only for postmenopausal women [145]–[147]. Furthermore, the differential effect of menopausal status has also been demonstrated *in vivo*, showing the effectiveness of ZOL in preventing the development of overt tumour from disseminated tumour cells varies between animal models mimicking the pre- and post-menopausal status [148], [149]. These data suggest that the bone microenvironment plays a key role in the progression of the metastatic disease, however the reason for this differential effect in pre- and post-menopausal women is unknown and the mechanism(s) behind it remains to be identified.

1.3.2 Targeting the microvasculature

The importance of angiogenesis for tumour development and progression is a well-known concept. In the 1970s, Folkman observed that in the absence of vascularisation, tumour growth was arrested and that pro-angiogenic factors were released not only by the microenvironment but also by the neoplastic cells, suggesting that the tumour vasculature could be a potential target in the treatment of cancers [150]. Stromal and tumour cells produce pro- and anti-angiogenic factors that modulate the vascularisation required for tumour growth; the key regulator factors include vascular-endothelial growth factor (VEGF), platelet-derived growth factor (PDGF), epidermal growth factor (EGF) and fibroblast growth factor (FGF) [151].

VEGF is one of the most important pro-angiogenic signals in tumour vascularisation from the early stages of the tumour development and high tumour expression of VEGF is considered a marker for a poor prognosis [152], [153]. Thus, VEGF was one of the first targets for the development of anti-angiogenic therapies in the treatment of cancer. Bevacizumab is a recombinant humanised VEGF-neutralising antibody that has been shown to reduce tumour growth in several human cell lines, such as ovarian, prostate, colon and breast cancer, in animal models and inhibit metastasis development; combination with chemotherapy or radiotherapy resulted in additive and synergistic effects [154], [155]. Bevacizumab received FDA approval for the treatment of several cancers, including cervical, colorectal, glioblastoma, ovarian and renal cancer [156], but the approval for breast cancer has been controversial. Clinical trials show modest effects of bevacizumab treatment that could not compensate for the risk of life-threatening side effects including hypertension, proteinuria, haemorrhage, wound healing complications, arterial thromboembolism and gastrointestinal perforation. As a result of these widespread toxicities, FDA approval has been revoked for the use of bevacizumab in the treatment of metastatic breast cancer [157]–[159].

1.3.2.1 Cediranib

Over recent years, additional agents targeting the VEGF pathway have been developed, including tyrosine kinase inhibitors (sunitib and sorafenib) that have shown therapeutic benefit in the treatment of several tumours [160], [161]. Receptor tyrosine kinase consists of an extracellular N-domain binding the ligand, a transmembrane domain, an intracellular C-terminal domain, with a kinase domain with binding cleft for ATP between the C- and the N-terminal. Binding of ligand to the extracellular domain results in dimerization of the receptor and stimulation of the tyrosine kinase activity, leading to activation of (multiple) signal pathways involved in biological responses such as cell activation, proliferation, differentiation, migration, survival, and vascular permeability [162].

Cediranib (AZD2171) is a highly potent, orally available novel pan-VEGF receptor tyrosine kinase inhibitor (TKI) developed by AstraZeneca (chemical structure and mechanism of action illustrated in figure 1.7). The key target of this drug is VEGFR-2, but cediranib has been shown to be active against VEGFR-1 and 3, c-KIT and with lower potency also inhibits PDGFR- α and PDGFR- β [163], [164]. Effective towards multiple targets, cediranib inhibits both angiogenesis and lymphangiogenesis and could therefore be potentially beneficial for the prevention of tumour growth. Moreover, the orally available formulation and the short half-life (12.5-35.4 hours) allow a daily dosing that could be performed autonomously by the patients.

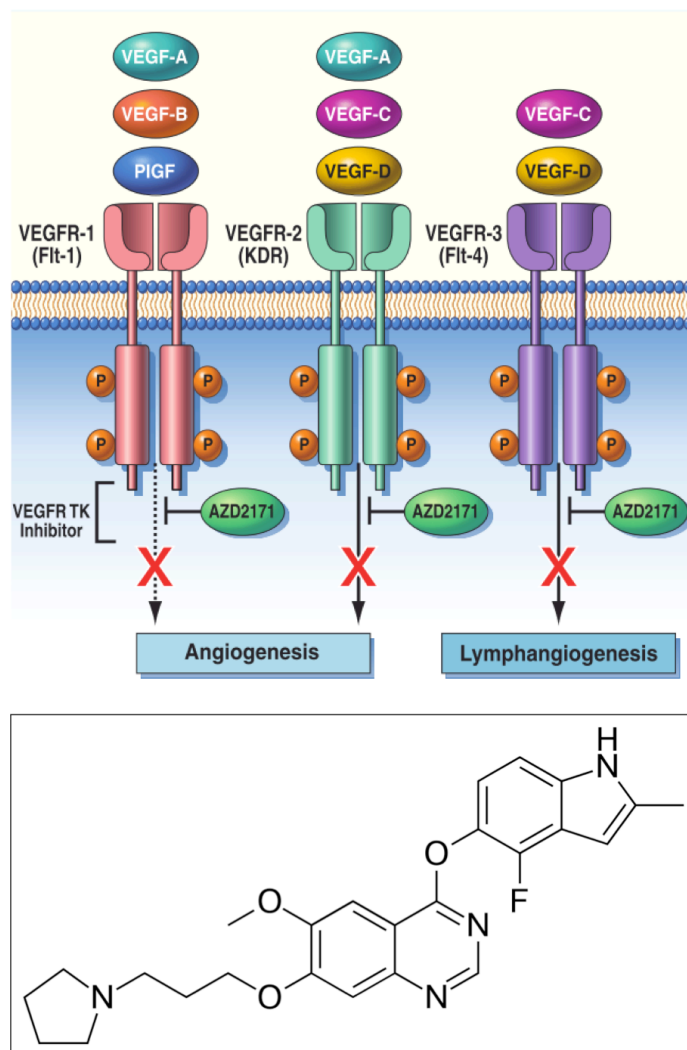


Figure 1.7 Chemical structure and mechanism of action of Cediranib

Chemical structure of the TKI cediranib is illustrated in the bottom panel. Cediranib is pan-VEGFR tyrosine kinase inhibitor; by blocking the action of VEGFR-1 and 2 the TKI inhibits angiogenesis while lymphangiogenesis is blocked by the inhibition of VEGFR-3. Flt-1=fms-like tyrosine kinase 1; KDR=kinase insert domain protein receptor; PlGF=placental growth factor; TK=tyrosine kinase. Adapted and reprinted by permission from Elsevier: Clinical Breast Cancer [165].

1.3.2.1.1 Anti-tumour effects of Cediranib

In addition to the anti-angiogenic activity of this TKI, the efficacy in several cancers has also been tested extensively *in vitro*, *in vivo* and in clinical studies, with multiple ongoing trials.

In vitro studies were performed to compare the efficacy of three TKIs, Cediranib, Sunitinib, and Imatinib, on viability, cell cycle, apoptosis, migration, and invasion on eight glioblastoma cell lines. Cediranib was found to be the most potent of the TKIs tested with a half-maximal inhibitory concentration (IC₅₀) of $1.71 \pm 0.97\mu\text{M}$ compared to Sunitinib (IC₅₀ $2.92 \pm 1.59\mu\text{M}$) and Imatinib (IC₅₀ $13.01 \pm 6.09\mu\text{M}$)[166]. Furthermore, the viability, migration, invasion and cell death was also investigated for three breast cancer cell lines, Hs578T (ER-), MDA-MB-231 (triple-negative) and T47D (ER+, PR+/-, HER2-) treated with Cediranib. Cediranib IC₅₀ were measured at 24, 48 and 72 hours and the values at 72h for the first two cell lines were comparable with the IC₅₀ observed for glioblastoma cell lines ($2.08 \pm 0.77\mu\text{M}$ Hs578T and $2.52 \pm 0.81\mu\text{M}$ MDA-MB-231) while the concentration needed to inhibit T47D was considerably higher (IC₅₀ $18.85 \pm 3.21\mu\text{M}$). Cytotoxic effects were measured analysing the poly(ADP ribose) polymerase (PARP) cleavage and the results indicated that Hs578T and MDA-MB-231 exhibit greater level of cleaved PARP than T47D cells following cediranib treatment, suggesting a resistant profile in this cell line. Wound-healing assays were performed to determine the migration of these cell lines after treatment with can results indicated Hs578T (80% inhibition) to be the most sensitive of the breast cancer cell lines analysed, followed by T47D (70%) and MDA-MB-231 (54%). Cediranib treatment significantly inhibited cell invasion in all breast cancer cell lines [T47D (70%), Hs578T (60%) and MDA-MB-231 (30%)] compared to control. Cediranib-induced modulation of miRNA expression showed that Hs578T is the most sensitive cell line used in this study, however targets shared with the MDA-MB-231 cell lines, including VEGFA, VEGFC, and PDGFRA, were implicated in important biological processes such development, metabolic processes, cell motility and homeostasis [167].

In addition to the *in vitro* studies indicating the potential of Cediranib as an anti-tumour drug, several investigations were performed *in vivo* to detect the efficacy of

the TKI in animal models across a number of cancer cell types. Wedge *et al.* described the broad-spectrum anti-tumour activity of Cediranib on growth of several subcutaneous tumours, including colon, lung, ovary, prostate and breast cancer. In this *in vivo* study nude mice were treated daily for 28 days (24 days in the case of breast cancer cell line MDA-MB-231) with a range of doses of TKI (0.75-6 mg/kg/daily) resulting in significant inhibition of tumour growth [168]. Several groups confirmed the anti-tumour efficacy of Cediranib in different animal cancers models, such as primary renal carcinoma [169], colorectal carcinoma [170], prostate cancer [171], glioblastoma [166], [172], ovarian carcinoma [173], thyroid cancer [174] and ovarian cancer [175].

Cediranib was associated with a reduction of tumour angiogenesis, but the effect that the administration of this drug has on the bone microenvironment, was only marginally investigated. Wedge and colleagues reported a severe epiphyseal growth plate dysplasia in rats treated with Cediranib for 28 days, that was reversed 28 days after stopping the treatment with the TKI [168]. Yin observed that metastatic growth in bone was reduced with the administration of Cediranib in both the treatment as well as in preventative settings, but any effects that the drug had on the bone microenvironment were not reported [171]. Thus, the aim of Chapter 6 of the work presented in this thesis was to fill the gap in the knowledge about the potential changes of the bone structure and microvasculature caused by treatment with Cediranib.

1.3.2.1.2 Clinical use of Cediranib

After obtaining promising data in pre-clinical models, the efficacy of Cediranib in various cancer types has been tested in clinical studies. Currently several trials using Cediranib as monotherapy or in combination with other compounds are ongoing, a summary of the clinical trials involving breast cancer can be found in table 1.2.

Table 1.2 Currently ongoing and completed clinical trials using cediranib for the treatment of breast cancer

Name	Phase	Patients/tumour type	ClinicalTrials.gov identifier
AZD2171 in addition to Fulvestrant in patients with advanced breast cancer	II	Advanced breast cancer (hormone sensitive breast cancer with histological evidence of metastatic disease)	NCT00454805
A phase II study of AZD2171 in breast cancer stage IV	II	<ul style="list-style-type: none"> • Male breast cancer • Recurrent breast cancer • Stage IV breast cancer 	NCT00244881
AZD2171 and combination chemotherapy in treating women with locally advanced breast cancer	N/A	Locally advanced breast cancer (stage IIIA-C)	NCT00310089
Cediranib maleate and Olaparib in treating patients with recurrent ovarian, fallopian tube, peritoneal cancer or recurrent triple-negative breast cancer	I/II	<ul style="list-style-type: none"> • Deleterious BRCA1/2 Gene Mutation • Estrogen Receptor Negative • HER2/Neu Negative • Ovarian Endometrioid Adenocarcinoma • Ovarian Serous Surface Papillary Adenocarcinoma • Progesterone Receptor Negative • Recurrent Breast Carcinoma • Recurrent Fallopian Tube Carcinoma • Recurrent Ovarian Carcinoma • Recurrent Primary Peritoneal Carcinoma • Triple-Negative Breast Carcinoma 	NCT01116648
Phase I/II study of the anti-programmed death ligand-1 antibody MEDI4736 in combination with Olaparib and or cediranib for advanced solid tumours	I/II	<ul style="list-style-type: none"> • Lung cancer • Breast cancer • Ovarian cancer • Colorectal cancer • Prostate cancer • Triple negative breast cancer 	NCT02484404
Gamma-secretase inhibitor RO4929097 and cediranib maleate in treating patients with advanced solid tumours	I	<ul style="list-style-type: none"> • Adult anaplastic Astrocytoma/Ependymoma/Oligodendroglioma • Adult Glioblastoma/Giant cell Glioblastoma/Brain stem Glioma/mixed Glioma/Gliosarcoma • Male breast carcinoma • Colorectal carcinoma (recurrent and stage III/IV) • Skin melanoma (recurrent and stage III/IV) • Ovarian cancer (recurrent and stage III/IV) • Breast cancer (recurrent and stage III/IV) • Pancreatic cancer (recurrent and stage III/IV) • Renal cancer (recurrent and stage III/IV) • Non-small cell lung cancer (recurrent and stage III/IV) 	NCT01131234
A phase II study of cediranib in combination with Olaparib in advanced solid tumours	II	<ul style="list-style-type: none"> • Pancreatic cancer stage III/IV • Non-small cell and small cell lung cancer stage III/IV • Oestrogen receptor negative, HER2 negative and triple-negative breast cancer stage III/IV 	NCT02498613

Hyams and colleagues investigated the effect of Cediranib in combination with the oestrogen receptor antagonist Fulvestrant for the treatment of post-menopausal women with metastatic hormone-sensitive breast cancer (n=75) [176]. Cediranib was administered at an initial dose of 45mg in combination with Fulvestrant, but this caused several side effects, such as diarrhoea, fatigue and hypertension, therefore doses were reduced. The results showed a trend in the progression-free survival and decrease of tumour size in the combination treatment but the data did not reach statistical significance. This indicates a potential beneficial effect of Cediranib in combination with hormonal agents or chemotherapy, possibly at a lower dose (30mg/day) [176]. Similar indication for the reduction of the dose of Cediranib was obtained in a small clinical trial (n=39) investigating the safety/tolerability of the TKI with Saracatinib (inhibitor of the proto-oncogene Src) for the treatment of advanced solid tumours, such as colorectal, pancreas, ovary, liver and breast cancer [177]. A 30mg/daily dose was used also in combination with the PARP-inhibitor Olaparib, and even though 75% of the patients experienced a grade 3 or higher toxicity, suffering from diarrhoea, fatigue, nausea, decreased neutrophil count and hypertension; these events were anticipated and manageable. This regime was used for the treatment of recurrent epithelial ovarian cancer and metastatic triple negative breast cancer. Ovarian cancer patients responded well to the treatment with a clinical benefit rate of 61%, the two patients with BRCA mutation carriers in metastatic triple negative breast cancer patients showed a reduction of approximately 27% of tumour size however due to the limited sample size it was not possible to draw conclusion on the effect of the combination therapy in this cancer type [178].

Even though several clinical trials did not meet their primary end point [179], [180], the investigation of the potential beneficial effects of treatment with the TKI as part as combination therapies continues to be evaluated.

1.3.3.1 Deferoxamine mesylate

One other important pathway target in anti-angiogenic treatment is the hypoxia inducible factor-1 α (HIF-1 α). When tumour cells proliferate quickly to generate solid masses, blood vessels get obstructed leading to poor oxygen supply to the centre of the tumour, creating a hypoxic region. To survive in this restrictive microenvironment, tumour cells activate the HIF-1 transcription factor which led to the activation of downstream genes required for the regulation of tumour survival in low oxygen condition, such as glucose metabolism, cell proliferation, migration and angiogenesis. Considering its function in tumour progression and metastasis, developing inhibitors targeting the HIF-1 α pathway has been of great interests. However, HIF-1 α pathway is involved in several physiological processes (e.g. angiogenesis, cell proliferation, metabolisms of iron and glucose), cell therefore targeting off only hypoxic tumours without disrupting normal homeostasis remains a considerable challenge [181].

In the work presented in Chapter 6 of this thesis, the HIF-1 α pathway was targeted to increase the microvascular activity to detect potential changes in the homing of tumour cells in an altered microenvironment, rather than trying to inhibit the pathway to obtain an anti-angiogenic and consequently an anti-tumour effect. Deferoxamine mesylate (DFM) was used to enhance HIF-1 α . This iron chelator inhibits the prolyl hydroxylase domain (PHD) resulting in stabilization of HIF-1 α which can then bind to HIF-1 β , translocation of the complex to the nucleus and induction of transcription of several hypoxia inducible genes [182], [183]. DFM has been shown to increase tubule formation by endothelial cells *in vitro* and to enhance angiogenesis in response to acute hindlimb ischemia *in vivo* [184], [185]. As discussed previously, angiogenesis and osteogenesis are tightly connected, therefore it is not surprisingly that several studies indicated that the pro-angiogenic effect of DFM is accompanied by an increase of bone mass in various animal models [97], [186]–[193]. Kusumbe and colleagues treated aged mice (60-65 weeks old) with DFM (15mg/ml per mouse every other day for 4-6 weeks) and they observed a significant increase in the trabecular bone, number of osteoprogenitors and presence of H-vessels in treated animals [97]. *In vivo* studies demonstrated the efficacy of this treatment to repair bone injuries. A rat model of was used to observe the effect of DFM on bone repair in combination with hindlimb

suspension. Hindlimb suspension-induced a reduction in the bone repair, however this effect was mitigated with the treatment with DFM (2 or 5 doses of 20 μ l of 200 μ mol/L on alternate days) that increased both the angiogenesis and osteogenesis [187]. Similar results were also obtained in a mouse model of hindlimb unloading, where animals receiving 10mg of DFM once a week for 3weeks showed an increase in the bone mass reverting the bone loss caused by the tail suspension [188]. Deferoxamine treatment in rat presenting mandibular distraction enhanced the angiogenesis and the osteogenesis [193]; furthermore, this results were obtained also when the animal models were exposed to radiation [190].

In addition to the investigation of the effect of DFM treatment on bone structure and microvasculature, a few studies examined whether DFM caused a change in the behaviour of cancer cells displaying a pro-tumorigenic effect *in vitro*. *In vitro* assays indicated that treatment with DFM increased migration and invasion of MDA-MB-231 without affecting their viability (dose range 30-300 μ M) [194]. The treatment induced an increase in intracellular level of iron in aggressive MDA-MB-231 cells, while this was deplete in MCF-7 cell line. Moreover, the MDA-MB-231 cells showed increased cell migration and higher level of mesenchymal markers after administration of DFM [195]. To support the theory that DFM should be carefully used in patients with breast cancer, Duarte and colleagues reported that HSCs homing to bone marrow is increased after administration with DFM [196]. Since HSCs and breast cancer cells are thought to use similar mechanism to home to the bone marrow, in chapter 6 of this thesis I investigated whether the treatment with DFM altered the components of the metastatic niche and if this modification of the microenvironment was reflected in a change in the number of tumour cells seeding to bone.

1.4 Summary, conclusion and outstanding questions

In summary, breast cancer cells colonise an area of bone marrow, known as the metastatic niche, where the HSC, osteoblastic and perivascular niche are at least partially overlapping. The components of the complex microenvironment that comprise the metastatic niche are key players that regulate multiple steps of the metastatic process, including the homing of cancer cells to bone, in the maintenance of dormancy, in the proliferation of tumour cells and finally in the creation of bone lesions. Moreover, the different cellular components of the metastatic niche are intimately interconnected and they can influence the activity of each other, both through direct cell contact and through release of soluble factors.

Currently there are no curative treatments available for metastatic disease, but only palliative measures that treat the symptoms of the secondary disease, such as slowing down the cancer-induced bone resorption. It has been demonstrated that alterations in the microenvironment cause changes in the growth of metastasis in bone, but it is still not fully understood to what degree modification of one component of the niche also influences the overlapping niches, or how this affects disseminated tumour cells. To date, most of the therapeutic approaches are focused on targeting bone cells (mainly osteoclasts) and tumour cells, but targeting only one of the key players of the progression of the secondary tumour is not sufficient to arrest the metastatic development. Little is known about the role of the bone microvasculature in bone metastasis and response to therapy. Additional information on the mechanism of response to therapies by the microenvironment are needed to eventually find new potential therapeutic targets.

1.5 Hypothesis, aims and objectives

The principal aim of this work was to increase the understanding of the role of the bone microvasculature in the early stages of breast cancer bone metastasis. To address this aim the following hypothesis will be tested:

Breast cancer cells located in a region of bone in which HSC, osteoblastic and perivascular niches (partially) overlap and the tightly connected components of the niche mediate the response to therapeutic agents.

The main aims of this thesis were as follows:

- To assess the pattern of homing of breast cancer cells in bone *in vivo* using several cell lines and routes of administration
- To characterize the microenvironment of tumour promoting (young mice) and of dormancy supporting (mature mice) animal models
- To determine whether the modification of the bone component of the niche was reflected in modification of the perivascular component of the niche and the homing of breast cancer cells to bone
- To investigate the effect of changes of the microvasculature on the bone component of the niche and the homing of breast cancer cells to bone

Chapter 2

Materials and Methods

Materials

Table 2. 1 Laboratory reagents or kits

Reagent or Kit	Supplier
Acetic Acid	AnalaR VWR
AMD3100	Sigma-Aldrich
Cediranib	Selleckchem.com
Cryo-M-Bed	Bright
DAPI	Invitrogen, Thermo Fisher Scientific
Deferoxamine mesylate	Sigma-Aldrich
DMEM culture medium	Gibco
DMSO	Sigma-Aldrich
DPX mountant	VWR
EDTA	Sigma-Aldrich
Eosin	Atom Scientific LDT
Gelatine for porcine skin	Sigma-Aldrich
Gill's haematoxylin solution	Merck
Isoflourane, IsoFlo	Abbott
Luciferin	Perkin Elmer
Masson-Goldner trichrome staining kit	Merck
Naphthol AS-BI phosphate (sodium salt)	Sigma-Aldrich
Paraformaldehyde	Sigma-Aldrich
PBS for <i>in vivo</i> studies and tissue culture	Gibco,
PBS tablets	Oxoid
ProLong Gold antifade reagent	Invitrogen, Thermo Fisher Scientific
PVP	Sigma-Aldrich
RPMI culture medium	Gibco
Sodium Hydroxide pellet (NaOH)	Fisher Scientific
Streptavidin/Biotin Blocking Kit	Vector Laboratories SP-2002
Sucrose	Fisher Scientific
Toluidine Blue O	Sigma-Aldrich
Triton-X 100	Sigma-Aldrich
Tween-80	Sigma-Aldrich
Vibrant-CM-Dil Cell-Labeling Solution	Life Technologies
Vibrant-DiD Cell-Labeling Solution	Life Technologies
Zoledronic Acid	Novartis

Table 2.2 Plastic and disposable equipment

Cell strainer 70µm	BD Biosciences
Cover slips (22x22 and 22x40mm)	Menzel-Gläser
Cryovials (1ml)	Thermo Scientific
Filter tips (10, 20, 200 and 1000µl)	STARLAB
Glass bottomed dish 12mm	Thermo Scientific
Insulin syringe (0.5 and 1ml) with needle (27G)	Terumo Europe N.V.
Microcentrifuge tubes (0.6 and 1.5ml)	STARLAB
Needle (25G)	Becton Dickinson UK Ltd.
Pipette tips (10, 20, 200 and 1000µl)	Costar
Strippets (5, 10 and 25ml)	Costar
SuperFrost PLUS microscope slides	Thermo Scientific
Syringe (1ml)	Terumo Europe N.V.
Tissue culture flasks (T75)	Nalgene Nunc Ltd.
Universal containers, Bijoux tubes	Starstedt

Table 2.3 Software used for data analysis

Aperio ImageScope	Leica Biosystems
CTAnalyser software	SkyScan, Burker microCT, CT-Analyser version
Fiji (ImageJ)	ImageJ, version
GraphPad Prism software	Prism, version
LAS AF	Leica
Living Image 4.0 software	Caliper Life Science
Nrecon	OsteoMetrics
Volocity software	Improvision, version 4.3.2
NIS-Element Confocal	Nikon
ZEN software	Zeiss

Table 2.4 Laboratory equipment

Benchtop Centrifuges	MSE Mistral 2000
Centrifuge	Beckman
Confocal microscope	Zeiss LSM880 AiryScan and Nikon A1
Cryostat	5030 Microtome, Bright
Cryostat	MICROM HM560
Desktop X-ray microtomograph	SkyScan 1272, Bruker microCT
IVIS Lumina II	Perkin Elmer
Multiphoton Confocal Microscope	Zeiss LSM510 NLO Inverted
Olympus BX53 microscope	Olympus BX53
pH meter SevenEasy	Mettler Toledo
Superfrost Plus Slides	Thermo Scientific, J1800AMNZ
Vortexer	Rotamixer, Hook&/tucker Instruments
Water bath	Grant JB Series
Widefield fluorescence microscope	Leica AF6000

Methods

In vitro experiments

2.1 Cell Lines

All the human breast cancer cell line were handled in aseptic conditions under laboratory containment level 2, as recommended by the European Collection of Cell Cultures (ECACC) and the American Type Culture Collection (ATCC) (table 2.5). DNA fingerprinting was used to confirm cell lines authenticity.

Table 2.5 Molecular classification of breast cancer cell lines used in this thesis

Cell line	Classification	Immunoprofile	Other characteristic
MCF-7	Luminal A	ER+, PR+/-, HER2-	Ki67 low, endocrine responsive, often chemotherapy responsive
T47D	Luminal A	ER+, PR+/-, HER2-	Ki67 low, endocrine responsive, often chemotherapy responsive
MDA-MB-231	Claudin-low	ER-, PR-, HER2-	Ki67, E-cadherin, claudin-3/4/7 low, intermediate response to chemotherapy

ER=oestrogen receptor, PR=progesterone receptor, HER2=human epidermal growth factor receptor

2.1.1 MDA-MB-231-GFP-IV bone homing

MDA-MB-231 cell line was first isolated from the pleural effusion of a 51-year old Caucasian woman presenting with breast adenocarcinoma. The characteristics of this cell line is that it does not express the receptors for oestrogen (ER), progesterone (PR) or human epidermal growth factor receptor-2 (HER-2) [197]. This triple negative breast cancer cell line is tumorigenic in a murine model and, when administered via intra-cardiac injection the animals develop bone metastasis, in particular in the metaphysis areas of the hind limbs. Tumour growth in non-bone sites is rarely seen using this injection route.

The cell line used to determine the homing pattern of tumour cells in the early stages of bone metastasis was a highly bone-seeking clone derived from the MDA-MB-231 cell line. MDA-MB-231 cells were previously transfected with enhanced green fluorescent protein (eGFP) [131] and subsequently the GFP positive clones were injected *in vivo* to obtain the bone-homing cell line. MDA-MB-231-GFP-IV. These cells were injected in the left cardiac ventricle and tail vein of immunocompromised mice, tumour colonies obtained were isolated from the bone marrow based on GFP expression and subsequently re-injected seven times [198]. These seven cycle of injections were required to generate a cell line that homes to bone following injection into the tail vein of animal models.

2.1.2 MDA-MB-231-B02

To compare the pattern of homing of breast cancer cells within the bone marrow, the MDA-MB-231-B02 cell line was used. The B02 clone was also generated following transfection with GFP to obtain a traceable cell line and the highly bone homing clone developed through repeated *in vivo* passages [129].

2.1.3 MDA-MB-231-NW1-Luc2

Tumour growth studies were performed with the MDA-MB-231-NW1-Luc2 cell line. This clone had been transfected with a luciferase vector by Dr. Ning Wang (University of Sheffield, UK), producing a cell line that can generate tumour colonies traceable with the In Vivo Imaging System (IVIS) following prior subcutaneous injection of the substrate luciferin. Mice administered via intra-cardiac injection (i.c.) with this clone develop detectable hind limb micro-metastasis as early as 3-5 days post injection, highlighting the aggressiveness of the cell line.

2.1.4 MCF-7

MCF-7, acronym of Michigan Cancer foundation-7, is a breast cancer cell line established in 1970 from the pleural effusion of a 69-year-old Caucasian patient with invasive breast adenocarcinoma [199]. In contrast to the MDA-MB-231 cell line, these breast cancer cells express both oestrogen and progesterone receptors, but they are HER-2 negative. MCF-7 cells are tumorigenic in mice when injected i.c. or in the

mammary fat pad even though they are slowly growing *in vivo* without estrogen supplementation. This clone of cells was used to determine the location within the bone marrow of ER +ve breast cancer cell followed i.c. injection.

2.1.5 T47D

Similar to the MCF-7 cell line, the T47D cell line is positive for both estrogen and progesterone receptors. This cell line was first isolated from the pleural effusion of a 54 year old patient presenting with ductal carcinoma [200].

The cell line was used to determine the homing pattern of a second ER +ve cell line after i.c. injection in immunocompromised mice.

2.2 Cell line subculture

Subcultures of cells were prepared by defrosting cells from a fresh batch of low passage number stored in liquid nitrogen, each experiment was performed using cells of similar passage number (passage 12-14). The previously described cell lines were grown in T75 flasks in RPMI-1640 medium supplemented with 10% foetal bovine serum at 37°C and 5%CO₂, or DMEM + Pyruvate medium enriched with 1% penicillin/streptomycin and 10% foetal bovine serum for the MDA-MB-231-NW1-Luc2 clone. Prior the addition in the culture medium, serum was heat inactivated in a water bath at 56°C for 45min. Cells were subcultured approximately trice a week under sterile condition in a tissue culture hood. Overcrowding of cells should be avoided, therefore cells were subcultured when reaching a confluence of about 80%. Culture medium was removed from the flask and cells were washed twice with sterile PBS. Cells were trypsinised with 0.15% Trypsin-EDTA and incubated for 2-3 min at 37°C and 5%CO₂. After the incubation, cells were harvested using 5ml of sterile RPMI-1640 10% FBS and pelleted in a sterile medium by centrifuging at 150g for 5 min. The supernatant was discarded and cells were resuspended in 10ml of fresh culture medium prior the seeding into a sterile culture flask at the desired concentration and placed in the incubator at 37°C and 5%CO₂. Routinely tests were performed once a month in all cell cultures to check for mycoplasma contamination.

2.2.1 Counting cell number by haemocytometer

A Haemocytometer was used to determine the cell number of the cell suspension obtained after trypsinising the monolayer of adherent cells from the culturing flask. An aliquot of cell suspension (typically 50 μ l) was mixed with a 0.4% (w/v) trypan blue solution (1:1) to discriminate between viable and non-viable cells. 10 μ l of the cell-trypan blue suspension were loaded in the counting chamber of the haemocytometer. The number of cells located on the four main squares of both grids was counted using an inverted light microscope as shown in figure 2.1. The average mean of the viable cells (unstained) counted in the main four squares was used to calculate the cellular concentration (cells/ml) of the suspension of origin.

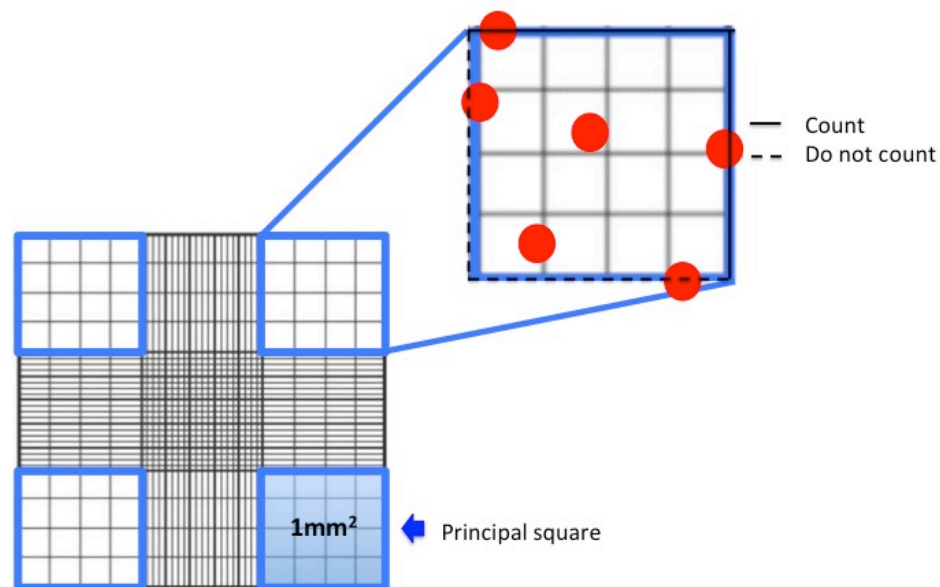


Figure 2.1 Schematic illustration of Haemocytometer

Cells are counted in the four principal squares, but in the event that cells are located on the borders of the square only two of its sides are included in the counting.

2.2.2 Storage and thawing of cells

Cell lines were stored in liquid nitrogen at a temperature of -196°C for long-period storage and in a -80°C freezer for short-term storage. Prior to freezing, cells were quickly washed twice with PBS, trypsinised with 0.15% Trypsin-EDTA and incubated at 37°C and 5%CO₂ to allow detachment from the bottom of the flask. Cells were counted

using a haemocytometer and pelleted at 150g for 5 min. Supernatant was removed and a suspension of 1×10^6 cells/ml was made in 10% FBS medium supplemented with 10% DMSO. Aliquots of 1ml were transferred in cryovials, stored over night at -80°C and finally placed into liquid nitrogen for long-term storage.

To revive frozen cells, the cryovials were quickly defrosted in a water bath at 37°C , suspended in 9ml of pre-warmed medium enriched with 10% FBS and centrifuged at 150g for 5 min. The supernatant was discarded and the cells pellet resuspended in 10ml of fresh medium and seeded into a T75 flask at the desired concentration.

2.3 Staining of cells with lipophilic membrane dyes

To trace single tumour cells within the bone microenvironment in histological sections or cryo-sections of tissue derived from the *in vivo* experiments using two-photon or fluorescence microscopy, the breast cancer cells were stained with the lipophilic membrane dyes Vybrant DiD and Vybrant CM-Dil (Life Technologies Ltd, Paisley, UK) according to the supplier's instructions. The characteristic orange and red fluorescence labels are retained in the lipid bilayer of the membrane of non-dividing cells [24], [201]–[204], while in dividing cells the dye is evenly distributed between the daughter cells and the intensity decreases progressively. Breast cancer cells were trypsinized, counted and resuspended at a concentration of 1×10^6 cells/ml of serum free medium for Vybrant-DiD labelling or Hanks' balanced salt solution (HBSS) for Vybrant-CM-Dil. A volume of $5\mu\text{M}$ of labelling dye per millilitre of cells suspension was added. Samples were protected from light and incubated at 37°C degree for 20 min (Vybrant DiD) or 5 min followed by 15 min on ice (Vybrant CM-Dil). Cell suspensions were then spun at 150g for 5min, the supernatant discarded and the resulting pellet of cells resuspended in PBS. The serial centrifugations and resuspensions were repeated three times. Vybrant DiD stains the membrane of the cells more evenly compared to Vybrant-CM-Dil and it can be detected by multiphoton microscopy for $100\mu\text{m}$ depth in the tissue while the laser used to detect Vybrant-CM-Dil could be used only for $70\mu\text{m}$ depth. The drawback of using Vybrant-DiD is that its fluorescent properties are lost during tissue fixation, therefore Vybrant-CM-Dil is recommended if the samples will undergo subsequent analyses which require fixation agents such as PFA.

***In vivo* work**

2.4 Home Office approval

The Research Ethics Committee of the University of Sheffield (Sheffield, UK) reviewed and approved all the *in vivo* experiments that were performed in conformity with the UK Animals (Scientific Procedures) Act 1986 under the Home Office regulations (Project license 70/8964 of Professor Nicola Brown and 70/8799 of Doctor Colby Eaton and Personal license 40/10823).

2.5 Animals

Young (6-week old) and adult (12-week old) female BALB/c nude mice were ordered from Charles Rives (UK) and Envigo RSM (UK). Mice were housed in individually ventilated cages in a controlled environment with a 12hrs light/dark cycle at 22 °C.

2.6 Tumour cell injection

2.6.1 Intravenous injection

On the day of the injection, MDA-MB-231-GFP-IV cells were harvested and stained with Vybrant-DiD or Vybrant-CM-Dil as described in section 2.3. A suspension of 1×10^6 labeled cells/ml was prepared in PBS. Prior to the injection the cell suspension was filtered using a cell strainer (70 μ m pores) to ensure the breast cancer cells were suspended as single cells and not clumps that could cause emboli in the animal.

Warming the animal in the incubator prior to the injection facilitated visualisation of the tail veins. The mouse was placed in the mouse restrainer holding the tail in position and the injection was performed keeping the tail under slight tension. An insulin syringe (27 gauge needle) was inserted, with the bevelled edge of the needle facing up, superficially under the skin and horizontally across the vein. Once the needle was placed in the correct position, the plunger of the syringe was pressed slowly to inject the cell suspension (100 μ l). After the injection, the needle was removed slowly and pressure was applied to the area to ensure haemostasis.

2.6.2 Intracardiac injection

Breast cancer cells were prepared as described for the intravenous injection (see section 2.6.1). This procedure was performed with the mouse under general anaesthesia. Isoflurane was vaporized in the chamber to provide a 5% concentration of anaesthetic vapour that was reduced to 2.5-3% to maintain the animal asleep, complete anaesthesia was assessed by the pinch reflex. The animal was placed supine and pressure on the chest was applied to tighten the skin and allow visualization of the bottom of the sternum. An insulin syringe was inserted through the abdomen (slightly lateral to the bottom extremity of the sternum) directly in the left heart ventricle. Gentle aspiration was recommended to verify the correct location of the needle in the heart of the mouse, bright red oxygenated blood is indication of it, prior the slowly injection of the cells suspension (100µl). After the injection, animals were monitored closely to ensure a complete recovery. Animals that experienced hind limbs paralysis were culled by cervical dislocation. This technique was used to inject MDA-MB-231-GFP-IV and MDA-MB-231-B02 (to investigate cell location using different injection routes), MDA-MB-231-NW1-Luc2, MCF-7 and T47D cell lines.

2.6.3 Intraarterial injection

Breast cancer cells were prepared as described in section 2.6.1 and animals were maintained under general anaesthesia as per the intracardiac injections (section 2.6.2). Dr. Hannah Brown kindly performed the intraarterial injection in the tail by restrain the animal in supine position to better visualise the arterial vein and slowly injecting the cell suspension (100µl) into the circulation. After the injection, animals were monitored closely to ensure a complete recovery and pressure was applied to the area to ensure haemostasis.

2.7 Administration of drugs and other solutions

2.7.1 Preparation of drugs

2.7.1.1 Luciferin

D-Luciferin solution (Perkin Elmer, # 122796), was kindly provided and prepared by Anne Fowles and Diane Lefley (University of Sheffield, UK). 1g of luciferin powder was hydrated in 160ml of distilled water to make a 6.25mg/ml stock solution and 5ml aliquots were stored at -20°C. Prior to the injection, the solution was defrosted and 100µl of the stock solution was administered subcutaneously at a concentration of 30mg/kg.

2.7.1.2 AMD3100 octahydrochloride hydrate

The CXCR4 inhibitor AMD3100 octahydrochloride hydrate was supplied as a white solid (Sigma-Aldrich, #155148-31-5). The powder was hydrated with PBS to prepare a stock solution of 1mg/ml, aliquots were stored at -20°C. A 5mg/kg AMD3100 solution was prepared from its stock solution, prior to intraperitoneal injection (i.p.) of a volume of 100µl PBS.

2.7.1.3 Zoledronic acid (ZOL)

The anti-resorptive Bisphosonate Zoledronic acid was provided as a disodium salt (Novartis). Stock solution was prepared in PBS by Alyson Evans (University of Sheffield, UK) to hydrate and prepare 10mg/ml stock that was aliquoted and stored at -20°C. Prior to i.p. injection, a fresh 100µg/kg solution was prepared in PBS.

2.7.1.4 Cediranib (AZD2171)

The VEGF tyrosine-kinase inhibitor Cediranib (AZD2171) was supplied as powder (Selleckchem.com, # S1017), 1% Tween-80 was used to hydrate and prepare a 50mg/ml stock solution. Aliquots were stored at -80°C and a working solution of 3mg/kg in 1% Tween-80 were prepared for the daily (5-days/week) oral administration of the drug.

2.7.1.5 Deferoxamine mesylate (DFM)

Deferoxamine mesylate (DFM) was provided as salt powder (Sigma). PBS was used to prepare a 50mg/ml stock solution, then aliquoted and stored at -20°C. Daily, prior to the i.p. administration, a working solution of 15mg/ml were prepared.

2.7.1.6 Phosphate buffered saline

Phosphate buffered saline (PBS) was used in all the *in vivo* studies except for the Cediranib study in which 1% Tween-80 was used. Volume (typically 100µl) and route of injection was the same as used for the experimental drug in use.

2.7.2 Route of administration

2.7.2.1 Subcutaneous injection

A sterile 1ml syringe with a 25-gauge needle was used to inject the luciferin solution subcutaneously (typically 100µl). The most common sites for s.c. injections are over the shoulders, into the loose skin of the neck, and over the flank. No anaesthesia is required.

2.7.2.2 Intraperitoneal injection

Mice were restrained manually to expose the abdomen and 100µl of solution were injected cranial and slightly medial to the last nipple of the animals with an angle of entry of approximately 30 degree using a 25-gauge needle. No anaesthesia is required.

2.7.2.3 Oral gavage

Mr. Matthew Fisher (University of Sheffield, UK) kindly performed the oral gavage gently restraining the animals and injecting the liquid compounds (typically 200µl), Cediranib or the control solution, using a rigid gavage needle. Particular attention must be paid to not damaging the trachea or perforating the oesophagus but no anaesthesia is required.

2.8 *In vivo* detection of tumour growth

Development of tumour was monitored weekly or twice a week using the *In vivo* imaging system (IVIS) Lumina II in combination with the Living Image software. Animals were anaesthetised with Isoflurane, as described in section 2.6.2, injected with 100µl of 30mg/ml Luciferin solution in PBS subcutaneously, placed into the imaging chamber and the non-invasive *in vivo* imaging was performed with animals both in the prone and supine position. The bioluminescent signal visualized, was overlaid on the photographs of the animals to detect the location of the growing tumours.

***Ex vivo* work**

2.9 Collection of bone samples

Animals were culled by i.p. injection of pentobarbital (50µl) followed by cervical dislocation. Hind limbs were collected, muscle tissue was removed from the bones and tibias and femurs were separated. Care was taken not to damage the joint.

2.9.1 Preparation of bone samples for histological analysis

4% (w/v) PFA was prepared dissolving paraformaldehyde (Sigma-Aldrich, # 30525-89-4) in pre warmed (55°C) PBS on a stirring hotplate, cooled on ice and stored at 4°C. Bones used for histology were fixed in 4% PFA for 72hrs followed by 2 weeks of decalcification in a 0.5M EDTA/ 0.5% PFA solution prior to processing, paraffin embedding and cutting sections of 3µm thickness. The decalcification solution was prepared by dissolving the EDTA in PBS, pH was adjusted with pellets of sodium hydroxide (NaOH) until reach pH8, PFA added to the pre-warmed (55°C) EDTA solution. The decal solution was changed trice per week and samples were kept at 4°C in constant shaking to allow a uniform decalcification. Decalcified tissue were then embedded in paraffin and kindly sectioned by Alyson Evans (University of Sheffield) with a rotary microtome (Leica RM2265) at a thickness of 3µm.

2.9.2 Preparation of bones for fluorescent immunohistochemistry

Hind limbs used for immunohistochemistry were fixed in 4% ice-cold PFA for 4hrs, incubated at 4°C for 24hrs in 0.5M EDTA in PBS. After the incubation bones were immersed in ice- cold CPT solution (20% Sucrose and 2% Polyvinylpyrrolidone (PVP) prepared in PBS) for at least 24hrs at 4°C under constant shaking. Bones were then placed in molds filled with embedding solution (8% gelatin from porcine skin, 20% sucrose and 2% PVP prepared in PBS) prior to warming up at 60°C in a water bath for 45 min, and set at ambient temperature for 30 min. The embedded samples were then stored at -80°C and cut with a cryostat (Microm HM 560, ThermoScientific) with a thickness of 30µm.

2.10 Two-photon microscopy

2.10.1 Preparation of the bone specimen

For two-photon microscopy analysis, hind limbs were collected, snap frozen in liquid nitrogen, tibias and femurs were embedded into the embedding medium for cryopreservation Bright Cryo-M-Bed (Bright Instrument, # B1056), left fibula facing the left side of the modules and the opposite direction for the right limb, and stored at -80°C.

After complete freezing of the embedded tissue blocks, the bone marrow was exposed using a Bright OTF Cryostat with a 3020 microtome (Bright Instrument Co. Ltd, Huntingdon, UK). The blade of the cryostat was regularly sharpened at a 45 degree angle with a Shandon Autossharp 5 knife sharpener (Labequip) and the cutting angle was adjusted at 22 degrees to obtain an even surface, necessary for optimal imaging of the specimen.

The exposed surface of the bone was placed onto a glass bottomed dish and to avoid the tissue moving during the scan a cover slip was applied. The dish was subsequently placed upside down onto a microscope slide presenting the bone surface upwards towards the upright two-photon microscope (Zeiss LSM510 NLO, Carl Zeiss, Cambridge, UK), see figure 2.2.

2.10.2 Imaging the bone

A Chameleon laser at 900nm (Coherent, Santa Clara, CA.) was used to generate the second harmonic generation to detect the calcified bone structure. To visualize the breast cancer cells homing in the bone marrow HeNe lasers were used, 633nm for Vybrant-DiD labeled cells and 543nm for Vybrant-CM-DiL labeled cells. The filters detecting the signal from the 900nm, 633nm and 543nm lasers were BP390-465 (blue), BP 650–710 (far red) and BP 565–615 (orange/red) respectively.

The specimen was visualized and focused using transmitted light, prior to scanning with the two-photon microscope. For the preliminary visualisation of the bone structure using the Chameleon laser at maximum speed, the frame size was set at 256 with a mean pixel depth of 1. The brightest level was set as the middle of the z stack and the focus was then moved upwards and downwards to find the upper and bottom layer of the tissue to scan. The depth of the scan was 70 μ m with an interval of 2 μ m between different levels and it was determined by the weaker laser used, the 543nm HeNe laser. To image the exposed bone marrow area, the growth plate and trabecular region, a stack area of 2104 μ m x 2525 μ m was set and the frame was changed to 512, mean pixel depth to 4 and the scan was performed using Multi Time Series (MTS) software [25].

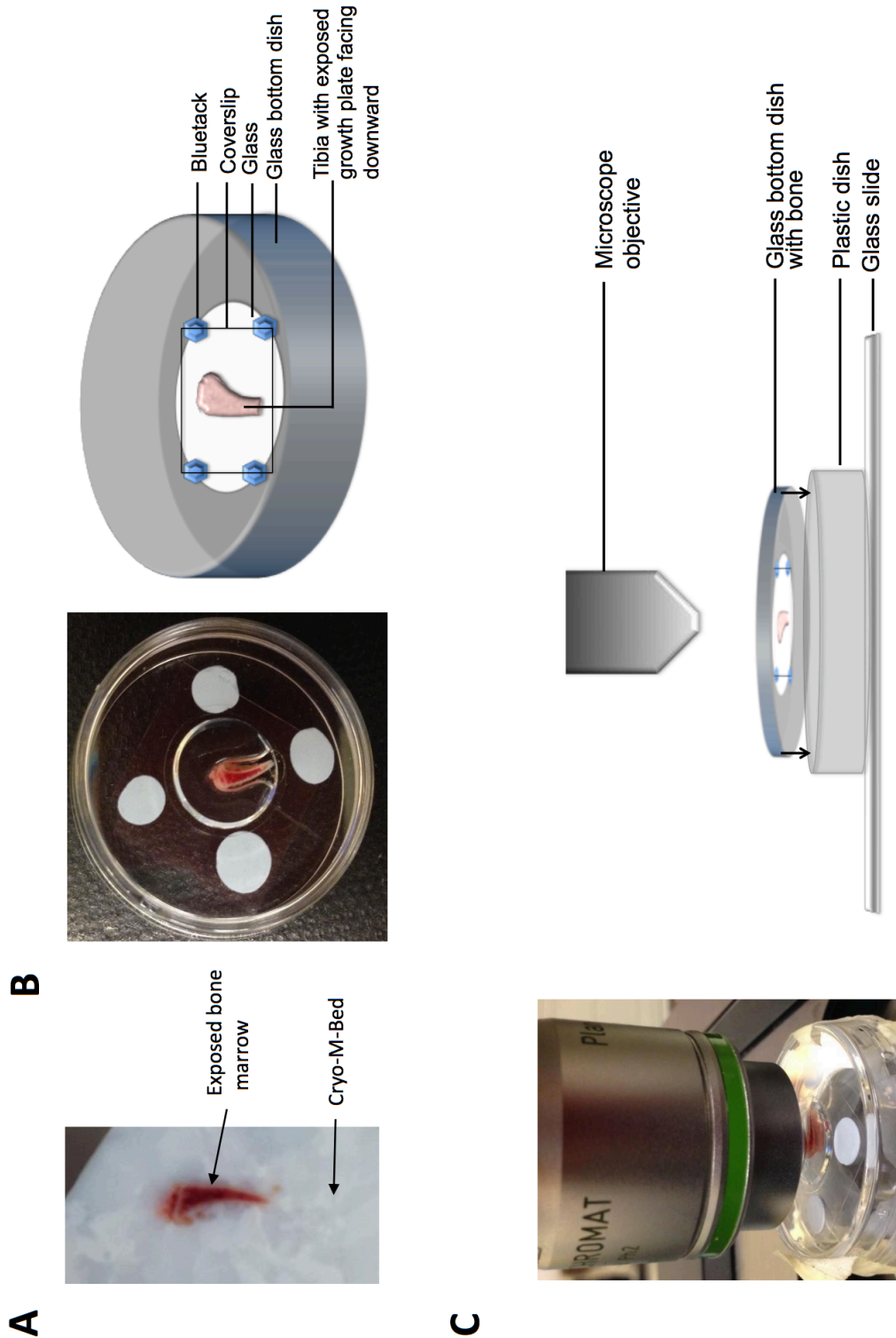


Figure 2.2 Preparation of the specimen for two-photon microscopy

(A) Tibia embedded in Bright Cryo-M-Bed and bone marrow exposed using a Bright OTF Cryostat with a 3020 microtome. (B) Specimen with the exposed marrow surface facing downwards placed in a glass bottom dish held in place with a cover slip as indicated in the schematic illustration. (C) Using an upright microscope the dish is placed facing upwards and onto a microscopy slide which positions the specimen. Reprinted with permission of SpringerNature: BoneKey [25].

2.10.3 3D reconstruction and analysis of the location of tumour cells within bone

Volocity 3D Image Analysis Software (PerkinElmer, Cambridge, UK) was used to reconstruct a three-dimensional image of the tissue scanned with the two-photon microscope. The bone signal was pseudo-coloured in white to accentuate the 3D structure and the signal from the HeNe 543nm laser was pseudocoloured in blue to enhance the contrast with the signal produced by the 633nm laser.

A threshold of $250\mu\text{m}^3$ was fixed to discriminate between objectives detected with the 633nm and 543 HeNe laser considered to be Vybrant-DiD and Vybrant-CM-DiI labelled breast cancer cells and background noise. The number of positive events detected from both lasers were counted and their distance to the nearest bone surface and the nearest tumour cell was measured in two different regions of interest (ROI), the growth plate and the trabecular region of the bone marrow (figure 2.3).

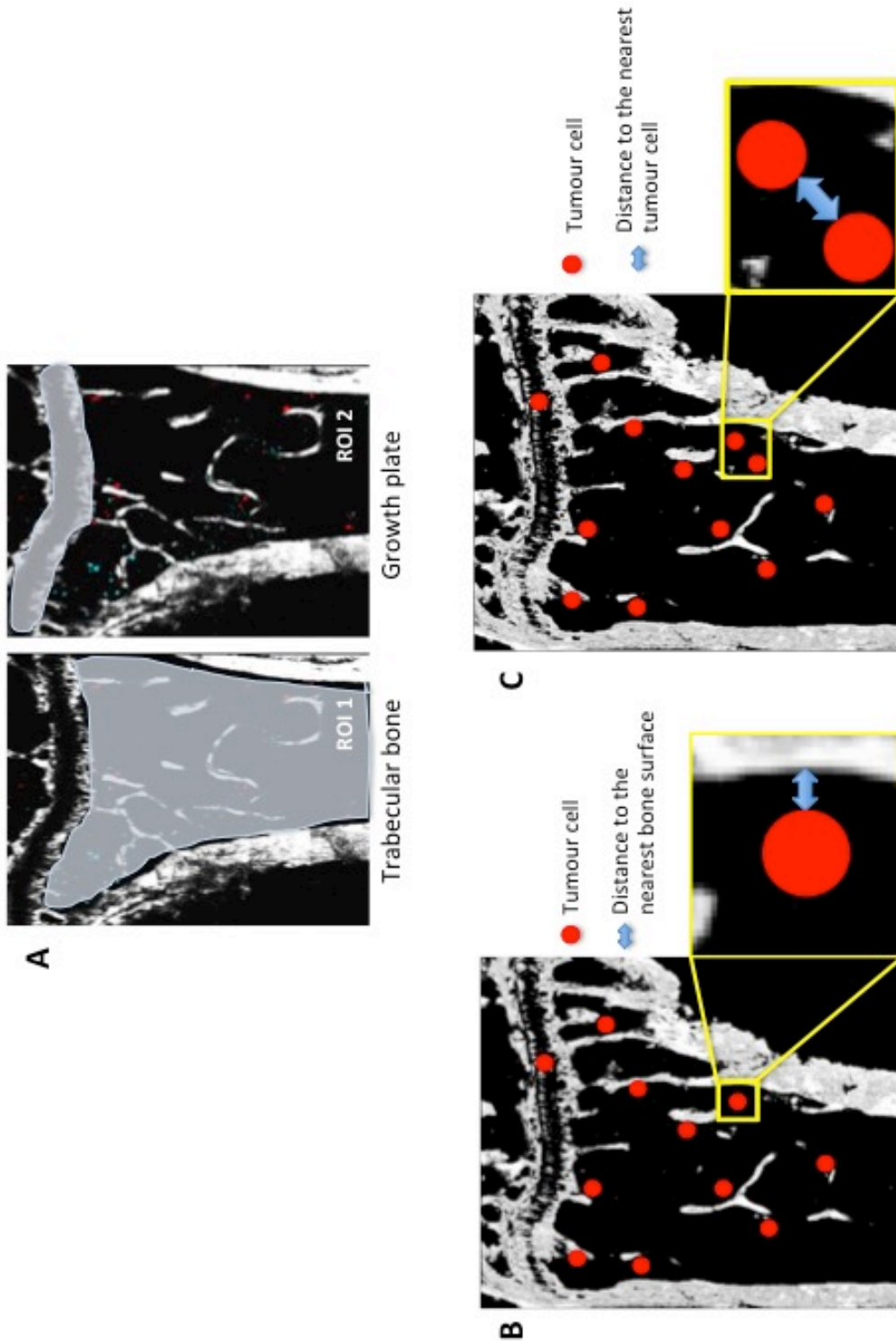


Figure 2.3 Schematic illustration of the analysis of the location of tumour cells within the bone marrow

The ROIs taken into consideration are shown in (A), ROI1 is the trabecular region of bone while ROI2 is the growth plate area. Cortical bone was excluded by the analysis. (B) Distance of tumour cells to the nearest bone surface and (C) nearest tumour cell.

2.11 Micro computed tomography (μ CT)

To detect changes in the calcified bone structure such as the ratio of bone volume/trabecular volume (BV/TV), trabecular thickness (Tb. Th.) and trabecular number (Tb. N.), tibias were scanned within the fixation time in 4% PFA prior to decalcification (48hr time frame for samples to be embedded in paraffin and 4hr for tissue to be embedded in gelatin). Bones were scanned using the SkyScan 1272 (Bruker), 200mA current, 51kV, a 0.5 aluminium filter, a medium resolution camera of 2016 x 1344 and the pixels size was set at 4.3 μ m. Images obtained from the SkyScan were reconstructed with NRecon software. CTAn software was used to determine the volume of interest (VOI) by manually drawing on the two-dimensional reconstructed images. A reference line was set at the lower part of the growth plate and from the reference point an offset of 0.5mm was fixed. For each bone a length of 1mm was analyzed for different bone parameters: trabecular bone volume (expressed as bone volume per tissue volume, BV/TV in %), trabecular number (Tb.N in mm⁻¹) and trabecular thickness (Tb. Th. in mm)(figure 2.4).

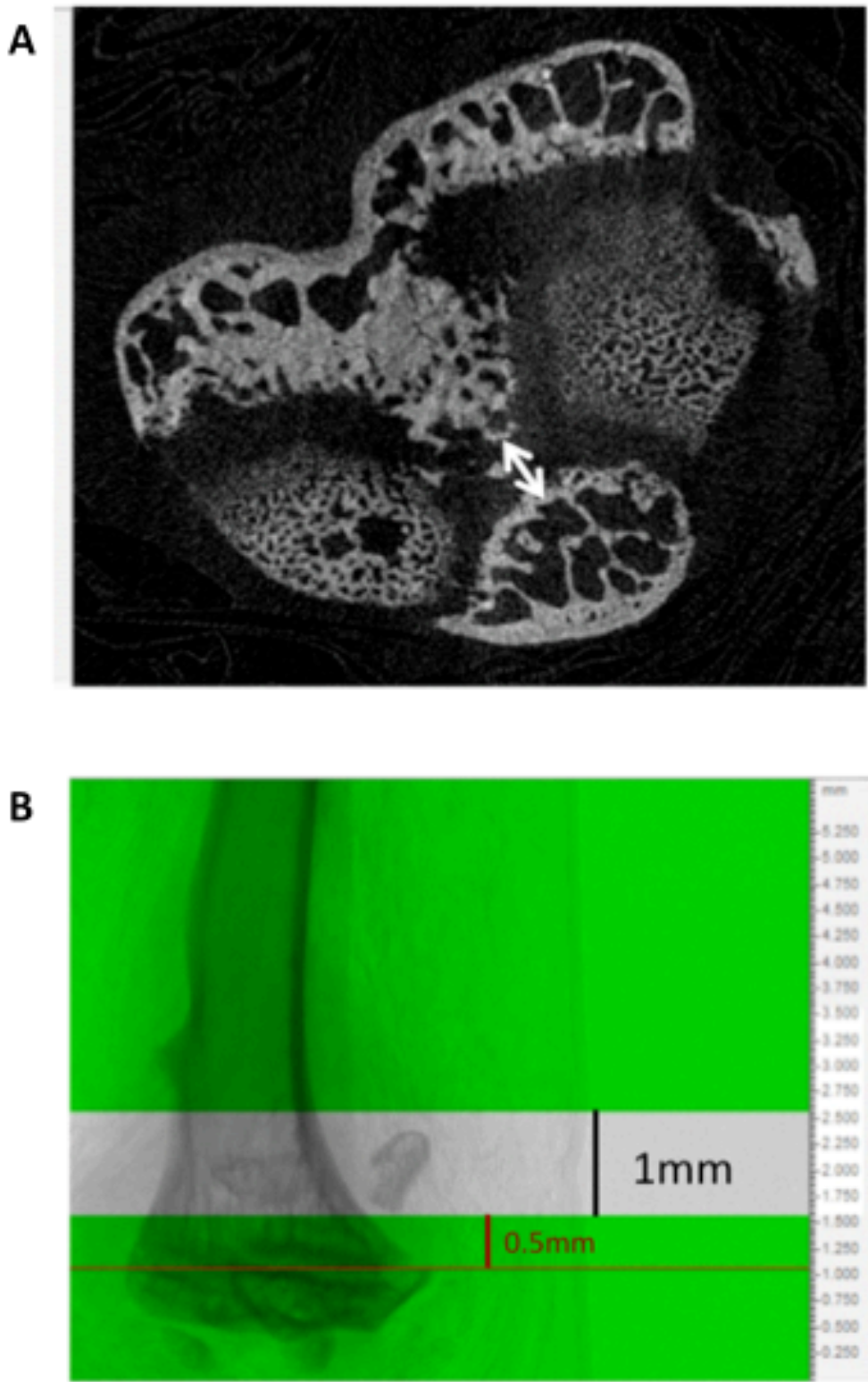


Figure 2.4 Illustration of the μ CT reference point

Example μ CT image (A). Panel B represents the reference point (red line) and respective cross section showing the break of the growth plate bridge (white arrow in A), offset of 0.5mm (red vertical line) and area of analysis of 1mm (vertical black line).

2.12 Staining of bone components

A variety of staining procedures were used to determine different cell types and structures on the histological sections (3µm) of paraffin embedded bones. All these techniques were performed accordingly to the standard operating procedures developed by the Bone Analysis Laboratory, University of Sheffield.

2.12.1 Dewaxing and dehydrating of paraffin embedded bones

The histological sections of paraffin embedded bones were dewaxed in xylene (2x5min) and rehydrated through decreasing concentration of alcohols (99%, 95%, 70%, 3 min each) to tap water. Prior to mounting and cover slipping with DPX [(distyrene), plasticiser (tricresyl phosphate) and xylene] mounting medium, the slides were dehydrated through 70%, 95% and 99% alcohol to xylene.

2.12.2 Haematoxylin and Eosin (H&E) staining

This protocol was used to visualize different structures, by the staining of the cell nuclei in blue (haematoxylin) and pink coloration (eosin) of the cytoplasm and connective tissue.

Rehydrated slides were incubated in Gill's Haematoxylin solution (VWR) for 2 min followed by a washing step in running water for 5 min. Samples were then incubated in 1% eosin solution for 5 min prior to washing in running tap water until completely clear. Histological sections were next dehydrated and the cover slip was mounted as described in section 2.12 (figure 2.5).

2.12.3 Masson-Goldner trichrome staining

Masson-Goldner trichrome staining is a histological technique that allows clear discrimination between different tissue components. Tissue stained with this particular method show nuclei stained in dark brown, cytoplasm and muscle in brick red, connective tissue and bone matrix in green and erythrocytes in bright orange.

The Masson Goldner staining kit (Merck KGaA, Darmstadt, Germany) was used according to the manufacturer's instruction. Briefly, rehydrated bone sections were incubated at ambient temperature for 5 min with Weigert's hematoxylin (Solution A: 1%

Heatoxylin in 95% alcohol, Solution B: 29% Ferric chloride in dH₂O/concentrated HCl; 1:1), washed for 5 min under running tap water and rinsed in 1% acetic acid for 30 seconds. Azophloxine solution was added onto the tissue slides for 10 min followed by another 30 seconds rinse in 1% acetic acid. Prior to a third rinse in 1% acetic acid, samples were incubated for 1 min in Tungstophosphoric acid Orange G solution. The final solution added to the samples was Light green solution, and following a 2 min incubation, 1% acetic acid was used to rinse. Specimens were finally dehydrated and mounted (figure 2.5).

2.12.4 Toluidine Blue staining

Toluidine Blue is a metachromatic dye that is highly acidophilic, used to stain acid proteoglycan, and to identify changes in the growth plate cartilage of tibiae histological sections.

Dewaxed and hydrated bone slides were incubated for 3min at ambient temperature in toluidine blue solution (Toluidine Blue O, Sigma Aldrich: 1% NaCl pH 2.0-2.5), followed by rinsing under running water, dehydration and cover slipping (figure 2.5).

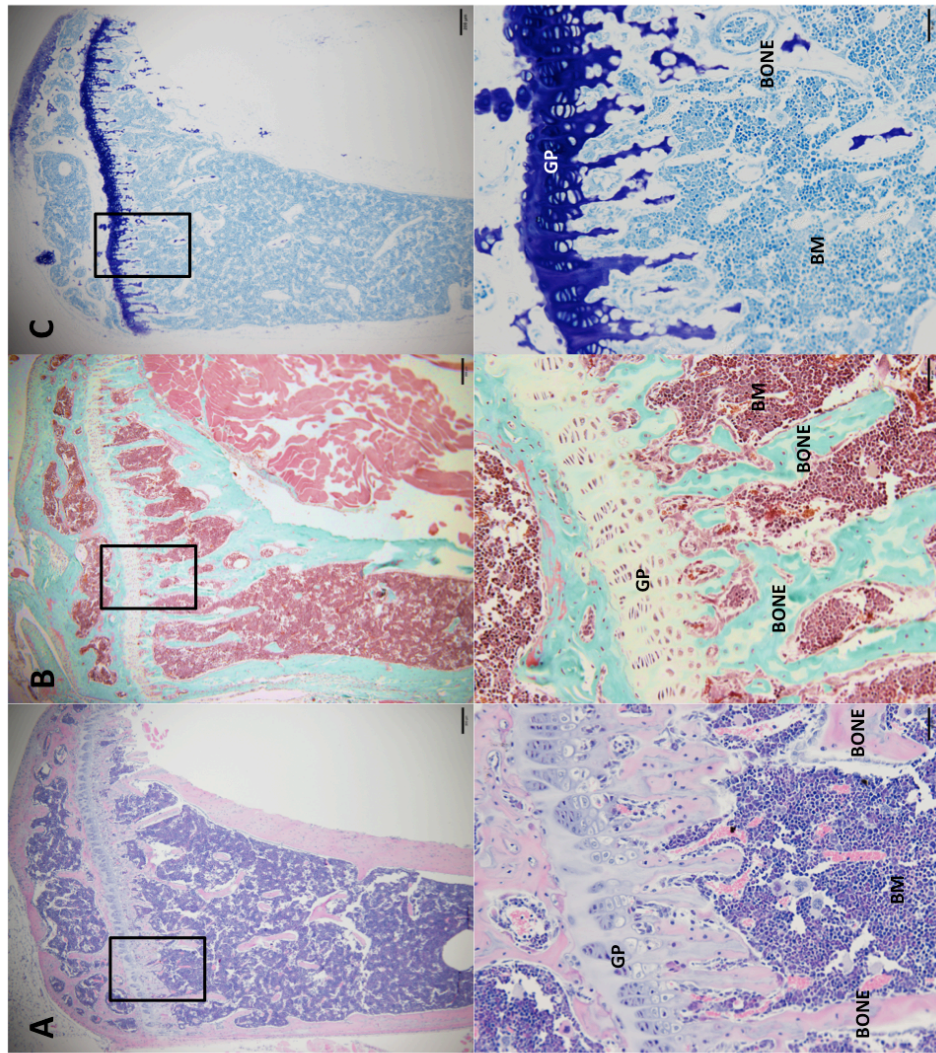


Figure 2.5 Histological sections showing tibial structures

Histological sections of tibia were stained with H&E staining (A), Glodner's trichrome staining (B) and Toluidine Blue staining (C). The top panel shows images took with a 4x objective (scale bar 200 μ m) while in the bottom panel are images took with a 20x objective (scale bar 50 μ m). GP=growth plate, BM=bone marrow.

2.13 Immunofluorescence

Immunofluorescence staining protocols to identify components of the perivascular niche were performed on 30µm thick frozen section of tibiae and femurs embedded in gelatin. The tissues were prepared using the protocol described by Dr. A Kusumbe [97] and briefly summarized in section 2.9.3.

2.13.1 Visualization of bone microvasculature on gelatin embedded sections

To visualize the bone marrow vasculature, with the help of Dr. R Hughes (University of Sheffield, UK) I adapted the protocol kindly provided by Dr. A Kusumbe, Kennedy Institute of Rheumatology, University of Oxford (Oxford, UK). Protocols optimisations consisted in testing different concentrations (1:300, 1:200, 1:100, 1:50 and 1:25) and incubation times (1h, 2h or overnight at room temperature and overnight at 4°C) of several clones of antibodies, antibodies selected for these protocols are in table 2.6 and 2.7.

The immunofluorescence staining was performed on 30µm thick sections of frozen tibiae and femurs. The slides were left to defrost at ambient temperature followed by permeabilisation in 0.3% Triton X-100 for 20 min. After the incubation, tissue were rinsed 3 times in PBS followed by incubation with the primary antibody (prepared in PBS, table 2.6) against endothelial marker Endomucin and α -SMA for 1h at room temperature or overnight at 4°C. For markers against CD31, CD34, TSP-1 and Osterix the incubation was performed either overnight at ambient temperature or amplification of the signal blocking for 15 min at room temperature with Streptavidin solution (Streptavidin/Biotin Blocking Kit – Vector Laboratories SP-2002) followed by 15 min at ambient temperature with Biotin solution, preceded by 1h at ambient temperature.

Three washes with PBS were performed and the bone slides were then incubated with the appropriate secondary antibody for 1h at ambient temperature. Samples treated with the Avidin/Biotin Blocking Kit were incubated with biotinylated secondary for 40min at ambient temperature followed by three washes in PBS and incubation for 30min with the fluorophore-conjugated streptavidin (table2.7). Incubation with the secondary antibody was followed by 3 washes with PBS and nuclei were

counterstained with DAPI (Prolong Gold antifade reagent with DAPI, Life Technologies P36935) and coverslips were mounted.

Table 2.6 Primary antibodies used for staining components of the perivascular niche

MOLECULE	SUPPLIER (CAT. NUMBER)	DILUTION
CD31 (rat anti-mouse)	DIA-310 (Clone: SZ31)	1:100
CD34 (rat anti-mouse)	BioRad (MCA1825)	1:100
ENDOMUCIN (rat anti-mouse)	Santa Cruz (Sc65495)	1:100
α-SMA (rabbit anti-mouse)	Abcam (Ab5694)	1:100
TSP-1 (rabbit anti-mouse)	Abcam (Ab85762)	1:100
OSTERIX (rabbit anti-mouse)	Abcam (Ab22552)	1:300

Table 2.7 Secondary antibodies used used for staining components of the perivascular niche

MOLECULE	SUPPLIER (CAT. NUMBER)	DILUTION
Alexa fluor 488 (goat anti-rat)	ThermoFisher (A11006)	1:200
Alexa fluor 555 (goat anti-rat)	ThermoFisher (A21434)	1:200
Alexa fluor 647 (goat anti-rat)	ThermoFisher (A21247)	1:200
Alexa fluor 488 (goat anti-rabbit)	ThermoFisher (A11034)	1:200
Alexa fluor 555 (goat anti-rabbit)	ThermoFisher (A21245)	1:200
*Biotinylated goat anti-rabbit	Vector Laboratories (BA1000)	1:200
*Biotinylated goat anti-rat	Vector Laboratories (BA9401)	1:200
*Streptavidin Alexa fluor 647	ThermoFisher (AF647)	1:200

*Antibodies used when the samples were treated with the Streptavidin/Biotin Blocking Kit

2.14 Scoring of histological slides

Bone histomorphometric analyses were performed on two non-serial 3 μ m paraffin sections and cortical bone was excluded from any analysis. Quantification of the immunofluorescent staining was carried out on three non-serial 30 μ m gelatin embedded bone slides.

2.14.1 Quantification of extracellular matrix composition

To identify any changes in the epiphysis of the bone, a proteoglycan-rich area, histological slides were stained with Toluidine blue as described in section 2.12.5. The area of interest (AOI) included the proteoglycan-rich growth plate and the trabecular bone surface connected with the epiphysis, and manually identified using Aperio ImageScope software (figure 2.6).

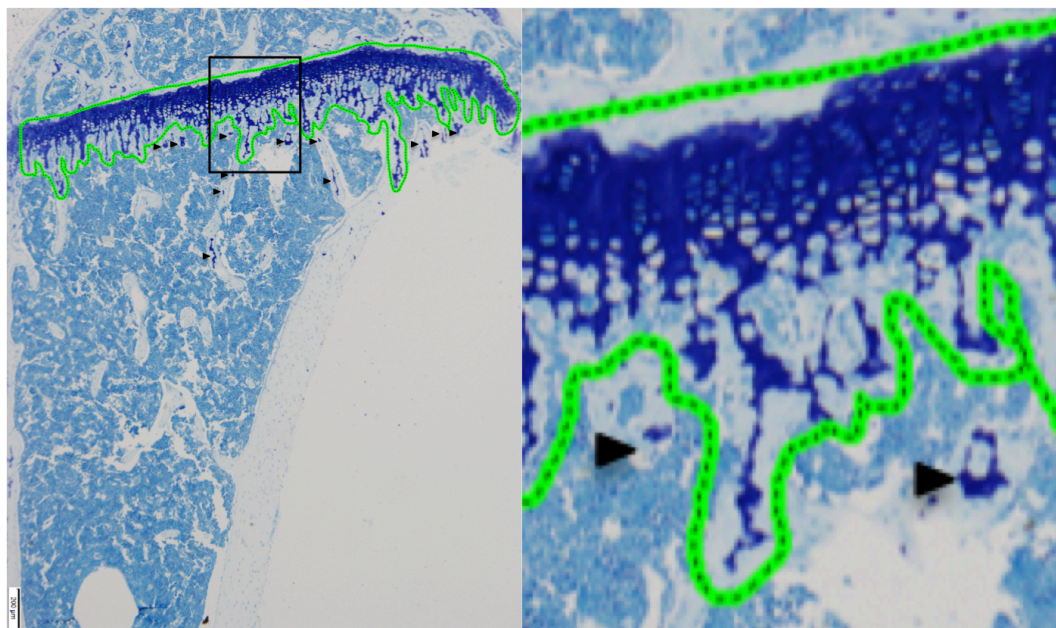


Figure 2.6 Area of interest quantified with Toluidine Blue staining

The extracellular matrix rich in proteoglycan included using Aperio ImageScope software. The area of interest (green line) covered the growth plate area and the trabecular bone connected to it. All cortical bone and trabecular bone not in contact with the proteoglycan-rich area (black arrows) were excluded from the analysis.

2.14.2 Quantification of Endomucin positive vessels

Images of the immunofluorescent staining were captured using an inverted fluorescence microscope (Leica AF6000). Aperio ImageScope software was used to manually track Endomucin positive microvessels and determine their length, number and area of bone marrow occupied. The structure of the vessels was used to discriminate between H- and L-vessels (figure 2.7).

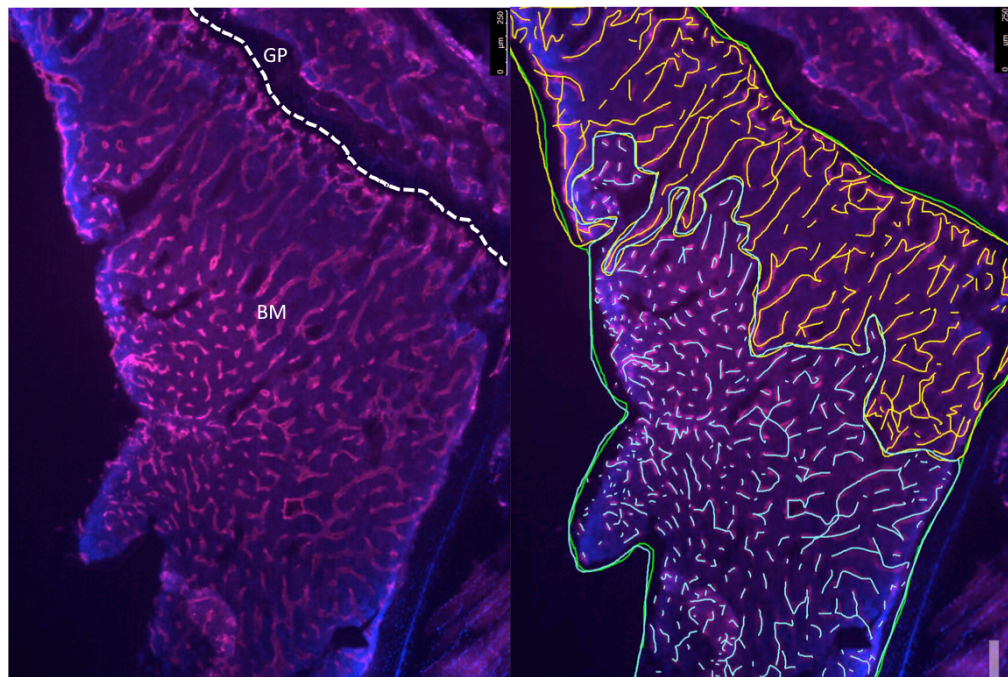


Figure 2.7 Endomucin positive vessel quantification

Image of the stained 30 μ m thick gelatin embedded bones were captured with a Leica AF 6000 and a 5x objective (left picture). Using Aperio ImageScope software the Endomucin positive vessels were manually identified. The parameters quantified included: (i) bone marrow area analysed (green), (ii) area of bone marrow covered by H-vessels, (iii) their length and (iv) number (yellow) and (v) bone marrow area occupied by L-vessels as well as their number and length (blue). GP=growth plate and BM=bone marrow.

2.14.3 Quantification of CD31 and CD34 positive vessels

Images of the immunofluorescent staining were captured using Zeiss LSM880 AiryScan Confocal microscope and ImageJ software was used to measure the expression of CD31 and CD34 markers. The region of interest of the bone marrow was manually identified and the signal outside of this ROI was removed. The vessel channel was transformed into a grey scale colour and a look-up-table (LUT) that transforms brightness into number value was applied. The LUT values were then inverted and the threshold was set so only the pixels with the maximum signal were count (figure 2.8). The results were expressed as percentage of area expressing the specific marker. Since CD31 and CD34 are also expressed also on Endomucin positive vessels, also the percentage of Endomucin⁺/CD31⁺ or CD34⁺ were measured

Aperio ImageScope software was used to manually track CD31/CD34 positive microvessels and determine their length, number and area of bone marrow occupied, as described for the Endomucin vessels.

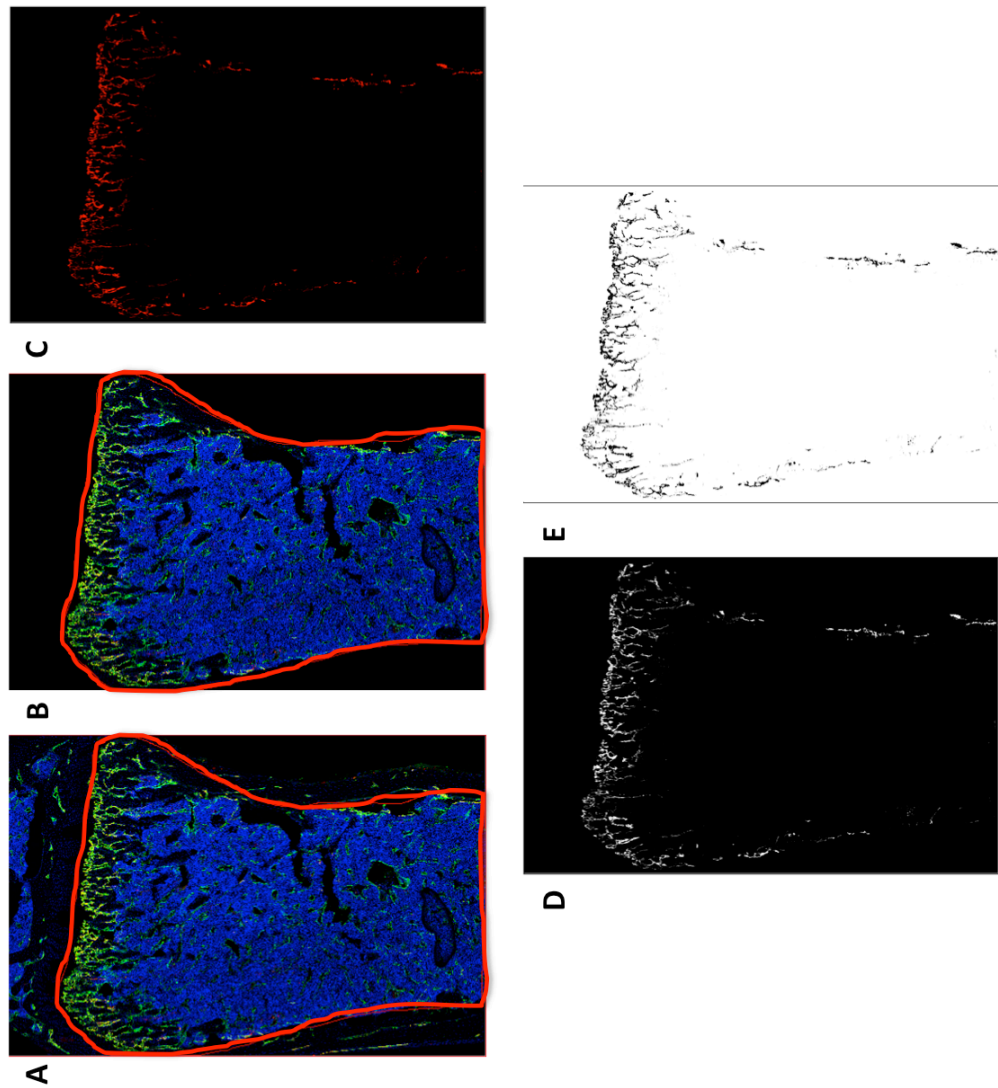


Figure 2.8 Schematic illustration of quantification of CD31/CD34 positive vessels

(A) ROI was manually drawn around the bone marrow (red line) and the outside signal was removed (B). The vessel channel (C) was transformed in LUT value using ImageJ software (D) and the inverted LUT (E) were quantified. The vessels were then manually drawn with Aperio ImageScope software to measure their number and length.

2.14.4 Quantification of α -SMA, TSP-1 and Osterix expression in the bone microenvironment

Zeiss LSM880 AiryScan confocal microscope was used to capture the images of 30 μ m thick gelatin sections of tibiae stained against Osterix, α -SMA or TSP-1. As described for the CD31/CD34 vessels, the quantification was performed using ImageJ software. ROIs were drawn, outside signal removed and inverted LUT were quantified following the setting of a threshold.

The 'cell counter' function of the software was also used to manually count the number of α -SMA positive vessels or TSP-1 positive megakaryocytes.

For the much more abundant Osterix positive cells, the function 'cell counter' was used to manually quantify a few slides and the numbers obtained were then compared with the ones produced by the automatic function '3D object counter', since there was a high correlation between the two values obtain all the other tissue sections were analysed using the automatic function.

2.15 Statistical analysis

GraphPad Prism software (Version 7.0) was used to perform statistical analysis. Student T-tests and Two-way ANOVA were used as indicated in the Materials and Methods section of each results chapter as well as in each figure legend. A p -value of $p < 0.5$ was considered significant.

Chapter 3

Homing of breast cancer cells in the bone microenvironment

3.1 Summary

Bone metastasis is one of the most common complications of advanced breast cancer and is associated with a considerable reduction in the quality of life of the patient. During the dissemination to the skeleton, breast cancer cells detach from the primary site, enter the circulation and home to a putative metastatic niche in the bone marrow where they can remain dormant for a considerable length of time. The cellular composition of this niche is not clearly defined, but there is evidence showing an overlap between the bone metastatic, perivascular and haematopoietic stem cell niches. The interaction and the signals from the bone microenvironment to the tumour cells and vice-versa are crucial for the progression of secondary disease. It is known that the components of the niche have a key role in homing, maintenance of the quiescence state and progression of tumour growth in bone, but the mechanisms that enable tumour cells to undergo these processes and develop overt metastases have not been fully elucidated. The identification of the specific components of the niche would give a better understanding of the cellular types involved in the metastatic process at its early stages and consequently improve the therapeutic approaches for patients with a poor prognosis.

The aim of the work described in chapter 3 to identify the pattern of location of breast cancer cells within the microenvironment in the early stage of bone colonisation, and investigate the effect of modification of the bone niche on the homing of tumour cells using an *in vivo* model.

3.2 Introduction

Bone metastasis is one of the most common complications of advanced breast cancer and is associated with a considerable reduction in the quality of life of the patient. Moreover, despite the improvement in the therapy it remains the major cause of female cancer related death [2], [205], [206]. Hypercalcemia, pathological fractures, spinal cord compression and pain are some of the complications related to skeletal metastasis [5].

The development of metastasis in secondary organs is a multistep process that begins with the detachment of the cancer cells from the primary tumour and entry into the blood stream, cells traveling through the circulation to reach bone where they integrate into specific niches and may remain dormant for long periods of time [14], [205], [207],[208]. Not all cells detached from the primary tumour will successfully seed in the distant organ resulting in overt metastasis, in fact these disseminated tumour cells (DTCs) can face several fates, including death by apoptosis or elimination by the immune system, return to the circulation or entering a quiescent state [7]–[10], [20], [209], [210]. When the malignant cells switch to a proliferative state they start to grow quickly, generating the metastases and eventually cause bone destruction [16]. The mechanism/s triggering breast cancer cells to leave the dormant state is not fully understood, but the role of the bone microenvironment malignant progression is a well-recognized concept firstly proposed in the ‘seed-and-soil’ hypothesis by Stephen Paget in 1889 [11]. Another example of how breast cancer cells and various cellular components of the bone microenvironment interact is the ‘vicious cycle’ created between osteoclasts and tumour cells which describes how the release of cytokines and growth factors aid the progression of the bone metastasis [9], [12], [13], [15]. Not only does the microenvironment influence the growth of tumour cells, Cox *et al.* recently described how cancer cells secrete factors that can create pre-metastatic lesions which will support the colonisation of this niche by DTCs [47]. Even though it is a well-accepted concept that the microenvironment plays an important role in all the stages of bone metastasis, the precise nature and composition of the metastatic niche is not well defined.

The bone microenvironment where the metastatic process takes place, is characterized by the presence of cytokines, hormones and other soluble factors produced by the different sub-populations of the bone marrow, which all influence the development of the metastasis in this fertile soil. Numerous cell types, including osteoclasts, osteoblasts, endothelial cells and hematopoietic cells, contribute to the complexity of this rich microenvironment which forms the bone metastatic niche [15], [40], [211]. It has been suggested that this rich soil where tumour cells seed, is located in regions of the bone marrow in which components of the HSC niche, osteoblastic niche and perivascular niche are overlapping [34], [39]–[41]. Supporting the hypothesis of an overlap between niches, Shiozawa and colleagues described a competition between HSCs and prostate cancer cells, for the space in bone, suggesting that tumour cells home to the HSC niche [28], [36]. Although it is believed that prostate and breast cancer cells locate in the same niches, it remains to be established whether breast cancer cells compete for the space in the niche as previously described for prostate cancer. The interrelationship between niches and the role played by multiple components of the bone microenvironment is also highlighted by the fact that the HSC niche is located in close proximity to the endosteal surface of the trabecular bone, an area that is highly vascularized [34], [55], [97], [212], [213]. *In vivo* model studies showed that tumour cells, in particular breast and prostate cancer cells, locate into the endosteal region of bone, the area in which HSC are also located [26], [36], [48], [118], [148], additional validation that this rich microenvironment accommodates the putative metastatic niche.

To date, most studies have focused on advanced stages of disease where the micro- or macro-metastases are already established, with only little information on the early stages of the breast cancer bone colonisation when tumour cells are still in a dormant state within the bone marrow. Although the focus of intensive research, the mechanisms initiating the metastatic process are not fully understood [214], and cannot be studied in patients. This highlights the need for *in vivo* models that mimic the early steps of cancer cell dissemination in bone. The introduction of novel technologies such as two-photon microscopy and the use of lipophilic dyes that are retained in non-proliferating (tumour) cells, it has made research on the initial stages

of the metastatic process possible. Combining these approaches has allowed the mapping of the location of single breast cancer cells (or small colonies) within the bone, investigate their interaction within the calcified structure and observe how changes in the bone cell population, affects the homing of tumour cells to bone [25], [215].

3.3 Aims

All work described in this chapter was carried out in *in vivo* models to test the following hypothesis:

Breast cancer cells home to a specific region of bone in which HSC, osteoblastic and perivascular niche overlap.

The main aims were as follows:

- To map the location of breast cancer cells within the bone microenvironment in the early stages of bone colonisation
- To assess whether there were difference in the homing of different breast cancer cell-lines, both ER positive and ER negative
- To investigate whether the seeding of tumour cells in the bone microenvironment was influenced by the route of injection
- To compare the homing of breast cancer cells to bone in young and mature murine models
- To determine how modification of the bone microenvironment affects the seeding of breast cancer cells.

3.4 Materials and Methods

Detailed information can be found in the main Materials and Methods Chapter 2.

3.4.1 Breast cancer cell-lines

Triple negative breast cancer cells MDA-MB-231-GFP-IV [198] and MDA-MB-231/B02-GFP cells [129] [kindly provided by Dr. Philippe Clezardin (INSERM, UFR de Médecine Lyon-Est, Lyon, France and University of Sheffield, UK)] and ER+ve breast cancer cell-lines MCF-7 and T47D were cultured in RPMI 1640 enriched with 10% FCS (Life Technologies/Invitrogen) at 37°C 5%CO₂. Prior to the injections, tumour cells were labeled either with the lipophilic membrane dye Vybrant-CM-Dil or Vybrant-DiD (Life Technologies Ltd, Paisley, UK) according to the manufacturer's instructions.

3.4.2 *In vivo* studies

All the *in vivo* experiment were approved and carried out in accordance with the UK Animals (Scientific Procedures) Act 1986 under the Home Office regulations (Project license 40/35319 held by Professor Nicola Brown and 70/8799 held by Doctor Colby Eaton and Personal license 40/10823).

3.4.2.1 Homing of breast cancer cells in mature animal models

To evaluate the homing of the bone-seeking breast cancer cell-line, 12-week old female BALB/c nude mice were injected with i.v. 100µl of PBS and on day 7 with i.v. 1×10^5 MDA-MB-231-GFP-IV cells labeled either with the membrane dye Vybrant-CM-Dil (n=6) or Vybrant-DiD (n=3, due to technical problems in the processing of the samples the size of the group was reduced to n=2). Animals were culled and long bones collected on day 12 (figure 3.1 A).

To determine whether different bone-seeking breast cancer cell-lines have the same pattern of homing, 12-week old female BALB/c nude mice were injected on day one with either 1×10^5 MDA-MB-231-GFP-IV cells (n=3) or MDA-MB-231/B02-GFP cells (n=2 due to an animal not recovery after the anaesthesia) labeled with the membrane dye Vybrant-DiD and culled on day 5 when long bones were collected (figure 3.1 B).

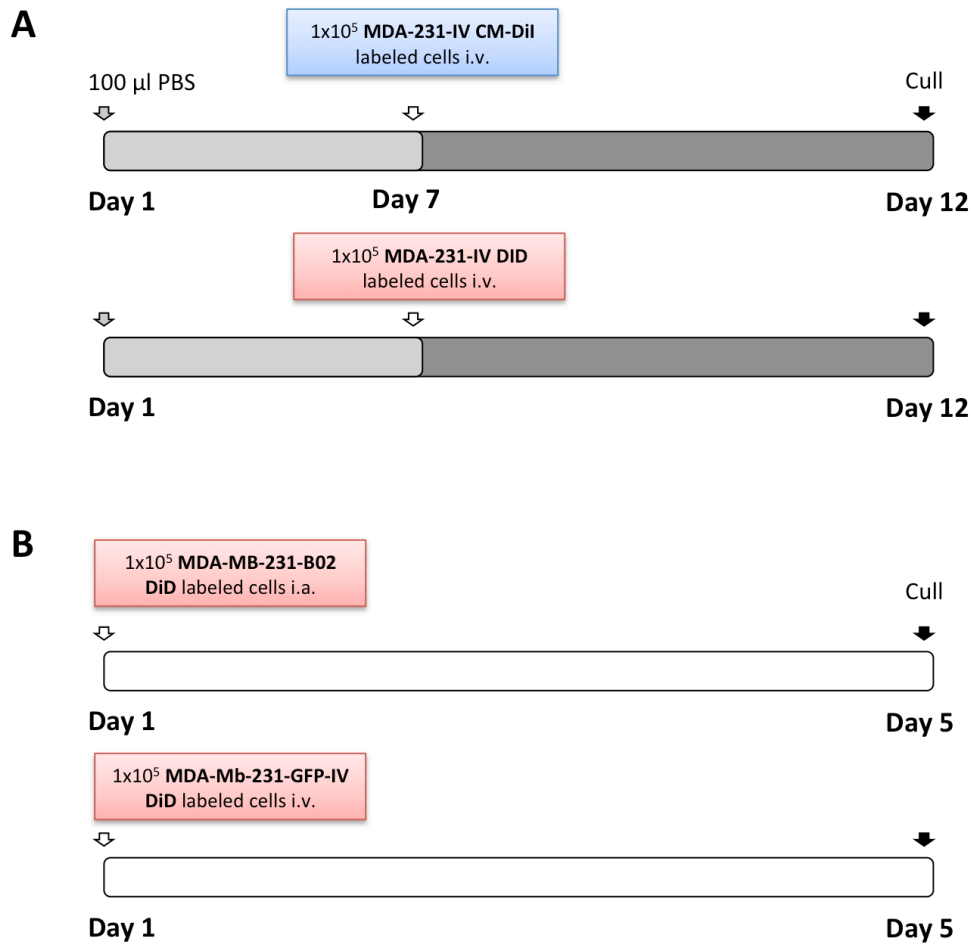


Figure 3.1 Outline for the in vivo studies evaluating homing of bone-seeking MDA-MB-231 cell-lines

Experimental outline. A) 12-week old female BALB/c nude female mice were injected intravenously (i.v.) with PBS on day 0 and on day 7 with 1×10^5 MDA-MB-231-GFP-IV cells labeled with Vybrant-CM-Dil (n=6) or Vybrant-Dil (n=2). Animals were culled on day 12 and tibiae and femora were collected for analysis by two-photon microscopy. B) 12-week old female BALB/c nude female mice were injected on day 1 i.v. with 1×10^5 MDA-MB-231-GFP-IV cells labeled with Vybrant-DiD (n=3) or i.a. with Vybrant-DiD labeled 1×10^5 MDA-MB-231-B02 cells (n=2). Five days after tumour cells inoculation, animals were culled and long bones collected for ex-vivo two-photon analysis.

To investigate whether the route of injection could affect the location of the tumour cells in the bone microenvironment, 12-week old female BALB/c nude mice were injected either i.v. (n=1) or i.c. (n=5) with 1×10^5 Vybrant-DiD labeled MDA-MB-231-GFP-IV and culled on day 5 (figure 3.2 A). Long bones were collected for two-photon microscopy.

To establish whether ER+ve cell-lines colonised the same area of bone compared with the triple negative MDA-MB-231-GFP-IV cells, 1×10^5 Vybrant-DiD labeled MCF-7 or T47D cell-lines were injected i.c. (performed under general anaesthesia with Isoflurane tested by pinch reflex) in 12-week old female BALB/c nude mice (n=5/group). Long bones were collected 5 days after cell injection (figure 3.2 B).

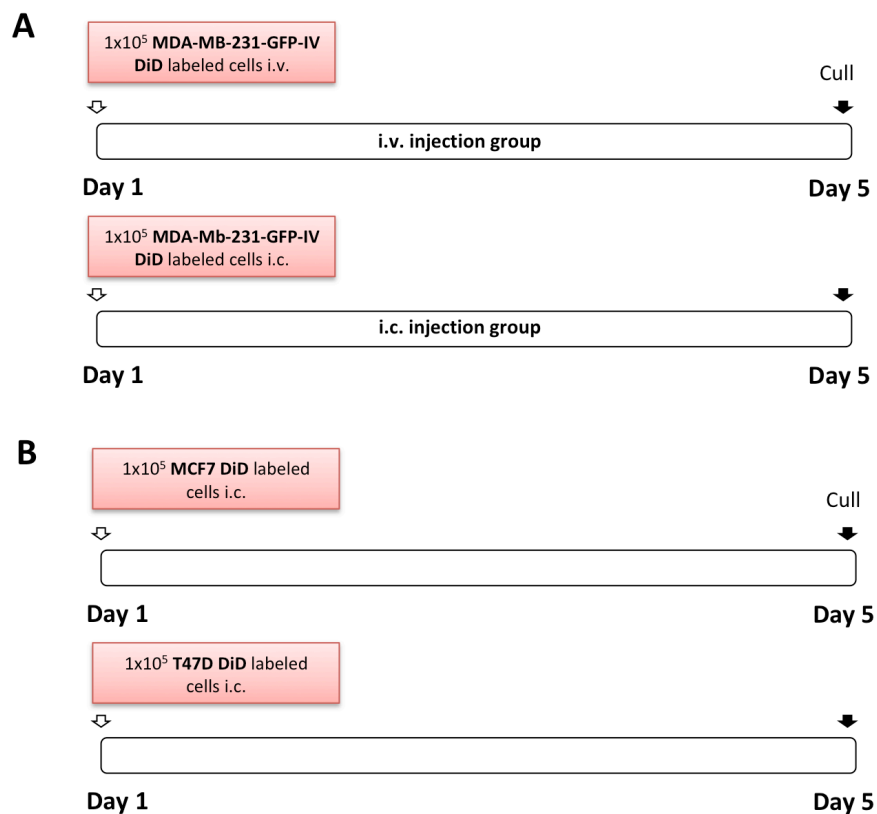


Figure 3.2 Homing after different routes of injection and both ER+ve and ER-ve cell-lines

A) 12-week old female BALB/c nude female mice were injected either i.v. (n=1) or i.c. with 1×10^5 MDA-MB-231-GFP-IV cells labeled with Vybrant-DiD (n=5) to compare the pattern of homing using different route of injection. B) 12-week old female BALB/c nude mice were injected on day 1 i.c. with 1×10^5 T47D or MCF7 Vybrant-DiD labeled cells (n=5/group) to compare the homing pattern of ER+ve cell-lines with the triple negative MDA-MB-231. Five days later, animals were culled and long bones collected for *ex vivo* multiphoton analysis.

3.4.2.2 Hematopoietic stem cell (HSCs) niche modification

To assess whether the mobilisation of hematopoietic stem cells (HSCs) would affect subsequent homing of breast cancer cells in bone, 12-week old female BALB/c nude were injected i.p. with the CXCR4 antagonist AMD3100 (Sigma-Aldrich) 5 mg/kg (100 μ l) or PBS daily for 5 days. 24 hours after the last injection, animals were injected i.v with 1×10^5 MDA-MB-231-GFP-IV Vybrant-DiD -labeled cells and culled at day 10 (figure 3.3).

3.4.2.3 Comparison between young and mature animal models

To compare the seeding of breast cancer cells in the bone microenvironment of young and mature animal models, 6- and 12-week old female BALB/c nude mice (n=8/group) were injected i.v. with 1×10^5 MDA-MB-231-GFP-IV cells labeled with the membrane dye Vybrant-CM-Dil. Animals were culled 5 days after tumour cells injection (figure 3.3).

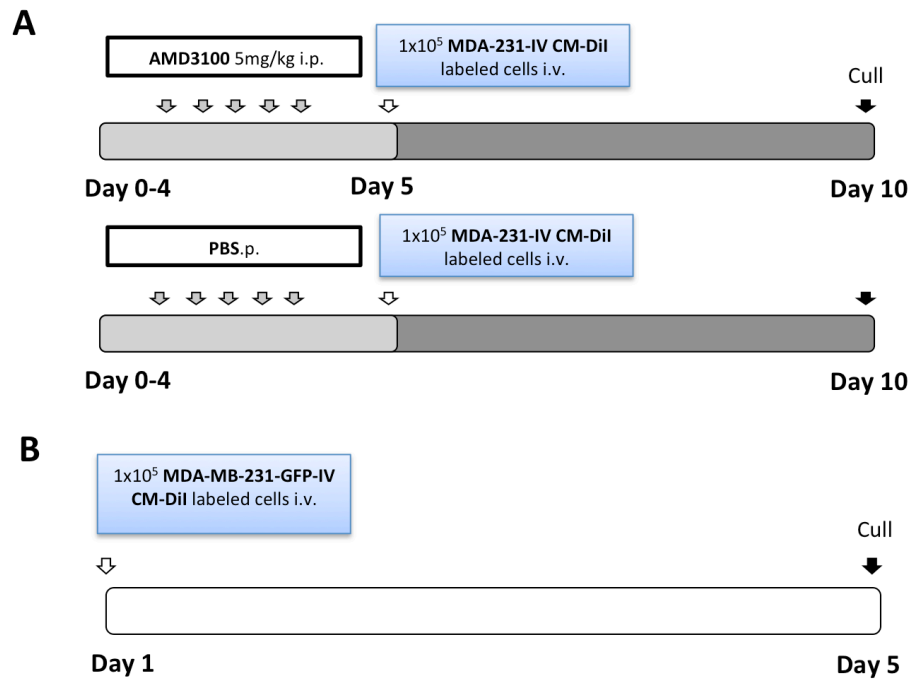


Figure 3.3 Modification of HSCs niche and comparison between young and mature mice

(A) 12-week old BALB/c nude female mice were injected daily for 5 days i.p. with PBS or AMD3100 (5mg/kg) (n=5/group). On day 5, animals were injected i.v. with 1×10^5 DiD labelled MDA-MB-231-GFP-IV cells and culled on day 10, tibias were collected for multiphoton microscopy B) 6- and 12-week old female BALB/c nude female mice (n=8/group) were injected on day 1 i.v. with 1×10^5 CM-Dil labelled MDA-MB-231-GFP-IV cells. Five days later, animals were culled and long bones collected for *ex-vivo* multiphoton analysis.

3.4.2.4 Collection and preparation of the samples

Animals were culled by an overdose of anaesthetic (i.p. 50 μ l Pentobarbital) and death was confirmed by cervical dislocation. Hind limbs were dissected, muscles were removed, femora and tibiae were separated and collected snap frozen in liquid nitrogen and stored at -80°C. For the *in vivo* study investigating the competition between HSCs and breast cancer cells, right tibiae were collected in 4% PFA and processed for fluorescent immunohistochemistry, as described in section 2.9.3.

3.4.3 Two-photon microscopy

Snap frozen long bones were embedded into Cryo-M-Bed (Instrument Co. Ltd, Huntingdon, UK) and a Bright OTF Cryostat and 3020 microtome (Bright Instrument Co. Ltd, Huntingdon, UK) was used to expose the bone marrow. The specimen was mounted on a glass bottom dish as described in section 2.10.1, with the exposed surface upwards towards the upright Zeiss LSM510 NLO two-photon microscope (Carl Zeiss, Cambridge, UK). An area of 2104 μm \times 2525 μm at 70 μm depth was captured using a Chameleon two-photon laser at 900nm (Coherent, Santa Clara, CA) to visualize the bone structure, a HeNe 633nm laser for Vybrant-DiD labeled cancer cells and a HeNe 543nm laser for Vybrant-CM-Dil dye. The tile scan of 2104 μm \times 2525 μm for 70 μm depth using two lasers (HeNe 633/543nm and Chameleon laser 900nm) took approximately 3 hours and 30 minutes per sample.

3.4.3.1 Mapping the location of breast cancer cells

Three-dimensional reconstruction of the image was performed with Volocity 3D Image Analysis software 6.01 (PerkinElmer, Cambridge, UK). To distinguish between positive events detected with the 543nm and 633nm HeNe (Vybrant-CM-Dil and Vybrant-DiD labeled breast cancer cells respectively) and the background noise, a threshold of 250 μm^3 was fixed. The positive events were counted and their distance from their edge to the nearest bone surface and the nearest cancer cell was measured. All the quantifications were performed in two different regions of interest (ROI) in which the cortical bone was excluded. Femora and tibiae were both analysed. The variability in the number of cells seeding in the bone microenvironment (0-97) influenced the length of the analysis, from few minutes up to more than 24h.

3.4.4 Statistical analysis

Statistical analyses were executed using GraphPad Prism software (Version 6.0 and 7.0). Student T-tests and Two-way ANOVA and Tukey post test were used as indicated in each figure legend. A p -value of <0.5 was considered significant.

3.5 Results

During the metastatic process, breast cancer cells home to a putative metastatic niche in the bone marrow cavity. In our *in vivo* models of bone metastasis, the majority of tumours develop in the metaphysis of long bones, tibia and femora (figure 3.4). Therefore these bones were analysed to assess the location of breast cancer cells within the bone microenvironment in the early stages of bone colonisation.

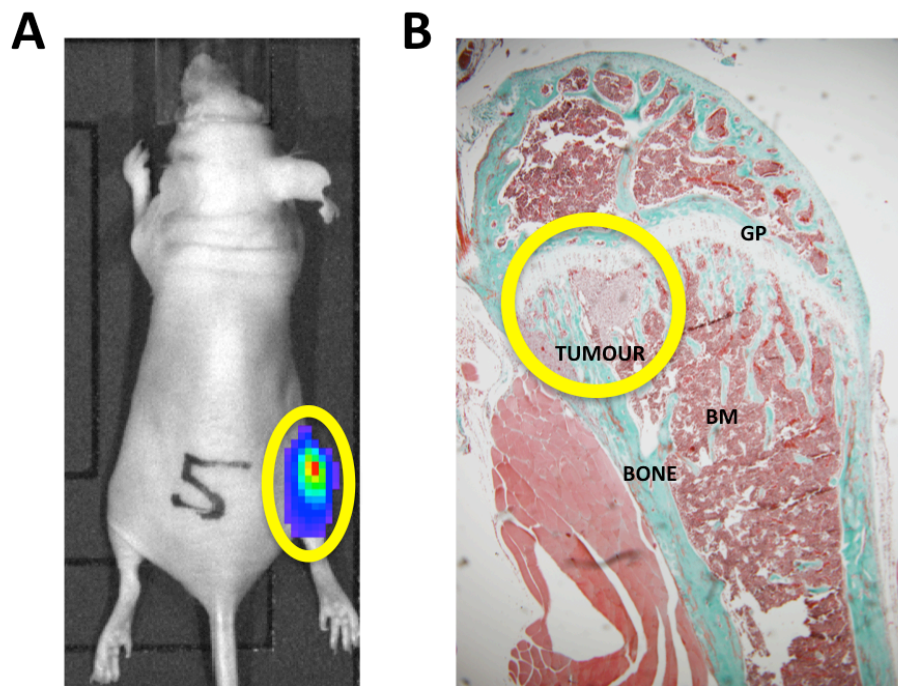


Figure 3.4 *In vivo* tumour model

(A) Representative image of an animal model used in our laboratory. The mouse was injected i.c. with MDA-MB-231-GFP cells transfected with luciferase, *in vivo* tumour growth was detected over time using an *in vivo* imaging system (IVIS). (B) Goldner's trichrome staining of a femur slide of a tumour bearing mouse. Yellow circle=tumour, BM=bone marrow, GP=growth plate.

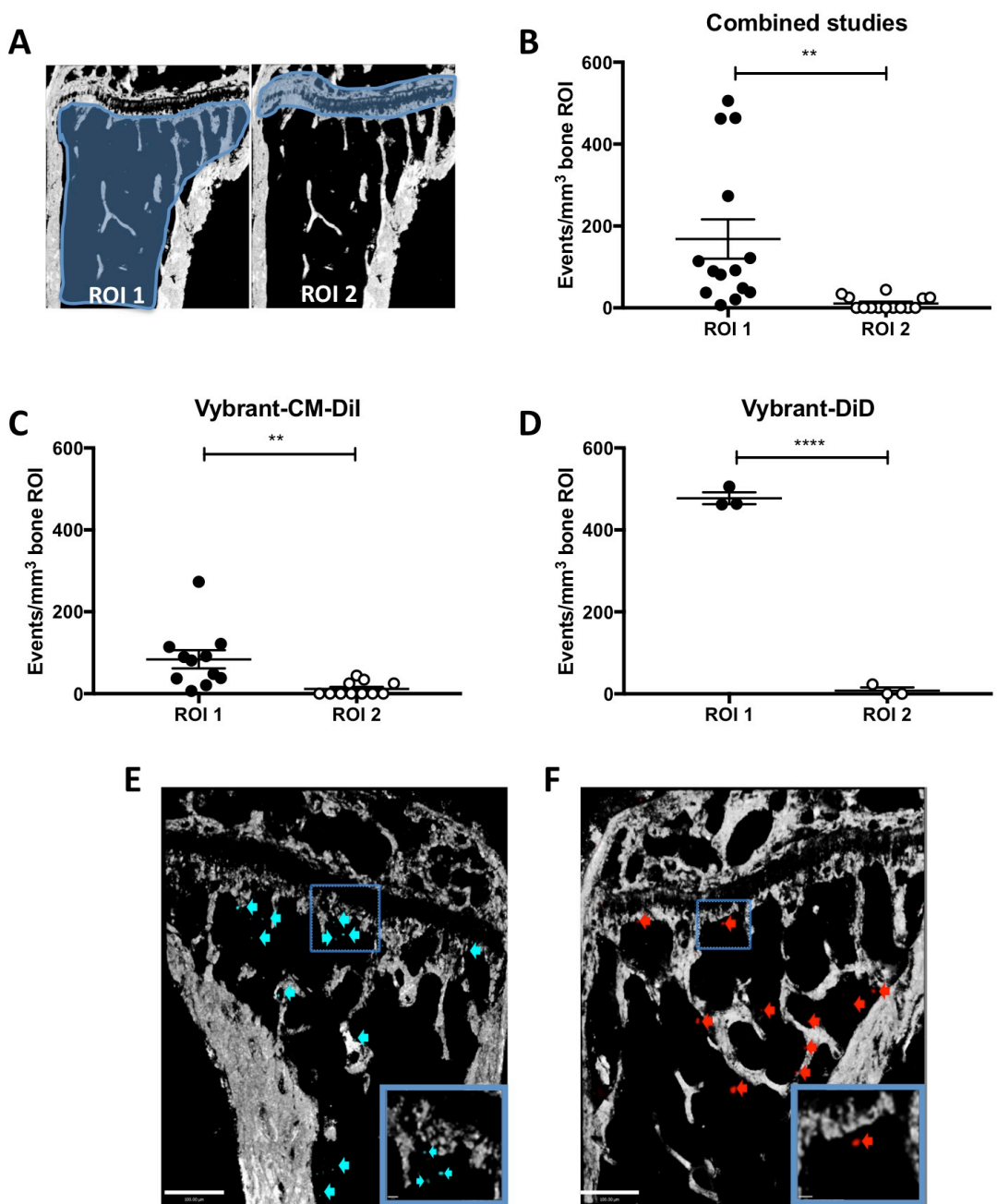
3.5.1 The MDA-MB-231-GFP-IV cell-line homes to the trabecular region of bone

Previous studies performed by our group demonstrated that injection in the tail vein of the bone-seeking cell-line MDA-MB-231-GFP-IV resulted in tumour growth in long bones of young (6-week old) animals two weeks after inoculation [198]. As the focus of my PhD project is on the early stages of the metastatic process, to investigate the bone colonisation I used mature mice (12-week old) known to have a low bone turnover and therefore be supportive of tumour cell dormancy [216]. As shown in figure 3.1, animals were culled 5 days after injection of the bone-seeking breast cancer cell-line MDA-MB-231-GFP-IV labeled with either Vybrant-DiD or Vybrant-CM-Dil. As explained in section 2.3 of the Materials and Methods Chapter, Vybrant-DiD is distributed more evenly on the lipophilic membranes and can be detected deeper in the specimen but the fluorescent properties do not resist fixation of tissue. In contrast, Vybrant-CM-Dil is not the most appropriate dye for two-photon microscopy but it is recommended if the samples require fixation such using e.g. PFA. In current *in vivo* studies I wanted to compare the reliability of the two dyes for two-photon analysis, since in future experiments the plan was to use Vybrant-CM-Dil would be used to detect tumour cells in fixed tissue.

Time point of five days was chosen to allow the tumour cells to localise within the bone marrow without starting to proliferate, and lose the fluorescent membrane dye. Moreover, at this time point cells that do not reach a niche have died and therefore I was able to quantify the cells in bone that most likely contain the metastasis-initiating population. In our *in vivo* models of bone metastasis, the majority of tumours developed on the metaphysis of long bones, predominantly tibia and femora, so I focused my analysis on these bones. On the day of cull, long bones were collected, snap frozen in liquid nitrogen, embedded in Cryo-M-Bed and stored at -80° until they were used for the two-photon scan. To assess whether this cell-line colonise preferentially to specific regions of the bone marrow, Volocity 3D Image Analysis software was used to count the number of events recorded using 633 and 543 HeNe lasers in two different ROIs: the growth plate area (ROI1) and the trabecular region of the bone (ROI2) (figure 3.5).

MDA-MB-231-GFP-IV cells localised preferentially in the trabecular region of the bone marrow (ROI1) rather than in the growth plate area (ROI2). In fact, the events/mm³ recorded in ROI1 were significantly higher compared to those in ROI2 ($p=0.0047$ for cells labeled with Vybrant-CM-Dil, $p<0.0001$ for Vybrant-DiD and $p=0.0031$ when the studies are merged) (figure 3.5). As described in section 2.3 of the Material and Methods Chapter, the fluorescent dye Vybrant-CM-Dil intercalate non-uniformly in the membrane of cells. Therefore a proportion of the cells partially labeled with this dye may have been excluded from the analysis, as they could not be distinguished from the background noise. This perhaps, explain why the overall number of Vybrant-CM-Dil was lower compared to the Vybrant-DiD positive events. Despite this dissimilarity, the pattern of tumour cell homing was identical regardless of the membrane dye used.

These results demonstrate that in this model, the bone-seeking triple negative MDA-MB-231-GFP-IV breast cancer cell-line, localise preferentially to the trabecular region of the bone metaphysis.



Homing of MDA-MD-231-GFP-IV cells

A) Schematic representation of the regions of interest (ROIs) of two-photon bone scan analyzed: ROI1 consists of the trabecular bone region and ROI2 the growth plate. Cortical bone was excluded. (B) Shows the results when the two studies are combined. (C) Graph showing the number of Vybrant-CM-Dil⁺ events/mm³ (n=6 animals, 11 bones analysed), Vybrant-DiD⁺ (n=2 animals, 3 bones analysed) events shown in (D). (E) and (F) are examples of two-photon scan showing bone (white), Vybrant-CM-Dil⁺ cells (blue and blue arrows) and Vybrant-DiD⁺ cells (red and red arrows). Scale bars 100µm and 10µm. ** $p \leq 0.005$ and **** $p < 0.0001$ student's *t*-test, graphs show mean \pm SEM.

3.5.1.1 MDA-MB-231-GFP-IV cells locate close to the bone surface

In order to determine the location of this breast cancer cell-line within the microenvironment more accurately, the distance from the edge of the tumour cells to the nearest bone surface, as well as the closest tumour cell, was measured using Volocity 3D Image Analysis software. In ROI1 the mean distance between tumour cells labeled with Vybrant-CM-Dil and the nearest bone surface was $71.90 \pm 11.82 \mu\text{m}$ (range between $23\text{-}144 \mu\text{m}$), for Vybrant-DiD cells was $108.27 \pm 42.19 \mu\text{m}$ ($63\text{-}192 \mu\text{m}$) while the overall mean was $79.70 \pm 12.66 \mu\text{m}$. Compared to ROI1, Vybrant-CM-Dil labeled cells were located significantly ($p=0.0373$) closer to the bone surface in ROI2 where the mean distance was $24.93 \pm 4.85 \mu\text{m}$ (figure 3.6). In contrast, the distance between tumour cells was significantly greater $384.30 \pm 129.80 \mu\text{m}$ in the growth plate area compared to the trabecular bone region with mean values of $174.9 \pm 26.07 \mu\text{m}$ respectively ($p=0.0239$). In both ROIs, the bone-seeking cell-line MDA-MB-231-GFP-IV was homing significantly ($p=0.0015$ in ROI1 and $p=0.0214$ in ROI2) closer to the bone surface than to the nearest tumour cell (figure 3.6). For Vybrant-DiD it was not possible to perform statistical analysis due to the low number of sample available for analysis.

Taken together, in both the ROIs analysed this cell-line located significantly closer to the nearest bone surface than to other tumour cells.

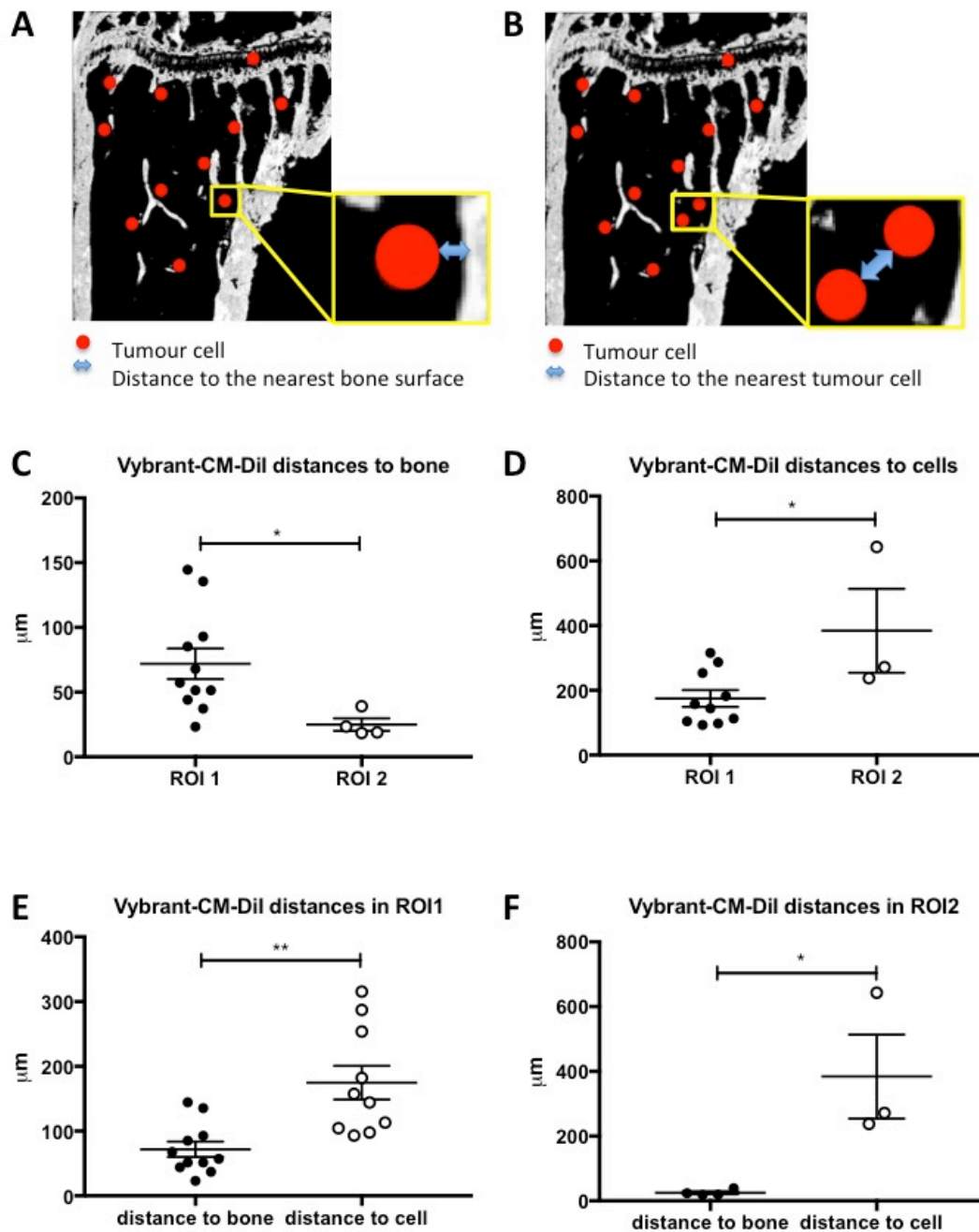


Figure 3.5 Location of MDA-MB-231-GFP-IV cells in the bone microenvironment

(A) Schematic illustration of the distances measurement from the edge of tumour cell to the nearest bone surface and (B) to the closest breast cancer cell. Graphs showing the distance of Vybrant-CM-Dil cells to the bone surface (C) and to other tumour cells (D) (n=6 animals, 11 bones analysed). The comparison between the distance to the bone and the distance to other tumour cells in the two ROI1 is shown in (E) and in ROI2 is shown in (F). * $p \leq 0.05$ and ** $p \leq 0.01$, student's *t*-test, graphs show mean \pm SEM.

3.5.2 Comparison between the pattern of homing of MDA-MB-231-GFP-IV and MDA-MB-231/B02-GFP cells

To assess whether the pattern of homing obtained with the MDA-MB-231-GFP-IV cells was characteristic of this particular cell-line (generated by Dr. Ottewell, University of Sheffield, UK [198]) I performed an *in vivo* study comparing this cell-line with the bone-seeking MDA-MB-231/B02-GFP cell-line (created by the team of Dr. Clezardin INSERM, UFR de Médecine Lyon-Est, Lyon, France and University of Sheffield, UK)[129]. Both bone-seeking cell-lines form metastasis in the metaphysis of young animals and are associated with lytic lesions, therefore a similar pattern of seeding was expected. Female 12-week old immunocompromised mice were injected with either Vybrant-DiD labeled MDA-MB-231-GFP-IV cells (i.v.) or MDA-MB-231/B02-GFP (i.a.), culled 5 days later and long bones were analyzed using two-photon microscopy. Although in the literature it has been reported that MDA-MB-231/B02-GFP colonise to bone following intravenous injection, previous studies in Prof. Holen's team have demonstrated that this cell-line predominantly localised to bone when injected via the intra-arterial route. Therefore this route of administration was used in the animal model with the kind help of Dr. Hannah Brown (University of Sheffield, UK).

MDA-MB-231-GFP-IV cells homed as previously described, with the majority of cells being located in the trabecular region of the bone even though in this study statistical significance was not reached ($p=0.2616$). In contrast, MDA-MB-231/B02-GFP cells were evenly distributed between the two regions of interest ($p=0.9896$) (figure 3.7).

Although the dissemination of the bone-seeking cell-lines in the bone microenvironment demonstrate differences, in both ROIs, the distance of the breast cancer cells to the nearest bone surface was comparable with mean value of $91.55\pm 21.27\mu\text{m}$ and $86.67\pm 30.72\mu\text{m}$ in ROI1 for MDA-MB-231-GFP-IV and MDA-MB-231/B02-GFP respectively ($p=0.9004$) and $16.62\pm 4.32\mu\text{m}$ and $14.01\pm 4.92\mu\text{m}$ in ROI2 ($p=0.7293$) (figure 3.7).

The data show that, despite a different distribution between different areas of the bone for the two triple negative bone-seeking MDA-MB-231 clones, both cell-lines maintain a close connection with the nearest bone surface.

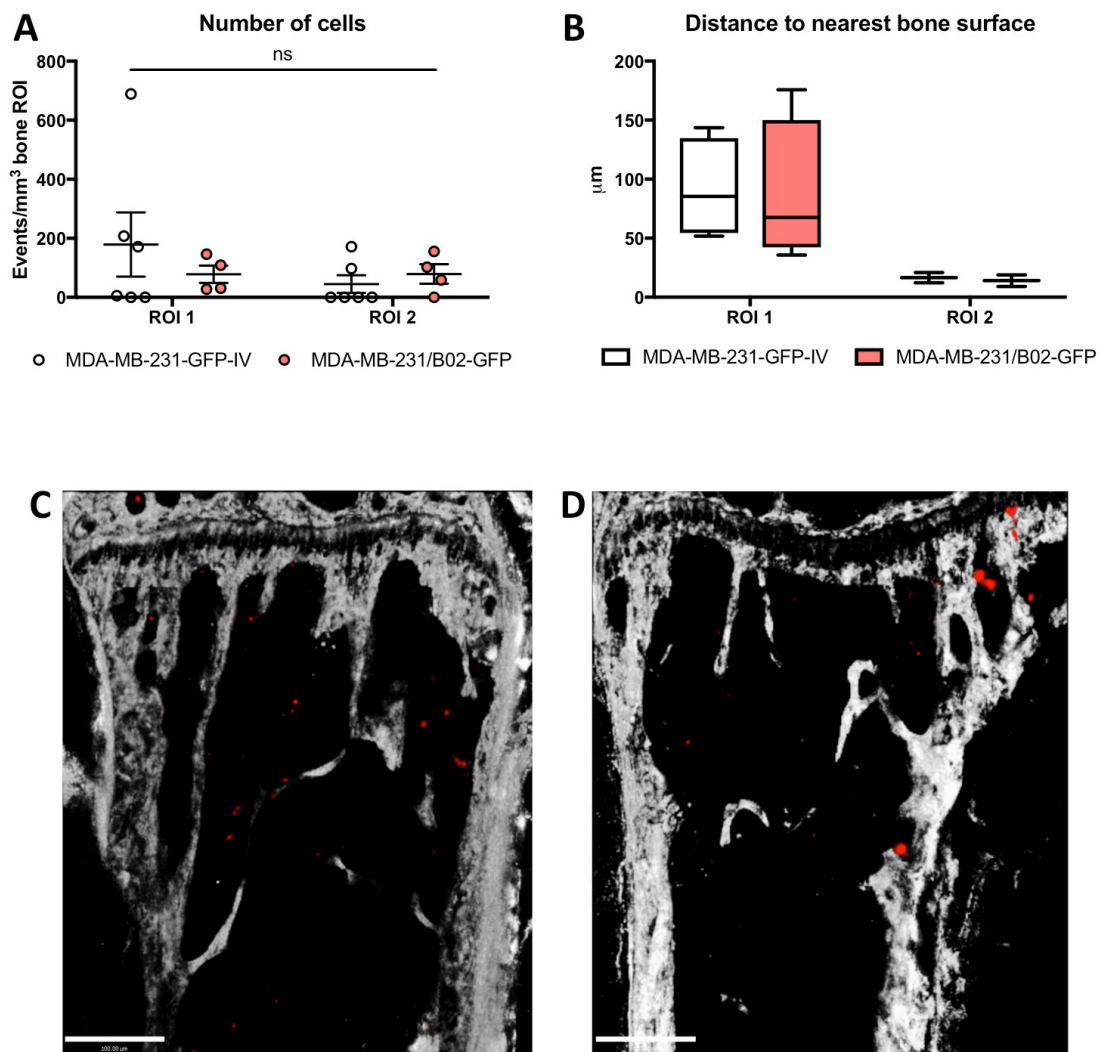


Figure 3.6 Comparison between homing of MDA-MB-231-GFP-IV cells and MDA-MB-231/B02-GFP cells

A) Graph showing the number of MDA-MB-231-GFP-IV (n=3 animals, 6 bones analysed) vs. MDA-MB-231/B02-GFP cells (n=2 animals, 4 bones analysed) labeled with Vybrant-DiD⁺, graph show events/mm³ mean ± SEM. (B) Distance of the bone-seeking breast cancer cell-lines to the nearest bone surface. Examples of two-photon scan showing bone (white), MDA-MB-231-GFP-IV cells (C, in red) and MDA-MB-231/B02-GFP cells (D, in red), scale bars 100µm.

3.5.3 The route of injection does not affect the homing of MDA-MB-231-GFP-IV cells to the bone microenvironment

Due to their characteristic bone tropism, MDA-MB-231-GFP-IV cells home to the bone marrow following tail vein injection. In contrast, most of the xenograft animal models of bone metastasis are obtained by administration of tumour cells via the intracardiac route, allowing the cells to reach the bone through the arterial network, as previously described in section 3.5.2.

To understand whether the route of injection could affect breast cancer cells bone colonisation, 12-week old BALB/c nude mice were injected with MDA-MB-231-GFP-IV Vybrant-DiD labeled cells either i.v. (n=1, just to confirm the pattern previously described in section 3.5.1) or i.c. (n=5) and after 5 days long bones were collected and tumour cells were visualized in the bone microenvironment using two-photon microscopy.

When injected via the tail vein, MDA-MB-231-GFP-IV cells displayed the preferential pattern of homing as previously described (ROI1>ROI2), but did not show significant difference, between events recorded in the trabecular region of the bone compared to the growth plate area. This was probably due to the reduced number of samples ($p=0.4480$) (figure 3.8).

As expected, the route of injection did not affect the seeding of the breast cancer cells within the bone microenvironment. In fact, the majority of MDA-MB-231-GFP-IV cells located to ROI1 compared to ROI2 ($p=0.0464$) when injected in the left ventricle of the heart (figure 3.7). Moreover, the breast cancer cells colonised areas in close proximity with the bone surface with a mean value of $56.99\pm 11.55\mu\text{m}$ in ROI1 and $10.30\pm 4.04\mu\text{m}$ in ROI2 ($p=0.0053$), while they located further away from other tumour, mean value of $253.50\pm 110.40\mu\text{m}$ in ROI1 and $174.90\pm 53.36\mu\text{m}$ in ROI2 ($p=0.1225$ and $p=0.0096$ in ROI1 and ROI2 respectively)(figure 3.8).

Taken together, these results show that the route of injection does not affect the way breast cancer cells colonised the bone microenvironment and confirm that triple negative breast cancer cells generally seed in the trabecular region of the metaphysis in close proximity with the bone surface.

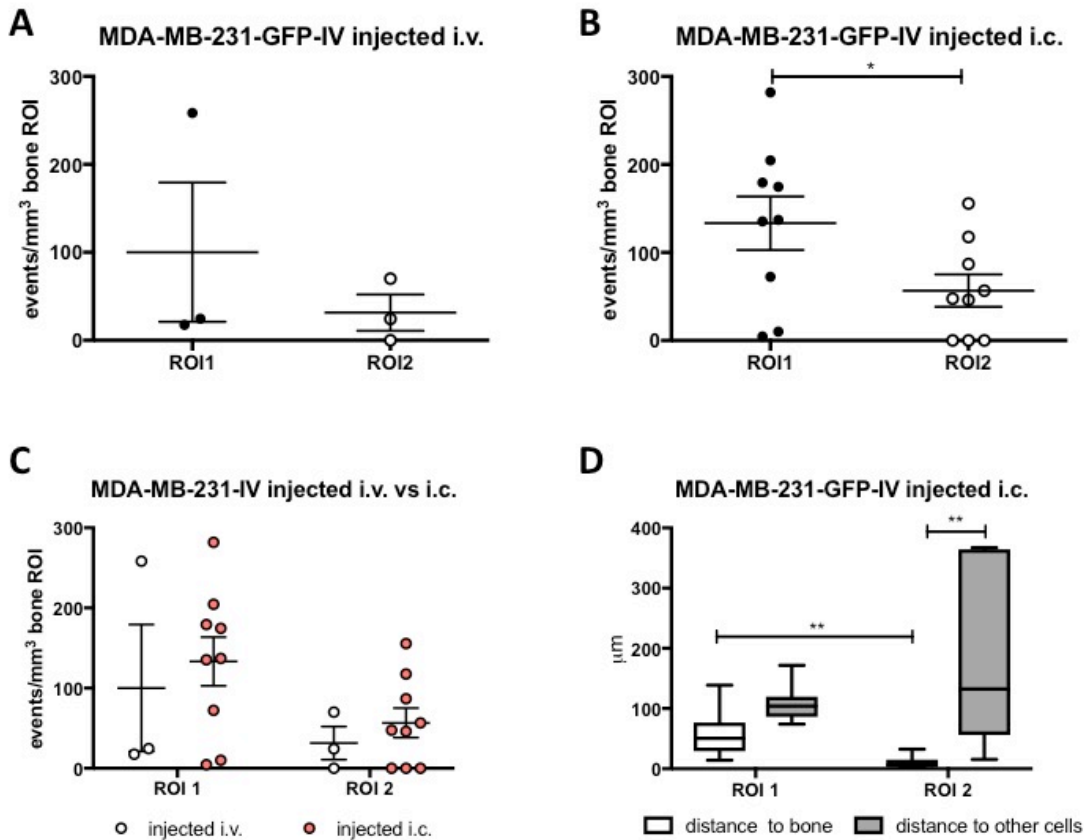


Figure 3.7 Comparison between different routes of injection

A) Graph showing the number of MDA-MB-231-GFP-IV cells localised in two ROIs when injected i.v. (n=1 animal, 3 bones analysed) and B) following i.c. injection (n=5 animals, 10 bones analysed). (C) Graph representing the direct comparison between the homing of MDA-MB-231-GFP-IV cells after i.v (squares) and i.c injection (circles). Comparison between the distance to the nearest bone surface and to the closest tumour cells after i.c. injection is show in (D) * $p \leq 0.05$ and ** $p \leq 0.01$ student's *t*-test and two-way ANOVA and Tukey post test.

3.5.4 ER+ve breast cancer cell-lines display the same pattern of seeding as triple negative cell-lines

The majority of breast cancers are oestrogen receptor positive (ER+ve) tumours, respond well to hormonal therapies and are commonly diagnosed before the tumour metastasize to bone. However, the majority of bone metastasis studies use triple negative breast cancer cell-line e.g. MDA-MB-231. To have a more comprehensive idea of whether tumour cells prefer to colonise particular areas of the bone marrow, an *in vivo* study to map the location of ER+ve cells within the bone was performed by injecting T47D and MCF-7 cells labeled with Vybrant-DiD i.c. into 12-week old mice.

Similar to the triple negative breast cancer cell-lines, the ER+ve cell-lines injected in the mature animal model also display a predilection for the trabecular region of the bone compared to the area adjacent to the growth plate, though the *p*-value did not reach statistical significance (*p*= 0.3481 for T47D and *p*= 0.2457 for MCF7 cell-line). Interestingly, the number of T47D cells reaching the bone microenvironment was lower than for the MCF7 cells, the difference in Vybrant-DiD positive events detected in ROI1 was statistically significant (*p*=0.0472) (figure 3.9).

MCF7 cells appear to home slightly further away from the bone surface in ROI1 compared to all the other cell-lines analysed, with a mean value of 118.50±48.44µm (42-257µm) while in ROI2 the mean value of 6.09±2.21µm (0-10µm) is comparable to both the triple negative cell-lines and the ER+ve clone T47D (figure 3.9).

Of all cell-lines investigated the T47D were the cells located in the closest proximity to the bone surface, exhibiting a mean distance of just 27µm (0-71µm) in ROI1 showing that there may be some cell-specific differences in location in the niche.

Additionally to the data discussed in the previous sections, these results confirm that breast cancer cells, both ER positive and negative, colonise some region of the bone microenvironment, regardless of the route of administration. Furthermore, all cell-lines except the bone-seeking MDA-MB-231/B02-GFP present some degrees of affinity for the trabecular area of the bone marrow compared to the growth plate region.

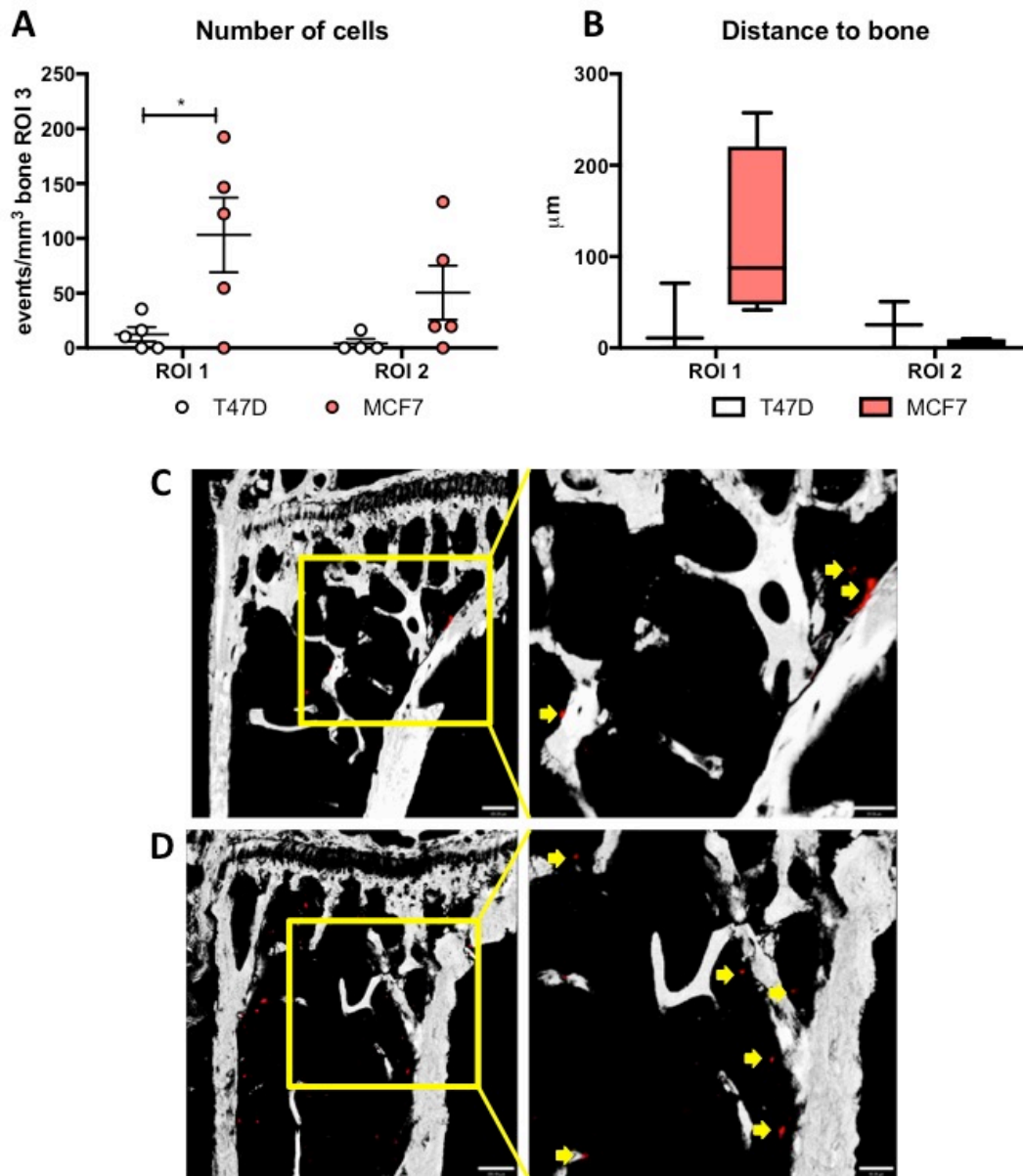


Figure 3. 8 T47D and MCF7 cell-lines colonisation of bone

(A) Graph representing the direct comparison between the homing of T47D cells vs MCF7 cells (n=5 animals and 5 bones/group analysed). (B) Comparison between the distances to the nearest bone surface of the two cell-lines injected. * $p \leq 0.05$ two-way ANOVA and Tukey post test. Examples of two-photon scan showing the proximity to the bone surface of T47D (C) and MCF7 (D), position of the cells is highlighted by the yellow arrows and scale bar are 100µm (right panel) and 50µm (left panel).

3.5.5 Modification of the HSCs niche changes the homing of breast cancer cells

It has been suggested that the metastatic niche broadly overlaps with the hematopoietic stem cell niche that can be found in the trabecular region of the metaphysis of long bones. Shiozawa *et al.* elegantly showed how prostate cancer cells and HSCs locate within the same niche [28], [36] using a CXCR4 antagonist to mobilize the HSCs. In the following study I used the same compound, AMD3100, with daily dosing for 5 days to “empty” the HSCs niche. Subsequently MDA-MB-231-GFP-IV cells labeled with Vybrant-CM-Dil were injected into the tail vein of the 12-week old mice. Animals were culled after 5 days and two-photon microscopy was used to count the number of cells able to colonise the bone marrow in control or treated animals and also to establish whether the location was affected.

As anticipated, the mobilization of the HSCs cells from their niche created more space available for the homing of breast cancer cells, resulting in a significantly greater number of tumour cells colonizing the trabecular region of the bone ($p=0.0409$). In contrast, no difference in tumour cell number was observed in the growth plate area of the bone ($p=0.7303$) which is usually less colonised and does not contain HSCs niches (figure 3.10).

These data showed how alteration of the HSCs population resulted in a modification of the number of breast cancer cell detected with two-photon microscopy. Modification of a component of the bone microenvironment changes the homing of tumour cells which indicates that the different cellular components of the metastatic niche influences the metastatic progression, from the early stages of breast cancer cell colonisation of bone.

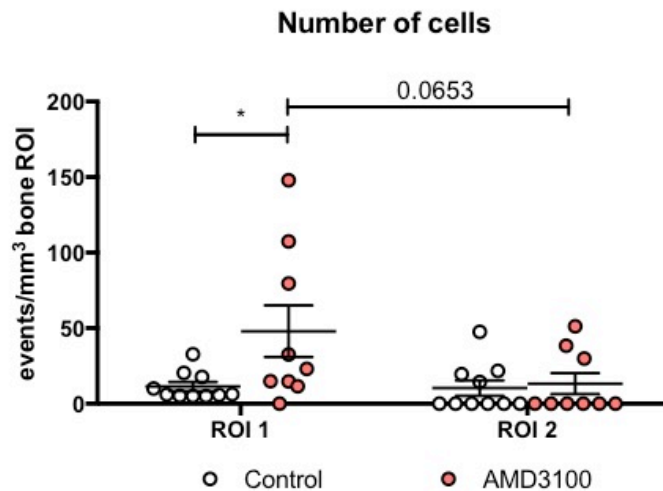


Figure 3.9 Modification of the HSCs niche

Graph representing the homing of MDA-MB-231-GFP-IV cells after treatment with the CXCR4 antagonist AMD3100 (n=5 animals, 9 bones analysed) or with PBS (n=5 animals, 10 bones analysed). Significantly greater number of tumour cells was detected in ROI1 after the mobilization of the HSCs cells outside the niche. * $p \leq 0.05$ two-way ANOVA and Tukey post test.

3.5.6 Breast cancer cells show no difference in the colonisation of young or mature animals

The animal model described earlier in this chapter (sections 3.5.1-5) involved mature mice (12-week old) with a low bone turnover that has been shown to support tumour cell dormancy [128], [216]. However, the majority of published *in vivo* studies evaluate the efficacy of therapeutic agents on tumour growth, therefore young animals (≈ 6 -week old) are usually utilized. To assess whether there were changes in the breast cancer bone colonisation in young compared to mature mice, 6- and 12-week old BALB/c nude (n=8/group) were injected i.v. with Vybrant-CM-Dil labeled MDA-MB-231-GFP-IV cells, long bones were collected and analyzed by multiphoton microscopy.

It is important to note that human cells were only detected in 50% (4 bones out of 8) of the long bones of young animals and their number was highly variable with a range of 9-2142 cells/mm³. In contrast, tumour cells were identified in 70% (7 out of 10) of mature mice and there was less variability in the number of cells homing to the bone marrow (5-58 cells/mm³) (figure 3.11). *In vitro* studies investigating this further

detected a small cytotoxic effect of the new batch of Vybrant-CM-Dil dye used that could have caused the reduced number of breast cancer cells homing within the bone microenvironment, in subsequent studies the concentration of this dye was therefore reduced from 5 μ M to 2 μ M.

The pattern of homing of MDA-MB-231-GFP-IV cells was maintained both in young (6-week old) and mature (12-week old) animals, although the preferential localization of the tumour cells in ROI1 compared to ROI2 was not statistically significant, $p=0.4312$ and $p=0.1213$ for young and mature respectively ($n=8$ /group).

In both the ages breast cancer cells homed really close to the nearest bone surface, with the mean value measure in ROI1 was $29.01\pm 9.97\mu\text{m}$ in 6-week old and $59.13\pm 17.14\mu\text{m}$ in 12-week old animals while in ROI2 this value were reduced to $3.72\pm 3.00\mu\text{m}$ and $2.24\pm 1.56\mu\text{m}$ respectively. As described earlier in this chapter, the breast cancer cells appear to locate closer to the bone surface in the growth plate area compared to the trabecular region of the bone, but this trend was not of significant, $p=0.0902$ and $p=0.0691$ for young mice vs mature animals (figure 3.11).

Another similarity between the colonisation of bone in young and mature animals was that tumour cells located closer to the nearest bone surface than to the nearest cancer cell. Despite the clear trend, this preferential spatial location was not statistically significant in neither ages nor ROIs.

These results demonstrate that there is no significant difference between young and mature animals in breast cancer cell colonisation of bone, not in the overall number of cells homing or in the location of these cells in relation to the bone surface and other tumour cells. Furthermore, the similarity in the pattern of homing suggests that the increased outgrowth of tumours in bones of young animals compared to mature ones is most likely due to differences in the dynamic process as in the bone microenvironment and associated with accelerated turnover.

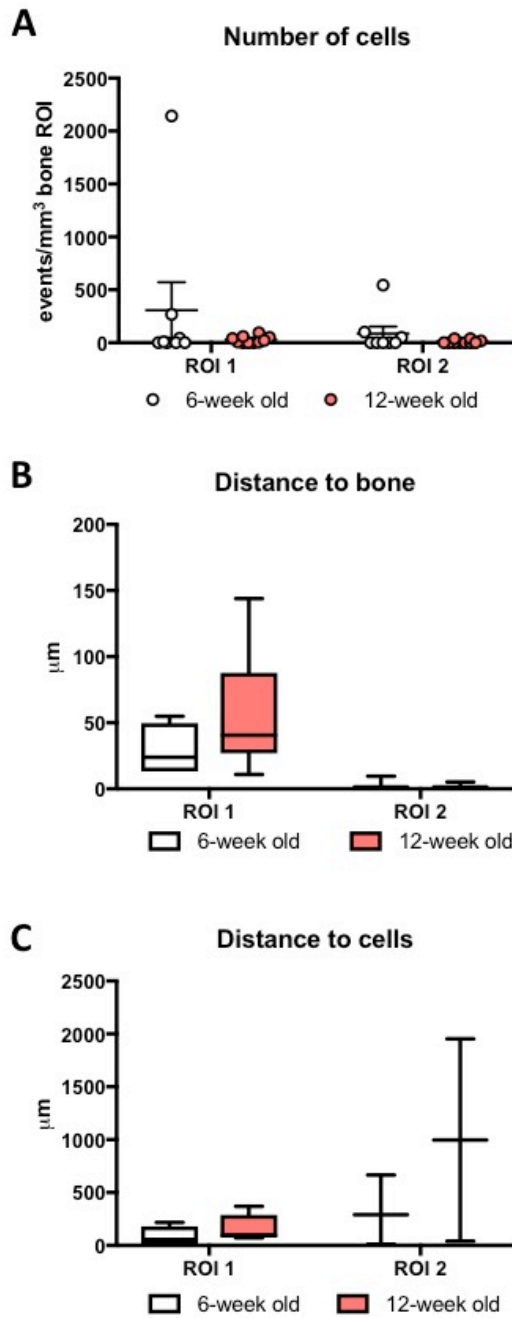


Figure 3.10 Homing of breast cancer cells in the young (6-week old) vs mature (12-week old) animal model

A) Graph shows the number of MDA-MB-231-GFP-IV cells detected in 6- and 12-week old mice 5 days after tumour cells i.v. injection (n=8 animals and bones analysed/group), graph shows mean \pm SEM. Distances of the tumour cells to the nearest bone surface and to the closest breast cancer cells are shown respectively in (B) and (C). No significant difference was observed between the homing of tumour cells in animal models of different ages, as assessed using a two-way ANOVA and Tukey post test.

Taken together, the studies described in this chapter show that using different membrane dyes, differences in the overall number of tumour cells are detected but their pattern of homing is not altered. Moreover there is a high similarity in the seeding of subtypes of breast cancer cell-lines, both ER+ve and ER-ve, regardless of the route of injection used or the age of the animal model used. The cell-lines utilised displayed an affinity for the trabecular region of bone metaphysis compared to the growth plate area, and they locate in close proximity to the bone surface. Modification of the microenvironment results in modulation of the total number of breast cancer cells detected in bone, supporting the theory of an overlap between the HSCs niche and the metastatic niche.

3.6 Discussion

The main aim of this chapter was to determine whether breast cancer cells, both ER+ve and triple negative, colonise the bone following a specific homing pattern. Investigating the location of breast cancer cells in the early events of the metastatic process to bone in *in vivo* models was made possible by the recent technological advances both in cell labelling and imaging. I have used these techniques to characterize the homing of tumour cells to long bones, tibiae and femora, and demonstrate that breast cancer cells locate to specific areas of the bone irrespective of whether they are ER+ve or ER-ve. The trabecular region of the bone, which was the preferential location for seeding of breast cancer cells colonizing the secondary organ, contains the HSCs niche, high numbers of osteoblasts as well as cells of the microvasculature. Intriguingly, all of these cellular populations thought to compose the metastatic niche, and are suggested to play a role in the maintenance of the quiescent state and subsequently in the progression of metastatic disease. Moreover, I established that, by changing the microenvironment and the space available in the metastatic niche, the number of breast cancer cells detected in the bone microenvironment increased. These findings emphasize the importance of cell populations resident in bone, in the homing to and maintenance of tumour cells in the putative metastatic niche, and not only during the late stages of the metastatic process. Despite the large number of breast cancer cells (1×10^5 /mouse) that were successfully injected into the circulation of the animal models, only a small portion (with a range of 0-97 cells/bone) colonised the long bones in the region analysed. Within five days, the majority of tumour cells have died, most likely due to an inability to locate to an appropriate niche. Furthermore, as in human disease, our *in vivo* model demonstrates that simply arriving in bone is not sufficient to cause the secondary tumour [2], [16], [205], [206], [214], [217]. Malignant cells must be able to interact with the microenvironment in order to receive and respond to signals to survive and proliferate [87], [218].

Although identification of these regulatory signals is a subject of intensive research, to date only little is known about their nature, and particularly in the early stages of bone colonisation. Moreover, while the function of osteoblasts and osteoclasts as players in

the vicious cycle that drives the late stages of bone metastasis is well established, their roles in the initial step of the metastatic process such as homing and/or initiation of the proliferation of DTCs in bone is still unclear [12], [14]–[16], [118]. Recent studies carried out in our laboratory provided evidence that increasing osteoclast activity, as a result of ovariectomy or castration, triggers the growth of disseminated breast and prostate cancer cells to form tumours in bone [128], [148]. It was established that this was an osteoclast-mediated effect the tumour growth was prevented using the anti-resorptive agent zoledronic acid or OPG-fc [149]. To further support that an alteration of the bone microenvironment results in changes in the homing of tumour cells, Dr Hannah Brown elegantly described that a reduction in the number of osteoblasts prior to breast cancer cell injection resulted in modification of the distribution of the tumour cells within the bone microenvironment attenuating the preferential pattern of location to the trabecular region, but with no effect on overall total number [118]. These data suggest that the location of the tumour cells influences their ability to proliferate and develop overt metastasis and data presented in this chapter demonstrate that breast cancer cells locate *in vivo* preferentially in the trabecular region of the bone, areas rich in cells of the osteoblastic lineage and vessels. It is important to note that, although the bone cell population, HSCs and microvasculature are the major focus of this thesis, they are not the only components of the bone microenvironment to play a role in the metastatic process. For example, a study from the Edwards group recently underlined the strong impact of bone adipose tissue on tumour growth [43] and others have reported that the innate immune system, in particular macrophages, has a role in the initiation and cancer progression [45].

As well as being rich in osteoblast and osteoclasts, the HSCs niche is located in the area of bone preferentially occupied by the breast cancer cells. It has been proposed that the space in the HSCs niche is limited and therefore only a certain number of HSCs can reside in the bone marrow [39], [51], [219], [220]. The mechanism behind the competitive access of the HSCs to this limited space in the niche remains to be identified. One possible alternative is that different ‘specialized niches’ are present in the bone marrow that allow entry and/or survival of only certain types of cells [41]. An opposing theory describes the space available as ‘equivalent niches’, in which the

number of HSCs that reside in the niche is limited by the competition with other cells that can seed in the same microenvironment [41]. The theory of 'equivalent niches' could explain the competition between prostate cancer cells and HSCs competing for spaces in the niche and the hypothesis of an overlap between the metastatic and the HSCs niche [36]. In their manuscript Shiozawa's group observed that modification of the HSCs population altered the number of prostate cancer able to seed in the partially emptied microenvironment. The experimental data described earlier in this chapter detailed that the same result was obtained using breast cancer cells. Shiozawa *at al.* monitored changes in the prostate cancer cell number by qPCR while in my *ex-vivo* analysis I utilized two-photon microscopy, that made it possible to investigate any potential alteration of the location of the tumour cells as well as their number. Here it is demonstrated for the first time for breast cancer that modification of the HSCs population results in an alteration of the overall number of breast tumour cells detected in the bone microenvironment. After the treatment with the CXCR4 inhibitor AMD3100, increased numbers of breast cancer cells were detected in the bone microenvironment, suggesting that liberating space in the HSCs niche allowed tumour cells to colonise this.

The trabecular region of the bone where breast cancer cells prefer to seed is highly vascularized [97], [106], [221]. The microvascular component of the bone microenvironment and understanding the importance of the perivascular niche is increasingly becoming a field of considerably interest in cancer research. The Adams group described the complexity of the microvascular structure in the metaphysis region in the bone, moreover this publication described a novel structurally distinct capillary subtype (H vessels) which mediates bone microvascular growth and maintains perivascular osteoprogenitors, coupling angiogenesis with osteogenesis [97]. Furthermore, it has recently been proposed that the microvasculature plays an important role in the maintenance of the quiescent state of breast cancer cells. Ghajar's group has demonstrated that expression of thrombospondin (TSP-1) by the stable microvasculature support dormancy, in contrast pro-tumourigenic molecules like periostin and TGF- β 1 production during vessels sprouting stimulate tumour cell proliferation [35].

In conjunction with the number of tumour cells seeding within the bone microenvironment, I also investigated their location with respect to the bone structure of the metaphysis. I found that breast cancer cells locate in closer proximity to the bone surface, rather than next to other tumour cells and this particular pattern of homing has been confirmed in several cell-lines and animals of different ages. This suggests that the composition of the microenvironment is key to tumour cell colonisation of bone, rather than the presence of “pioneering “ DTCs that signal to attract further tumour cells. The proximity to the bone surface was particularly accentuated in the T47D cell-line. Moreover, T47D seeded more evenly between the ROIs analysed compared to the other cell-lines investigated. The difference recorded in the homing of the two ER+ve cell-line was surprising since MCF7 and T47D share the same classification and immunoprofile (luminal A, ER+ve, PR+ve/-ve and HER2-ve) but it has been reported that these cell-lines present differential expression of a high number of proteins involved in various biological functions including carcinogenesis [222].

In summary, my data demonstrate that breast cancer cells present a preferential pattern of seeding to bone in *in vivo* models, regardless of the route of injection, the characteristic of the cell-line used or the age of the animals. Moreover, I have demonstrated that alteration of the bone cell population is reflected in a modification in the number of cancer cells homing to bone. Taken together, the data validate the theory that several components of the microenvironment, above all osteoblast, osteoclast, HSCs and microvasculature, influence the metastatic process not only in late stages of metastasis formation but also in the earlier steps of colonisation. Further characterization of the components of this niche and their interactions with tumour cells is required to create a better understanding of the early stages of the metastatic process and consequently improve the therapeutic approaches for patients with a poor prognosis.

Chapter 4

Characterisation of the metastatic niche in young and mature mice

4.1 Summary

During dissemination to distant organs, breast cancer cells detach from the primary site, enter the circulation and finally reach the bone marrow where they can remain dormant for extended periods of time. Despite the large number of breast cancer cells that successfully locate in the bone microenvironment, only a very limited number of colonies develop to form overt tumours. The bone microenvironment plays a crucial role in the homing of cancer cells to the metastatic site and in the maintenance of the dormant state and/or progression of tumour growth, but the cellular and molecular components that enable tumour cells to undergo these processes have not been fully elucidated.

The aim of this study was to characterise *in vivo* models of breast cancer bone metastasis in young animals (6-week old) with high bone turnover that promotes tumour growth and in mature animals (12-week old) in which dormancy is supported. Different aspects of the bone microenvironment were investigated using two-photon microscopy to map the location of single tumour cells within the bone microenvironment, μ CT to visualise the bone structure and immunofluorescent protocols to investigate variation in the bone microvasculature of the two animal models used.

Young animals appear to have a denser bone structure and the organisation of their microvasculature network shows an expansion of different vessel sub-types in the metaphysis in long bones when compared to mature animal. Intriguingly, the only marker expressed in higher levels in the 12-week old animal is TSP-1, which is known to support tumour dormancy. The results described here highlight the close association between the different components of the bone microenvironment, bone turnover and the microvasculature, and breast cancer cell dormancy.

4.2 Introduction

The metastatic niche(s) is the region of bone where breast cancer cells seed. These regions of bone present a complex microenvironment in which components of the HSC niche, osteoblastic niche and perivascular niche are overlapping [34], [39]–[41]. Once in bone, tumour cells interact with the microenvironment receiving signals that influence either the development of the metastasis in the fertile soil or the maintenance of a dormant state [10], [16], [48], [118], [211], [223]. The importance of the extensive cross-talk between tumour cells and the microenvironment for the progression of disease explains why, despite hundreds of breast cancer cells reaching the bone marrow only a limited number develop to form secondary tumours [87], [217], [218], [224], [225].

The well-recognised concept of the ‘vicious cycle’ between osteoclasts and tumour cells is just one example of how the progression of bone metastasis is influenced by the presence of cytokines and growth factors [9], [12], [13], [15]. However the specific mechanism(s) that triggers DTCs to escape quiescence and proliferate is less well understood. One of the major issues in treating metastatic breast cancer is that it is not known which patients will develop metastasis and when this will occur. The metastases can form decades after the initial diagnosis, long after the primary tumour is removed or successfully treated. This is caused by the presence of dormant tumour cells in the microenvironment. This type of cell remains quiescent in the secondary organ, neither proliferating nor undergoing apoptosis [20], [209], [210].

The engagement with the bone microenvironment regulates the preservation of the dormant state or the transition to a proliferative phenotype [34]. It is a well-recognised concept that the mechanisms tumour cells use to retain the quiescent state is similar to the ones used by the HSCs [211]. Even though the exact mechanism that attract these cells to the niches, keep them in a quiescent state and guide their proliferation and differentiation is not fully understood. It is clear that both the endosteal and the perivascular component of the HSC niches contribute to the recruitment and preservation of HSCs [34], [39], [87], [226], [49]–[51], [62], [65], [73], [74], [86]. Several studies have reported cross-talk between the osteoblastic and

perivascular populations, emphasising the theory of overlapping niches rather than distinct compartments. The HSC niche is in fact most commonly described as a highly vascularised endosteal region [67]. In addition to their function in retaining HSCs in the niche, osteoblasts have a role in the attraction and interaction with cancer cells that colonise the marrow cavity [87], [91]–[94], [227], [228] and it has been proposed that direct contact between osteoblasts and cancer cells is needed for tumour cell proliferation in the bone microenvironment, in the early stages of the metastatic colonisation [87].

Less well understood is the interaction between tumour cells and the perivascular niche components. It has been proposed that the microvasculature may support tumour cell dormancy through secretion of Thrombospondin [8], [31], [35], [107], [109]. *In vitro* and *ex vivo* studies described that this angiogenesis inhibitor is expressed by the stable microvasculature, while it is reduced in the presence of sprouting vessels where its expression is replaced by the tumour-promoting factors Periostin and TGF- β 1 [35].

The trabecular region of bone where the metastatic niche(s) reside has a characteristic plasticity due to the continuous remodelling mediated by action of the bone forming osteoblasts and bone-resorbing osteoclasts. Moreover, the plasticity of this microenvironment it is also reflected in the changes detected in the microvasculature of aging mice. Kusumbe *et al.* described a novel capillary subtype (CD31^{hi} Endomucin^{hi}, H-vessels) that is localised in the metaphysis of the bone, couples angiogenesis and osteogenesis and decreases with age [97], [221]. In experimental models, tumour take is reduced in ageing when compared to young mice and changes in both bone turnover and in the perivascular niche may explain this observation; young animals represents a tumour growth promoting microenvironment while the bone microenvironment of mature animals supports dormancy.

4.3 Aims

The aim of the work presented in this chapter is to characterize the bone microenvironment and the perivascular niche in two *in vivo* murine models to test the following hypothesis:

The differential growth rate of breast cancer bone metastases in young and mature animal models is caused by differences in the bone microenvironment.

The main goals of the work are to use young and mature mice to performed as follows:

- To assess the bone structure of the *in vivo* models
- To compare the pattern of the Endomucin positive vessel network in young and mature murine models
- To determine the presence of CD31 and CD34 positive vessels and relative expression compared to Endomucin vessels
- To investigate whether there are difference in the abundance of Thrombospondin-1 (TSP-1) expression and TSP-1+ve cell populations between the two murine models analysed
- To evaluate the changes in the presence of Osterix positive cell population with age

4.4 Materials and Methods

Detailed information can be found in the main Material and Methods Chapter 2.

4.4.1 Breast cancer cell lines

The triple negative MDA-MB-231-GFP-IV breast cancer cell line was cultured in RPMI 1640 medium enriched with 10%FCS while MDA-MB-231-NW1-Luc2 cells were cultured in DMEM + Pyruvate medium enriched with 1% penicillin/streptomycin and 10%FCS and at 37°C 5%CO₂. Once reaching confluence, breast cancer cells were labelled with the lipophilic dye Vybrant-CM-Dil as explained in detail in section 2.3.

4.4.2 *In vivo* study

The *in vivo* study was carried out accordingly to local guidelines and with Home Office approval under project licence PPL 70/8964 held by Professor Nicola Brown, University of Sheffield, UK.

To assess the differences in the microenvironment of young and mature animals, 6- and 12-week old BALB/c nude mice (n=5/age group) were injected i.v. with 1×10^5 MDA-MB-231-GFP-IV cells labelled with the membrane dye Vybrant-CM-Dil. Five days after the injection, animals were culled and hind limbs were collected for *ex vivo* analysis (Figure 4.1).

To visualise the microenvironment components in tumour bearing mice, 6-week old BALB/c nude mice (n=24) were injected i.v. with 0.75×10^5 MDA-MB-231-NW-Luc2 cells labelled with the membrane dye Vybrant-CM-Dil. Tumour growth was monitored twice weekly using In Vivo Imaging System (IVIS). Animals were culled after the detection of a small (4 days after first detection), medium (7-11 days) and large sized tumour (14-17 days) and hind limbs were collected for fluorescent immunohistochemistry (Figure 4.1).

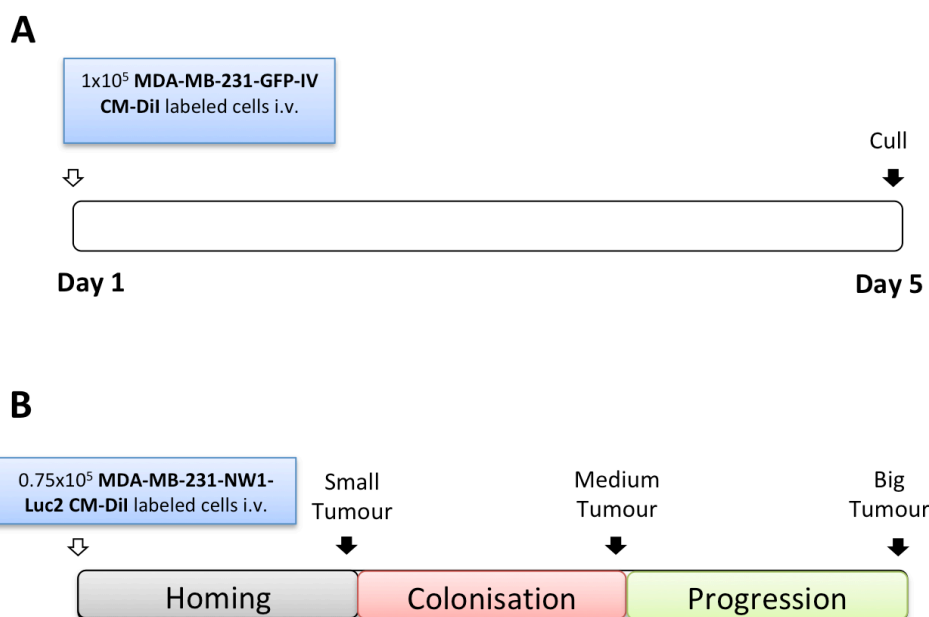


Figure 4.1 Outline of the in vivo studies evaluating homing of bone-seeking MDA-MB-231 cell-lines

Experimental outline. A) 6- and 12-week old female BALB/c nude mice were injected intravenously (i.v.) with 1×10^5 MDA-MB-231-GFP-IV cells labeled with Vybrant-CM-Dil ($n=5$ animals/group). Animals were culled five days after the injection and tibiae and femora were collected for *ex-vivo* analysis. B) 6-week old female BALB/c nude mice were injected i.c. with 0.75×10^5 MDA-MB-231-NW1-Luc2 cells labelled with Vybrant-DiD ($n=24$). Animals were monitored twice weekly with IVIS and mice were culled when tumour colonies were formed, colonies grown for 0-4 days were considered a small tumour, medium size after growth of 7-11 days and large tumour within 14-17 days after the first detection. White arrow=tumour cells injection and black arrow=culling time point.

4.4.2.1 Collection and preparation of the bones for two-photon microscopy

Animals were overdosed with an i.p. injection of Pentobarbital (50 μ l) and cervical dislocation was used to confirm death. Hind limbs were dissected carefully removing the tissue surrounding the bones and tibiae and femora were separated. Femora were wrapped in aluminium foil and collected snap frozen in liquid nitrogen. Snap frozen bones were placed into freezing blocks, embedded with Cryo-M-Bed and stored at -80°C.

Snap frozen femora were cut longitudinally using a Bright OTF Cryostat and a 3020 microtome and the bones were then placed onto a glass-bottomed dish with the exposed bone marrow facing downwards, as described in section 2.10.1.

4.4.2.2 Collection and preparation of the bones for micro computed tomography (μ CT) and fluorescent immunohistochemistry

On the day of cull, femora were collected for two-photon microscopy while tibiae were processed for micro computed tomography and fluorescent immunohistochemistry. After dissection tibiae were placed in 4% PFA for up to 6h, during which they were analysed by μ CT, and afterwards were processed for fluorescent immunohistochemistry. 4% PFA was replaced by 0.5M EDTA for 48h and bones were then immersed in CPT solution and subsequently embedded in gelatine as explained in section 2.9.3. Gelatine blocks were stored at -80°C until they were cut into $30\mu\text{m}$ thick sections with the Microm HM 560 cryostat.

4.4.3 Two-photon microscopy and location of cancer cells within the bone structure

A glass bottomed dish containing the specimen was mounted on a histological slide with the exposed bone marrow facing upwards as described in section 2.10.1. A Zeiss LSM510 NLO upright two-photon microscope was used to scan the growth plate and the metaphysis area of the bone ($2104\mu\text{m} \times 2525\mu\text{m}$ field of view and $70\mu\text{m}$ depth) a Chameleon two-photon laser at 900nm was used to visualise the bone structure and HeNe 543nm to visualize Vybrant-CM-Dil labelled breast cancer cells.

Volocity 3D Image Analysis software 6.01 was used to analyse the reconstructed three-dimensional image acquired with the two-photon microscope. Quantifications were performed in two different ROIs, the first one consisting of the growth plate area and the second one of the trabecular region of the bone marrow. Objects of a volume larger than $250\mu\text{m}^3$ detected by the HeNe 543nm laser were considered breast cancer cells and their number, distance to the nearest bone surface and to the closest cancer cell were calculated, as described in section 2.10.3.

4.4.4 Micro computed tomography (μ CT)

Micro computed tomography was used to determine the difference in the bone structure of young and mature animal models. As described in section 2.11, tibiae were scanned with SkyScan 1272 during the incubation time in 4% PFA and the reconstructed images were analysed with CTAn software to determine the VOI. Trabecular bone volume, trabecular number and thickness were the parameters considered in the analyses of the bone structure.

4.4.5 Immunofluorescence protocols for the staining of the perivascular niche components

Perivascular niche components were stained using immunofluorescence protocols using 30 μ m thick sections of gelatine embedded tibiae as described in the following sections.

4.4.5.1 Visualisation of Endomucin positive vessels

Tibiae frozen sections were incubated with an antibody against Endomucin for 1h at ambient temperature or overnight at 4°C after a permeabilisation step in 0.3% Triton X-100 (30min ambient temperature) and a quick wash in PBS. After the incubation with the primary antibody and three washes in PBS, the slides were incubated for 1h at room temperature with a secondary antibody conjugated with a fluorophore. The last step of the staining consisted of counterstaining the nuclei with DAPI (Vectashield mounting medium with DAPI, Vector Laboratories H-1200; Prolong Gold antifade reagent with DAPI, Life Technologies P36935) and mounting of the coverslips.

4.4.5.2 Staining of CD31 or CD34 and Endomucin positive vessels

The 30 μ m thick tissue section were permeabilised with 0.3% Triton X-100 for 30min at ambient temperature followed by blocking for 15min with Streptavidin and 15min in Biotin (Streptavidin/Biotin Blocking Kit – Vector Laboratories SP-2002). Bone slides were then incubated with the primary antibody against CD31 or CD34 for 1h at ambient temperature. The sections were then incubated for 40min at ambient temperature with a biotinylated secondary antibody prior to incubation for 30min at

ambient temperature with polyclonal rat-IgG. Tissue sections were then carefully washed in PBS and staining with the antibody against Endomucin (1h, ambient temperature) followed by an incubation for 40min at ambient temperature with the appropriate secondary antibody. The final steps of this double staining, consisted of incubation for 20min at ambient temperature with fluorophore-conjugated streptavidin, nuclei counterstaining with DAPI (Vectashield mounting medium with DAPI, Vector Laboratories H-1200; Prolong Gold antifade reagent with DAPI, Life Technologies P36935) and mounting of coverslips.

4.4.5.3 Visualisation of Osterix, α -SMA or Thrombospondin

Permeabilisation of the frozen sections was performed using 0.3% Triton X-100 for 30min at ambient temperature followed by a blocking step with Streptavidin/Biotin Blocking Kit, 15min incubation at ambient temperature for each reagent. The blocking step was followed by incubation with primary antibodies Osterix, α -SMA or TSP-1 and Endomucin for 1h at ambient temperature. Prior to incubation with fluorophore-conjugated streptavidin, bone sections were incubated with the appropriate secondary antibodies. After the incubation with streptavidin and careful washing in PBS, nuclei were counterstained with DAPI and coverslips were mounted.

4.4.6 Scoring of immunofluorescence stainings

Analyses of gelatine embedded tibiae were performed on three non-serial 30 μ m thick sections stained against different components of the perivascular niche.

4.4.6.1 Quantification of Endomucin positive vessels

A Leica AF6000 inverted fluorescence microscope was used to capture the images of the immunofluorescent staining against the endothelial marker Endomucin. The distinctive structure of H- and L-vessels was manually tracked using the Aperio ImageScope software and the length, number and area of bone marrow occupied by the different microvessels were determined.

4.4.6.2 Quantification of vessels positive for both Endomucin and CD31 or CD34

Immunofluorescent stained tissue sections were imaged using a Zeiss LSM880 AiryScan Confocal microscope and ImageJ software was used to quantify the amount of vessels positive for both the markers CD31/CD34 and Endomucin. The region of interest was manually drawn around the metaphysis area of the bone marrow and the expression of CD31 or CD34 was calculated as a percentage of the microvasculature stained positive for the endothelial marker Endomucin.

4.4.6.3 Quantification of Osterix, α -SMA or Thrombospondin expression

Similar to the CD31/CD34 staining, images were captured with the confocal microscope Zeiss LSM880 AiryScan and the expression of Osterix, α -SMA or TSP-1 was measured within the desired ROI using ImageJ software. The function 'cell counter' of the software was also used to count the number of α -SMA positive vessels or TSP-1 positive megakaryocytes. For Osterix positive cells the function of the 'cell counter' was used to manually quantify a few slides and the numbers obtained were then compared with the values produced by the automatic function '3D object counter'. Since there was a high correlation between the two values obtained, all further tissue sections were analysed using the automatic function.

4.4.7 Statistical analysis

GraphPad Prism software (versions 6.0 and 7.0) was used to perform statistical analyses, as stated in each figure legend. A student T-test and Two-way ANOVA with Tukey post test were used and a p -value of $p < 0.05$ was considered significant.

4.5 Results

It is a broadly accepted concept that homing to bone is necessary but not sufficient for breast cancer cells to develop over tumour, cancer cells in fact need a fertile soil to allow their growth. The exact mechanisms that enable the establishment of secondary colonies have not been fully elucidated but it has been reported that high bone turnover promotes this process [101](Figure 4.2). The present study investigated the differences in the bone microenvironment of young (6-week old) and mature (12-week old) animal models to identify components playing a role in the maintenance of the dormant state and/or progression of tumour growth.

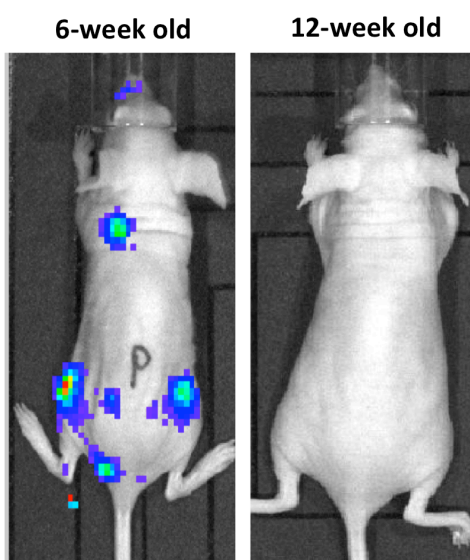


Figure 4. 2 *In vivo* tumour model

Representative image of the animal model used in our laboratory. Mice were injected i.c. with MDA-MB-231 cells transfected with luciferase (MDA-MB-231-NW1-Luc2), *in vivo* tumour growth was detected over time using an *in vivo* imaging system (IVIS). Images show tumour growth 14 days post injection, young animals develop tumour quicker than mature animals in which no colonies was detected at this time point.

4.5.1 Breast cancer cell bone colonisation in young and mature animal models

As shown in figure 4.1, when tumour cells (1×10^5 cells) are injected in young mice they develop tumour faster than when the same number of cells are injected in mature animal model. To verify that this difference in the growth of metastasis was not due to the number of cells reaching the tumour microenvironment, 1×10^5 MDA-MB-231-GFP-IV cells labelled with Vybrant-CM-Dil were injected i.v. in 6- and 12-week old BALB/c nude ($n=5$ /group). Five days after injection the animals were culled and long bones were collected for two-photon microscopy (femora) and for fluorescent immunohistochemistry (tibiae). As described in section 3.5.6, the previous *in vivo* study performed to map the location of single tumour cells in the bone microenvironment of young and mature animals showed a slight cytotoxic effect due to the concentration of the membrane dye used. In this case a concentration of $2 \mu\text{M}$ of Vybrant-CM-Dil (instead of $5 \mu\text{M}$) was used, resulting in a considerable reduction of bones in which no cells were detected (1 out of 5 femora from young mice). The preferential pattern of homing of this breast cancer cell line was maintained with fewer cells homing to ROI2 compared to ROI1, even though this did not reach the significance level in the young animal group ($p=0.1654$ in 6-week old mice, $p=0.0119$ in 12-week old mice). The variability between cells counted was also reduced with a range of 39-390 (112.60 ± 70.86) and 46-101 (85.81 ± 13.30) cells/ mm^3 in ROI1 and 0-21 (4.25 ± 4.25) and 0-55 (22.64 ± 11.74) cells/ mm^3 in ROI2 for young and mature animals respectively (figure 4.3A).

Irrespective of age, breast cancer cells locate close to the bone surface with a mean value of $42.76 \pm 15.55 \mu\text{m}$ (18-66 μm range) in 6-week old and $33.95 \pm 7.77 \mu\text{m}$ (21-56 μm range) in 12-week old mice in the trabecular region of the bone. In the growth plate region, these values were significantly reduced in the mature group (mean value $7.38 \pm 4.80 \mu\text{m}$, range 0-16 μm , $p=0.0456$) while in young animals this comparison was not possible since only one bone contained cells in this ROI (figure 4.3B). As described in the previous chapter, tumour cells prefer to home significantly closer to the bone surface than to other tumour cells ($167.60 \pm 34.63 \mu\text{m}$, $p=0.0137$ in young animals and $144.50 \pm 10.29 \mu\text{m}$, $p=0.0001$ in mature animals). This analysis was carried out only in ROI1 because of the low number of bones in which tumour cells were detected in ROI2.

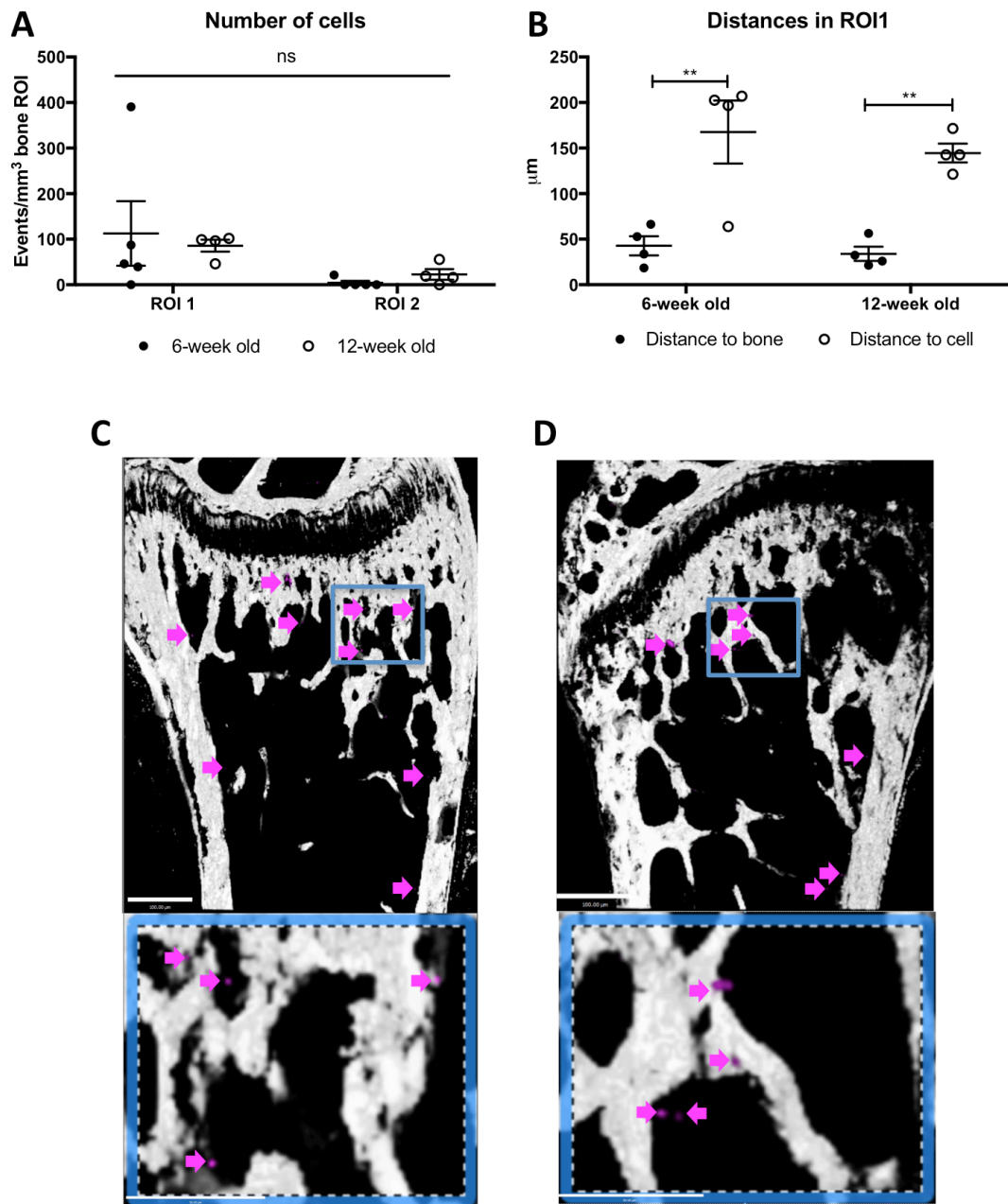


Figure 4.3 Homing of MDA-MD-231-GFP-IV cells in young and mature animals

A) Graph shows the number of MDA-MB-231-GFP-IV cells detected in 6- and 12-week old mice 5 days after tumour cell injection (n=5 animals, 4 bones analysed/group), represented as mean \pm SEM. (B) Distances of the tumour cells to the nearest bone surface in ROI1. (C) and (D) are examples of a two-photon scan of 6- and 12-week old animals showing bone (white), Vybrant-CM-Dil⁺ cells (pink and pink arrows) and Vybrant-CM-Dil⁺ cells (pink and pink arrows). Scale bars 100µm. Two-way ANOVA and Tukey post test, graphs show mean \pm SEM, ** $p \leq 0.005$ and ns is not significant.

Taken together, these results confirm the pattern of breast cancer to bone colonisation with a significantly higher number of events encounter in ROI1 compared to ROI2, a real close proximity to the nearest bone surface and a significantly higher distance to the nearest tumour cell. Moreover, the data showed in this section confirm that there is no significant difference in the early steps of the breast cancer bone metastasis, neither in the number of cells homing to bone nor in their location within the bone microenvironment, suggesting that the differences in outgrowth is due to the microenvironmental signal that the tumour cells receive once arrived in the bone.

4.5.2 Trabecular bone of young animals is more dense than bone of mature animals

To investigate the differences between the bone structure of young and mature animals, micro-Computed Tomography (μ CT) was performed as explained in section 2.11 comparing tibiae of 6- and 12-week old BALB/c nude female mice (n=7/group).

μ CT analysis revealed that there was no difference in the trabecular bone volume at the two different ages ($p=0.1023$) while a significant difference was found both in the number and in the thickness of the trabeculae. As shown in figure 4.4, the trabeculae of young animals were significantly thinner ($p<0.0001$) and their number was significantly higher ($p=0.0034$) when compared with mature animals (table 4.1).

Table 4.1 Summary of μ CT analysis

Analysis	Age of animals	Mean \pm SEM	Student t-test
Trabecular volume (BV/TV %)	6-week old	14.84 \pm 0.73	NS
	12-week old	13.04 \pm 0.71	
Trabecular thickness (Tb. Th.)	6-week old	0.03 \pm 0.00	****
	12-week old	0.04 \pm 0.00	
Trabecular number (Tb. N.)	6-week old	4.86 \pm 0.33	**
	12-week old	3.44 \pm 0.21	

NS= not significant $p>0.05$, ** is $p\leq 0.01$, **** is $p\leq 0.0001$

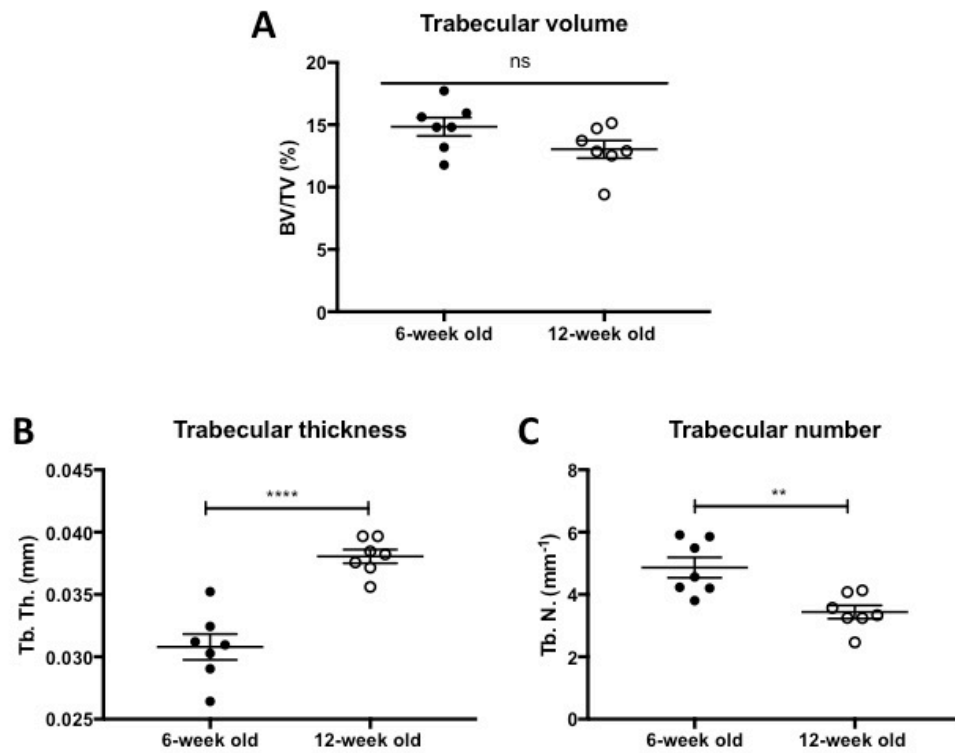


Figure 4. 4 Quantification of trabecular bone volume, thickness and number

A) Quantification of trabecular bone volume (BV/TV), (B) trabecular thickness and (C) number of tibiae of 6- and 12-week old animals (n=5 animals, 7 bones analysed/group). Student t-test, **p<0.01,***p<0.0001 and ns is not significant.

This bone micro architecture is shown in figure 4.5 and 4.6 where it is highlighted how the trabecular bone of young animal consists in a much more dense spongy structure compared to the mature animals.

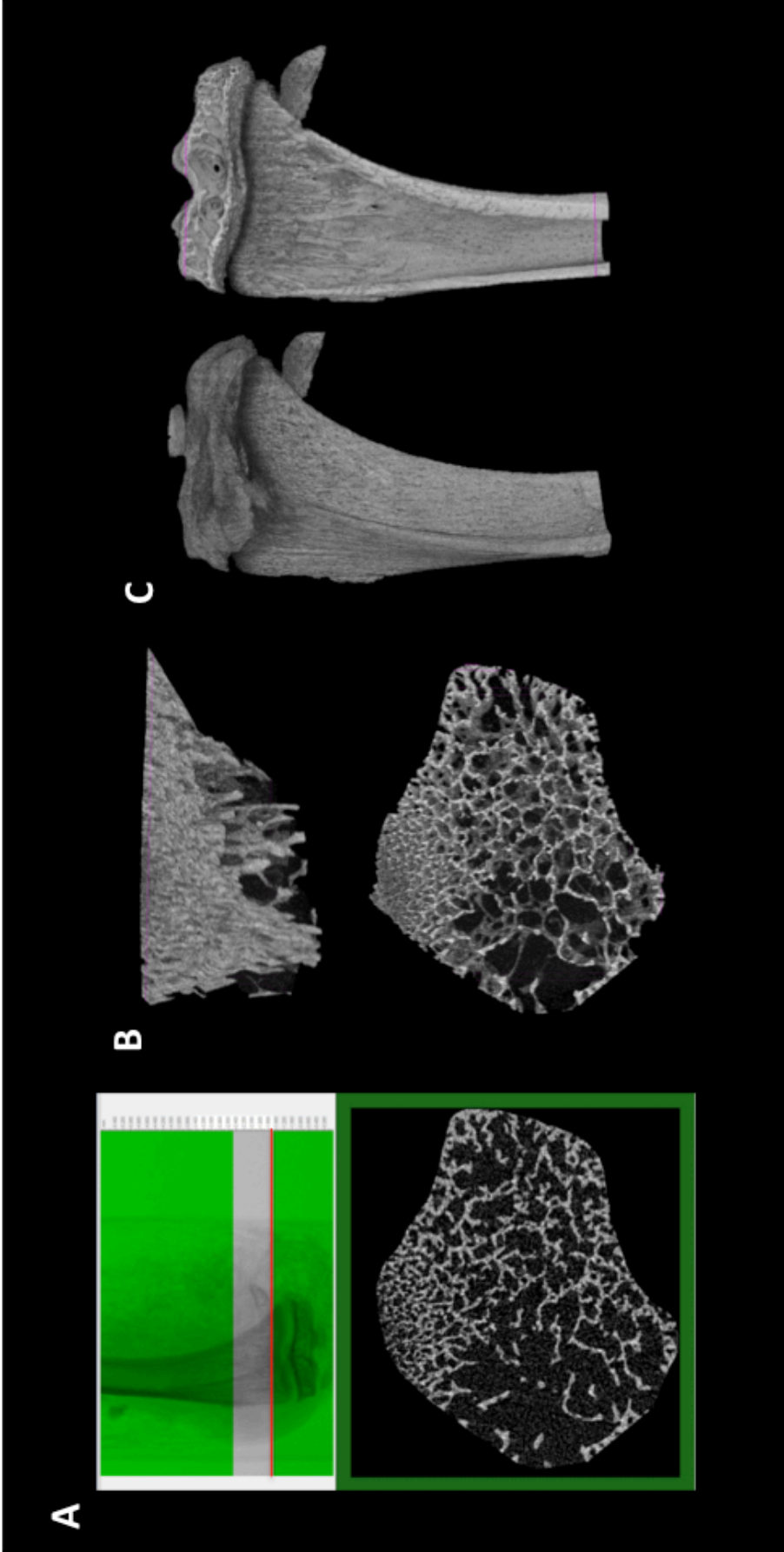
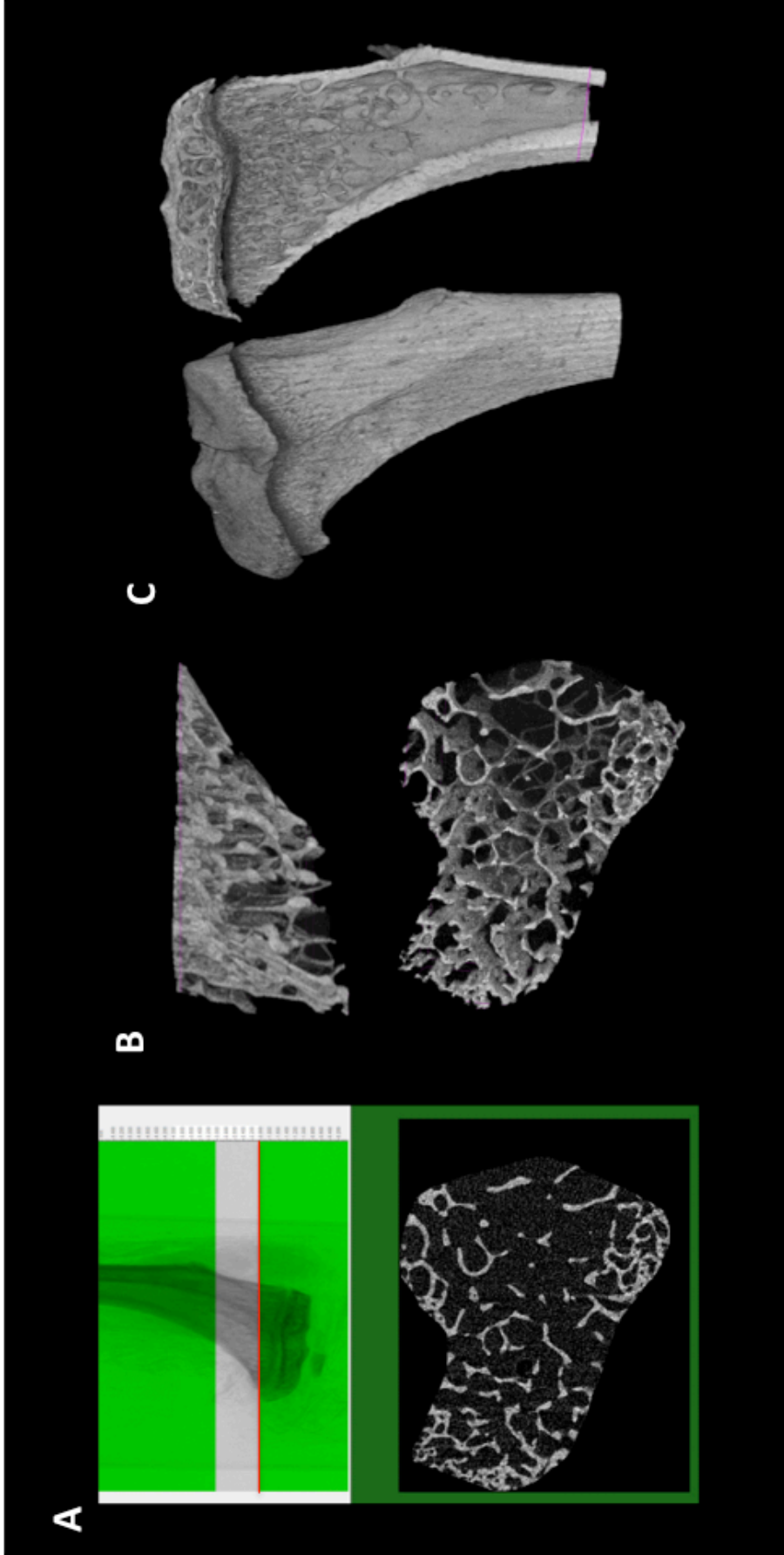


Figure 4.5 Representative mCT analysis and reconstruction of bone of young animals

A) Images taken from μ CT scans of tibiae of 6- week old mice. The bottom panel shows the cross section of the bones where the analysis started (red line on the radiograph). Three-dimensional reconstruction of the trabecular bone analysed (B) and the entire bone scanned (C).



A) Images taken from μ CT scans of tibiae of 12-week old mice. The bottom panel shows the cross section of the bones where the analysis started (red line on the radiograph). Three-dimensional reconstruction of the trabecular bone analysed (B) and the entire bone scanned (C).

4.5.3 Differences in the metastatic niche between young and mature mice

By developing an innovative protocol for the cryopreservation and immunofluorescent staining against endothelial cells, Kusumbe *et al.* made it possible to visualise the microvasculature of the bone marrow [25], [97]. With the help of Dr Russell Hughes and Dr Hannah Brown (University of Sheffield, UK) we modified this protocol to visualise the bone marrow microvasculature and other components of the perivascular niche using the equipment available in our department.

4.5.3.1 Young animals have more osteoprogenitors cells than mature animals

To visualise the osteoprogenitor component of the bone microenvironment of young and mature animals, tibia sections were stained with an antibody against Osterix using the immunofluorescent protocol described in section 2.14.3 (figure 4.7). Images of three non-consecutive 30 μ m section of tibia (n=3/ages) were captured using the Zeiss LSM880 AiryScan Confocal microscope. The area of bone marrow analysed was $2.50\pm 0.25\text{mm}^2$ for the 6-week old animals and $2.30\pm 0.99\text{mm}^2$ for the 12-week old animals ($p=0.5059$)(figure 4.8). Osterix⁺ cells were found mostly in the metaphysis of the bone section in close proximity to the Endomucin⁺ vessels (figure 4.7) and Osterix expression overall was higher in young animals compared to mature mice, although this was not significant ($p=0.1241$)(figure 4.8). The size of the objects detected was measured to verify that only cells of the same size were stained with Osterix, $90.28\pm 0.66\mu\text{m}^3$ and $88.64\pm 2.93\mu\text{m}^3$ for 6- and 12-week old animals respectively ($p=0.6147$) (figure 4.8). Three slides were chosen at random and the number of Osterix⁺ cells were counted both manually, using the 'cell counter' function of ImageJ, and automatically, the '3D object counter'. The value obtained were compared using a paired Student's t-test and no significant difference was detected ($p=0.5503$); moreover a very strong positive correlation was observed when a Pearson correlation test was performed ($r=0.9713$)(figure 4.8). Following confirmation of the high reliability of the automatic quantification, this system was used to count the number of Osterix⁺ cells of the entire dataset. As expected, a significantly higher number of osteoprogenitors/ mm^2 of the bone marrow area analysed was observed in young animals compared to the mature animals (273.80 ± 4.43 vs 230.40 ± 6.30 ; $p=0.0049$).

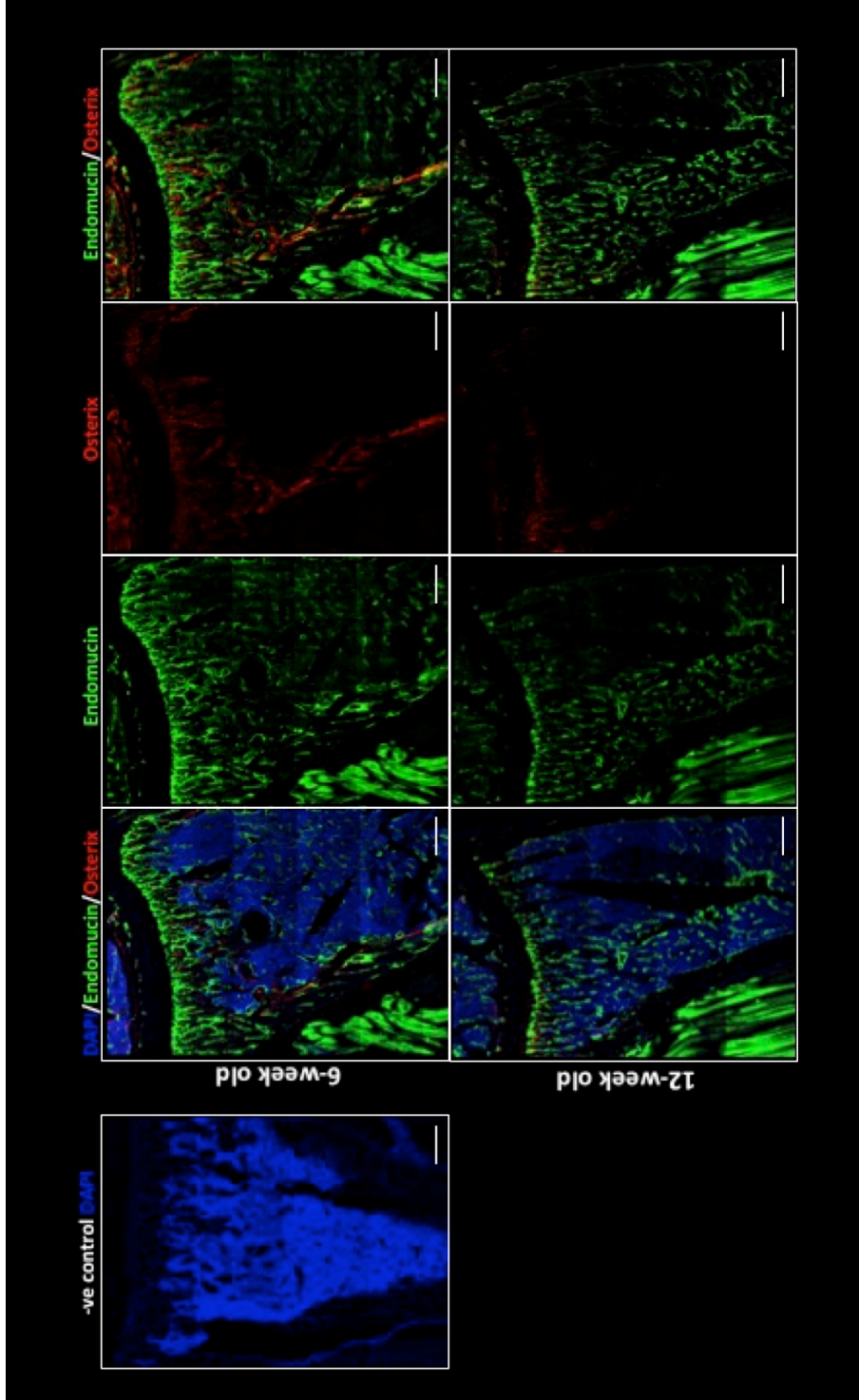


Figure 4.7 Representative images of immunofluorescent staining against Osterix

Immunofluorescent staining against Osterix and Endomucin was performed on gelatin embedded tibiae (30 μm) of 6- and 12-week old female BALB/c nude mice. Nuclei were counterstained with DAPI, vessels with Endomucin (1:100) and goat anti-rat AlexaFluo 488 (1:200) and osteoprogenitors with Osterix (1:300) and Streptavidin AlexaFluo 647 (1:200). Blue=DAPI, green=Endomucin and red=Osterix. Scale bar 200 μm .

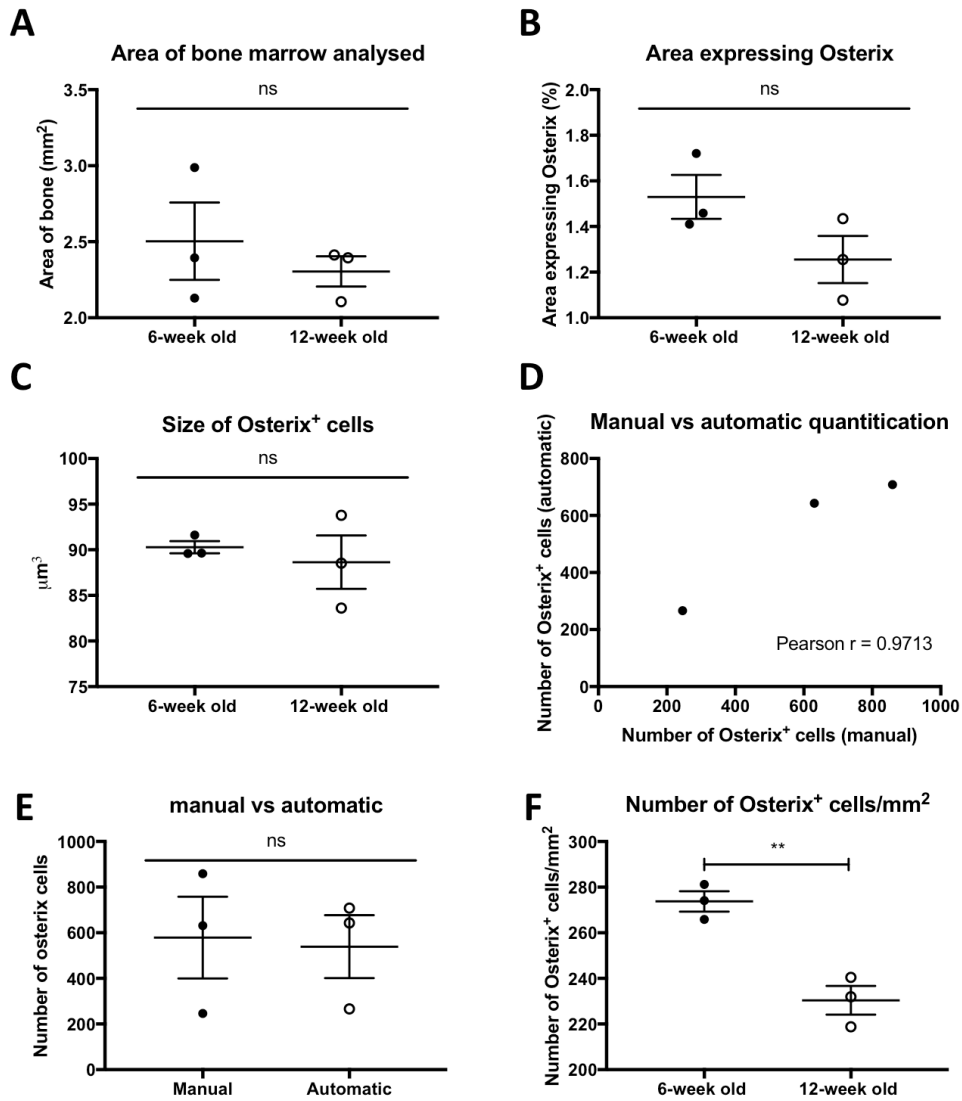


Figure 4.8 Quantification of immunofluorescent staining against Osterix

A) Area of bone marrow analysed. (B) Percentage area of bone marrow expressing Osterix. (C) average size of cells stained with Osterix. (D) and (E) are comparisons between Osterix⁺ cells counted manually vs automatically analysed with Pearson comparisons and paired t-test respectively. (F) Number of Osterix⁺ cells detected/mm² using the automatic function of ImageJ. Graphs show mean \pm SEM (n=5 animals, 3 bones analysed/group), **p<0.01.

4.5.3.2 Endomucin expression is higher in mature mice than in young mice

Endomucin is a marker expressed both in the metaphysis and in the diaphysis of long bones, therefore this marker was used to visualise the intricate microvasculature network within the bone marrow. Gelatine embedded frozen sections of tibia were stained using the immunofluorescent protocol against the endothelial marker Endomucin described in section 2.14.3. Three non-consecutive sections were stained for each bone (n=9 and n=10 for 6- and 12-week old animals respectively) and images were taken with an inverted widefield fluorescence microscope Leica AF6000. As shown in figure 4.9B, a surface area of bone marrow of approximately 2.5mm² was analysed for both ages (2.67±0.13 and 2.34±0.14 for 6- and 12-week old animals respectively; $p=0.1163$). The overall expression of the Endomucin marker was significantly higher ($p=0.0123$) in the mature group (16.16±0.70) compared to the young mice (12.99±0.90) (figure 4.9C).

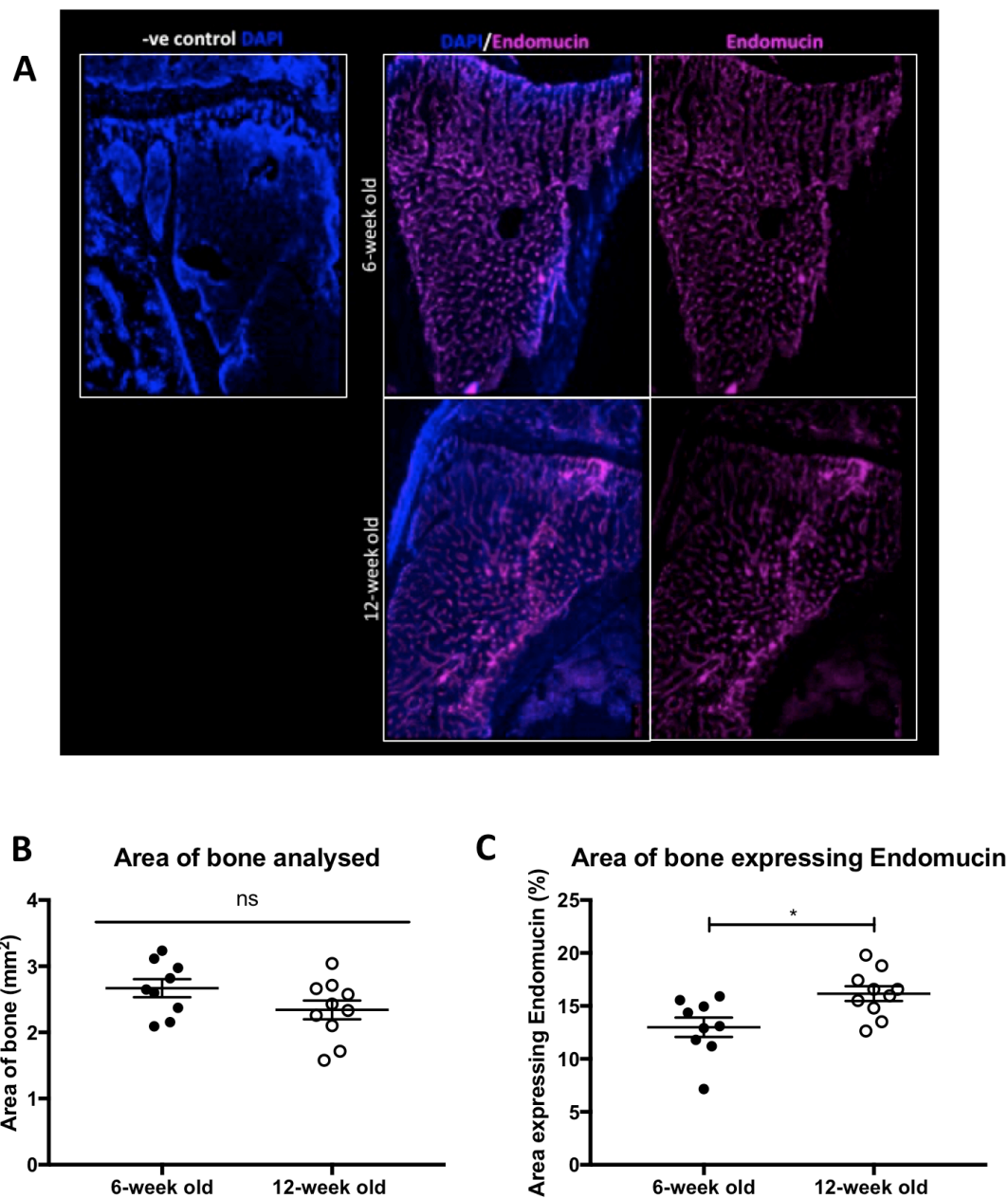


Figure 4.9 Immunofluorescent staining against Endomucin

A) Immunofluorescent staining of vessels was performed on gelatin embedded tibiae (30 μm) of 6- and 12-week old female BALB/c nude mice (Endomucin 1:100, goat anti-rat Alexa flour 555 1:200, DAPI to counterstain nuclei). (B) Area of bone marrow analysed for both ages. (C) Percentage of area of bone marrow analysed expressing Endomucin. Graphs show mean \pm SEM (n=5 animals/group, 9 bones analysed 6-week old and 10 bones analysed 12 week-old), Student t-test, * $p < 0.05$ and ns is not significant. Scale bar 250 μm .

4.5.3.2.1 Area occupied by different vessels sub-types

As elegantly explained by Kusumbe *et al.* [97], the bone vascular bed contains of a newly identified vessel subtypes that couple angiogenesis and osteogenesis. This consists of straight column like vessels interconnected by loops (H-vessels) in the metaphysis of bones, while in the diaphysis the microvasculature has a more sinusoidal conformation creating a more extensive network (L-vessels). Using Aperio ImageScope software, vessels were manually tracked using the specific structure of H- and L-vessels to discriminate between the two different sub-types. The first parameter measured was the area of bone marrow occupied by H- and L-vessels. There was no difference in the area occupied by L-vessels between the two ages ($p=0.7320$), however for the H-vessels the difference was not significant ($p=0.0603$)(figure 4.10B and C). When considering the surface occupied by the two vessel sub-types within the age groups, a significant difference was detected only in the young animal group ($p=0.0328$, $p=0.3073$ for the mature mice) (figure 4.10D and E). However, irrespective of age, these comparisons were significant when the area occupied by H- and L-vessels was normalised to the area of bone analysed ($p=0.0082$ 6-week old, $p=0.0359$ 12-week old). These data highlight that the H-vessels occupied most of the area analysed in both age. No changes were detected when H- and L-vessel area were compared in the two age groups (6-week old vs 12-week old; $p=0.4211$ vs $p=0.3209$)(figure 4.11).

These results suggest that the total area of bone analysed was the same in each age group, the surface occupied by H-vessels slightly decrease with age and that irrespective of age, the percentage of area occupied by H-vessels is greater than that occupied by L-vessels.

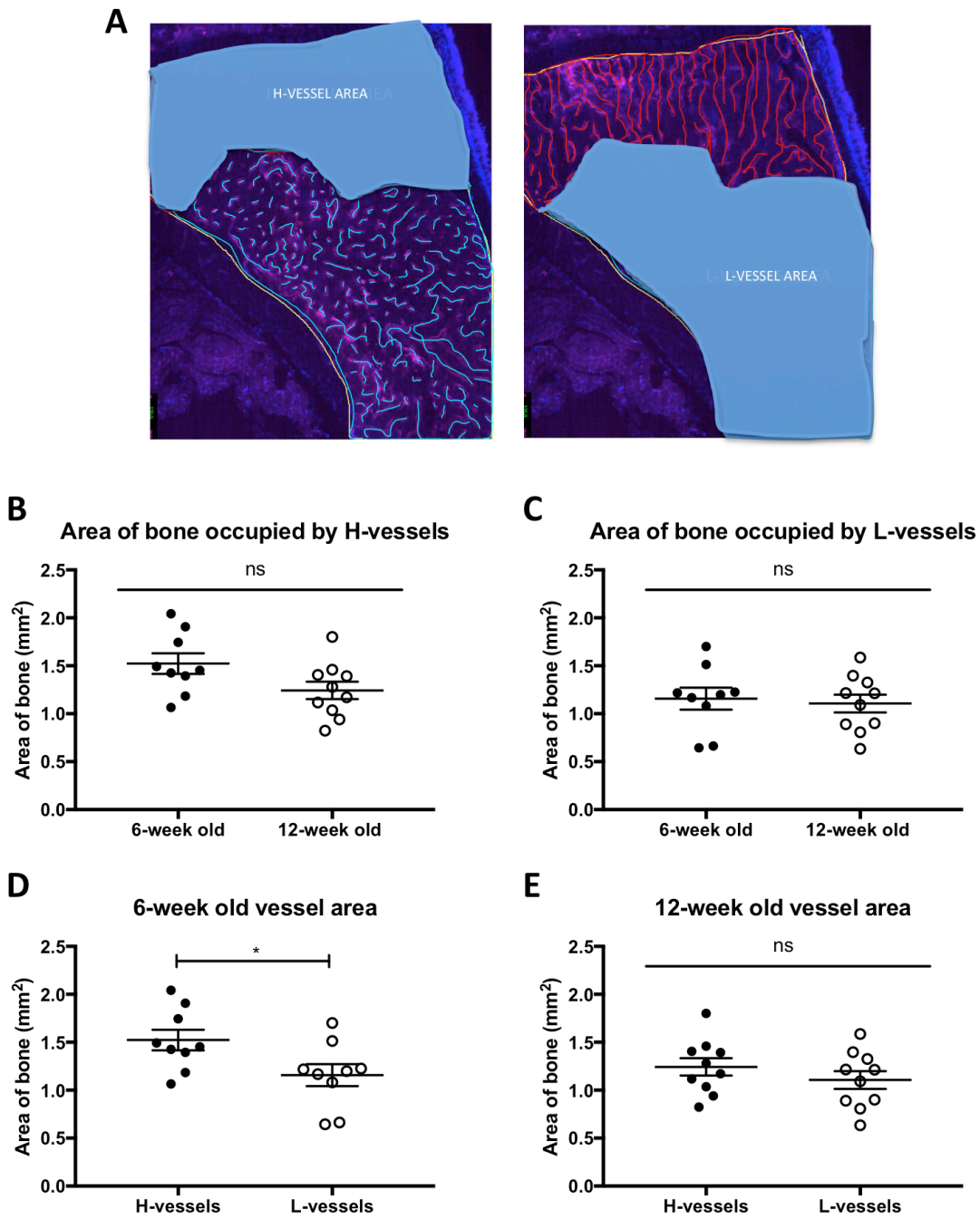


Figure 4.10 Quantification of area of bones occupied by H- and L-vessels

A) Schematic illustration of areas of bone marrow occupied by H- and L-vessels. (B) and (C) show the area of bones occupied by the two vessels sub-types in the different ages. (D) and (E) display how the vessels sub-types are distributed within the two ages analysed. Graphs show mean \pm SEM (n=5 animals/group, 9 bones analysed 6-week old and 10 bones analysed 12 week-old), Student t-test, * $p < 0.05$ and ns is non-significant.

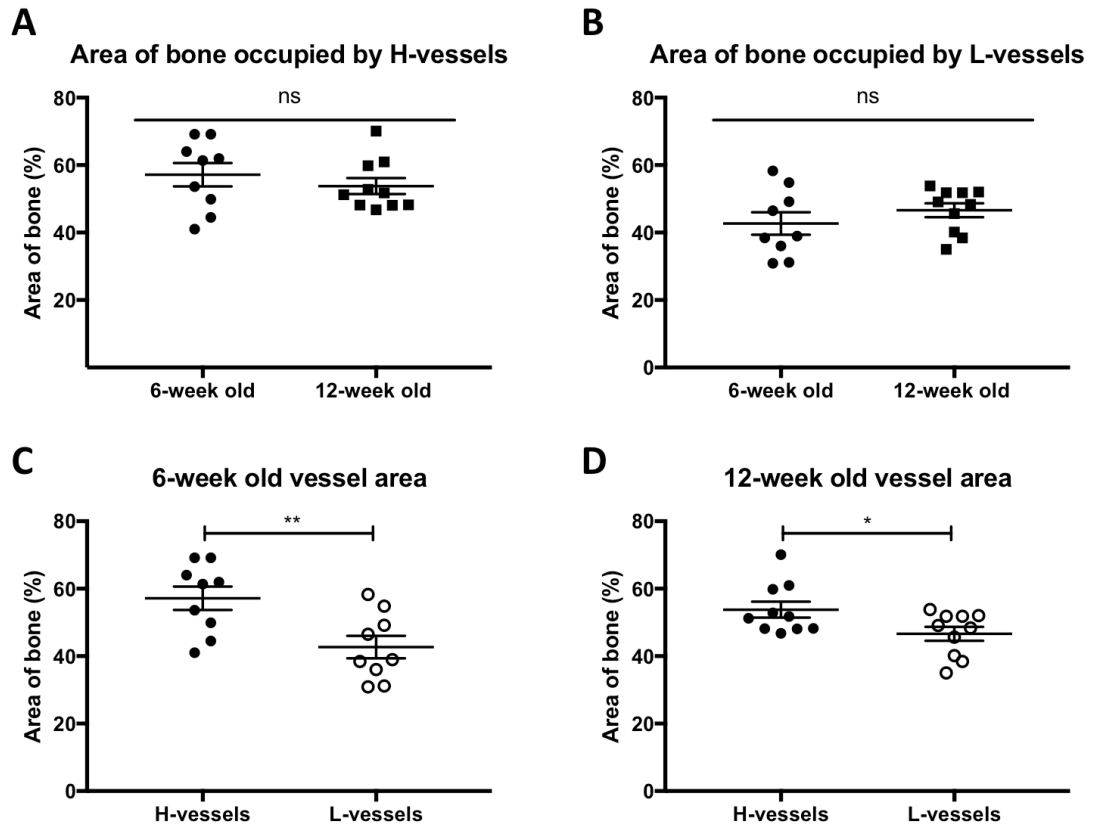


Figure 4.11 Percentage of bone marrow occupied by H- and L-vessels

A) and (B) show the percentage of area of the bone marrow occupied by H- and L- vessels, while (C) and (D) define the proportion of bone marrow occupied by the two vessels sub-types within the different ages. Graphs show mean \pm SEM (n=5 animals/group, 9 bones analysed 6-week old and 10 bones analysed 12 week-old), Student t-test, * $p < 0.05$, ** $p < 0.01$ and ns is not significant.

4.5.3.2.2 Reorganisation of the vascular bed with aging

Bone turnover decreases during aging and Kusumbe *et al.* stated that the expression of the vessel subtype that couples angiogenesis and osteogenesis is reduced in aged mice (11- and 70-week old compared to 4-week old) [97]. To verify how this particular component of the microvascular niche changes with age, the number and length of H- and L-vessels were measured and compared between the two age groups.

Unexpectedly, 12-week old animals had a significantly higher total number of vessels/mm² when compared with young animals ($p=0.0179$). The vessels were analysed separately as H- and L-vessels, there was no difference in the number of column like (H) vessels of the metaphysis between the two ages ($p=0.2893$). The L-vessels located in the diaphysis of the bone appeared to be more numerous in mature animals but this did not reach statistical significance ($p=0.0734$)(figure 4.12). Irrespective of age, H-vessels were significantly fewer than L-vessels p -value were 0.0340 and 0.0003 for the 6- and 12-week old animals respectively.

As explained in the previous section, there were some differences in the area occupied by the different vessels in mature and aged mice. To understand if the difference in the number of vessels/mm² was due to these changes, the number of vessels were normalised against the surface occupied by the vessel subtype analysed and not against the total bone area (figure 4.13). Regardless of age, the number of H-vessels/mm² was significantly lower than the number of L-vessels/mm² counted with Aperio ImageScope with a p -value <0.0001 for both young and mature mice. Surprisingly the number of both H- and L-vessels/mm² increased significantly with age, $p=0.0082$ and $p=0.0359$ respectively (figure 4.13). Vessel length differed between the two vessel sub-types, with a visible greater elongation of the vessels present on the metaphysis of the bone compared to the ones found in the diaphysis of both groups ($p<0.0001$). While the L-vessels maintained their length during the aging process ($p=0.5361$), the length of H-vessels was considerably reduced in 12-week old when compared with 6-week old animals ($p=0.0052$)(figure 4.14).

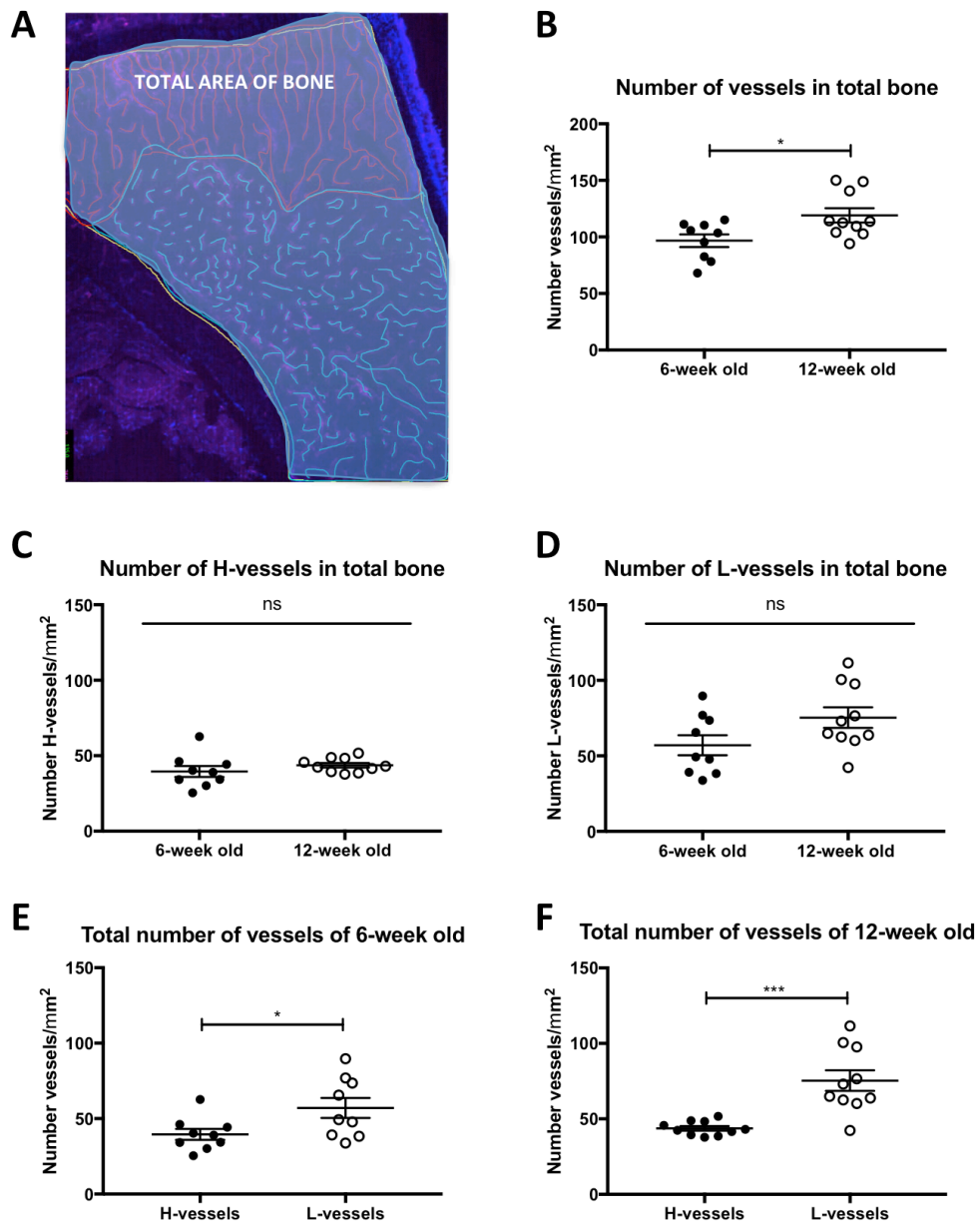


Figure 4.12 Number of H- and L-vessels quantified in the total area of bone marrow

A) Illustration of the area used in this analysis. (B) Total number of vessels counted in both ages. (C) and (D) show the number of H- and L-vessels/mm² of total area of bone in the different ages. (E) and (F) are the number of H- and L-vessels in young and mature animal. Graphs show mean \pm SEM (n=5 animals/group, 9 bones analysed 6-week old and 10 bones analysed 12 week-old), Student t-test, * $p < 0.05$, *** $p < 0.001$ and ns is not significant.

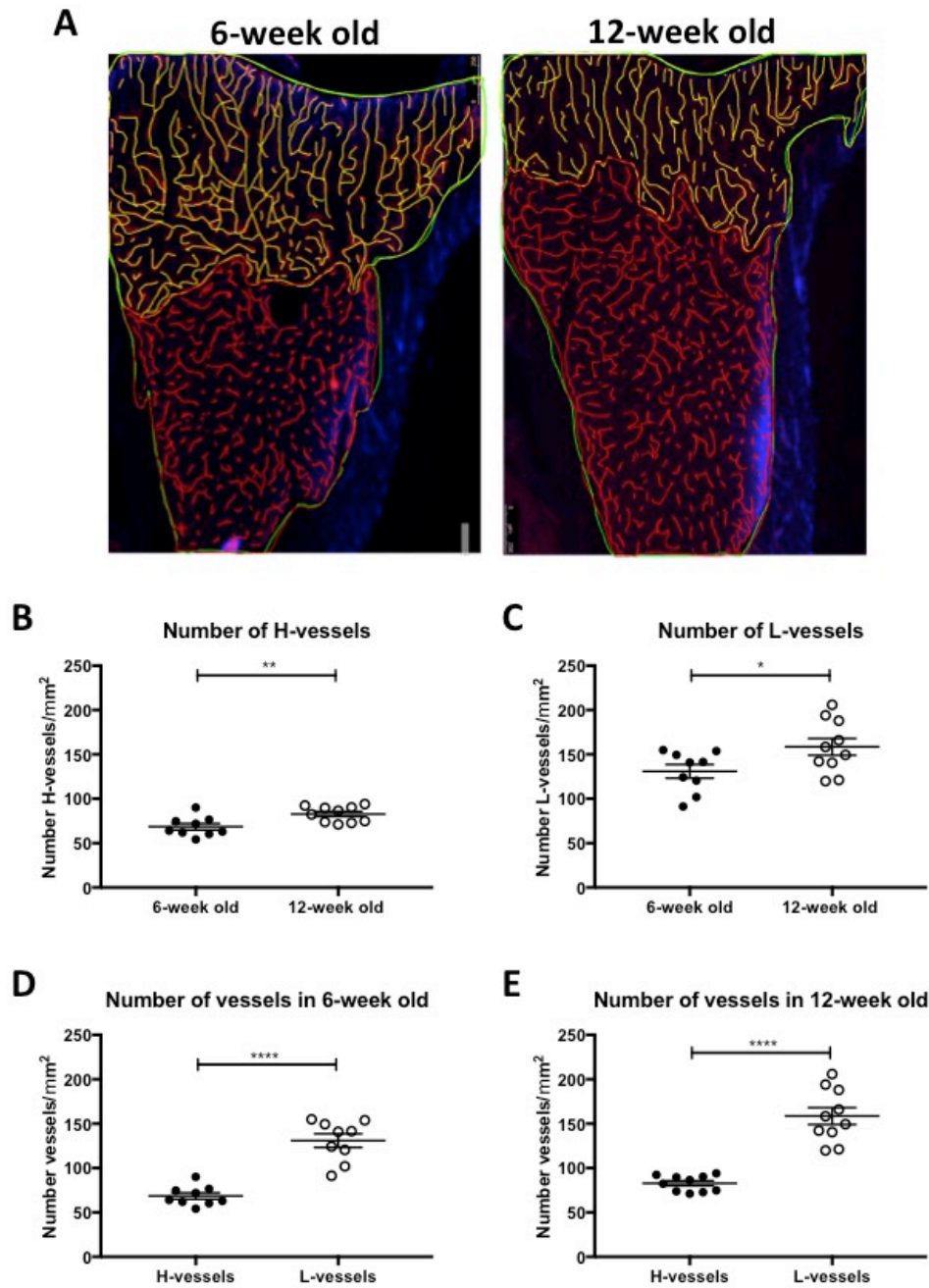


Figure 4.13 Quantification of the number of H- and L-vessels

A) Representative images of the H-vessels (yellow) and L-vessels (red) manually tracked with Aperio ImageScope software. (B) and (C) show the number of H- and L-vessels/mm² of area occupied by the vessel sub-type considered in the different ages. (E) and (F) are the number of H- and L-vessels in young and mature animal. Scale bar 250µm. Graphs show mean ± SEM (n=5 animals/group, 9 bones analysed 6-week old and 10 bones analysed 12 week-old), Student t-test, **p*<0.05, ** *p*<0.01 and **** *p*<0.0001.

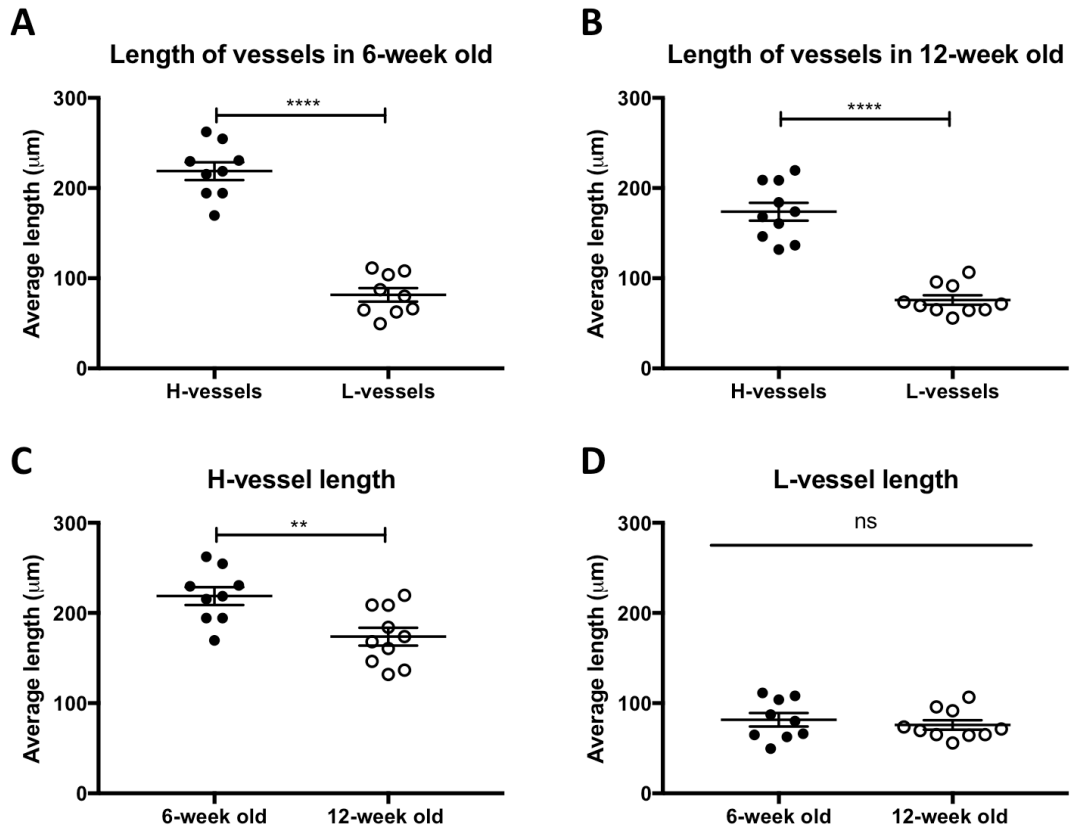


Figure 4.14 Average length of the two vessels sub-types

A) and (B) average length of H- and L- vessels of 6- and 12-week old animals respectively. (C) and (D) comparisons of H- and L-vessels average length between the two ages analysed. Graphs show mean \pm SEM (n=5 animals/group, 9 bones analysed 6-week old and 10 bones analysed 12 week-old), Student t-test, ** $p < 0.01$ and **** $p < 0.0001$.

The data indicate that even though mature animals appear to have more vessels in their microenvironment, the vessels in the metaphysis shorten with age reflecting the reduced osteogenesis in aging animals.

4.5.3.3 Ageing results in decreased CD31 expression

In addition to the characteristic elongated column like shape, the H-vessels are characterised by expressing high levels of the platelet endothelial cell adhesion molecule (PECAM-1), known as cluster of differentiation 31 (CD31) [97].

To quantify the changes in expression of this marker with age, three non-consecutive sections of tibiae were stained both for Endomucin and CD31 using the protocol described in section 4.4.5.2 and the tissue slides were then imaged using a Zeiss LSM880 AiryScan Confocal microscope. As for the images acquired using the inverted widefield fluorescence microscope Leica AF6000, the image obtained using the confocal microscope demonstrated no difference in the size of the bone marrow area analysed between the two groups studied ($p=0.2754$). The trend of an increased Endomucin expression in the mature animals compared to the young ones was maintained, even though in this case it did not reach the significance level ($p=0.1839$) (figure 4.15A and B). The overall expression of CD31 and the percentage of vessels expressing both endothelial markers were significantly higher in the 6-week old compared to the 12-week old animals, $p=0.0278$ and $p=0.0081$ respectively (figure 4.15C and D).

The number of CD31⁺ vessels/mm² in the total bone marrow surface analysed was not different between the two age groups ($p=0.4530$). Unexpectedly, mature animals had significantly more CD31⁺ vessels/mm² than young animals when we considered only the area occupied by this sub-type of vessels ($p=0.0025$). Even though the number of CD31⁺ was increased in the 12-week old mice, these vessels were significantly shorter compared to the 6-week old group ($p=0.0137$), explaining why the overall expression of this marker was reduced with aging (figure 4.16).

CD31 quantification highlighted the overall decreased expression of CD31 and in particular CD31⁺Endomucin⁺ vessels. This vessel subtype was increased in aged mice, but the microvasculature positive for CD31 in mature mice did not exhibit the characteristic column-like shape, appearing much shorter than the vessels detected in young animals.

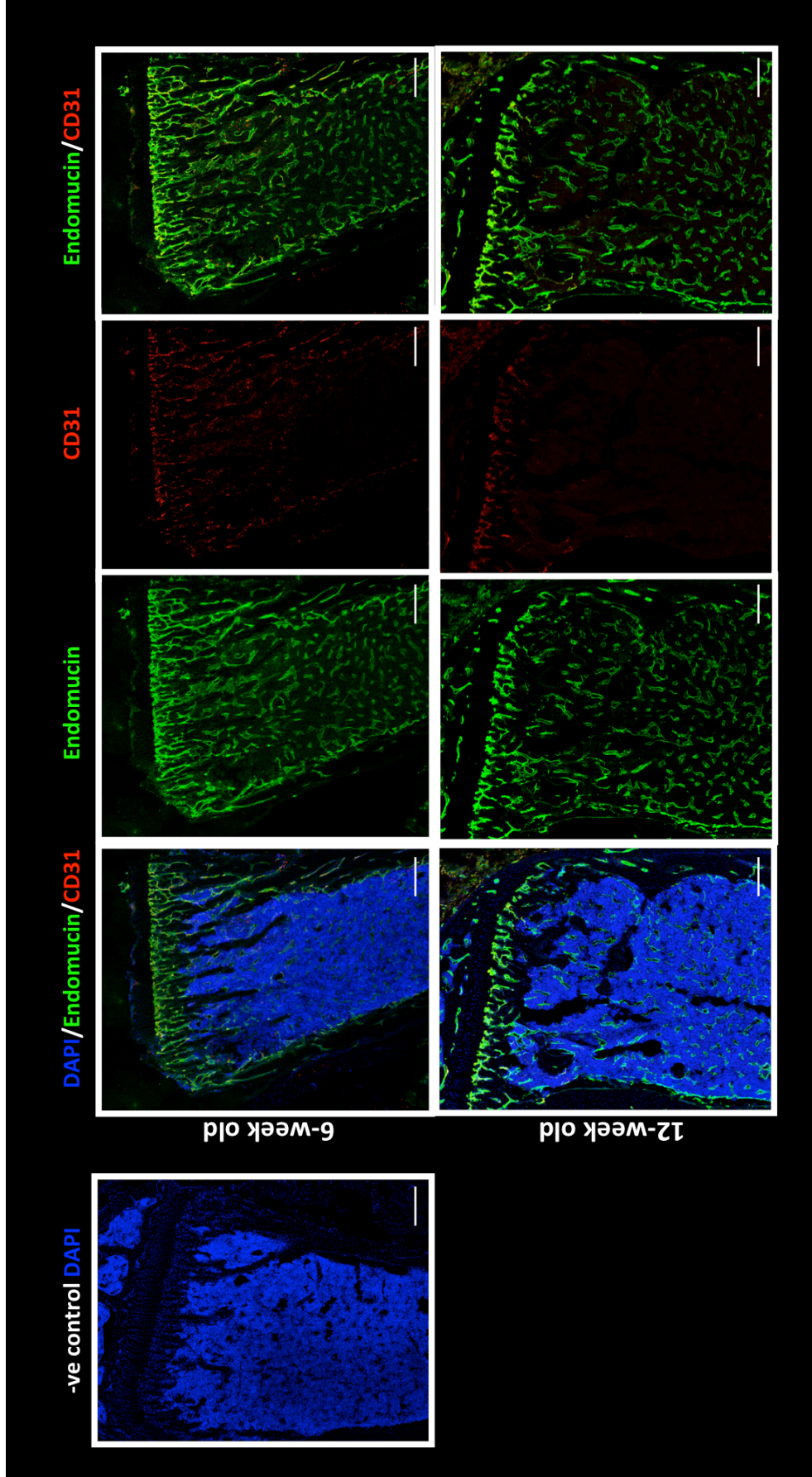


Figure 4.15 Representative images of immunofluorescent staining against CD31

Immunofluorescent staining against CD31 and Endomucin was performed on gelatin embedded tibiae (30 μm) of 6- and 12-week old female BALB/c nude mice. Nuclei were counterstained with DAPI, vessels with Endomucin (1:100) and goat anti-rat AlexaFluo 488 (1:200) and with CD31 (1:100) and Streptavidin AlexaFluo 647 (1:200). Blue=DAPI, green=Endomucin and red=CD31. Scale bar 200 μm .

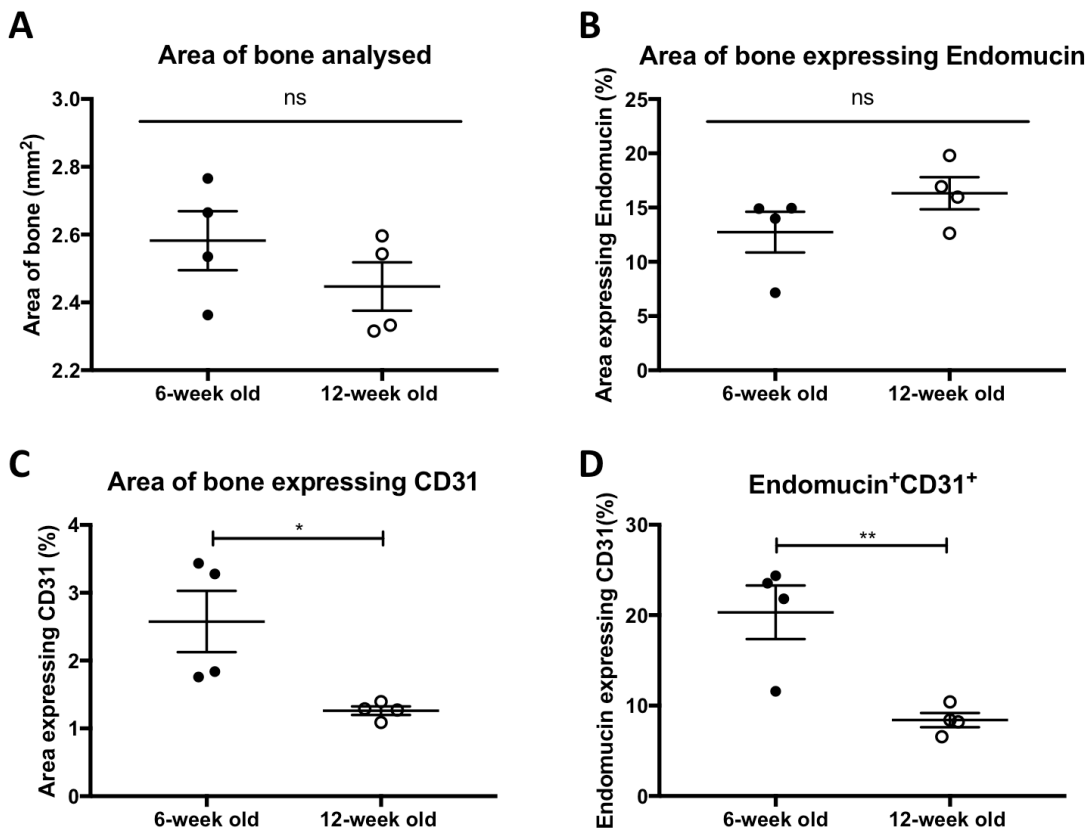
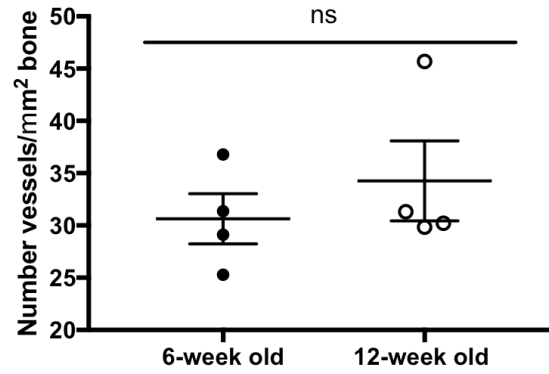


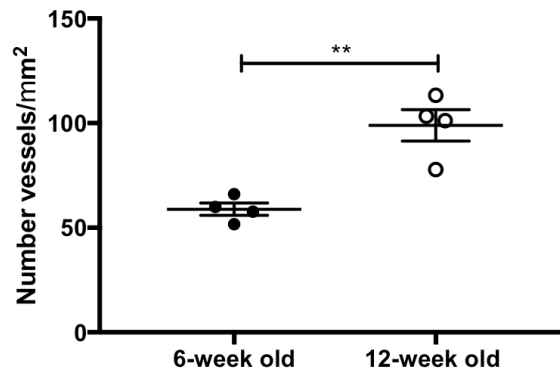
Figure 4.16 Quantification of immunofluorescent staining against CD31

A) Area of bone marrow analysed in the two different ages. B) and (C) show the overall expression of Endomucin and CD31 respectively while (D) displays the percentage of Endomucin⁺ vessels that are also expressing CD31. Graphs show mean \pm SEM (n=5 animals and 3 bones analysed/group), Student t-test, * $p < 0.05$, ** $p < 0.01$ and ns is not significant.

A Number of CD31⁺vessels in total bone



B Number of CD31⁺ vessels



C Average length of CD31⁺ vessels

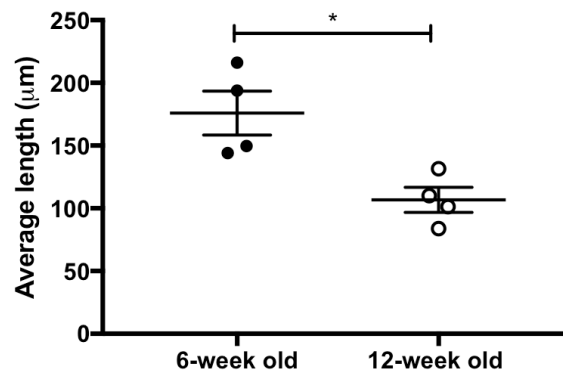


Figure 4.17 Quantification of CD31+ vessels

A) Shows the number of CD31⁺ vessels/mm² in the total area of bone while (B) shows this quantification normalised to the area of bone marrow occupied by this vessel sub-type. (C) is the average length of CD31⁺ vessels of young and mature animals. Graphs show mean \pm SEM (n=5 animals and 3 bones analysed/group), Student t-test, * $p < 0.05$ and ** $p < 0.01$.

4.5.3.4 Aged animals have less expression of CD34

To further characterise the perivascular niche, the immature vasculature was stained for the endothelial marker CD34 using the protocol described in section 4.4.5.2.

Quantification of the double staining of Endomucin and CD34 was performed in an area of approximately 2.5mm^2 for both age groups, 2.67 ± 0.19 and 2.53 ± 0.21 for 6-week and 12-week old respectively ($p=0.6294$). There was trend of increased Endomucin expression in the mature animals compared to the young animals, however this did not reach statistical significance ($p=0.1367$). The overall expression pattern of CD34 and percentage of Endomucin⁺ and CD34⁺ vessels were comparable to CD31 expression, with a significantly higher level in 6-week old mice, $p=0.0470$ and $p=0.0125$ respectively (figure 4.19).

Between the two groups analysed there was no difference in the number of CD34⁺ vessels/ mm^2 counted in the total area of bone marrow analysed ($p=0.2722$). However in the area containing CD34⁺ vessels, the mature animals had a significantly higher number of CD34⁺ vessels/ mm^2 ($p=0.0007$) and similar to the CD31⁺ vessels, these were considerably shorter than in the young animals ($p=0.0003$) (figure 4.20).

Aged mice demonstrated loss of CD34⁺ expression and this is due to the reorganisation of the vasculature, with a higher number of short vessels compared to young animals. This change in the shape of the CD34⁺ vessels could contribute to the dormancy promoting microenvironment of the mature animals.

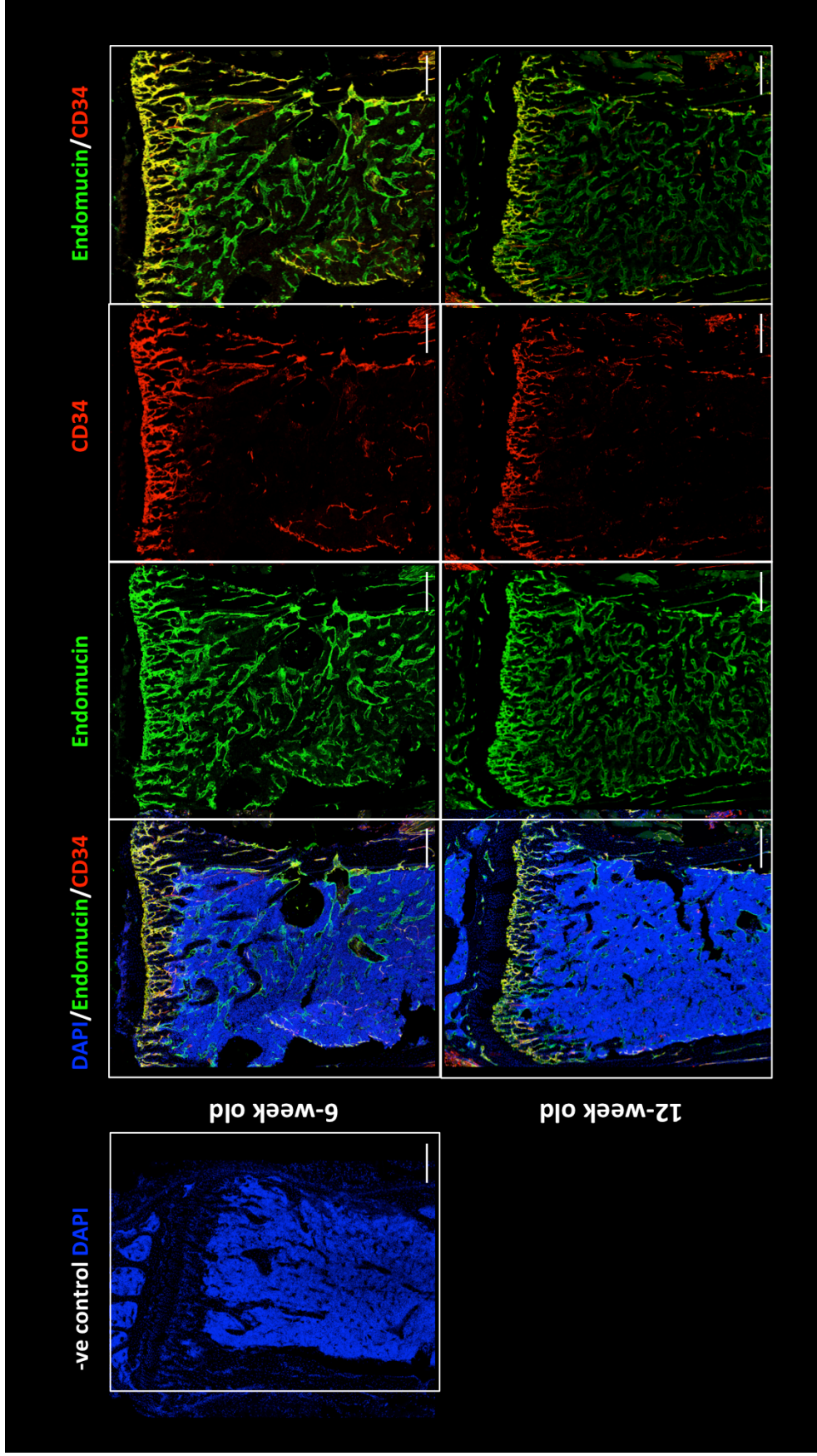


Figure 4.18 Representative images of immunofluorescent staining against CD34

Immunofluorescent staining against CD31 and Endomucin was performed on gelatin embedded tibiae (30 μm) of 6- and 12-week old female BALB/c nude mice. Nuclei were counterstained with DAPI, vessels with Endomucin (1:100) and goat anti-rat AlexaFluo 488 (1:200) and with CD34 (1:100) and Streptavidin AlexaFluo 647 (1:200). Blue=DAPI, green=Endomucin and red=CD34. Scale bar 200 μm .

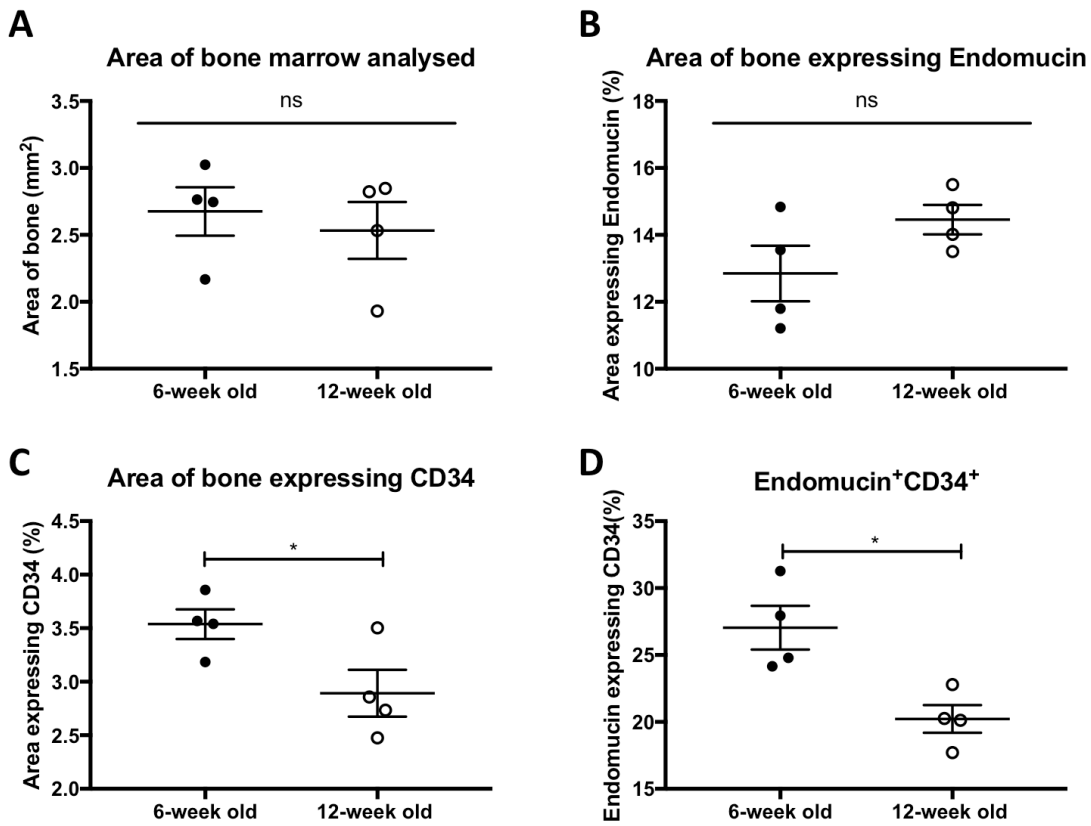
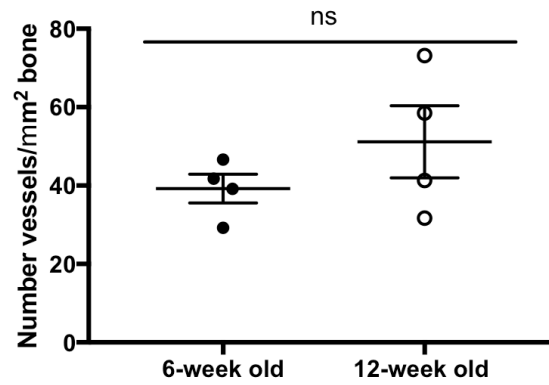


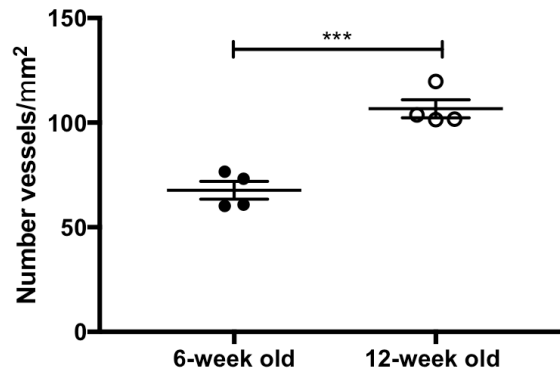
Figure 4.19 Quantification of immunofluorescent staining against CD34

A) Area of bone marrow analysed in the two different ages. B) and (C) show the overall expression of Endomucin and CD34 respectively while (D) displays the percentage of Endomucin⁺ vessels that are also expressing CD34. Graphs show mean \pm SEM (n=5 animals and 3 bones analysed/group), Student t-test, * $p < 0.05$ and ns is not significant.

A Number of CD34⁺ vessels in total bone



B Number of CD34⁺ vessels



C Average length of CD34⁺ vessels

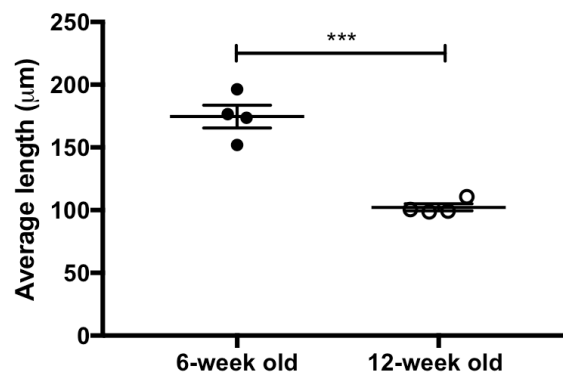


Figure 4.20 Quantification of CD34⁺ vessels

A) Represents the number of CD34⁺ vessels/mm² in the total area of bone while (B) shows this quantification normalised to the area of bone marrow occupied by this vessel sub-type. (C) is the average length of CD34⁺ vessels of young and mature animals. Graphs show mean \pm SEM (n=5 animals and 3 bones analysed/group), Student t-test, *** $p < 0.001$.

4.5.3.5 Arterial component of the bone microenvironment does not change with age

It has been reported that alpha-smooth muscle actin (α -SMA) covered arteries enter the bone through the cortical bone. The bone diaphysis contains a few large unbranched whereas surrounding the growth plate region these structure are more branched [97].

To detect the arterial component of the bone microenvironment, the immunofluorescent protocol described in section 2.14.3 was performed using an antibody against α -SMA.

The area of bone marrow imaged with the Zeiss AiryScan confocal microscope was $2.19 \pm 0.19 \text{mm}^2$ and $1.90 \pm 0.10 \text{mm}^2$ in young and mature animals, respectively ($p=0.3072$). Regardless of age, only few α -SMA⁺ vessels/ mm^2 were detected in the bone marrow (1.27 ± 0.41 and 1.38 ± 0.63 , young and mature animals respectively, $p=0.8934$) and therefore the overall expression of this marker was very low 0.07 ± 0.02 in 6-week old and 0.04 ± 0.00 in 12-week old mice ($p=0.2781$) (figure 4.22).

As shown in figure 4.21, the majority of α -SMA⁺ vessels were detected outside the bone marrow in the muscle surrounding the bone. For this reason the analysis were repeated to include the entire region imaged with the confocal microscope ($3.88 \pm 0.11 \text{mm}^2$ and $3.93 \pm 0.38 \text{mm}^2$, young and mature animals respectively, $p=0.8925$). Even including the tissue adjacent the bone, the level of α -SMA expression remained barely detectable, 0.16 ± 0.05 in 6-week old and 0.18 ± 0.06 in 12-week old mice ($p=0.7757$). As expected, the number of α -SMA⁺ vessels/ mm^2 slightly increased for both ages analysed, 2.49 ± 0.75 in young and 3.34 ± 1.34 in mature animals ($p=0.6112$) (figure 4.22).

Taken together, this data underline that, irrespective of age, the bone microvasculature does not contain many small arteries.

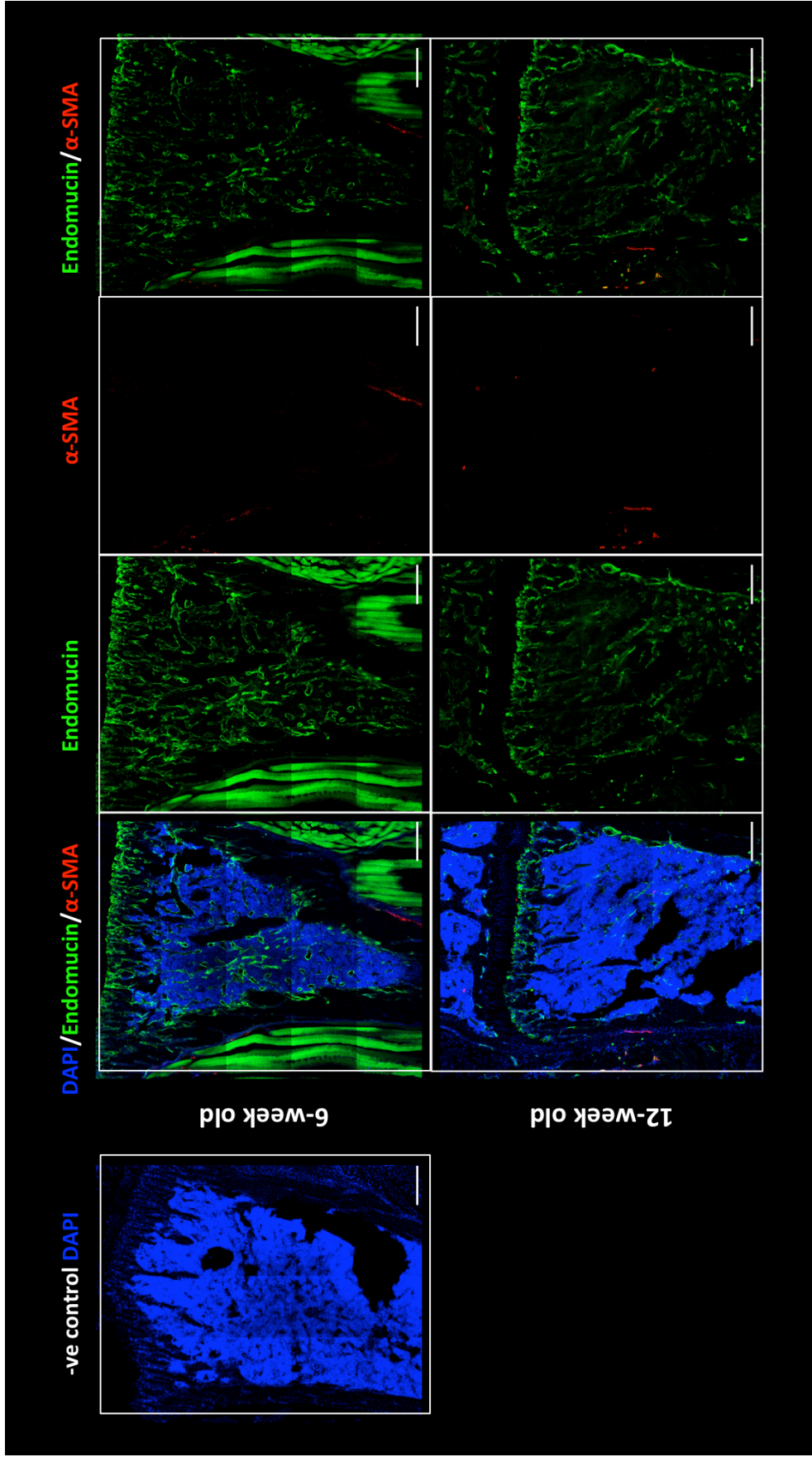


Figure 4.21 Representative images of immunofluorescent staining against α -SMA

Immunofluorescent staining against α -SMA and Endomucin was performed on gelatin embedded tibiae (30 μ m) of 6- and 12-week old female BALB/c nude mice. Nuclei were counterstained with DAPI, vessels with Endomucin (1:100) and goat anti-rat AlexaFluo 488 (1:200) and with α -SMA (1:100) and Streptavidin AlexaFluo 647 (1:200). Blue=DAPI, green=Endomucin and red= α -SMA. Scale bar 200 μ m.

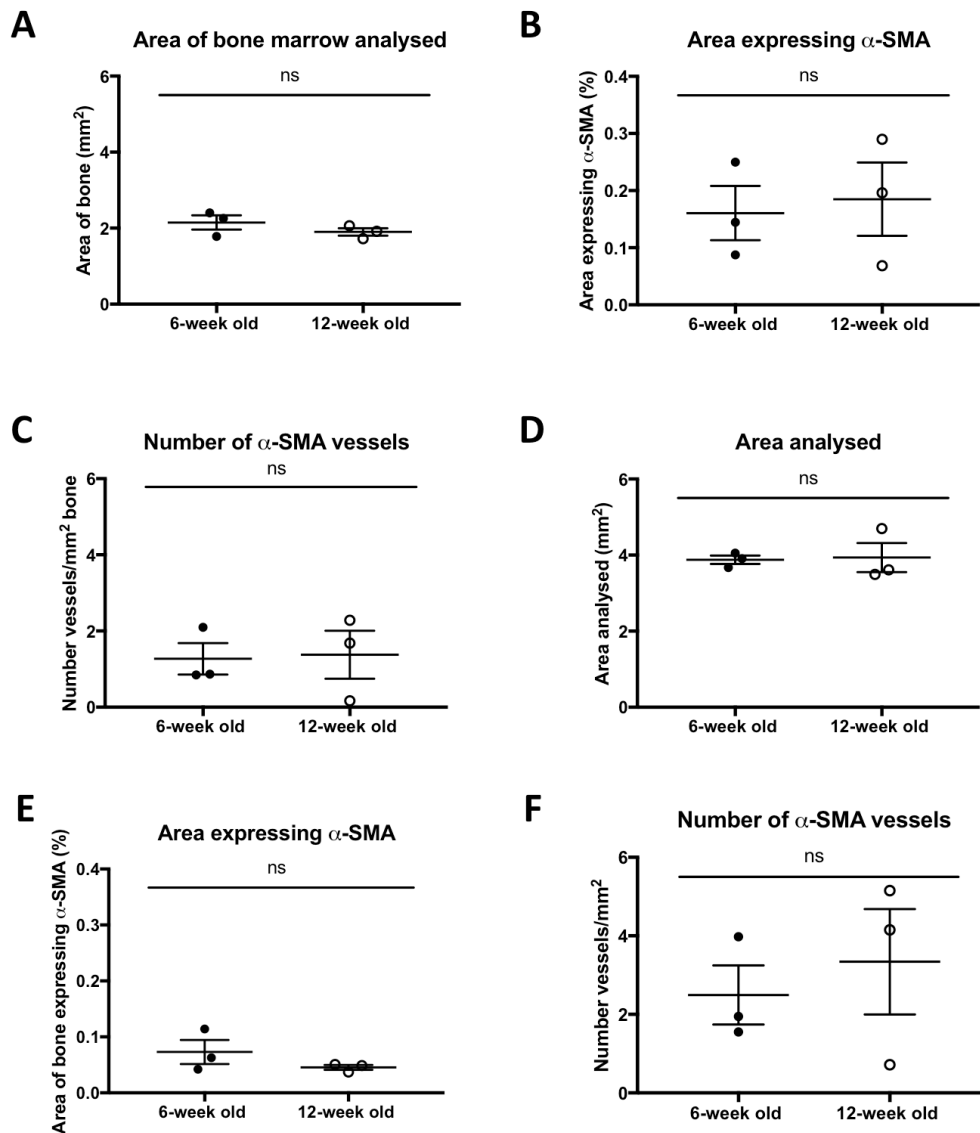


Figure 4.22 Quantification of immunofluorescent staining against α -SMA

Graphs shows the area of bone marrow analysed (A), the percentage of this area expressing α -SMA (B) and the number of α -SMA⁺ vessels/mm² of area analysed (C). The same analyses were repeated including the total area imaged (D), (E) and (F). Graphs show mean \pm SEM (n=5 animals and 3 bones analysed/group), ns is not significant

4.5.3.6 Dormancy-supporting Thrombospondin-1 levels are increased in the microenvironment of mature animals

In studies using an ex vivo model system, Thrombospondin-1 (TSP-1) has been suggested to be involved in regulating tumour cell dormancy [8], [35], [107], [109]. To verify whether there was a difference in expression of this marker between the tumour growth promoting (young) and the dormancy supporting (mature) bone microenvironment, 30 μ m thick sections of tibiae were stained with antibodies specific for Endomucin and TSP-1.

Zeiss LSM880 AiryScan Confocal microscope was used to acquire the image of the bone marrow, $2.83\pm 0.17\text{mm}^2$ for young and $2.93\pm 0.12\text{mm}^2$ for mature animals ($p=0.6450$). As shown in figure 4.23, Thrombospondin-1 is expressed in the proximity of Endomucin⁺ vessels and its levels are significantly higher in 12-week old animals compared to the 6-week old mice ($p=0.0061$). Moreover, mature animals also have a higher number of TSP-1 expressing Megakaryocytes/ mm^2 compared to young animals ($p=0.0429$ (figure 4.24)).

It is interesting to note that TSP-1 expression appears to follow the trabecular and cortical bone structure while the TSP-1⁺ megakaryocytes are distributed evenly in the bone marrow. Taken together, these results show that mature animals present higher levels of the dormancy-supporting molecule TSP-1, compared to that of the tumour growth promoting microenvironment of young animals.

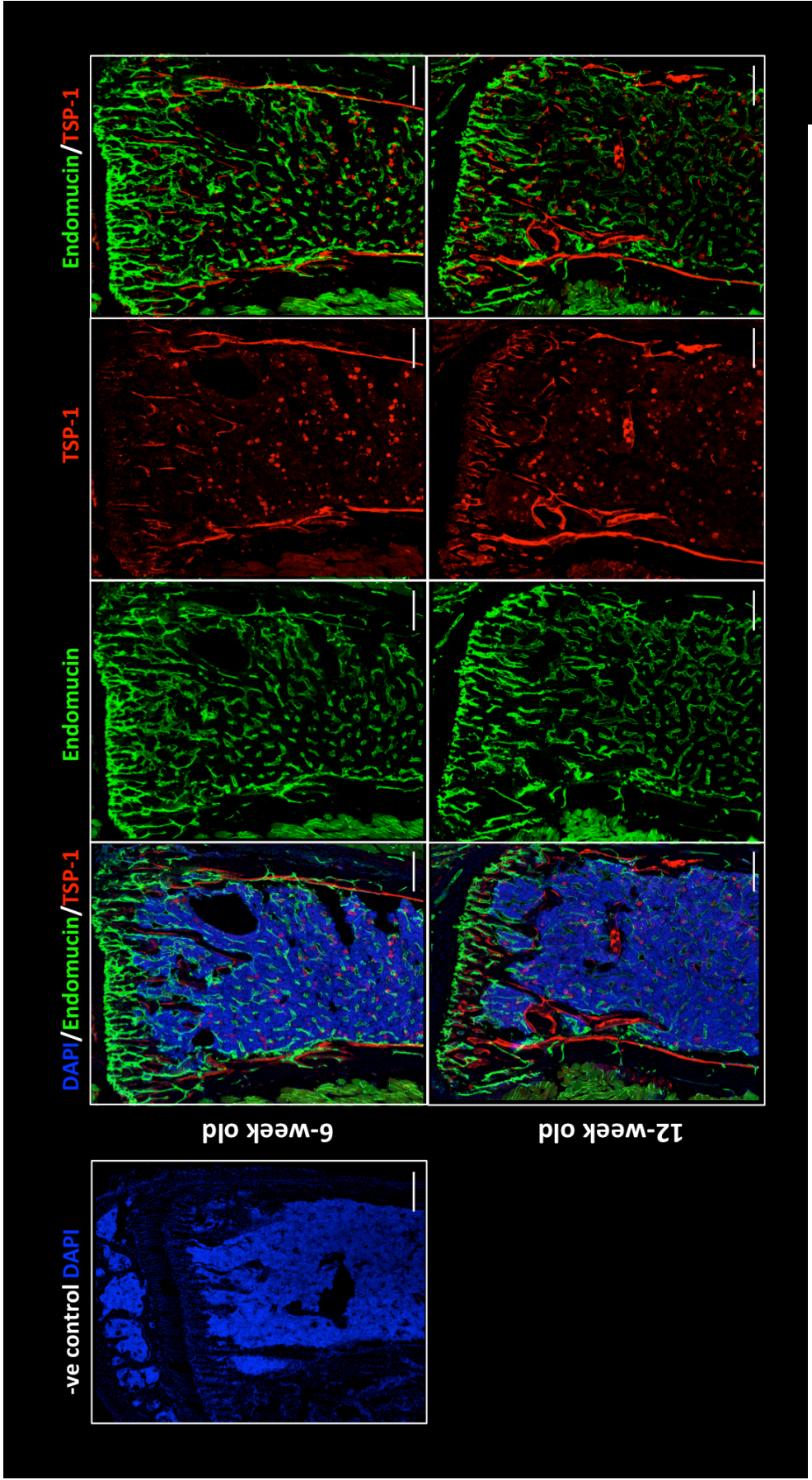


Figure 4.23 Representative images of immunofluorescent staining against Thrombospondin-1 (TSP-1)

Immunofluorescent staining against TSP-1 and Endomucin was performed on gelatin embedded tibiae (30 μ m) of 6- and 12-week old female BALB/c nude mice. Nuclei were counterstained with DAPI, vessels with Endomucin (1:100) and goat anti-rat AlexaFluo 488 (1:200) and with TSP-1 (1:100) and Streptavidin AlexaFluo 647 (1:200). Blue=DAPI, green=Endomucin and red=TSP-1. Scale bar 200 μ m.

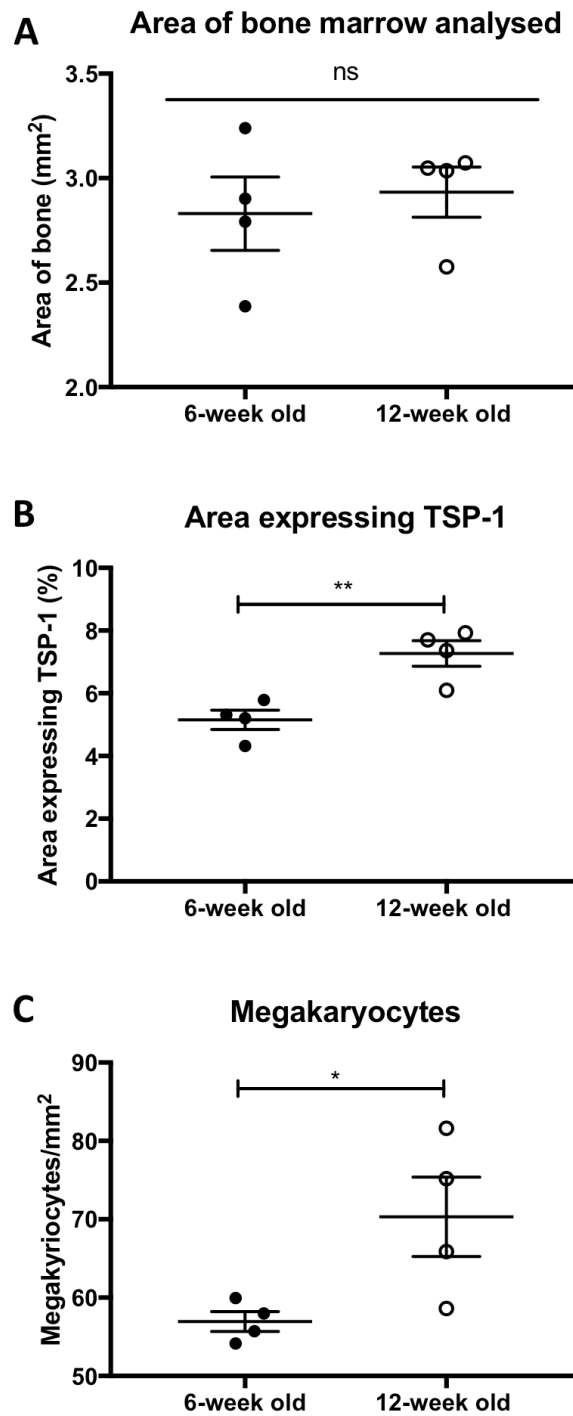


Figure 4.24 Quantification of immunofluorescent staining against Thrombospondin-1

A) Area of bone marrow analysed in the two different ages. B) shows the overall expression of TSP-1 in the two ages analysed. (C) Number of megakaryocytes/mm² stained with TSP-1 counted in bones of young and mature animals. Graphs show mean \pm SEM (n=5 animals and 3 bones analysed/group), Student t-test, * $p < 0.05$, ** $p < 0.01$ and ns is not significant.

4.5.4 DTC in bone marrow locate next to components of the perivascular niche

In addition to characterisation of the bone microenvironment of young and mature animal models, 30µm thick tibia sections were stained with antibodies against different components of the perivascular niche (Endumucin and CD31, CD34 or TSP-1) and the stained slides were then screened with an inverted widefield fluorescence microscope Leica AF6000 to detect single tumour cells within the bone microenvironment. Histological sections in which DTC were present were imaged using a Nikon A1 confocal microscope with the help of Dr Russell Hughes (University of Sheffield, UK).

Due to the low number of tumour cells detected it was not possible to perform any statistical analysis, however it was interesting to note that, irrespective of age, breast cancer cells disseminated in the bone microenvironment in close proximity to the bone microvasculature network (figure 4.25).

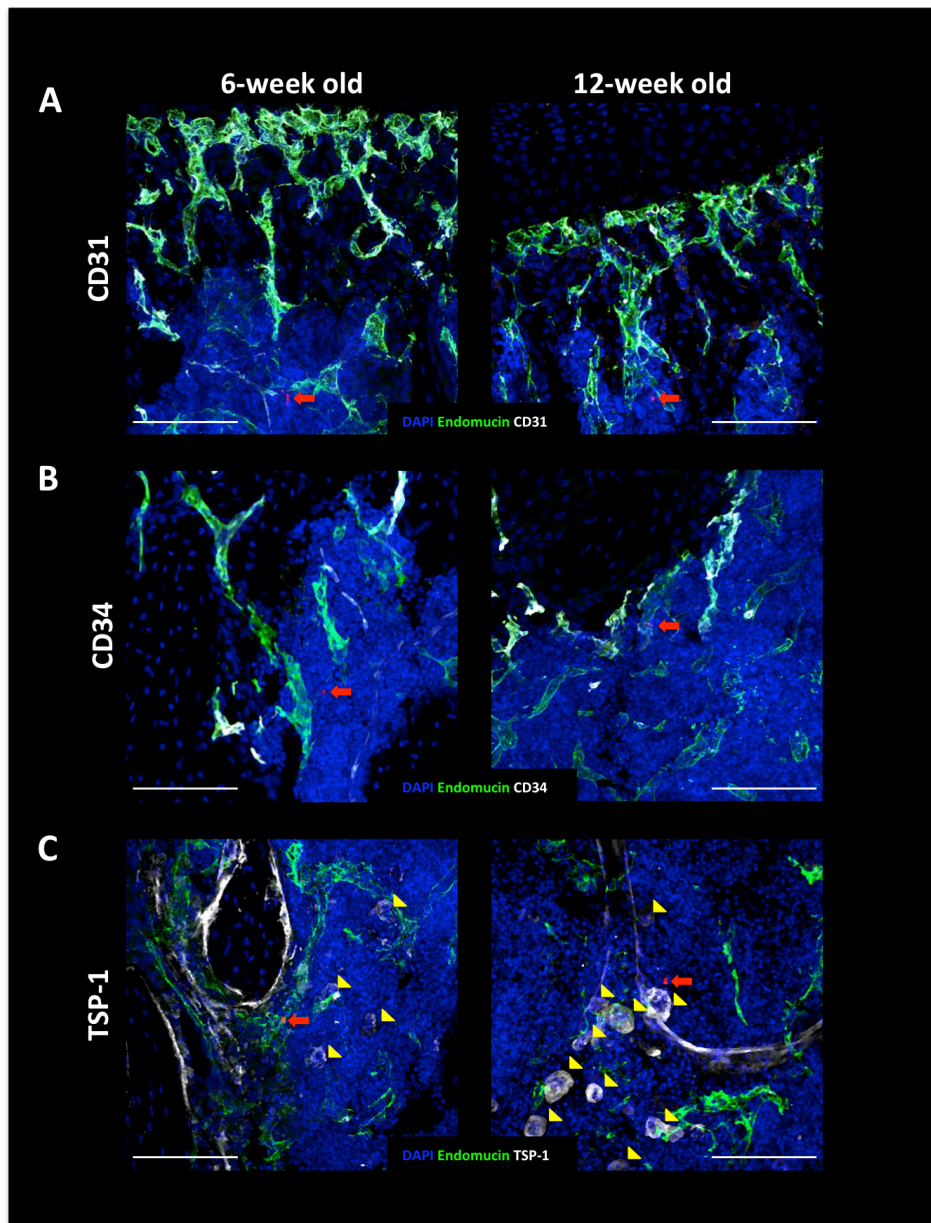


Figure 4.25 Representative images of the location DTC in bone microenvironment

DTC were found in the microenvironment in close proximity of to (A) Endomucin⁺CD31⁺ and (B) Endomucin⁺CD34⁺ vessels in the metaphysis area of the bone. (C) DTC were also found close to areas rich in TSP-1 and TSP-1 expressing megakaryocytes. Red arrow=DTC and yellow arrow=megakaryocytes. Scale bar 100μm.

4.5.5 Reorganisation of the microvasculature and TSP-1 expression in presence of tumours

To investigate the structure of the microvasculature network in the presence of tumour in the bone microenvironment, MDA-MB-231-NW-Luc2 cells were injected i.c. in 6-week old BALB/c nude mice and tumour growth was monitored with IVIS. Immunofluorescent staining of gelatine embedded long bones allowed qualitative assessment of the changes in the bone marrow vasculature in the presence of developing tumours.

The established microvasculature visualised with the antibody against CD31 was considerably reduced in bone with tumour present (figure 4.26), in contrast the newly formed vasculature positive for CD34 was highly expressed both within the tumour and in the surrounding bone microenvironment (figure 4.27). Endomucin⁺ vessels maintain their characteristic shape in the tumour-free microenvironment, while in the tumour this structured network is completely lost and replaced by what appears to be a non-organised arrangement.

TSP-1 is thought to support dormancy therefore it was interestingly to investigate its pattern of expression in the presence of developed tumour within the bone marrow. As show in figure 4.28, TSP-1 is expressed even in bones containing bone metastasis, but inside the tumour or in their close proximity its expression is substantially reduced.

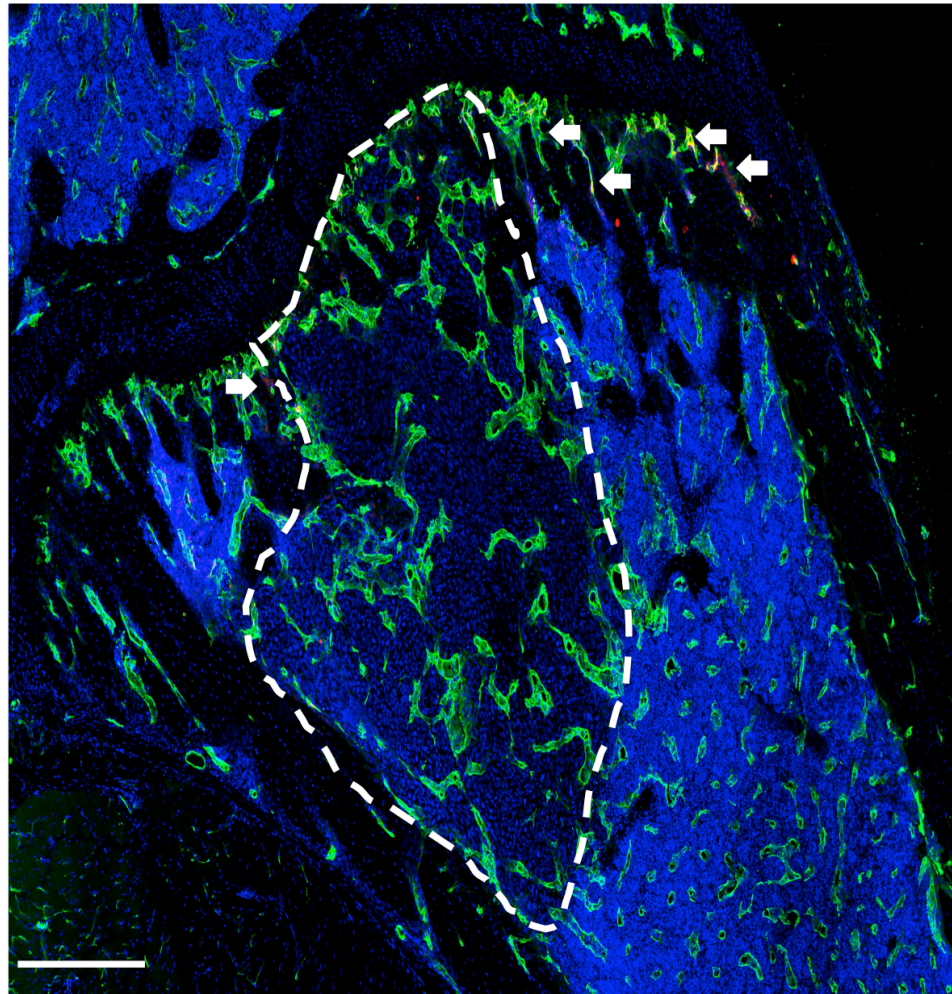


Figure 4.26 Endomucin+CD31+ microvessels in presence of bone metastasis

Representative image of a 30µm thick section of tibia stained with antibodies against Endomucin and CD31. CD31 signal is overall reduced and completely lost inside the tumour. Blue=DAPI, green=Endomucin, red=CD31, white arrow=CD31⁺ vessel and dotted white line=tumour. Scale bar 200µm.

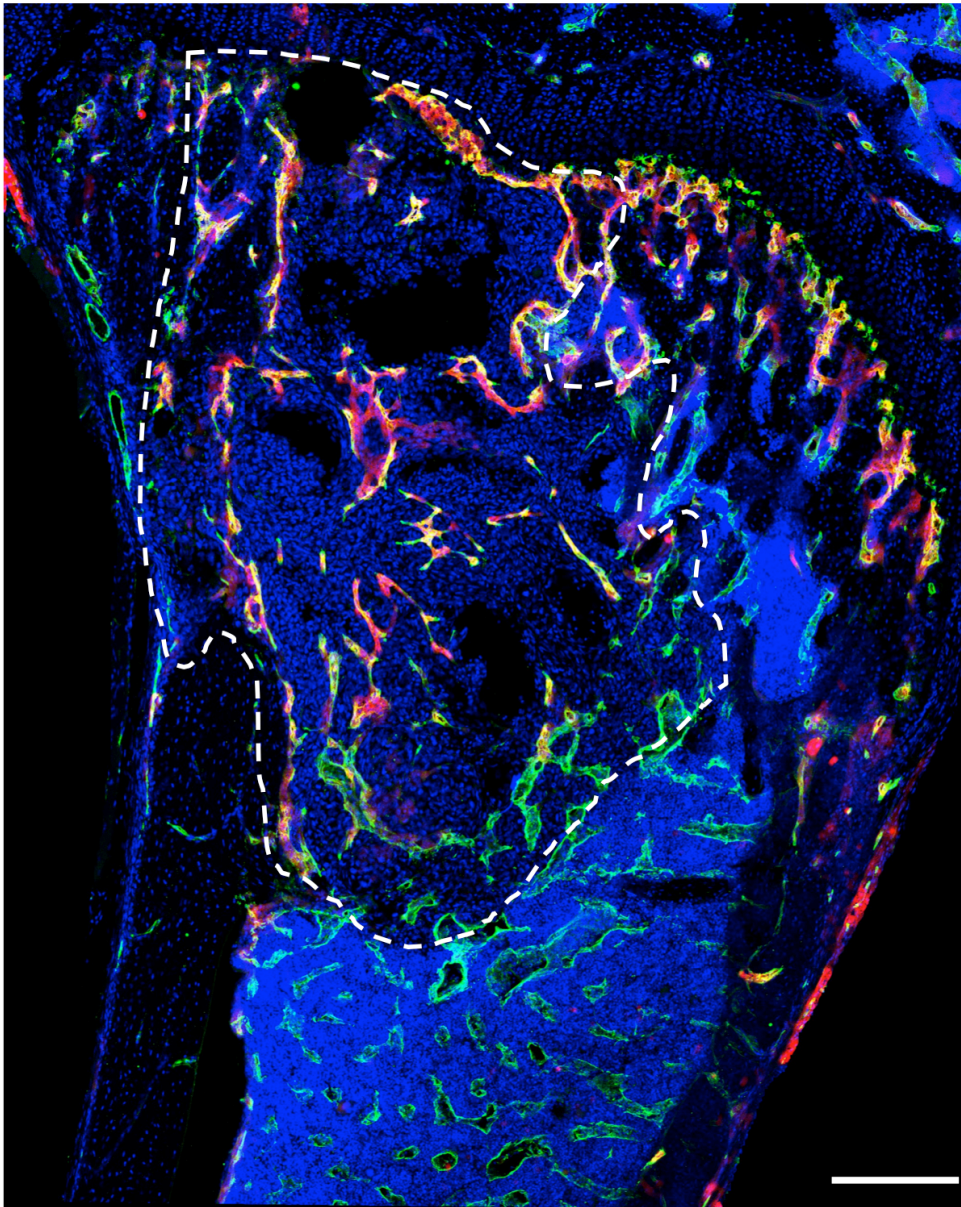


Figure 4.27 Endomucin+CD34+ microvessels in presence of bone metastasis

Representative image of 30µm thick section of tibia stained with antibodies against Endomucin and CD34. CD34 expression is abundant inside the tumour and also in the microenvironment surrounding it. Blue=DAPI, green=Endomucin, red=CD34 and dotted white line=tumour. Scale bar 200µm.

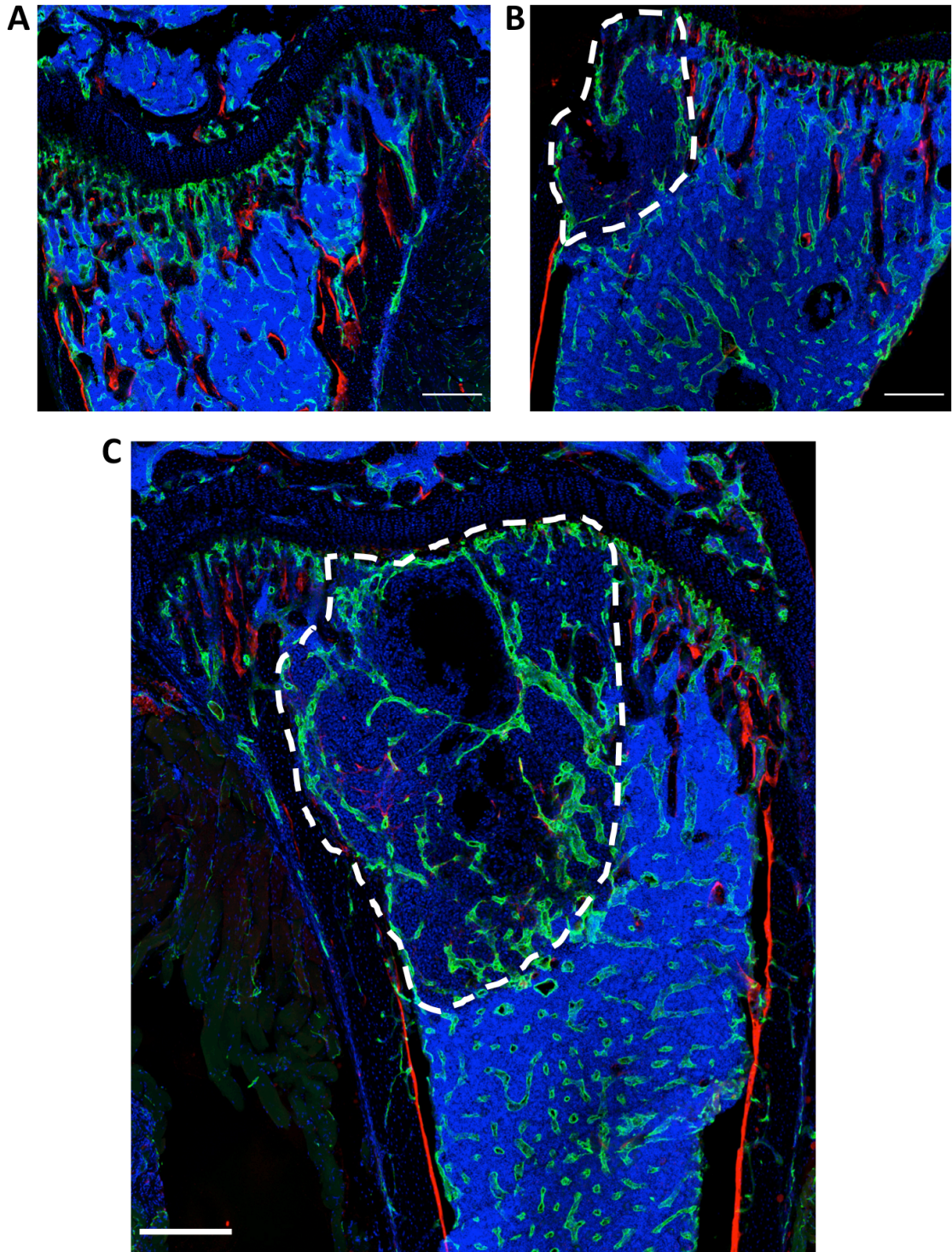


Figure 4.28 Expression of TSP-1 in bones with and without tumour

Representative images of 30µm thick section of tibia stained with antibodies against Endomucin and TSP-1. (A) Shows an age-matched bone without tumour in the microenvironment to show the overall expression of TSP-1 in the bone microenvironment. Bones with small tumour is shows in (B) and large tumour in (C). Blue=DAPI, green=Endomucin, red=TSP-1 and dotted white line=tumour. Scale bar 200µm.

4.6 Discussion

The main aim of this chapter was to characterize the bone microenvironment of young and mature animals with emphasis on the bone structure, cell components and different vessel sub-types that form the complex microvascular network. It is known that both the bone and the perivascular components of the metastatic niche play a role in the fate of the breast cancer cells that reach the bone microenvironment, so the focus of this chapter was to determine whether there were difference in the structures that form the metastatic niche of 6-week old animal where tumour growth is promoted and of 12-week old animals in which dormancy is supported. I used two-photon microscopy to map the location of single tumour cells in the bone microenvironment of young and mature mice, micro computed tomography to assess the differences in the bone structure of these animals and immunofluorescent protocols to determine age related changes in the detection of osteoprogenitors, alteration in the presence and pattern of Endomucin⁺, CD31⁺, CD34⁺ and α SMA⁺ vessels and modification in the expression of the dormancy supporting molecule Thrombospondin-1. Intriguingly, the only component that was not altered in the groups analysed was the arterial microvasculature (α SMA⁺ vessels) that was detected primarily outside of the bone marrow cavity. Mature animals have a lower bone turnover and this was reflected in the less dense structure of the trabecular bone and in the lower presence of osteoprogenitors when compared to young animals. Furthermore, the microvasculature was significantly altered with the aging process, resulting in changes in both the numbers and length of the all the sub-types of microvessels analysed. Not surprisingly, the overall expression of Thrombospondin-1 was increased in the 12-week old animals confirming its proposed role in maintaining tumour cell dormancy.

As previously described (chapter 3), breast cancer cells prefer to locate in the trabecular region of the bone in close proximity to the nearest bone surface. Between the two ages analysed no difference was detected in the overall number of tumour cells reaching the bone microenvironment, in their location and proximity to the nearest bone surface or distance to other tumour cells. These results suggest that the

growth of bone metastasis is influenced by the condition of the soil in which they seed. The quantification of the tumour cells in young vs mature animals are in line with the findings of Wang *et al.* who studied the importance of bone turnover in the development of osteolytic lesions in both prostate and breast cancer [101]. Even though my *in vivo* study was focused of the early stages of the bone metastasis while Wang and colleagues investigated the later events when bone disease had already occurred, both studies underline that there are no differences in the homing of breast cancer cells in the initial stages after tumour cell injection, 5 days in my *in vivo* and 1-7 days in the previously published study [101].

During the physiological process of bone resorption in a mature animal, osteoclasts resorb old bone and osteoblasts form an equal amount of bone, in contrast in young animals the constant remodelling of the bone matrix allows the growth of the bone itself [229]. This process releases growth factors stored in the bone matrix and in the presence of tumour cells these factors feed back to the malignant cells, creating a 'vicious cycle' between tumour cells and the microenvironment [9], [12]–[16], [113], [230]. Young animals have a higher bone turnover compared to mature animals in which the bone remodelling process slows down. In young mice the intense remodelling process constantly degrades and rebuilds the thin trabeculae of the spongy bone, resulting in the less dense mature trabecular structure found in aged mice. This situation is reflected in pre- and post-menopausal women, in which the bone turnover is altered by the reduced levels of reproductive hormones causing a differential response to the anti-resorptive drugs used for the treatment of the bone metastasis [148], [231].

The age-related reduction in bone turnover was reflected by alterations of the number of osteoprogenitors detected in bone. Moreover, in young animals the Osterix⁺ cells were found in the metaphysis of tibiae and lining the surface of the trabecular bone, as well as on compact bone towards the diaphysis. In contrast, in mature animals the few cells detected were located only in the metaphysis area. Irrespective of age, the osteoprogenitors were more abundant in the border with the growth plate area. It is known that osteogenesis and angiogenesis are closely coupled and the fact that the

osteoprogenitors reside mostly in area of the bone marrow which is highly vascularised reinforce this concept [88], [97], [221], [232].

It is proposed that a particular sub-type of vessel expressing high levels of Endomucin and CD31 (H-vessels) couple these processes [97]. This specific category of vessel is located in the metaphysis of long bones and has a characteristic straight column-like shape interconnected by loops that allows to discriminate it from the highly branched sinusoidal network present in the diaphysis of bones which express low level of Endomucin and CD31 (L-vessels) [97], [221]. Irrespective of age, the H-vessels occupied a greater portion of bone marrow compared to the area occupied by L-vessels even though the number of L-vessels/mm² in the total bone was higher than the H-vessels. Overall the mature animals had more vessels/mm² but the length of the vessel sub-type that couple angiogenesis with osteogenesis appeared to be considerably shorter than the H-vessels measured in the young animals, suggesting that not only the presence of this particular vessel but also its shape contributes to its specific function.

All these quantifications were performed using the characteristic shape of the two different vessel sub-types as discriminant between H- and L-vessels. Visual identification used to classify as H- or L-vessels was not always easy due to the angle of the sections, also the L-vessels appeared elongated in a few bone samples. To verify that the quantification made was accurately describing changes in the H-vessels in this chapter I also performed double staining of two endothelial markers highly expressed by this vessels sub-type, Endomucin and CD31. Kusumbe and colleagues described that H-vessels are lost when comparing the vasculature of young animals (4-week old) to the adult (11-week old) and aged (70-week old) mice [97], the overall expression of CD31 in the bone marrow was reduced in aged animals and also the presence of Endomucin⁺CD31⁺ vessels was lower in 12-week old compared with 6-week old mice. Intriguingly, the lower expression of CD31⁺ vessels was not due to their number (which was higher in mature vs young animals) but to their average length. Also the H-vessels (Endomucin⁺CD31⁺) appeared to increase their number/mm² but reduce in length with aging.

Vessels positive for the endothelial marker CD34 were another important component of the vessel sub-type analysed in this chapter. It has been shown that a high expression of CD34⁺ vessels in primary breast tumours could be used as a predictive marker of bone metastasis occurrence [233], [234]. Furthermore, high expression levels of CD34 in patient tumour samples has been suggested to predict the behaviour and prognosis of the giant cell tumour of bone [235]. The data described in this chapter concerning the presence of CD34⁺ positive vessels support the theory that an increase in the level of this endothelial marker results in a poorer prognosis. In fact, the tumour growth promoting microenvironment of 6-week old animals have a higher overall expression of CD34 compared to the dormancy supporting microenvironment of 12-week old animals. Similar to the CD31⁺ vessels, this increase in the level of CD34 expression was due to the length of the vessels stained with this marker and not their number, which was greater in the mature mice when compared to the young ones.

In this chapter I have also investigated the arterial component of the bone marrow, staining the bone microenvironment with an antibody against alpha-smooth muscle actin (α -SMA). Interestingly, this marker was the only marker analysed that did not change its expression between the different ages. Only a few α -SMA⁺ vessels were detected in the specimens and the majority of these were observed in the muscular tissue surrounding the bone marrow and not within the area normally colonised by tumour cells. Despite reports that α -SMA⁺ vessels are connected with Endomucin positive vessels in the metaphysis of long bones [97], [232], [236], this association was not observed in the bone specimens analysed, here probably because the sections used by our group are considerably thinner than those used by the Adams group (30 μ m vs 300 μ m).

A relative recent focus of investigation is the function of blood vessels in the maintenance of dormancy. Endothelial-derived Thrombospondin-1 (TSP-1) is one of the factors that has been shown to play a key role in supporting human cells quiescence [8], [35], [107], [237]. Ghajar *et al.* investigated extensively, the correlation between tumour cell dormancy and the expression of TSP-1. They firstly noticed that *in vivo*, dormant breast cancer cells locate in close proximity to microvasculature both in lungs and in bone marrow. Then human umbilical vein endothelial cells (HUVEC) were

cultured with lung fibroblast or bone marrow mesenchymal cells and different breast cancer cell lines were seeded on the microvascular network formed *in vitro*. Tumour cells appeared to have a reduced rate of growth when in close proximity to microvessels than when in contact to stromal cells. This suggested that the microvasculature may have an effect in inhibiting tumour growth. Moreover, breast cancer cells seemed to maintain dormancy when surrounded by an established microvasculature however if located next to neovascular sprouting tips, tumour growth occurred. Proteomic and mass spectrometry analyses indicated that the established microvasculature expressed high levels of TSP-1 while in sprouting vessels this molecule was replaced by a high expression of periostin and transforming growth factor beta-1.

The analyses described in this chapter confirm that TSP-1 is expressed to a greater level in a microenvironment supporting dormancy (mature animal model) compared to microenvironment in which tumour growth is promoted (young animal model). It was also interesting to observe that TSP-1 was not only localised in the proximity of Endomucin⁺ vessels but also expressed in Megakaryocytes. The number of Megakaryocytes/mm² of bone marrow was greater in 12-week old than in 6-week old animals and this has influenced the overall expression of the marker analysed, supporting the theory that these cells might have a function in the maintenance of tumour cells dormancy in the bone microenvironment even though the mechanism(s) implicated have not yet been elucidated [110].

The work described in this chapter has characterised some components of the metastatic niche in young and mature animals models. The majority of *in vivo* studies on tumour growth are performed in young animals and it is clear that this model is very different from the mature animals. Taking into consideration these differences it is important to plan and carry out research that could be better translated to the clinical setting in which the majority of the patients are elderly women with a lower bone turnover. Ideally this study should have been carried out in old animals (30+ week old) instead of using 12-week old animals but the necessary steps to process the samples for the immunofluorescent staining were difficult to achieve in bones with a highly fragile bone structure.

In summary, the data described in this chapter support the notion that components of the tumour microenvironment, bone turnover and microvasculature are closely associated. Furthermore, I have demonstrated that the ageing process changes not only the bone structure and osteoprogenitor number but also the perivascular components of the metastatic niche. The microenvironment of mature mice is known to support dormancy of tumour cells, and it was interesting to observe a large reduction of the microvasculature in the bones of these animals compared to the level of vascularisation detected in the tumour growth-promoting microenvironment of young mice. These findings contribute to an improved characterisation of the metastatic niche and in particular of the players involved in supporting dormancy. This could ultimately lead to new approaches in the treatment of the metastatic disease from the early stages of the tumour cell colonisation.

Chapter 5

Effect of ZOL on the bone microvasculature structure

5.1 Summary

Bone metastasis is one of the major causes of cancer death. Unfortunately, currently there is no cure for this secondary disease and the treatment are restricted to palliative care. Bisphosphonates, and in particular ZOL (ZOL), are often used in the treatment of cancer-induced bone disease. This drug is used for its anti-resorptive action slowing down the formation of bone lesions and eventually fractures and for the management of bone pain. In several studies, it has been shown that ZOL has an anti-cancer effect through the modification of the bone microenvironment, reducing the incidence of tumour relapse in animal models. The changes induced by ZOL are caused by alterations to the physiological presence and activity of the osteoblast and osteoclast populations, resident in the bone and not due to the alteration of the total number of malignant cells located in the secondary organ. *In vivo* studies have demonstrated variable efficiency of this anti-resorptive drug between animal models mimicking pre- and post-menopausal status [148]. These findings suggest that the success rate of the treatment is influenced by the different organisation of the bone marrow between the two statuses. As described in the previous chapter of this thesis, young and mature animals have a substantially different organisation of the bone components, including the composition and architecture of the different vessels sub-types.

The hypothesis to be tested in this chapter, is that ZOL treatment alters not only the bone structure and cell populations but also modifies the surrounding microvascular network. The data presented show that a single dose of this anti-resorptive drug causes major changes in the bone structure, extracellular matrix and osteoprogenitors with minimal changes to the vessel organisation in animals models with high and low bone turnover.

5.2 Introduction

In the latest stages of bone metastasis the tumour cells that establish in the bone and escape the dormancy state, start to proliferate and develop both micro- and macro-metastases in response to the signals generated by the bone microenvironment. Breast cancer cells are known to interact with osteoblasts and this cell population ultimately induces osteoclast bone resorption, resulting in bone lesions [14], [230], [238]. This cancer-induced bone disease is the cause of severe morbidity and mortality in cancer patients. Unfortunately, there is no way to predict which patient will develop bone metastasis and when the secondary disease will occur, hence the treatment of bone disease usually takes place when the metastasis is sufficiently big to cause a detectable lesion. The goal of bone-targeted treatments is to improve the quality of life of cancer patients and ultimately increase the disease-free and overall survival [5].

For the development of bone metastasis the interaction with the bone microenvironment is crucial, therefore to effectively inhibit the metastatic process it is necessary to not only target the tumour cells but also the microenvironment hosting and supporting their proliferation. The therapies presently available are designed to target only one component of the metastatic niche, either the osteoblast and osteoclast populations or the microvasculature.

Bisphosphonates, and particularly ZOL, are one of the most commonly used bone-targeted therapeutic agents [5]. Due to their structure, bisphosphonates have the ability to bind divalent metal ions, such as Ca^{2+} . This ability allows binding to the bone surface in particular in regions where bone remodelling is active, the agent is then released locally during bone resorption by osteoclasts. Uptake by the osteoclasts during bone remodelling, explains the high selectivity of the bisphosphonates for osteoclasts. However, with repeated administration these drugs can be internalised by other bone resident cells, such as osteoblasts or tumour cells [117].

It has been shown that this potent anti-resorptive drug targets the osteoblastic niche and this modification of the microenvironment results also in alteration of metastatic disease progression [30], [32], [126]–[128]. Further more, alteration of the bone microenvironment also results in a reduction in the incidence of tumour relapse in

animal models [129], [130]. Even though imbalance of the bone turnover caused by therapeutic administration of ZOL reduces the development of overt metastases, a successful anti-tumour effect has only been identified in combination with other drugs, such as Doxorubicin in animal models [126].

Intriguingly, the rapid changes in the bone marrow induced by ZOL treatment affect both osteoblasts and osteoclasts and this results in a modification of the characteristic pattern of breast cancer cell homing in the bone microenvironment, without altering the total number of tumour cells detected within the bone [118]. This variation in the location of tumour cells may represent adaptation to the newly organised microenvironment after treatment with ZOL.

In the past few years it has been shown that the effectiveness of ZOL in preventing the development of overt tumour from disseminated tumour cells varies between animal models mimicking the pre- and post-menopausal status [148], [149]. In animals undergoing ovariectomy to mimic the post-menopausal setting, ZOL is beneficial preventing the development of tumour while this effect is not observed in the pre-menopausal group. Also the overall number of tumour cells present in the bone marrow is not altered by the administration of the anti-resorptive drug. These fascinatingly results from in vivo models reflect what has been shown in clinical trials. In particular the AZURE clinical trial, testing whether administration of ZOL in addition to standard adjuvant therapy improved the outcome in breast cancer patients that had no detectable distant metastasis when entering the study, revealed that the anti-resorptive drug was beneficial in women that were postmenopausal for 5 years or longer at the start of the treatment. Post-menopausal women in fact not only had a reduced development of bone metastasis but also the dissemination to other sites was prevented compared to the pre-menopausal breast cancer patients, where administration of ZOL prevented bone metastasis but appeared to increase the development of extraskeletal metastasis [141], [142], [146], [147], [239].

Taken together, these data indicate that alterations of only the bone cellular populations is not sufficient to arrest the progression of the metastatic disease suggesting that further studies determining the mechanism of response to therapies, by the microenvironment are needed. As described in the previous chapter, the

perivascular component of the bone microenvironment displays a considerable difference between the young and mature animal models. This age-related modification of the fertile soil for the progression of the metastatic disease could partially explain the differential effectiveness of ZOL between pre- and post-menopausal status. Therefore in this chapter I investigated whether the administration of a single clinically relevant dose of ZOL induced alterations of the microvascular component of the metastatic niche in young and mature animal models.

5.3 Aims

The aim of this chapter was to test the hypothesis that:

Therapeutic treatment with ZOL influences both the bone and the perivascular component of the metastatic niche.

This will be tested by the following objective that will characterise the effects of ZOL on:

- Bone structure
- Bone microvasculature
- Breast cancer bone colonisation
- Expression of dormancy-supporting Thrombospondin

5.4 Materials and Methods

Detailed information can be found in the main Material and Methods Chapter 2.

5.4.1 Breast cancer cell line

The triple negative breast cancer cell line MDA-MB-231-NW1-Luc2 was cultured in DMEM + Pyruvate medium enriched with 1% penicillin/streptomycin and 10% foetal bovine serum at 37°C and 5%CO₂. As explained in detail in section 2.3, breast cancer cells were trypsinized once confluent and labelled with the membrane fluorescent dye Vybrant-CM-Dil.

5.4.2 *In vivo* studies

In vivo studies were performed to investigate the effect of ZOL on the principal components of the metastatic niche. All the studies here described were executed in conformity with Home Office guidelines and approval under the project licences PPL 70/8964 held by Professor Nicola Brown (University of Sheffield, UK) and PPL 70/8799 held by Dr Colby Eaton (University of Sheffield, UK).

To assess any changes in the bone structure and perivascular niche caused by the anti-resorptive agent ZOL (ZOL) and how this influences the colonisation of tumour cells to bone, 6- and 12-week old female BALB/c nude mice (n=10/age group) were injected i.c. with 0.75×10^5 MDA-MB-231-NW1-Luc2 cells labelled with the membrane dye Vybrant-CM-Dil. Two days after the injection, animals were injected i.p. with 100µg/Kg freshly prepared ZOL (100µl/mouse) or PSB control (100µl/mouse). On day five animals were culled and hind limbs were collected for *ex vivo* analysis (figure 5.1).

5.4.2.1 Preparation of long bones for *ex vivo* analysis

On the day of cull, animals were injected i.p. with an overdose of Pentobarbital (50µl/mouse) and cervical dislocation was performed to ensure death. Dissection of the hind limbs was executed by meticulous removal of tissues surrounding the long bones followed by careful separation of tibiae and femora. Subsequent processing of the bone are described in the Materials and Methods chapter and summarised in the following table (table 5.1).

Table 5.1 Summary of the bone sample preparations for the different analyses performed.

Sample	Analysis	Preparation
Left Femora	<ul style="list-style-type: none"> • Two-photon microscopy 	<ul style="list-style-type: none"> • Bones were snap frozen in liquid nitrogen • Bones were then placed in modules and embedded in Bright Cryo-M-Bed and stored at -80°C • On day of analysis, the bone marrow was exposed using Bright OTF Cryostat with a 3020 microtome • Specimen was placed on a glass bottomed dish and immobilised with a coverslip
Left Tibiae	<ul style="list-style-type: none"> • μCT • Histology 	<ul style="list-style-type: none"> • Bones were scanned during the incubation in 4%PFA prior to decalcification (48-72hrs) • 4% PFA was changed to 0.5M EDTA/0.5% PFA for 2 weeks (refreshed three time/week) prior to processing and paraffin embedding • Blocks were sectioned to a thickness of 3μm
Right Tibia and Femora	<ul style="list-style-type: none"> • μCT • Immunofluorescent staining 	<ul style="list-style-type: none"> • Bones were scanned during the incubation in 4%PFA prior to decalcification (4-6hrs) • 4% PFA was changed to 0.5M EDTA for 48hrs • Bones were immersed in CPT solution (20% Sucrose and 2% Polyvinylpyrrolidone (PVP) prepared in PBS) for at least 24hrs at 4°C • Bones were warmed up to 60°C in a water bath for 45 min in EMB (8% gelatin from porcine skin, 20% sucrose and 2% PVP prepared in PBS) • Specimens were embedded in molds and stored at -80°C • Tissue was cut with cryostat to a thickness of 30μm

5.4.3 Two-photon microscopy

An area of 2104 μm \times 2525 μm of the exposed bone marrow surface (70 μm depth) was imaged using Zeiss LSM510 NLO upright two-photon microscope, as described in section 2.10.2. Chameleon two-photon laser was used to visualise the calcified bone structure (900nm) and HeNe laser to capture Vybrant-CM-Dil labelled breast cancer cells (543nm). The reconstructed three-dimensional image was analysed using Volocity 3D Image Analysis software version 6.01 and the parameters measured were the number of Vybrant-CM-Dil⁺ breast cancer cells in two different ROIs, distance to the nearest bone surface and to the closest tumour cell as described in section 2.10.3.

5.4.4 Micro Computed tomography

Trabecular bone volume, trabecular number and thickness were measured using CTAn software on the images captured with SkyScan 1272 during the incubation time in 4% PFA and reconstructed with NRecon software. The μCT analysis is detailed in section 2.11.

5.4.5 Toluidine Blue staining

Paraffin embedded tibiae were sectioned by Mrs Alyson Evans (University of Sheffield, UK) at a thickness of 3 μm . The histological sections were dewaxed in xylene (2x5min) and rehydrated through decreasing concentration of alcohols (99%, 95%, 70%, 3 min each) to tap water. The metachromatic staining to identify the proteoglycan rich area of the growth plate cartilage was performed by incubating the tissue slides for 3 min at ambient temperature with toluidine blue solution (Toluidine Blue O, Sigma Aldrich: 1% NaCl pH 2.0-2.5), followed by rinsing under running water. Stained sections were subsequently dehydrated through 70%, 95% and 99% alcohol to xylene and cover slips were applied with DPX. Images of the stained bones were captured using a 20x objective of an OM-AFHM advanced histomorphometry microscope and Aperio ImageScope software was used to identify and then outline the area of interest (AOI) covering the proteoglycan-rich growth plate and the trabecular bone surface connected with the epiphysis. Analyses were performed on two non-serial sections and cortical bone was excluded from any measurement.

5.4.5 Immunofluorescent staining of the components of the metastatic niche

Bones used for immunofluorescence staining protocols were prepared as explained in table 5.1. Tissue sections were left at ambient temperature to defrost and rehydrate in PBS before the start of the immunostaining protocols summarised in table 5.2 and antibodies used listed in table 2.6 and 2.7.

Table 5.2. Summary of immunofluorescent protocols used to visualise components of the metastatic niche

Marker	Protocol*
Endomucin	<ul style="list-style-type: none"> • Permeabilisation in 0.3% Triton X-100 for 20 min at ambient temperature • Incubation with primary antibody (1:100) for 1hr at ambient temperature or overnight at 4°C • Incubation with secondary antibody (1:200) for 40min at ambient temperature • Nuclei counterstaining with DAPI and coverslip
Endomucin and CD31/CD34	<ul style="list-style-type: none"> • Permeabilisation in 0.3% Triton X-100 for 20 min at ambient temperature • Amplification of the signal blocking for 15 min at ambient temperature with Streptavidin solution followed by 15 min at ambient temperature with Biotin solution • Incubation with primary antibody (CD34 or CD31; 1:100) for 1hr at ambient temperature • Incubation with biotinylated secondary antibody (anti-rat; 1:200) for 40min at ambient temperature • Incubation with rat IgG for 30 min at ambient temperature • Incubation with primary antibody (Endomucin; 1:100) for 1hr at ambient temperature • Incubation with secondary antibody (1:200) for 40min at ambient temperature • Incubation with fluorophore-conjugated Streptavidin for 20min at ambient temperature • Nuclei counterstaining with DAPI and coverslip
Endomucin and Osterix/TSP-1	<ul style="list-style-type: none"> • Permeabilisation in 0.3% Triton X-100 for 20 min at ambient temperature • Amplification of the signal blocking for 15 min at ambient temperature with Streptavidin solution followed by 15 min at ambient temperature with Biotin solution • Incubation with primary antibodies (Endomucin 1:100 and Osterix 1:300 or TSP-1 1:100) for 1hr at ambient temperature • Incubation with secondary antibodies (Alexafluor anti-rat 1:200 and biotinylated anti-rabbit 1:200) for 40min at ambient temperature • Incubation with fluorophore-conjugated Streptavidin for 20min at ambient temperature • Nuclei counterstaining with DAPI and coverslip

*Each step is followed by three washes in PBS

Images of the immunofluorescent staining against the endothelial marker Endomucin were captured using an inverted fluorescence microscope (Leica AF6000) while the bone sections stained for multiple markers were imaged using the Zeiss LSM880 AiryScan Confocal microscope. Aperio ImageScope software was used to manually track the distinctive structure of H- and L-vessels on Endomucin stained slides and to trace the CD31 and CD34 positive vessels. Parameters considered in these analyses were the number and length of these microvessels and the area of bone marrow occupied by them. The overall expression of CD31, CD34, TSP-1 and Osterix and CD31/Endomucin and CD34/Endomucin was measured using ImageJ software as explained in detail in section 2.14.2-3. TSP-1 expressing megakaryocytes were manually counted using the function 'cell counter' of the software while Osterix⁺ osteoprogenitors were quantify using the automatic function '3D object counter'. All the analyses were performed on three non-serial 30µm thick section to minimise the variations due to the angle of cut with the cryostat.

5.4.6 Statistical analyses

Statistical analyses were performed using GraphPad Prism software (versions 6.0 and 7.0), student T-test and Two-way ANOVA with Tukey post test were used as stated in each figure legend and the *p*-value of *p*<0.5 was considered significant.

5.5 Results

The current treatments for breast cancer bone metastasis are focused on treating the advanced stages associated with lytic bone lesions. Moreover, most of the drugs currently available are designed to target one of the multiple components of the bone microenvironment; bone structure in the case of the anti-resorptive agent ZOL. It is not known how these drugs affect the other components of the metastatic niche. The aim of this chapter was to determine the response to therapeutic modification of the microenvironment with ZOL on both the bone and the perivascular components of the metastatic niche and on breast cancer bone colonisation.

5.5.1. ZOL changes the bone structure

To investigate the effect of a single dose of ZOL on the bone microenvironment and breast cancer bone colonisation, Vybrant-CM-Dil labelled MDA-MB-231-NW1-Luc2 cells were injected i.c. in 6- and 12-week old BALB/c nude (n=10/group). Two days after tumour cell injection, 5 animals/group were treated with 100µg/Kg of ZOL while the remaining 5 mice/group received the vehicle control (PBS)(figure 5.1). Animals were culled 3 days after drug administration and long bones were collected for two-photon microscopy (femora) and for fluorescent immunohistochemistry and histology (tibiae).

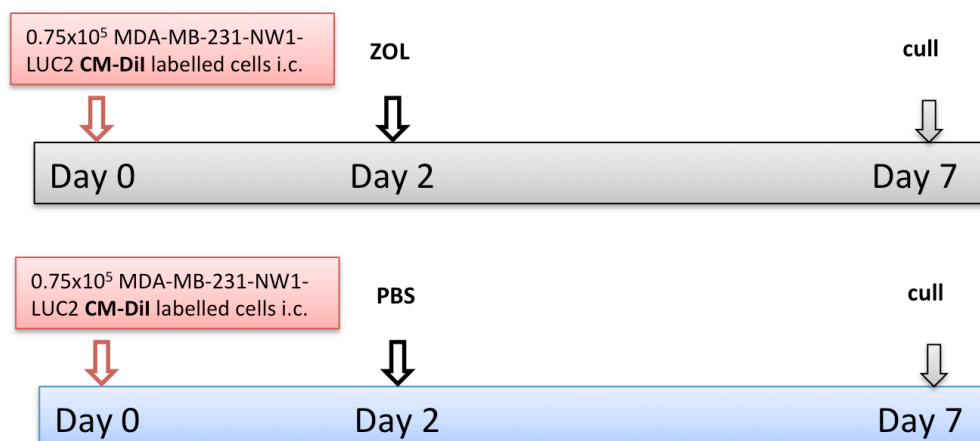


Figure 5.1 Outline for the *in vivo* studies evaluating the effect of ZOL on the bone microenvironment

6- and 12-week old female BALB/c nude female mice were injected via the intracardiac route with 0.75×10^5 Vybrant-CM-Dil labelled MDA-MB-231-NW1-Luc2 cells ($n=5$ mice/group). Two days after, animals were injected i.p. with $100 \mu\text{g}/\text{kg}$ freshly prepared ZOL ($100 \mu\text{l}/\text{mouse}$) or PBS control ($100 \mu\text{l}/\text{mouse}$). On day five, animals were culled and hind limbs were collected for *ex vivo* analysis.

To determine whether the anti-resorptive agent caused any alteration in the bone structure of long bones, tibiae were analysed with μCT as described in section 2.11 (6-week old mice $n=3$ PBS and $n=5$ ZOL, 12-week old $n=4$ PBS and $n=5$ ZOL (figure 5.2).

As expected, the treatment with ZOL increased the bone volume/ trabecular volume ratio, significantly in the young (6-week old) animals and with a trend towards significance level in the mature animals (12-week old) ($p=0.0372$ and $p=0.0684$ respectively). These changes in the trabecular volume were caused by modification of the trabeculae structure that resulted in slightly thinner but more numerous trabeculae. Statistical analysis did not reach significance level in neither of the ages for both parameters analysed but the effects of ZOL on the bone structure was more pronounced on the young animals compared to the mature ones (trabecular thickness $p=0.1300$ and $p=0.7599$; trabecular number $p=0.0989$ and $p=0.1269$ for 6- and 12-week old respectively)(figure 5.3).

These results showed that the imbalance on the forming and resorbing cell populations caused by ZOL results in bones with an increased trabecular volume in the treated animals when compared to the control group.

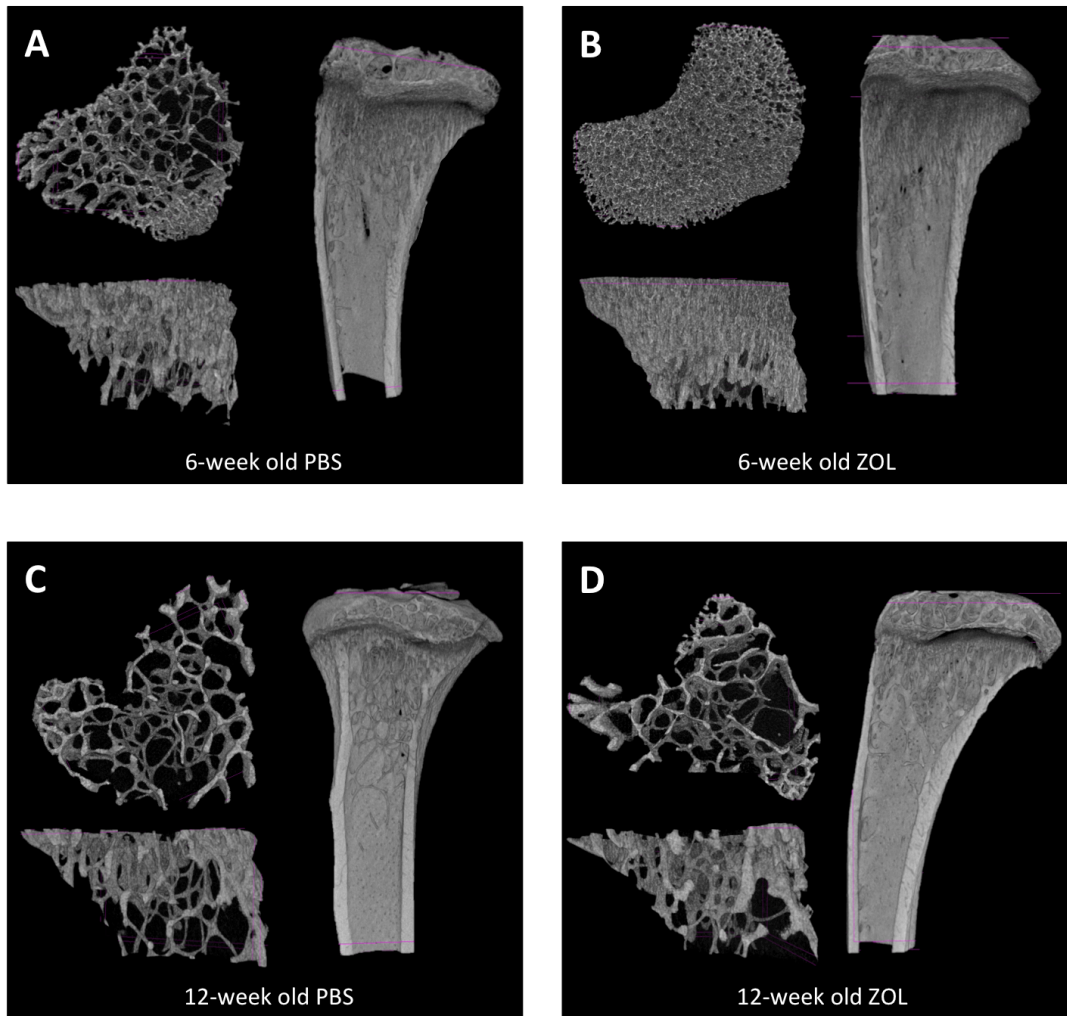


Figure 5.2 Representative images of reconstructed bone after mCT analysis

Every panel shows the three-dimensional reconstruction of the trabecular bone analysed and the open cross section of the entire bone scanned. (A) Tibia of 6-week old animal receiving PBS and (B) ZOL. (C) and (D) are tibia of 12-week old animal receiving PBS and ZOL respectively.

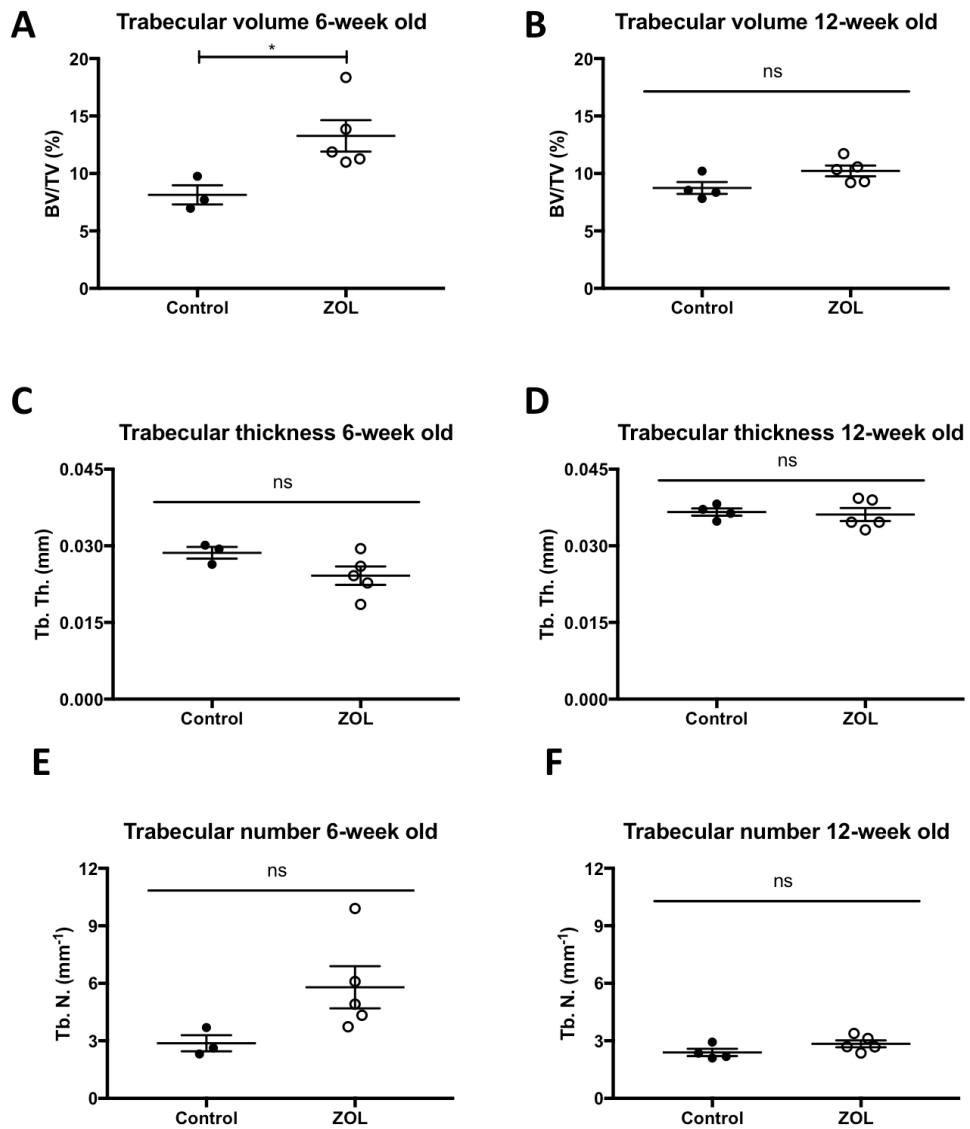


Figure 5.3 Effect of a single dose of ZOL on bone structure of young and mature animal models

A) Quantification of the trabecular bone volume after ZOL treatment of 6- and (B) 12-week old BALB/c nude, (C) and (D) trabecular thickness and (E) and (F) trabecular number. 6-week old n=5 animals, 3 bones analysed PBS and n=5 animals and bones analyse ZOL, 12-week old n=5 animals, 4 bones analysed PBS and n=5 animals and bones analyse ZOL. Graphs show Mean \pm SEM, Student t-test, *p<0.05 and ns is non-significant.

5.5.1.1. ZOL causes an expansion of the proteoglycan-rich area of the growth plate

According to the literature, a single dose of ZOL decreases the number of osteoclasts, resulting also in increased endochondral ossification that fails to be resorbed by the osteoclasts [118].

To detect changes in the proteoglycan rich area of the metaphysis, Toluidine blue staining was performed as described in section 2.12.5. As shown in figure 5.4, ZOL treated animals appear to have an excess of this matrix compared to the control mice even though, irrespective of age, the increase was not statistically significant ($p=0.0585$ in 6-week old mice and $p=0.1175$ in 12-week old).

The decrease in the number of osteoclasts in bones treated with ZOL resulted in the accumulation of excess of proteoglycan rich matrix, particularly in young animals.

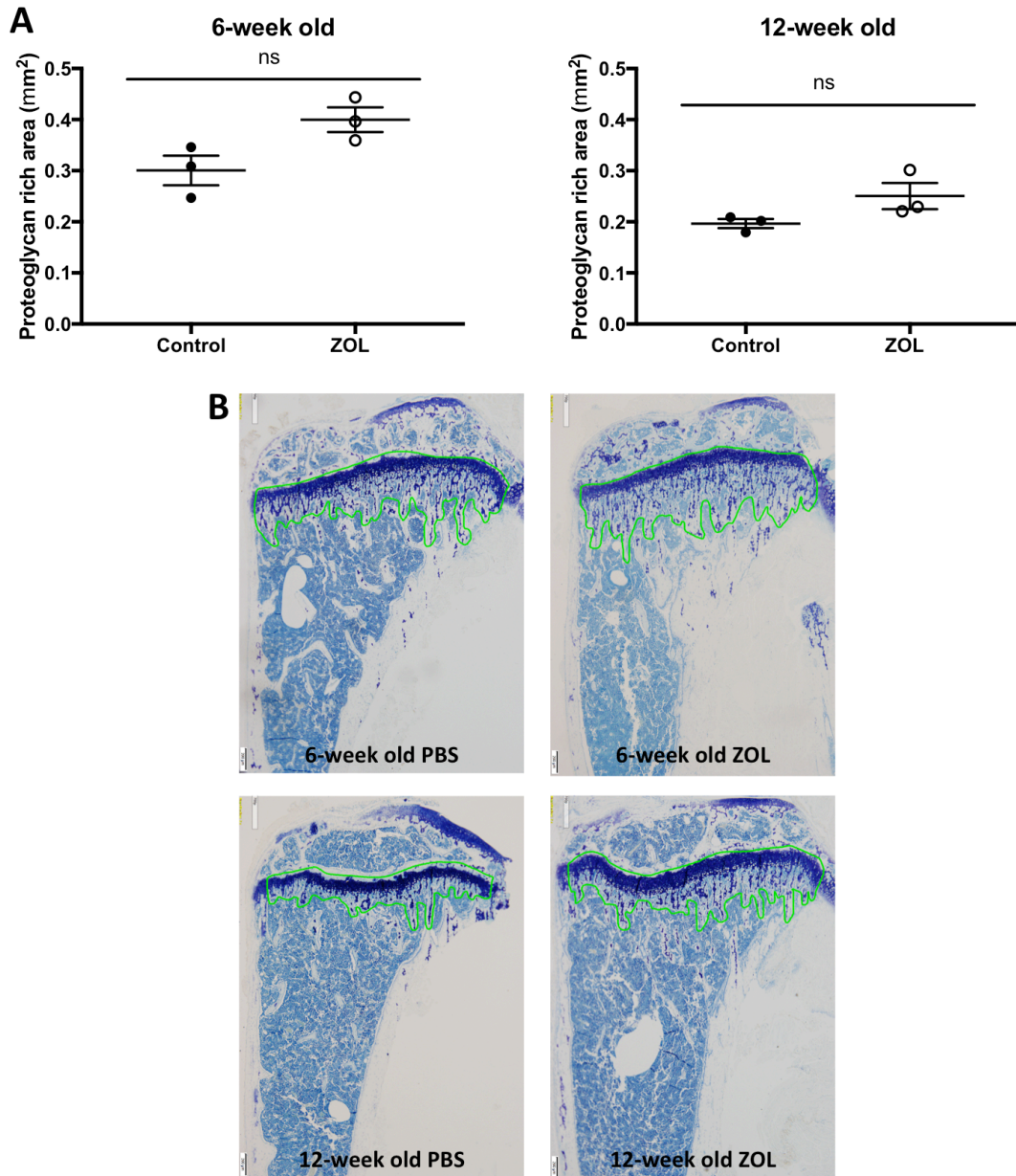


Figure 5.4 Quantification of the proteoglycan-rich area of bone

(A) Quantification of extracellular matrix visualised with Toluidine Blue staining of histological sections of tibiae. (B) Aperio ImageScope software was used to manually draw around the area of proteoglycan in the epiphysis and the trabecular bone directly connected to it (green line). Fragments of bone and cortical bone were excluded from the analysis. Graphs show mean \pm SEM ($n=5$ animals, 3 bones analysed/group), Student t-test, ns is non-significant.

5.5.1.2 Alteration of the bone structure is reflected in the osteoprogenitor population

It has been reported that the increase in bone volume caused by ZOL treatment is the result of decreased numbers of osteoclasts resorbing the calcified matrix and increased osteoblasts forming the bone [118].

Mesenchymal precursor cells that differentiate into osteoblasts and then osteocytes as express Runx-2 and Osterix [240]. Therefore I used the expression of this protein to investigate whether modification of the bone structure caused changes in the osteoprogenitors; tibiae were stained using the immunofluorescent protocol explained in section 2.14.7 (figure 5.5 and 5.7). Regardless of age, there was no difference in the area of bone marrow analysed for both treated and control animals ($p=0.4717$ and $p=0.5306$ for young and mature animals respectively) (figure 5.5 and 5.6). The overall expression of the Osterix marker was measured using ImageJ software and in both ages analysed it was evident that a single administration of ZOL caused a trend in the reduction in Osterix expression compared to the control animals ($p=0.0599$ in young animals and $p=0.0079$ in mature mice, figure 5.6 and 5.8). Surprisingly, mature animals had a greater response to the drug treatment. In fact, both the overall number of Osterix⁺ cells and the number of Osterix⁺ cells/mm² was significantly reduced in the ZOL treated group compared to the control ($p=0.0364$ and $p=0.0192$ respectively, figure 5.6 and 5.8), while no changes in the number of osteoprogenitors were detected in young animals ($p=0.4242$ and $p=0.9283$ respectively, figure 5.6 and 5.8).

The changes in the bone structure caused by a single dose of ZOL, induced a reduction in the Osterix⁺ osteoprogenitors detected in mature animals compared to the control mice, no statistically significant differences were detected in young mice. This change in the presence of Osterix⁺ cells could be due to the limited sample size analysed and further investigations are required.

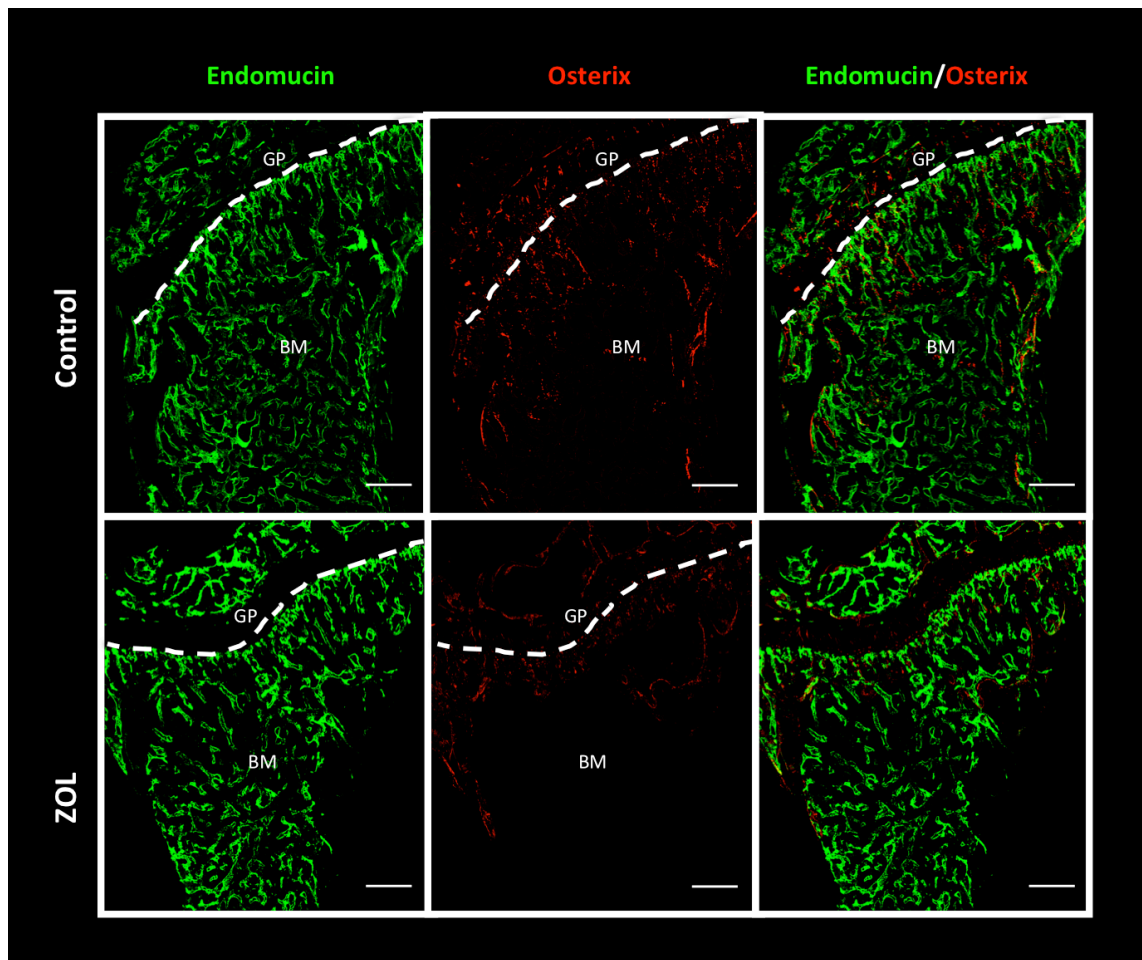


Figure 5.5 Representative image of the effect of ZOL treatment on Osterix expression in 6-week old animals

Immunofluorescent staining against Osterix and Endomucin performed on 30 μ m tibia sections of 6-week old animals receiving PBS or ZOL. GP=growth plate, BM=bone marrow, Green=Endomucin and red=Osterix. Scale bar 200 μ m.

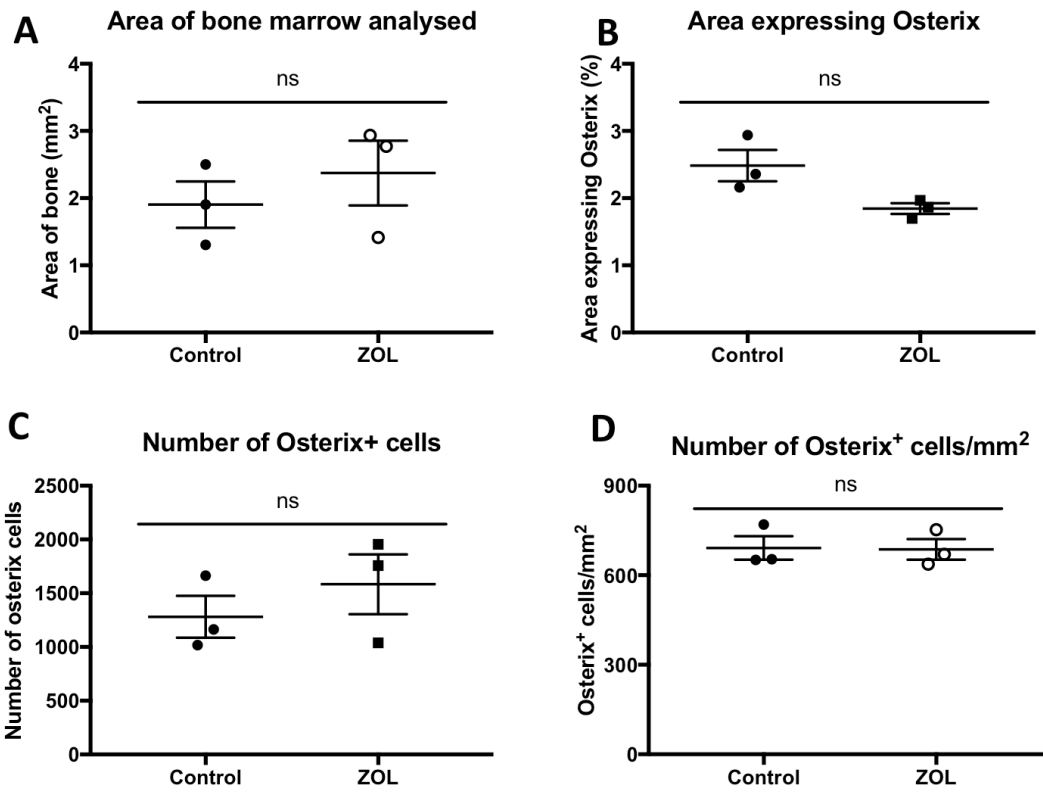


Figure 5.6 Quantification of the effect of ZOL treatment on Osterix expression in 6-week old animals

(A) Area of bone marrow analysed. (B) Percentage area of bone marrow expressing Osterix. (C) Overall number of Osterix⁺ cells and (D) Osterix⁺ cells/mm². Graphs show mean ± SEM (n=5 animals, 3 bones analysed/group), Student t-test, ns is non-significant.

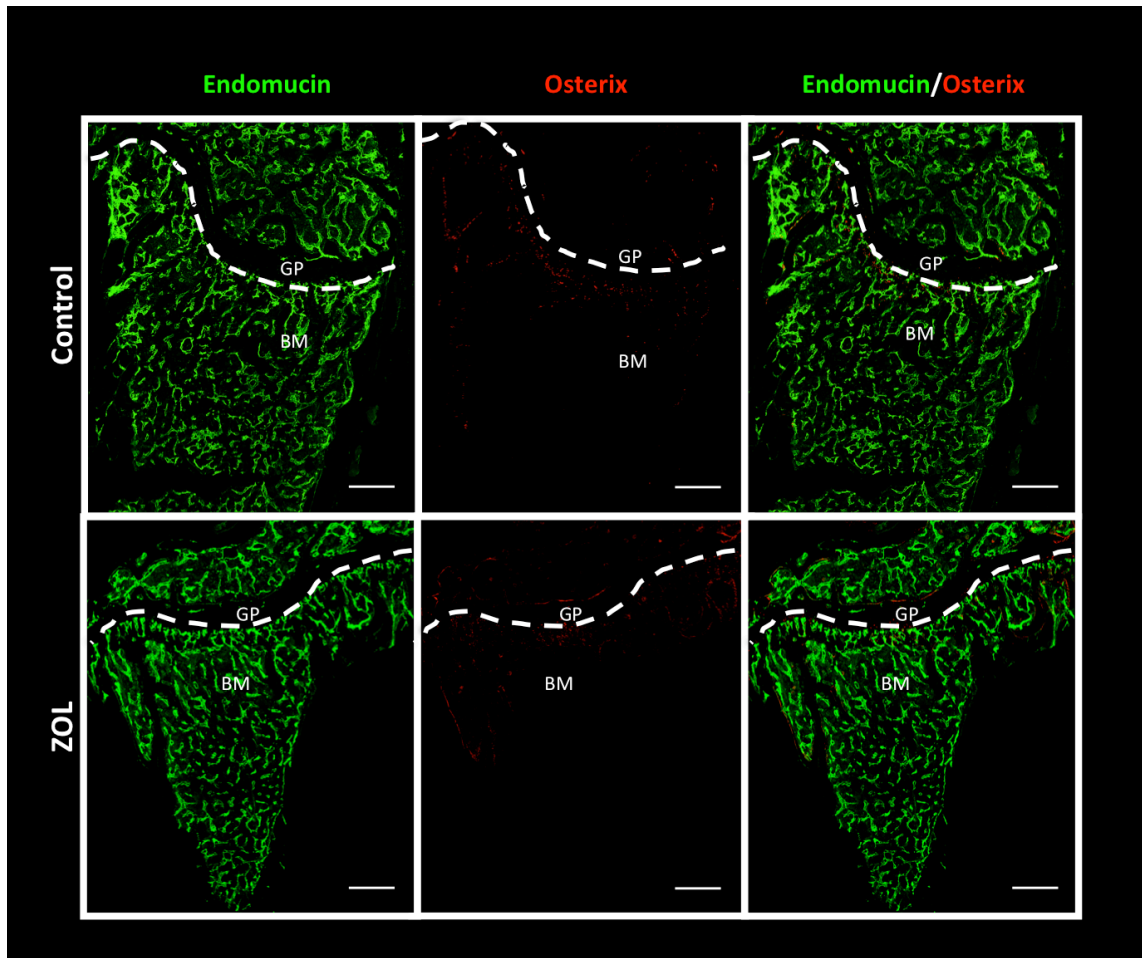


Figure 5.7 Representative image of the effect of treatment on Osterix expression in 12-week old animals

Immunofluorescent staining against Osterix and Endomucin performed on 30 μ m tibia sections of 12-week old animals receiving PBS or ZOL. GP=growth plate, BM=bone marrow, Green=Endomucin and red=Osterix. Scale bar 200 μ m.

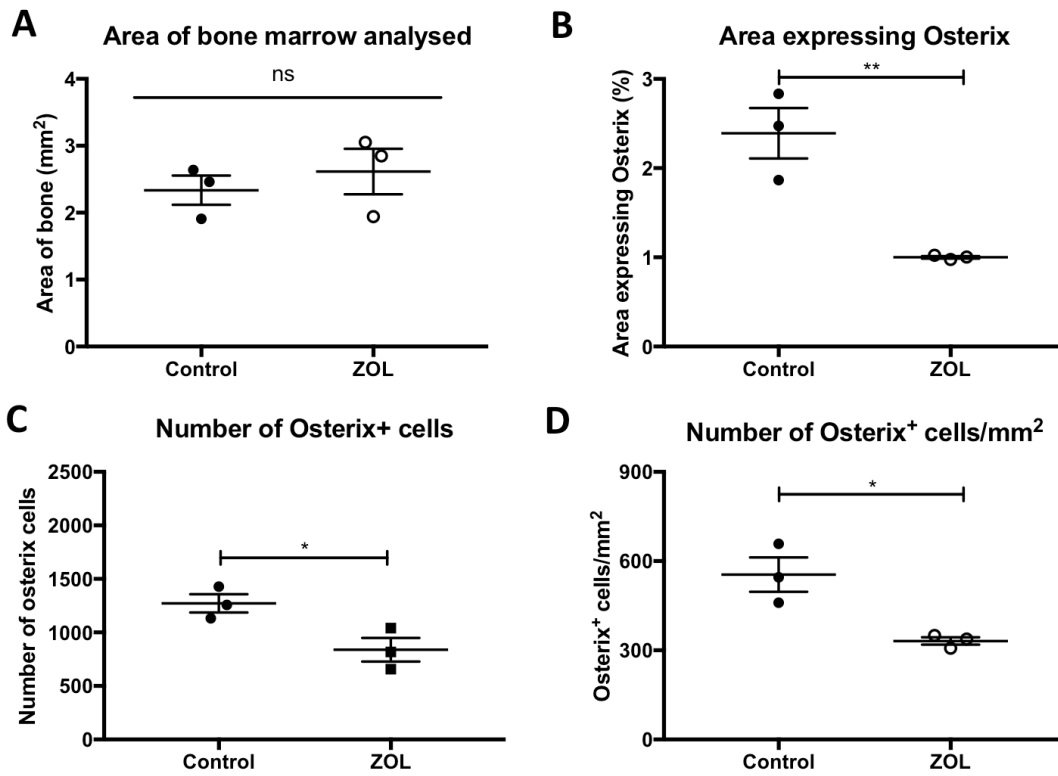


Figure 5.8 Quantification of the effect of ZOL treatment on Osterix expression in 12-week old animals

(A) Area of bone marrow analysed. (B) Percentage area of bone marrow expressing Osterix. (C) Overall number of Osterix⁺ cells and (D) Osterix⁺ cells/mm². Graphs show mean ± SEM (n=5 animals, 3 bones analysed/group), Student t-test, *p<0.05, **p<0.005, ns is non-significant

5.5.2 ZOL treatment affects the bone microvasculature

The effect of ZOL on the bone microenvironment has always been focused on the bone cell components and there is no comprehensive analysis of the effect of ZOL on the perivascular component of the metastatic niche. Therefore, frozen sections of tibia and femora were stained against multiple components (Endomucin, CD31, CD34 and TSP-1) of the perivascular niche as explained in detail in section 2.13.1 and all the analyses were performed on three non-serial sections of bone.

5.5.2.1 Effect of ZOL on Endomucin positive vessels of young and mature animals

Using the immunofluorescent protocol with an antibody against the endothelial marker Endomucin it is possible to visualise the complex microvasculature network of bone. The vessels positive for this marker are present both in the metaphysis (H-vessels) and in the diaphysis of long bones (L-vessels).

Irrespective of age, images captured using an inverted widefield fluorescence microscope Leica AF6000 consisted of an area of 2.5mm² approximately. No difference was detected between control and ZOL treated animals (2.78±0.10 and 2.83±0.14, $p=0.7753$ for 6-week old; 2.30±0.12 and 2.57±0.12, $p=0.1807$ for 12-week old)(figure 5.9). Moreover, no difference in the area of bone marrow occupied by H- and L-vessels was detected between treatment groups in the 6-week old animals (control vs. ZOL $p=0.7107$ and $p=0.9702$ respectively). In mature animals ZOL treatment increased the area of bone marrow occupied by L-vessels ($p=0.0225$) whereas the area occupied by H-vessels was not altered ($p=0.4886$) (figure 5.10). Since the overall area of bone marrow occupied by the different vessels sub-types was changed in the 12-week old mice treated with ZOL, it is not surprising that the area of bone marrow analysed occupied by H-vessels was reduced in the mature ZOL treated animals compared to the control while the area of L-vessels was enlarged (control vs. ZOL $p=0.0316$ H-vessels and $p=0.0301$ L-vessels) (figure 5.11).

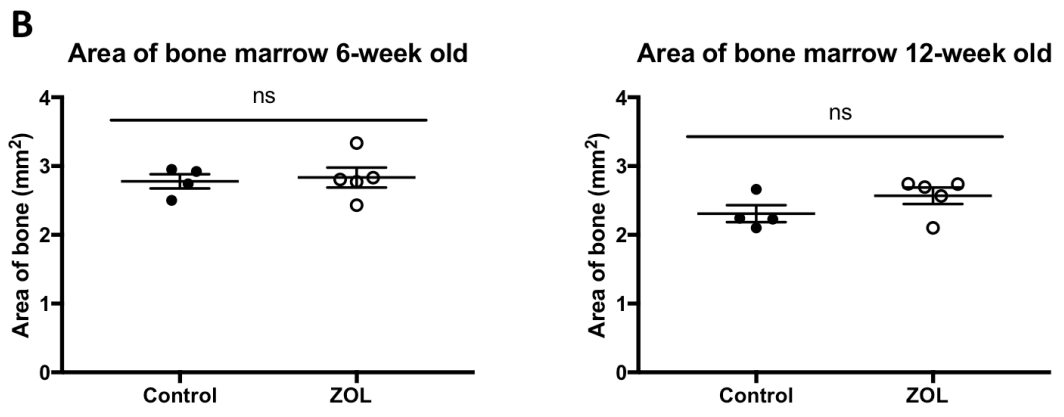
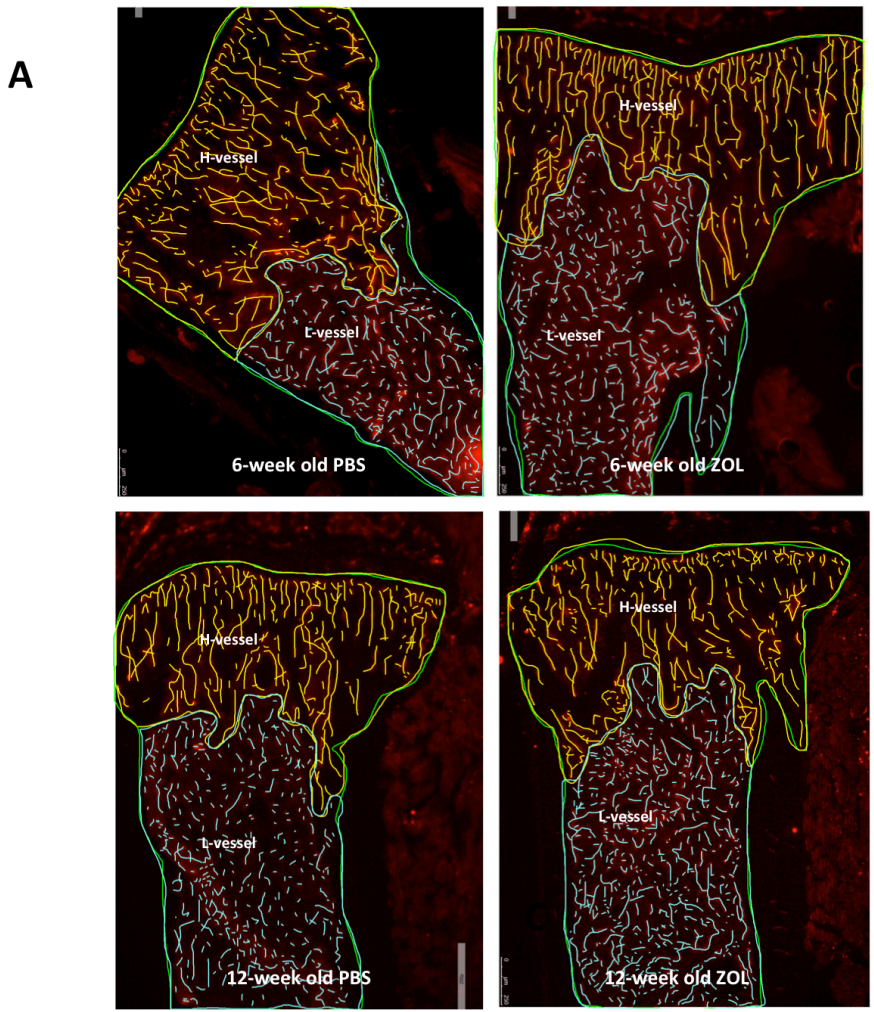


Figure 5.9 Quantification of immunofluorescent staining against Endomucin

A) Representative images of the H-vessels (yellow) and L-vessels (blue) manually tracked with Aperio ImageScope software. Area of bone marrow analysed is drawn in green and quantification in 6- and 12-week old is shown in (B) and (C). Graphs show mean \pm SEM (n=5 animals, 4 bones analysed control and 5 bones analysed ZOL), Student t-test, ns is non-significant

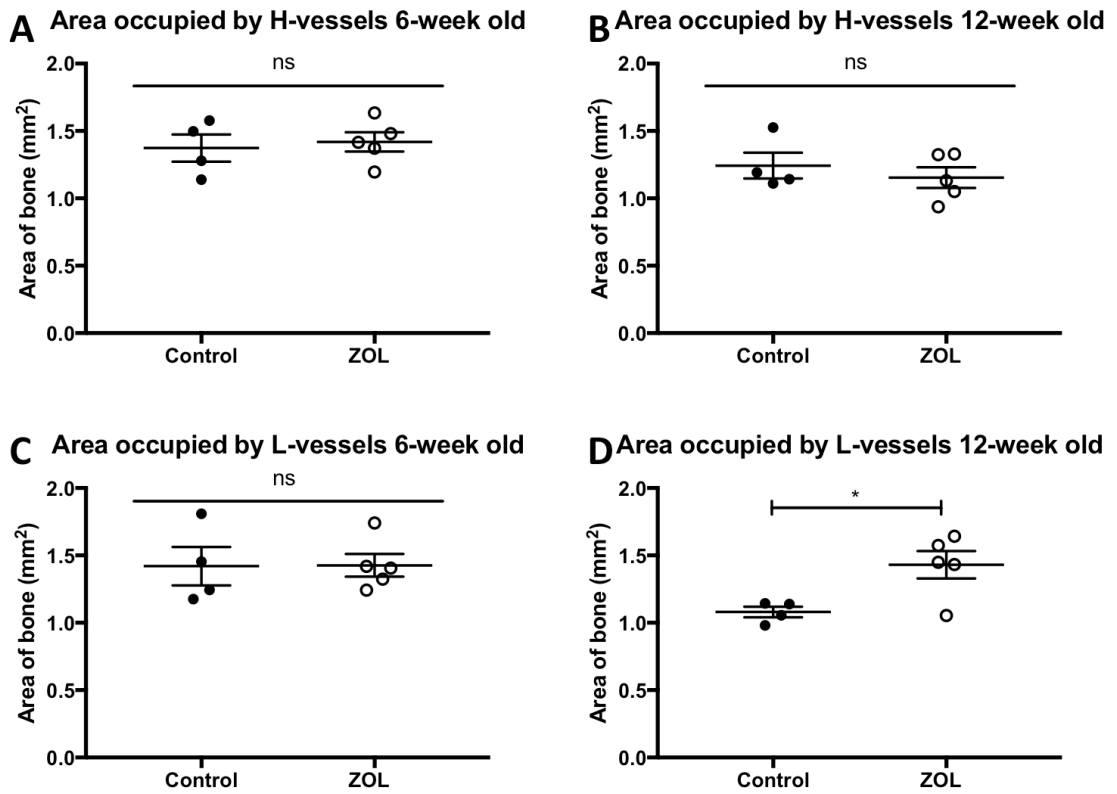
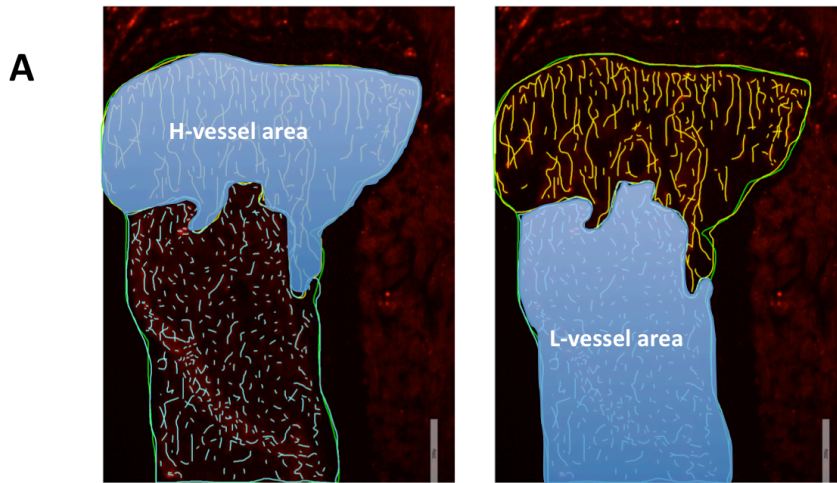
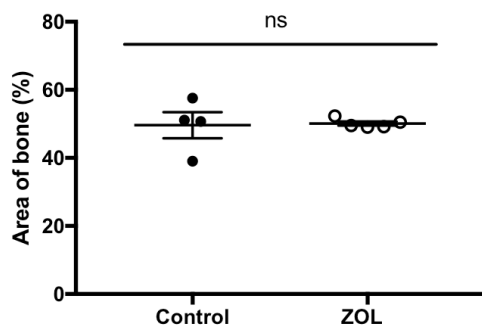


Figure 5.10 Area of bone marrow occupied by H- and L-vessels

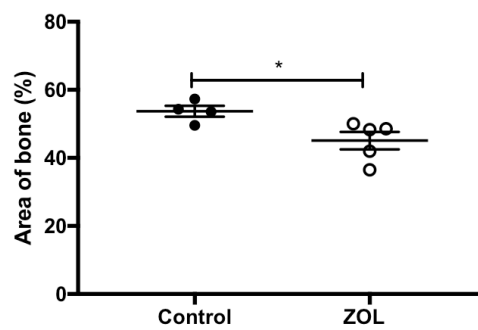
(A) and (B) show the area of bones occupied by H-vessels in 6- and 12-week old respectively. (C) and (D) show the area of bones occupied by L-vessels in 6- and 12-week old respectively. Graphs show mean \pm SEM (n=5 animals, 4 bones analysed control and 5 bones analysed ZOL), Student t-test, * $p < 0.05$ and ns is non-significant



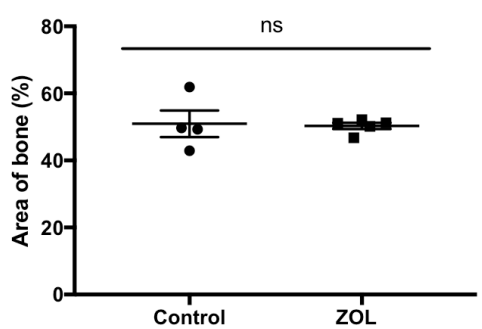
B Area occupied by H-vessels 6-week old



C Area occupied by H-vessels 12-week old



D Area occupied by L-vessels 6-week old



E Area occupied by L-vessels 12-week old

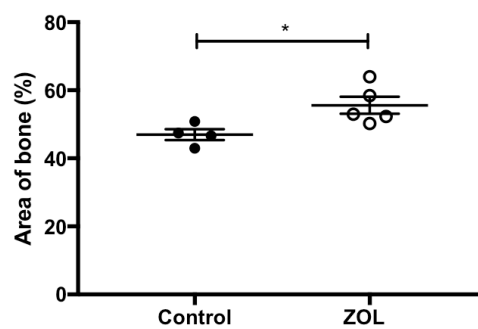


Figure 5.11 Percentage of bone marrow occupied by H- and L-vessels

A) Schematic illustration of the area occupied by H- and L-vessels. (B) and (C) show the percentage area of the bone marrow occupied by H-vessels in 6- and 12-week old animals, while (D) and (E) show the percentage area of the bone marrow occupied by L-vessels in 6- and 12-week old animals, Graphs show mean \pm SEM (n=5 animals, 4 bones analysed control and 5 bones analysed ZOL), Student t-test, * $p < 0.05$ and ns is non-significant

The next parameter analysed was the overall number of vessels in the bone marrow, manually traced with Aperio ImageScope software. Once again it was unexpected that ZOL treated 6-week old animals did not show any difference in the number of vessels in the total area of bone marrow analysed while 12-week old mice displayed a significantly higher overall number of vessels in the ZOL treated group compared to the control ($p=0.9106$ and $p=0.0010$ respectively, figure 5.12). This increase in the number of vessels detected in the entire bone marrow was due to the significantly greater number of L-vessels present in the diaphysis of mature animals receiving a single dose of ZOL compared to animals in the control group ($p=0.0035$). No changes were detected in the number of H-vessels in mature mice ($p=0.2763$) or in H- or L-vessels number in 6-week old mice ($p=0.4870$ and $p=0.6574$ respectively, figure 5.12).

Since the area of the bone marrow occupied by the L-vessels was enlarged in the animals treated with the anti-resorptive drug compared to the animals receiving the vehicle, next the number of vessels/mm² was normalised against the surface occupied by the subtype analysed (and not against the total bone area). This analysis showed that treatment with ZOL did not affect the number of vessels in young animals ($p=0.4006$ and $p=0.5964$ H- and L-vessels respectively), whilst this normalisation highlighted that ZOL increased the number of both H- ($p=0.0326$) and L-vessels ($p=0.0016$) in 12-week old animals when compared to the control group (figure 5.13).

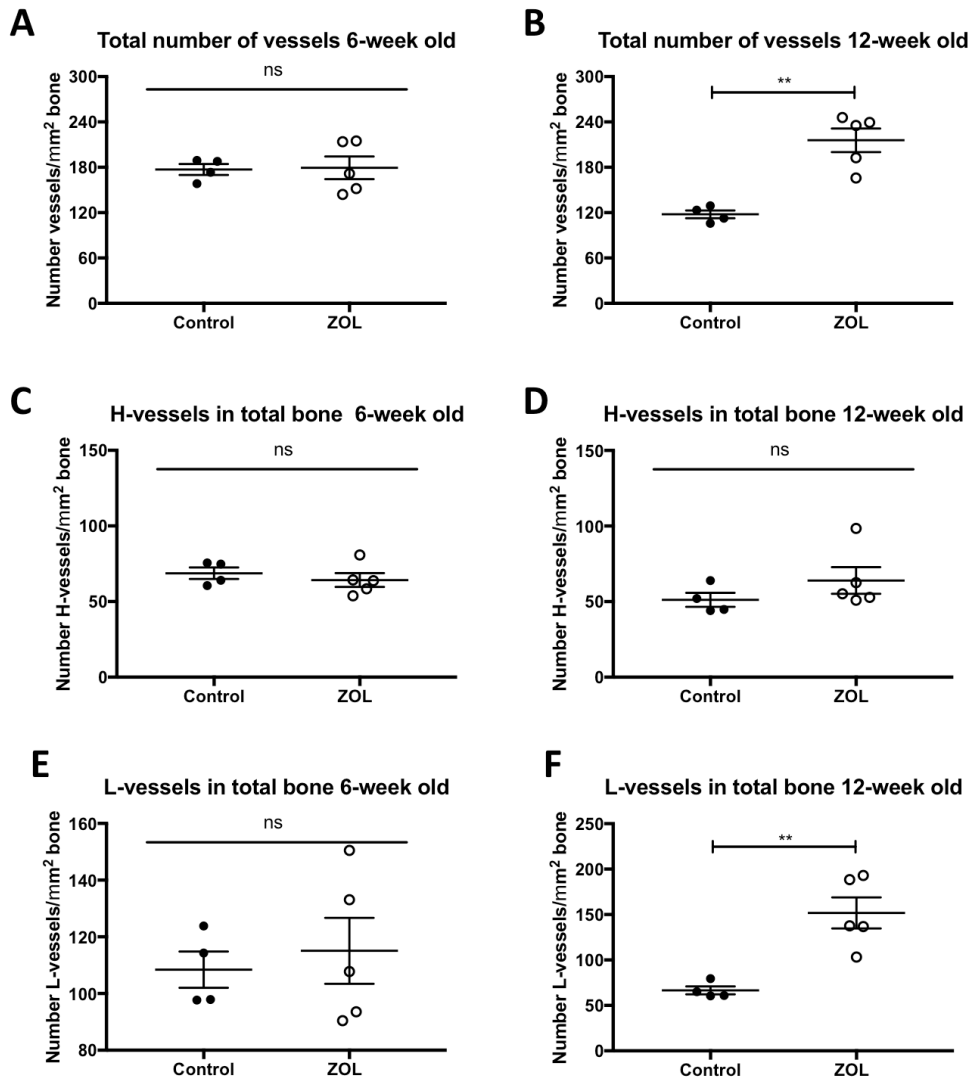


Figure 5.12 Number of vessels quantified in the total area of bone marrow

A) and (B) total number of vessels counted in both ages. (C) and (D) show the number of H-vessels/mm² of total area of bone in the different ages. (E) and (F) show the number of H-vessels/mm² of total area of bone in the different ages. Graphs show mean \pm SEM (n=5 animals, 4 bones analysed control and 5 bones analysed ZOL), Student t-test, ** $p < 0.01$ and ns is non-significant

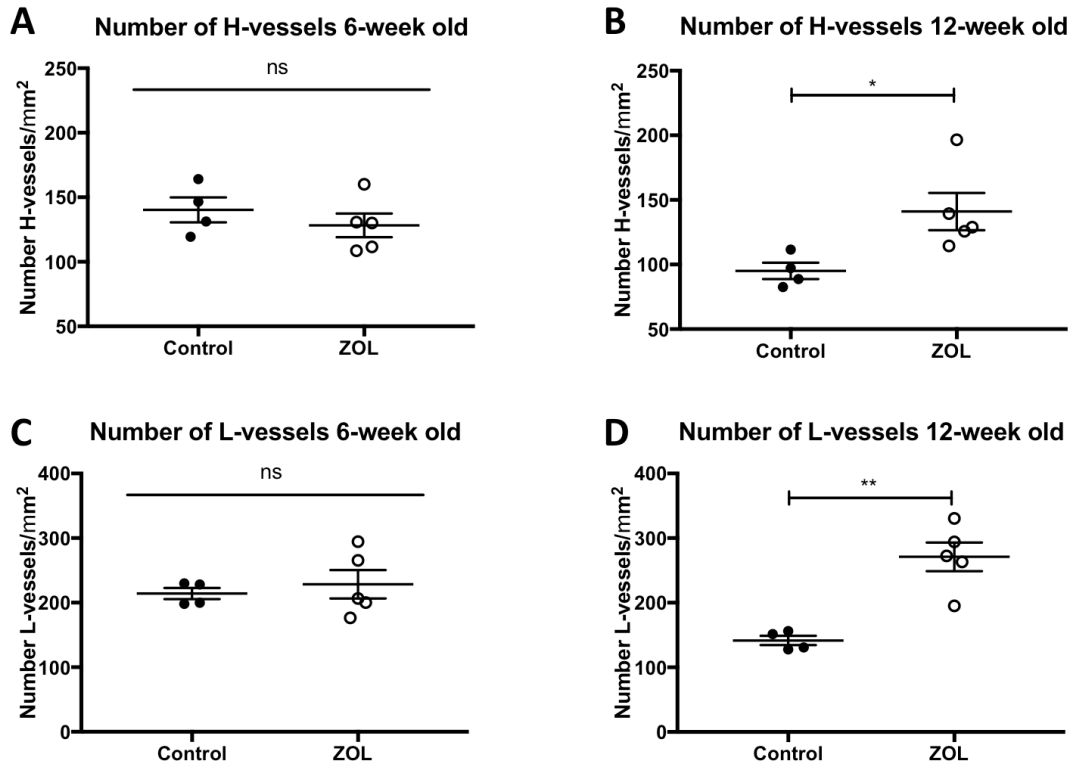


Figure 5.13 Number of H- and L-vessels quantified in the area of bone they occupy

(A) and (B) show the number of H- vessels/mm² of area occupied by the vessel sub-type in 6- and 12-week old animals. (C) and (D) show the number of L- vessels/mm² of area occupied by the vessel sub-type in 6- and 12-week old animals. Graphs show mean \pm SEM (n=5 animals, 4 bones analysed control and 5 bones analysed ZOL), Student t-test, * $p < 0.05$, ** $p < 0.01$ and ns is non-significant

Irrespective of age, the H-vessels were longer than the L-vessels in both the PBS ($p < 0.0001$ and $p = 0.0877$ 6- and 12-week old respectively) and the ZOL group ($p < 0.0001$ for both 6- and 12-week old). However, it was interesting to notice that whereas treatment with ZOL did not cause change in the average length of H- or L-vessels in young animals ($p = 0.4088$ and $p = 0.4357$ H- and L-vessels respectively), the vessels in mature mice receiving a single dose of ZOL appear to be shorter compared to the control, even though this difference did not reach statistical significance for the H-vessels analysis ($p = 0.0926$ and $p = 0.0004$ H- and L-vessels respectively)(figure 5.14).

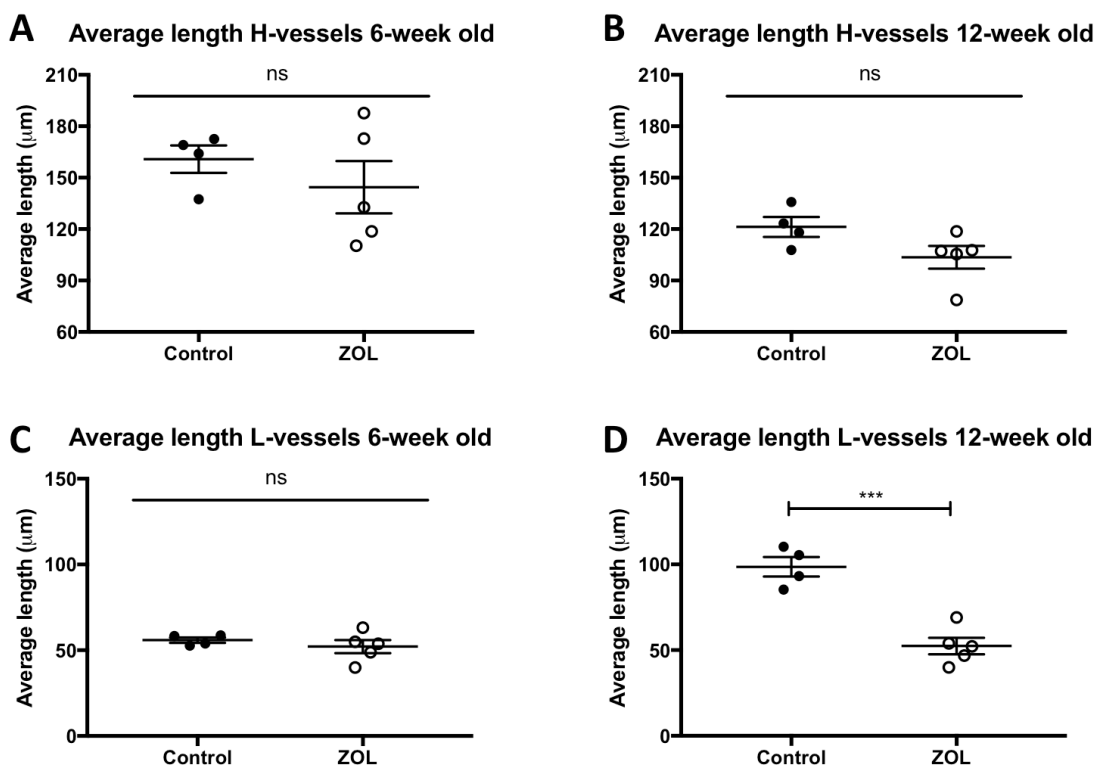


Figure 5.14 Average length of the H- and L-vessels sub-types

A) and (B) average length of H-vessels of 6- and 12-week old animals respectively. (C) and (D) average length of L-vessels of 6- and 12-week old animals respectively. Graphs show mean \pm SEM (n=5 animals, 4 bones analysed control and 5 bones analysed ZOL), Student t-test, *** $p < 0.001$ and ns is non-significant

These data indicate that regardless of age or ZOL treatment, there was no difference in the total area of bone analysed. Unexpectedly, ZOL treatment caused changes in the organisation of the microvasculature in mature but not young animals, which corresponded to the ZOL-induced change in bone structure. In fact, it appears that a single dose of ZOL is sufficient to modify the distribution of the different vessels subtypes in mature animals, increasing the area containing L-vessels at the expense of the area of bone marrow occupied by H-vessels. Moreover, ZOL causes an increase in the number of vessels in the mature animals even though these vessels appear to be shorter than the ones detected in the control animals.

5.5.2.2 ZOL treatment does not cause alteration in CD31 vessels

CD31 is a marker associated with established, mature microvasculature in the bone microenvironment and this marker decreases with the aging process [97]. To investigate whether ZOL treatment changes the expression of the endothelial marker CD31, frozen sections of tibia and femur were stained for both Endomucin and CD31 using the immunofluorescent protocol described in section 2.13.1 (figure 5.15).

The first parameter analysed was the area of bone marrow, imaged using the Zeiss LSM880 AiryScan Confocal microscope (figure 5.16). Regardless of age, no difference was discovered between treated and control groups ($p=0.7304$ for 6-week old animals and $p=0.2638$ for the 12-week old animals). Treatment with ZOL did not modify the expression of Endomucin when compared to the control group in neither of the age groups ($p=0.9407$ and $p=0.8770$ 6- and 12-week old mice respectively) (figure 5.16). Moreover, the overall expression of CD31 and the percentage of vessels expressing both endothelial markers were not altered between drug- and PBS-treated groups (CD31: $p=0.3151$ and $p=0.3981$ 6- and 12-week old mice respectively; CD31/Endomucin: $p=0.93559$ and $p=0.5123$) (figure 5.16).

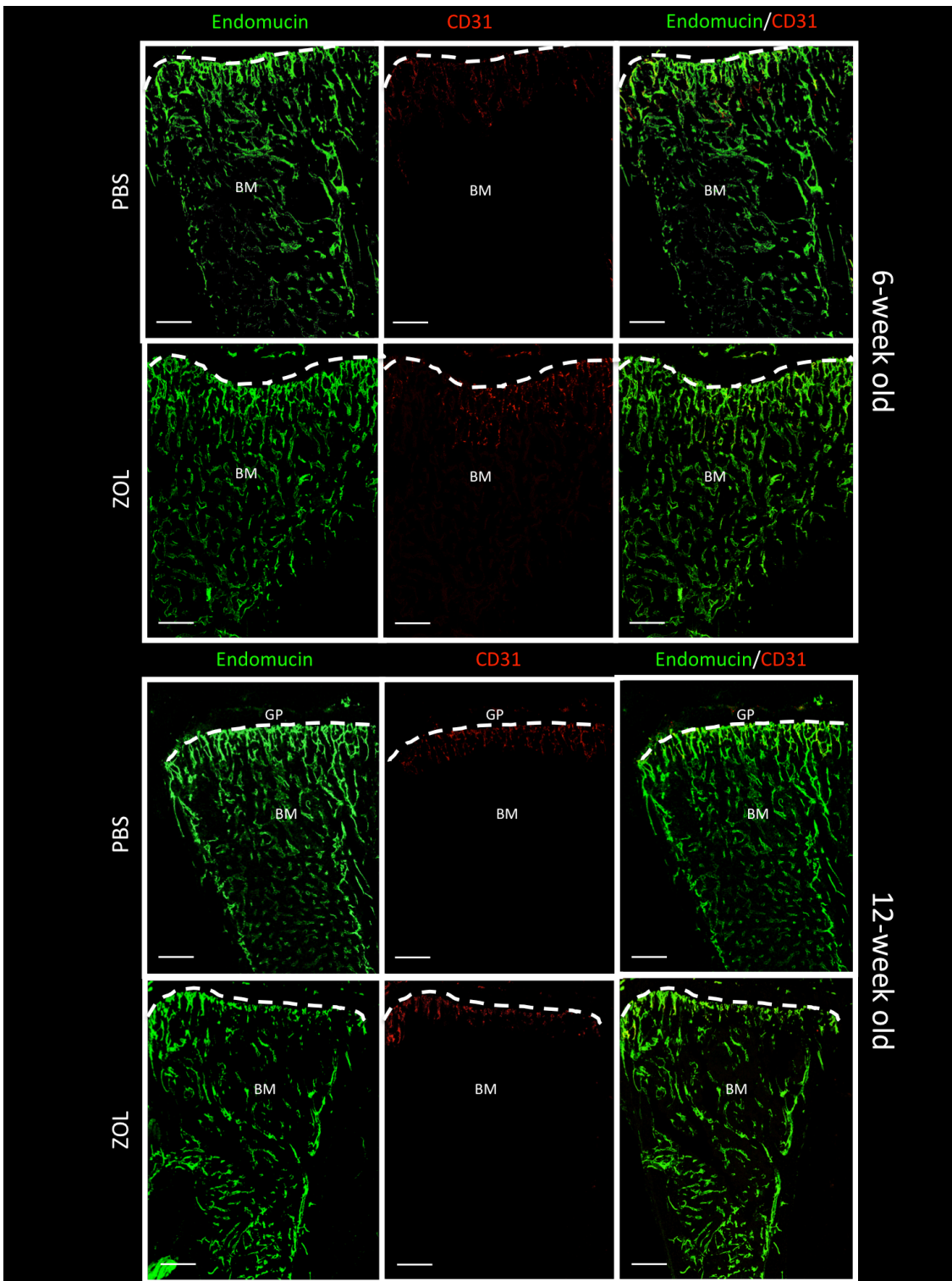


Figure 5.15 Representative image of the effect of ZOL treatment on CD31+ vessels

Immunofluorescent staining against CD31 and Endomucin performed on 30 μ m tibia section of 6-week old (A) and 12-week old (B) animals receiving PBS or ZOL. Green=Endomucin and red=CD31. Scale bar 200 μ m.

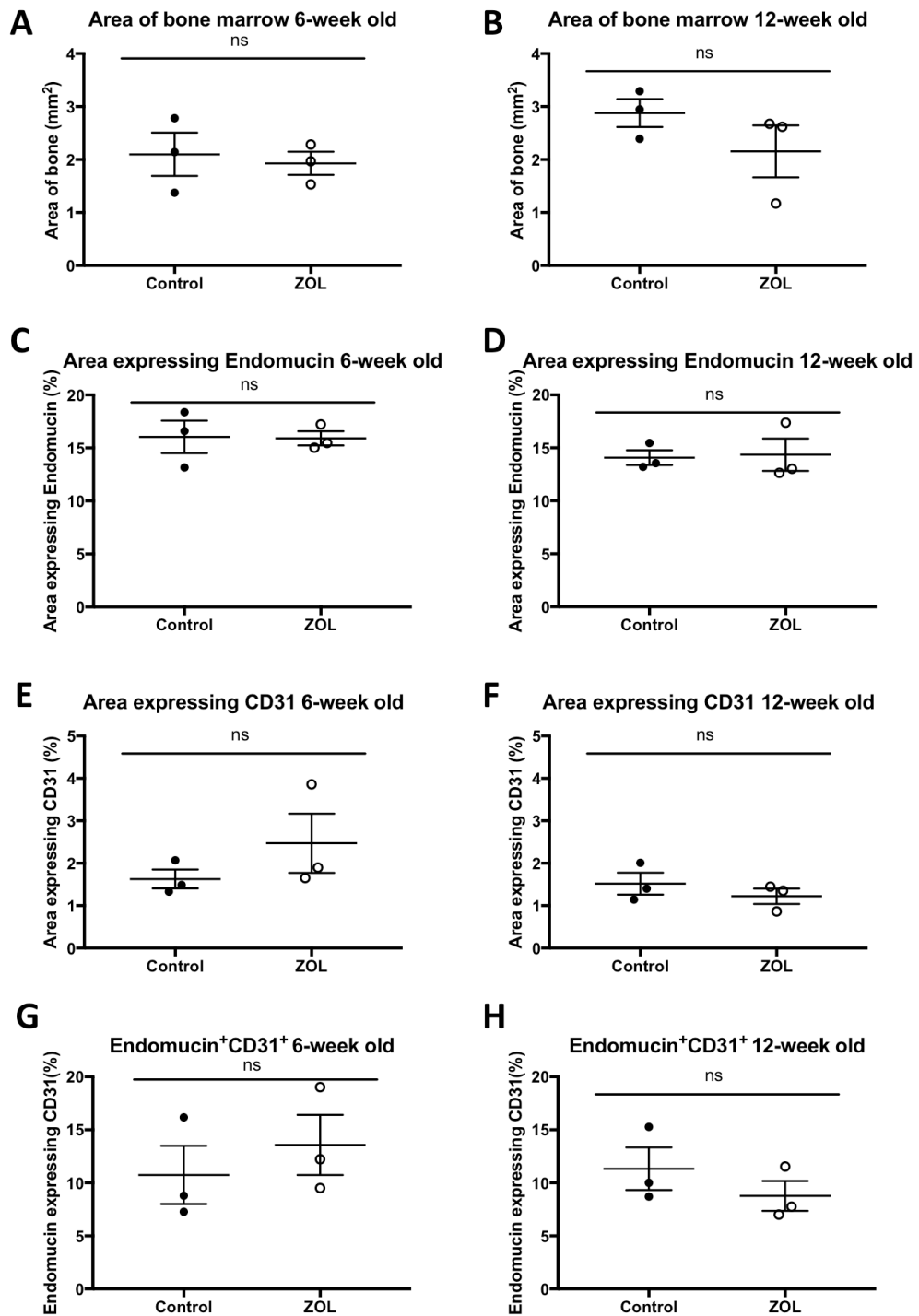


Figure 5.16 Quantification of immunofluorescent staining against CD31

A) and (B) Area of bone marrow analysed in the two different ages. C) and (D) show the overall expression of Endomucin in 6- and 12-week old animals respectively while in (E) and (F) the expression of CD31 is shown. (G) Percentage of Endomucin⁺ vessels that also express CD31 in 6- and 12-week old animals (H). Graphs show mean \pm SEM (n=5 animals, 3 bones analysed/group), Student t-test, ns is non-significant

As expected, no differences were detected in the number of CD31⁺ vessels/mm² counted in the total bone marrow surface analysed, nor in the area solely occupied by this vessel sub-type, in animals treated with ZOL, compared to animals receiving PBS (total bone marrow: $p=0.95781$ and $p=0.7835$ 6- and 12-week old mice respectively; area occupied by CD31⁺ vessels: $p=0.6842$ and $p=0.8110$)(figure 5.14). The average length of this vessel sub-type was not modified by the single dose of ZOL in the 6-week old animals ($p=0.2811$) and unexpectedly there was also no response in the 12-week old animals ($p=0.6585$)(figure 5.17).

These results show that the number of CD31 expressing vessels was unaffected by a single dose of the anti-resorptive agent Zolendronic acid compared to the control group. This was in contrast to the ZOL-induced changes in bone microarchitecture and total vessel observed at the same time point.

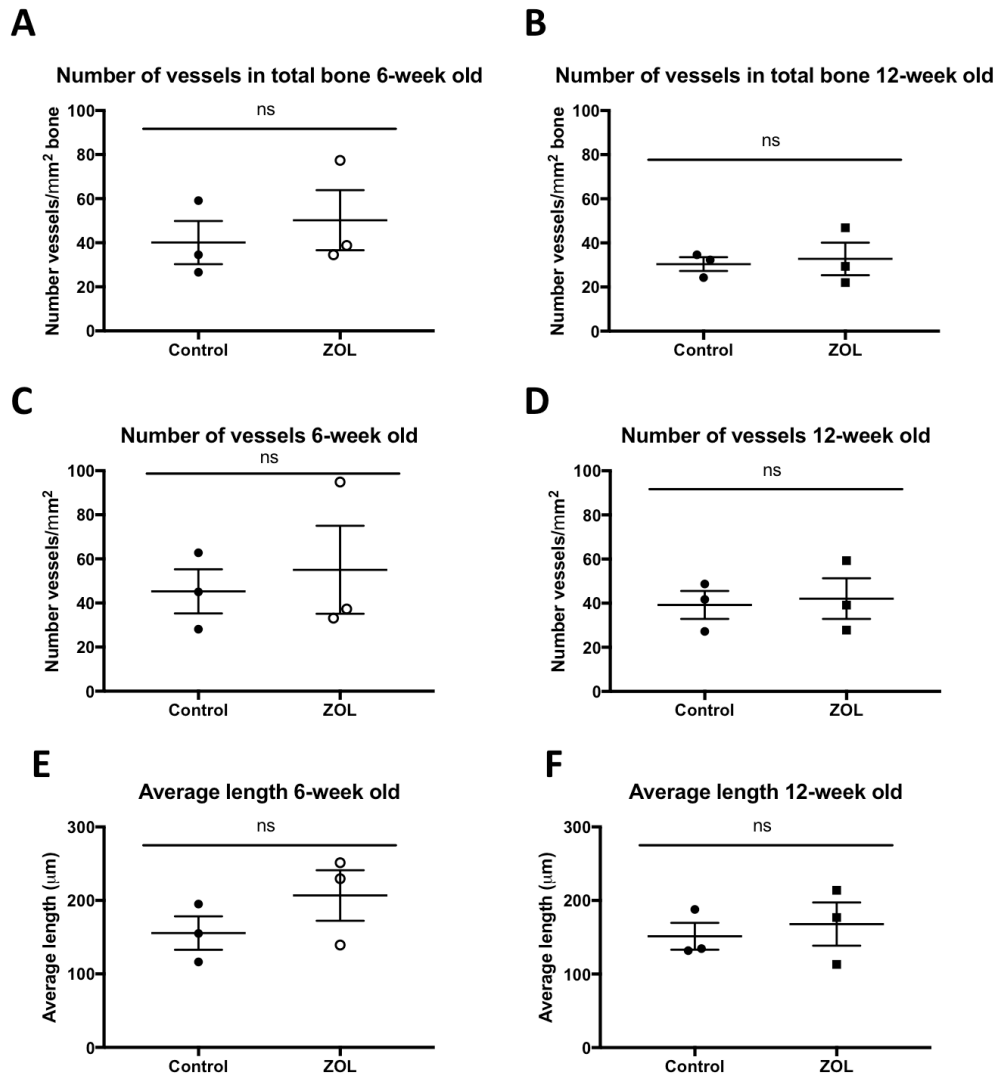


Figure 5.17 Number and average length of CD31⁺ vessels measured with Aperio ImageScope

A) and (B) show the number of CD31⁺ vessels/mm² of total bone in 6- and 12-week old. (C) and (D) show the number of CD31⁺ vessels/mm² of area occupied by the vessel sub-type in 6- and 12-week old animals. (E) and (F) display the average length of CD31⁺ vessels. Graphs show mean ± SEM, (n=5 animals, 3 bones analysed/group), Student t-test, ns is non-significant

5.5.2.3 Newly formed CD34⁺ vessels are not influenced by the ZOL treatment

To detect changes in the newly formed microvasculature of the bone microenvironment, tibia sections were stained using the immunofluorescent protocol described in section 2.13.1, with antibodies against CD34.

The quantification of tissue slides stained for Endomucin and CD34 was performed using ImageJ and Aperio ImageScope softwares on images captured with the Zeiss LSM880 AiryScan Confocal microscope. The area analysed was approximately 2.0 mm² for the young animals (2.05±0.39 for the PBS group and 1.97±0.31 for the ZOL treated animals) and 2.5mm² for the mature animals (2.76±0.24 PBS group and 2.44±0.08 ZOL group, figure 5.18 and 5.19). Regardless of age, the overall expression of Endomucin was not affected by the single dose of ZOL ($p=0.5977$ and $p=0.3038$ for 6- and 12-week old respectively, figure 5.18 and 5.19). Likewise, the expression of CD34 and percentage of Endomucin⁺ and CD34⁺ vessels were comparable between groups (CD34: $p=0.9076$ and $p=0.1120$; CD34/Endomucin: $p=0.4126$ and $p=0.1017$ for 6- and 12-week old respectively, figure 5.18 and 5.19). Irrespective of age and treatment, no differences were detected in the number or length of CD34⁺ vessels (number of CD34⁺ vessels/mm²: $p=0.7206$ and $p=0.6708$; length of CD34⁺ vessels: $p=0.2631$ and $p=0.3871$ for 6- and 12-week old respectively, figure 5.20).

Taken together, these data show that a single dose of ZOL does not alter the formation of new microvessels within the bone microenvironment within the 5-day time frame.

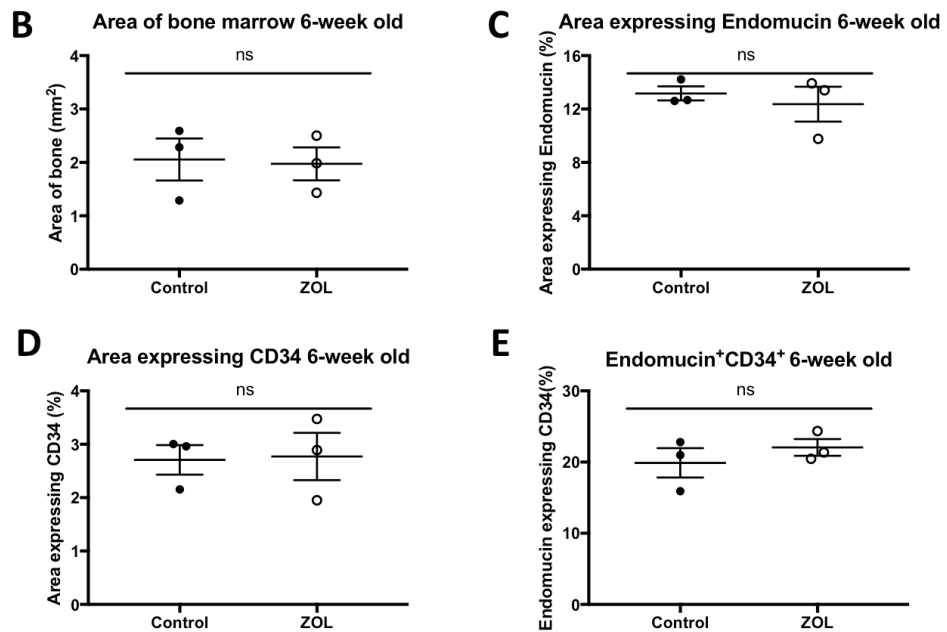
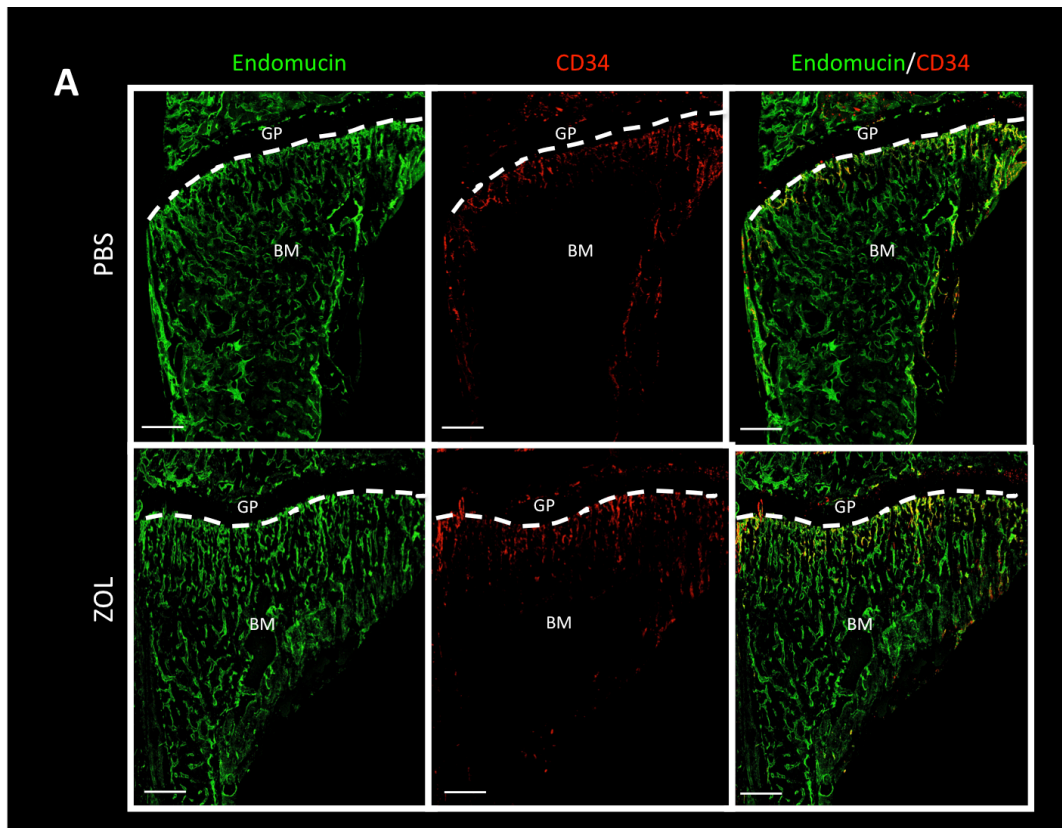


Figure 5.18 Effect of ZOL treatment on CD34+ vessels of young animals

A) Immunofluorescent staining against CD34 and Endomucin performed on 30µm tibia section of 6-week old animals receiving PBS or ZOL. Green=Endomucin and red=CD34. (B) Area of bone marrow analysed. (C) Shows the overall expression of Endomucin while in (D) and (E) the expression of CD34 and the percentage of Endomucin⁺ vessels that are also expressing CD31 is shown. Graphs show mean ± SEM, (n=5 animals, 3 bones analysed/group), Student t-test, ns is non-significant. Scale bar 200µm.

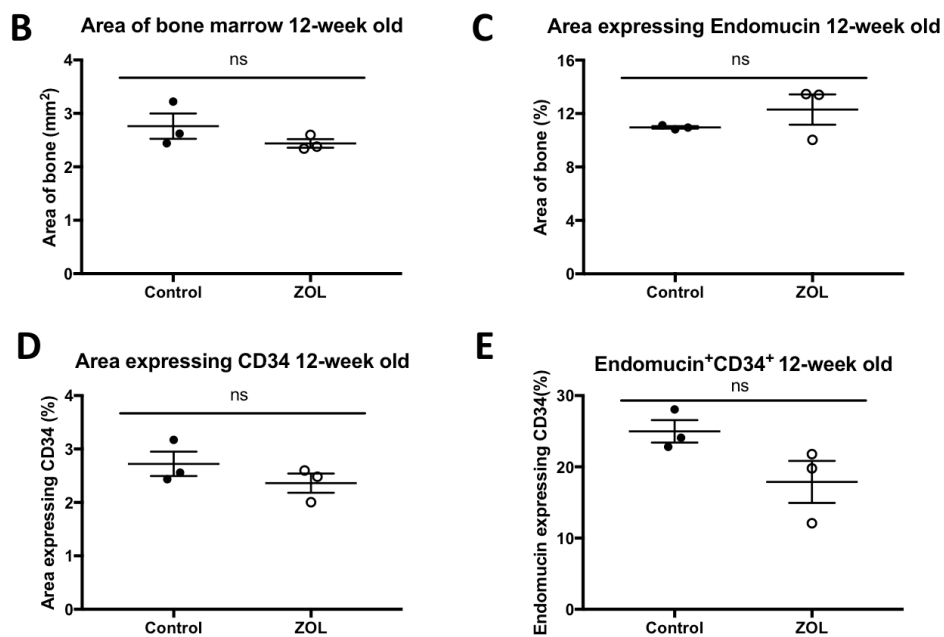
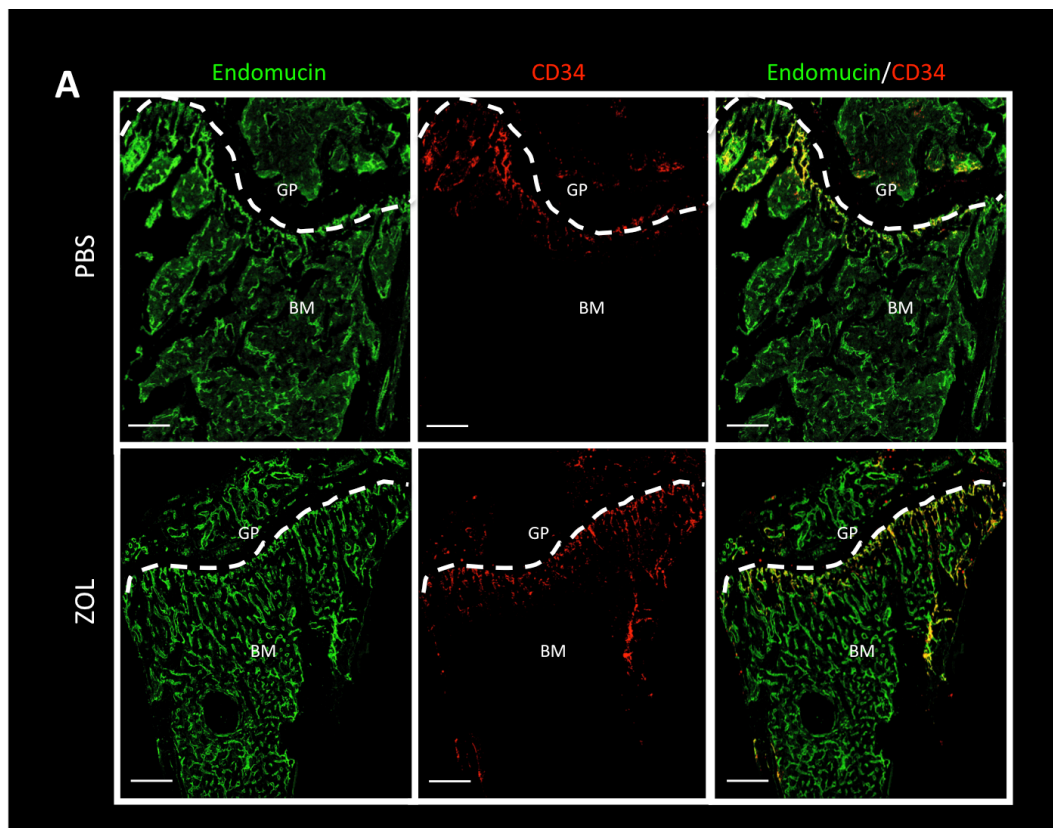


Figure 5.19 Effect of ZOL treatment on CD34+ vessels of mature animals

A) Immunofluorescent staining against CD34 and Endomucin performed on 30µm tibia section of 12-week old animals receiving PBS or ZOL. Green=Endomucin and red=CD34. (B) Area of bone marrow analysed. (C) Shows the overall expression of Endomucin while in (D) and (E) the expression of CD34 and the percentage of Endomucin⁺ vessels that are also expressing CD31 is shown. Graphs show mean ± SEM, Student t-test, (n=5 animals, 3 bones analysed/group), ns is non-significant. Scale bar 200µm.

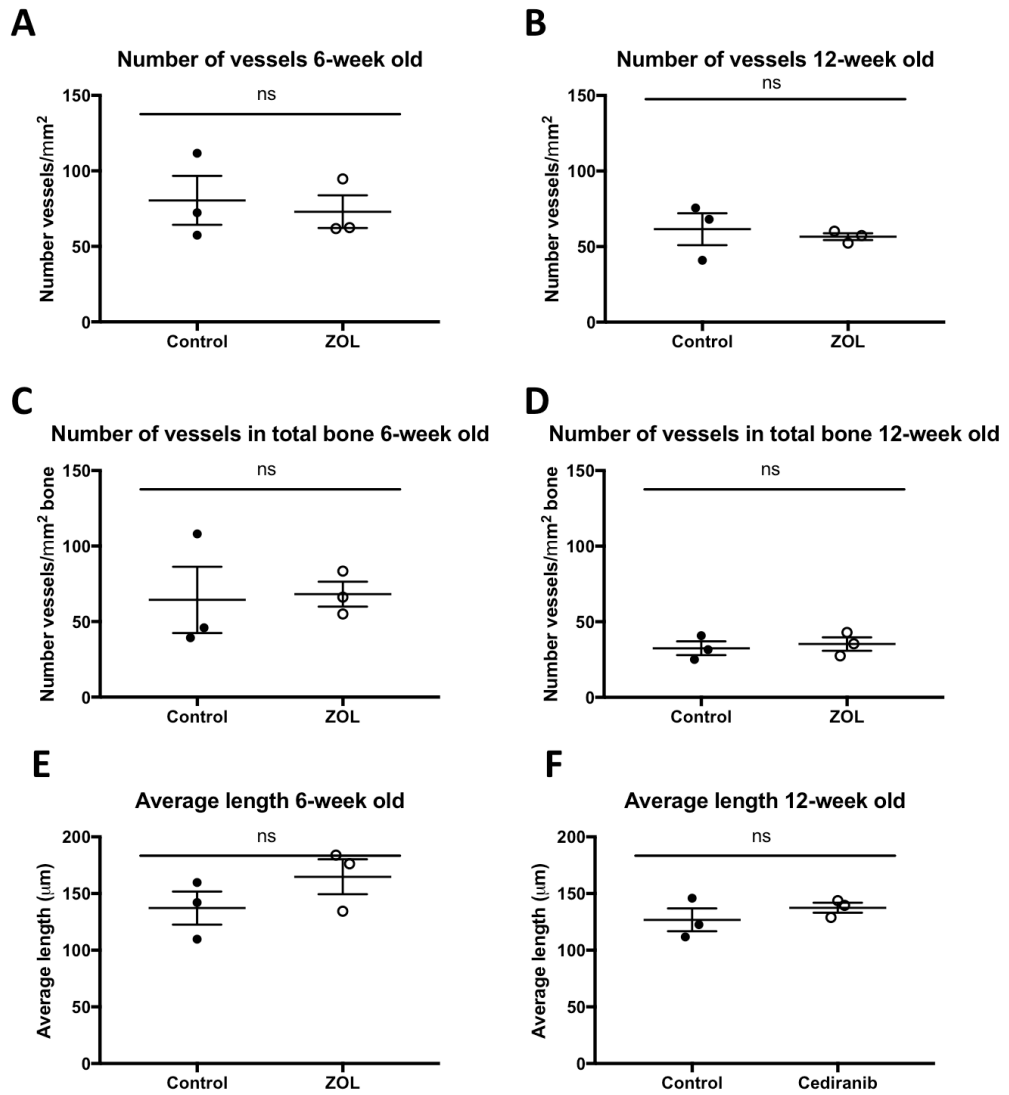


Figure 5.20 Number and average length of CD34+ vessels

A) and (B) show the number of CD34⁺ vessels/mm² of total bone in 6- and 12-week old. (C) and (D) show the number of CD34⁺ vessels/mm² of area occupied by the vessel sub-type in 6- and 12-week old animals. (E) and (F) display the average length of CD34⁺ vessels. Graphs show mean \pm SEM, (n=5 animals, 3 bones analysed/group), Student t-test, ns is non-significant

5.5.3 ZOL treatment and the homing of breast cancer cells in the bone microenvironment

To establish whether treatment with a single dose of ZOL altered the pattern of homing of breast cancer cells to the metastatic niche, two-photon microscopy on femora was performed to determine if there were variation in the number and/or location of the tumour cells between the control and the treated group. MDA-MB-231-NW1-Luc2 breast cancer cells were labelled with the membrane dye Vybrant-CM-Dil were injected i.c. in immunocompromised mice, two days post injection the animals were treated with ZOL or control and culled five days after. Hind limbs were collected for *ex vivo* analyses.

As previously discussed in section 3.5.6, the concentration of the lipophilic dye used to label the tumour cells caused a cytotoxic effect reducing considerably the numbers of bones in which we could detect tumour cells. In the 6-week old group only two bones out of the three analysed for the control group and one out of three of the treated group contained tumour cells in the trabecular region of the bone (ROI1), no cells were detected in the growth plate area (ROI2). The injection in the 12-week old animals were more successful, with four femora out of five in the control group and two out of four of the ZOL group having detectable tumour cells in ROI1, while only one bone/group had detectable tumour cells in ROI2. As shown in figure 5.21, no difference in the number of cells located in the bone marrow was found between the different groups ($p=0.7835$ and $p=0.5436$ for ROI1 of 6- and 12-week old respectively). The low number of cells homing to the bone, limited the analysis that could be performed.

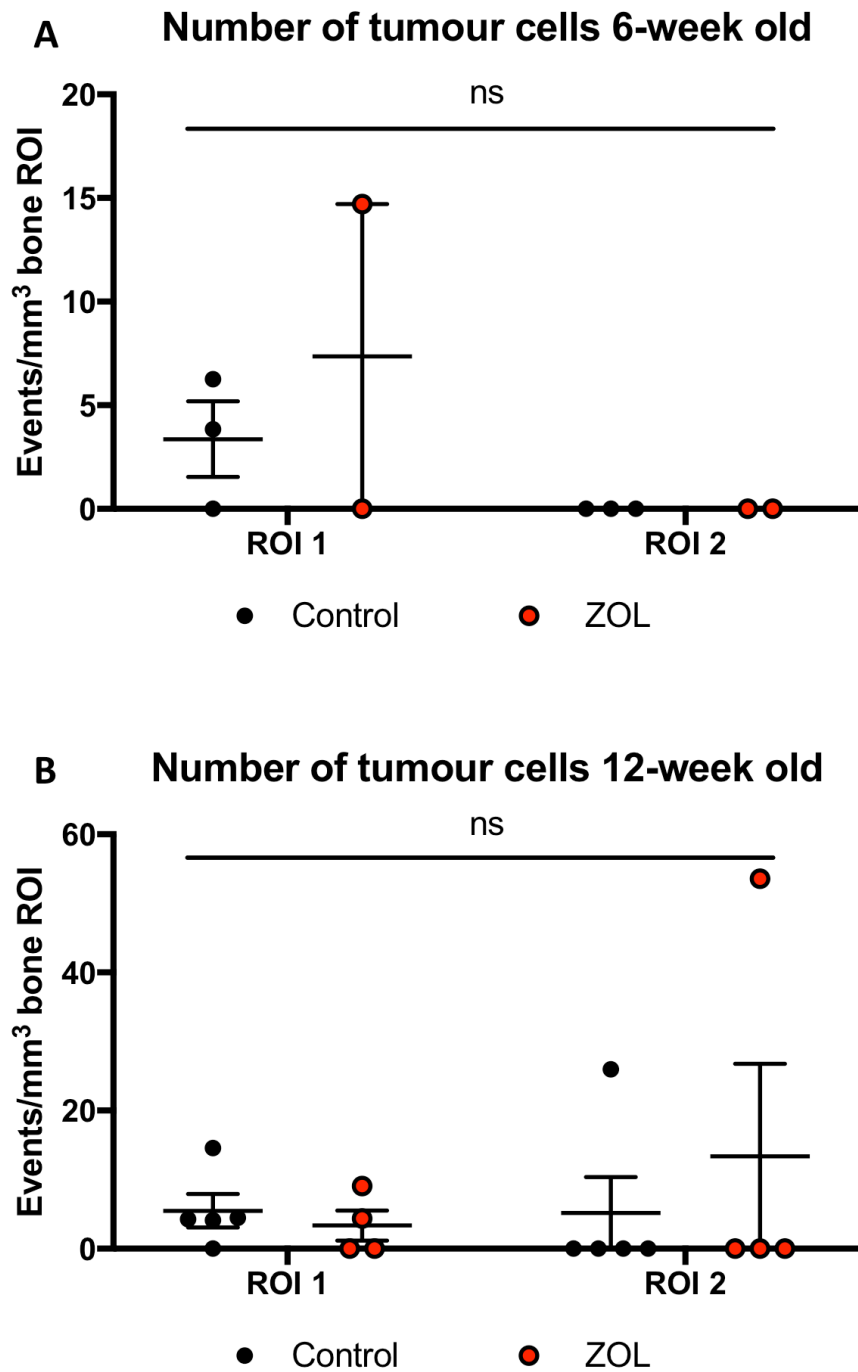


Figure 5.21 Homing of MDA-MD-231-NW1-Luc2 cells to bone in young and mature animals after the treatment with ZOL

Graph shows the number of MDA-MB-231-NW1-Luc2 cells detected in bone in 6- (A) and 12-week old mice (B) 5 days after i.c. injection of 0.75×10^5 tumour cells. Graphs show mean \pm SEM, (n=5 animals/group, 6-week old 3 bones analysed control and 2 bones analysed ZOL, 12-week old 5 bones analysed control and 4 bones analysed ZOL). Ns is non-significant.

5.5.4 ZOL modification of expression of TSP-1

To investigate whether the administration of a single dose of ZOL altered the expression of the dormancy-supporting Thrombospondin, 30µm thick sections of tibiae were stained against Endomucin and TSP-1 following the immunofluorescent protocol described in section 2.13.1.

Images of the bone marrow were acquired using the Zeiss LSM880 AiryScan Confocal microscope and an area of approximately 2.0mm² was analysed for the young animals (1.907±0.4540 PBS control and 1.764±0.5102 ZOL treated animals, $p=0.8439$) and 2.8mm² for the mature mice (2.885±0.1328 PBS control and 2.793±0.3182 ZOL treated animals, $p=0.8035$)(figure 5.22 and 5.23). Interestingly, ZOL increased the expression of TSP-1 in 6-week old mice even though this change was did not reach statistical significance ($p=0.0762$), but no alterations were detected in the 12-week old animals ($p=0.2929$)(figure 5.22 and 5.23). Moreover, there was no difference in the number of megakaryocytes counted with ImageJ software between animals receiving the anti-resorptive drug or the vehicle control ($p=0.9164$ and $p=0.3780$ for young and mature animals) and there were no changes between the groups when the number of megakaryocytes was normalised on the area analysed ($p=0.5402$ and $p=0.2295$ for young and mature animals)(figure 5.22 and 5.23).

The data here presented suggest that ZOL does not affect the expression of TSP-1 or the number of Megakaryocytes located in the bone marrow.

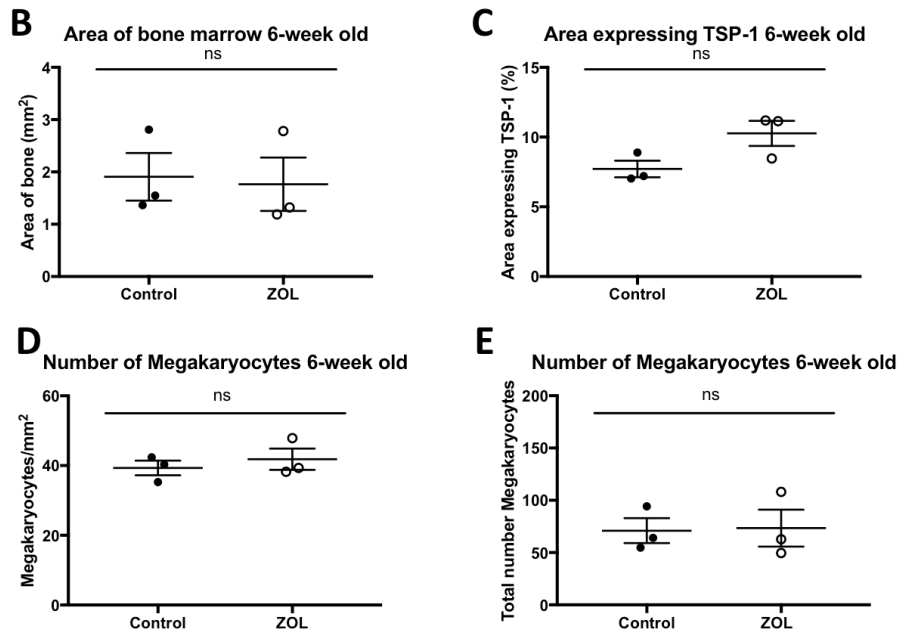
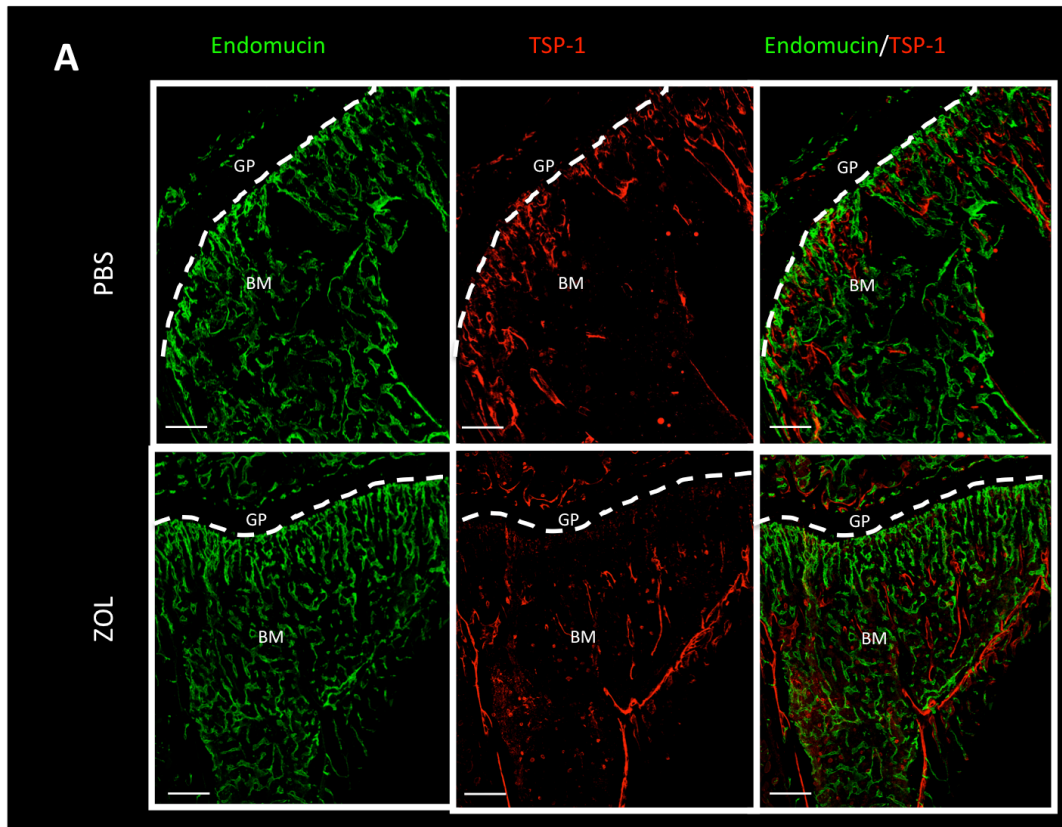


Figure 5.22 Effect of ZOL treatment on TSP-1 expression in 6-week old animal

(A) Immunofluorescent staining against TSP and Endomucin performed on 30µm tibia section of 6-week old animals receiving PBS or ZOL. (A) Area of bone marrow analysed. (B) Percentage area of bone marrow expressing TSP=1. (D) number of Megakaryocytes/mm² and overall number (D). Graphs show mean ± SEM (n=5 animals, 3 bones analysed/group), Student t-test, ns is non-significant. Green=Endomucin and red=TSP-1. Scale bar 200µm.

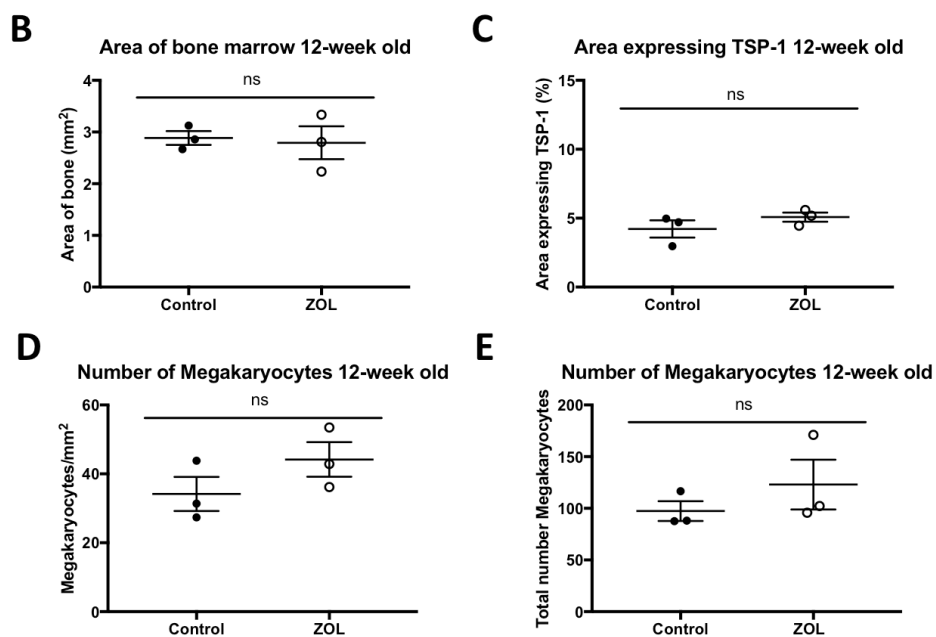
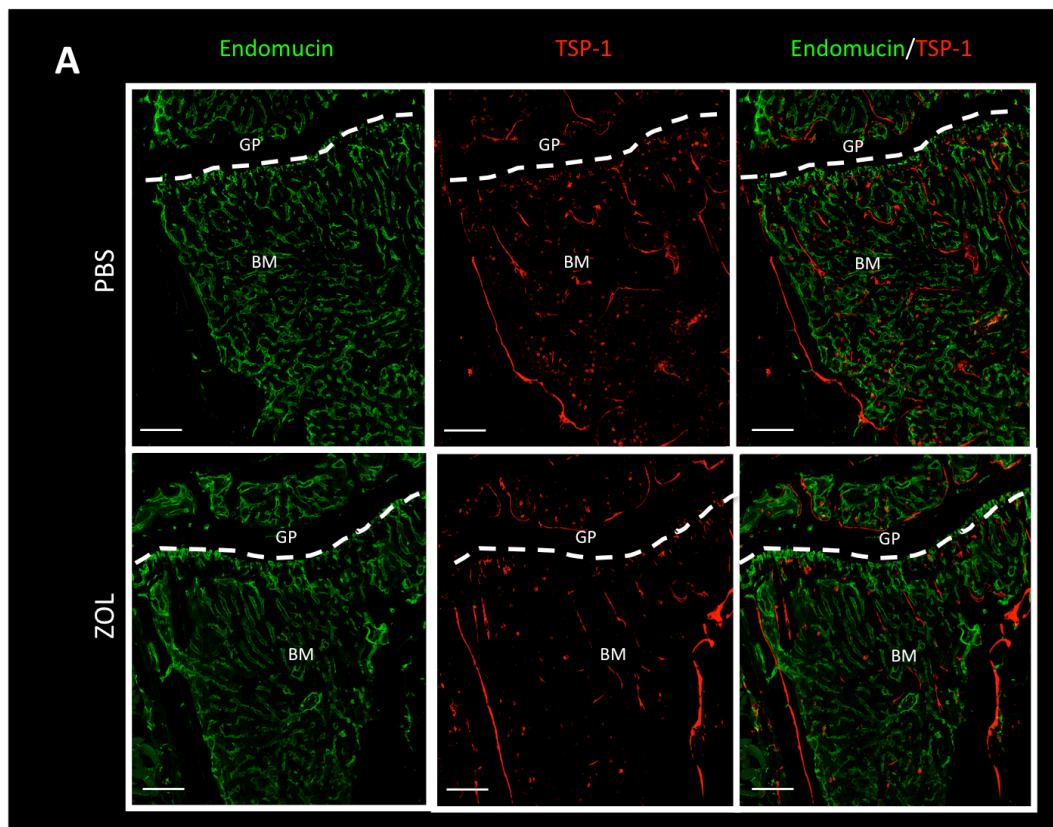


Figure 5.23 Effect of ZOL treatment on TSP-1 expression in 12-week old animal

(A) Immunofluorescent staining against TSP and Endomucin performed on 30µm tibia section of 12-week old animals receiving PBS or ZOL. (A) Area of bone marrow analysed. (B) Percentage area of bone marrow expressing TSP=1. (D) Number of Megakaryocytes/mm² and overall number (D). Graphs show mean ± SEM (n=5 animals, 3 bones analysed/group), Student t-test, ns is non-significant. Green=Endomucin and red=TSP-1. Scale bar 200µm.

5.6 Discussion

The main objective of the work described in this chapter was to investigate whether the administration of a single, clinical relevant, dose of ZOL affects the bone microenvironment, with particular attention given to the perivascular component of the niche, comparing young and mature animal models. Differences in the bone structure between animals treated with ZOL and animals receiving the vehicle control were measured using μ CT. Changes in the number of osteoprogenitors and megakaryocytes detected and in the pattern of expression of Endomucin⁺, CD31⁺ and CD34⁺ vessels and the dormancy supporting molecule Thrombospondin-1 were assessed on tissue sections stained with specific antibodies immunofluorescent protocols. As anticipated, young animals displayed a considerable change in the bone structure, while the effect of the anti-resorptive drug on the structure of mature animals was less extensive. Surprisingly, the alterations in the bone structure of young animals did not result in corresponding alterations of the microvascular component of the niche. In fact, none of the microvasculature markers investigated were altered by ZOL treatment in the young animals, while, unexpectedly, the organisation of Endomucin⁺ vessels was modified in the mature animals.

It is known that the treatment with ZOL causes a reduction in number and activity of both bone-resorbing osteoclasts and bone-forming osteoblasts during the early days of administration. These effects were detected as early as three days after the administration of a single dose of ZOL and the modification of the bone cell population resulted in an increase in the trabecular volume in 6-week old mice [118]. In agreement with this, in the current study I found that the bone of young animals treated with ZOL had a significant increase in trabecular volume compared to the control group. Even though an increase was also present in the mature animal model, the changes in the bone structure did not reach a statistical significance, probably due to the lower level of bone turnover in this group.

The increased trabecular volume could have been influenced by the expansion of the proteoglycan-rich extra-cellular matrix detected by Toliudine blue staining. In the physiological bone development, the chondrocytes residing in the growth plate area produce high amounts of this matrix and this process is followed by the remodelling of

ossificated matrix by osteoblasts and osteoclasts [241]. Furthermore, the reorganization of the growth plate area of the bone resulted in a considerable decrease in the presence of osteoprogenitor cells (figure 5.5-8). It was interesting to notice that the number of Osterix⁺ cells /mm² was affected by treatment with ZOL only in the mature animals. Intriguingly, it has been shown that ZOL also modifies the number of HSCs and promotes differentiation towards lymphoid progenitors and expansion of myeloid progenitors in both immunocompetent and immunocompromised animal models after a short period of time (3-5 days after administration of a single clinically relevant dose of ZOL) [134].

The accumulation of extra-cellular matrix and the redistribution of the osteoprogenitors in the modified microenvironment suggest that ZOL treatment could influence the structure of the microvasculature in the metaphysis of the bone and therefore affect homing of tumour cells to the bone microenvironment. The major physical effect of ZOL treatment on the bone marrow structure and enlargement of the proteoglycan-rich area were detected in young animals, while in mature animals these changes were marginal. It was expected therefore to detect substantial modification of the microvascular structure of the 6-week old animals and only a minimal change, if any, in the 12-week old mice. Surprisingly, analysing the expression and pattern of the Endomucin⁺ vessels revealed contrasting data. The microvasculature of young animals was not altered by ZOL, while most of the parameters analysed for the mature animals were significantly different between the treated and control group. The area of bone marrow analysed has been identified to be evenly distributed between H- and L-vessel content, while in 12-week old mice the L-vessels component of the microvasculature occupied most of the bone marrow area. Moreover, the administration of ZOL caused an increase in the total number of vessels/mm² and in particular the number of L-vessels was greater in ZOL treated animals compared with the animals receiving the control vehicle. In both age group of mice the average length of H- and L-vessels decreased after the single dose of ZOL, but only in the mature animals was this modification statistically significant.

Since the Endomucin⁺ microvasculature network is highly interconnected with the CD31⁺ and CD34⁺ vessels, it was predicted that ZOL treatment also influenced these

vessel sub-types. Surprisingly, irrespective of age, the CD31⁺ and CD34⁺ vessels in bone were not affected by the treatment with the anti-resorptive drug, despite the effects on bone structure and growth plate area.

It has already been suggested that ZOL has an anti-angiogenic activity, but most of these studies have investigated this action of ZOL. Independent *in vitro* studies performed by Wood *et al.* and Misso *et al.* described the inhibitory effect of ZOL in the proliferation, migration and tubule formation of HUVEC cells [135], [136]. Furthermore, both groups demonstrated that ZOL has an anti-angiogenic effect *in vivo*. Wood's group observed reduction of angiogenesis in implants with or without growth factor (VEGF and basic fibroblast growth factor (bFGF)) in animals treated with repeated administration of ZOL, while Misso's group detected a reduction in angiogenesis in a matrigel plug assay. Moreover, the anti-angiogenic effect of ZOL was investigated in the clinical setting. It has been reported that intermittent treatment (once weekly for 4 weeks) with low-dose (1mg) ZOL, caused a reduction in VEGF-circulating levels that persisted even after the treatment with ZOL returned to the normal administration of 4mg ZOL/monthly [138]. These studies therefore demonstrated the action of ZOL in interfering either directly or indirectly with pathways involving angiogenesis though not in bone.

It has been suggested that ZOL inhibits the differentiation of endothelial progenitor cells (EPC) when administered at low concentrations, while at higher doses it also induces apoptosis in the differentiated EPC [137]. Ottewell *et al.* described that, in subcutaneous tumours, administration of ZOL alone was not sufficient to suppress the formation of new vasculature positive for the endothelial marker CD34, but that the combination therapy of ZOL and Doxorubicin (DOX) inhibited the angiogenic process in the subcutaneous tumours [131]. Furthermore, it has been shown that repeated ZOL treatment (once a week for 6 weeks) alone does not affect presence the CD31⁺ and CD34⁺ vessels in mammary gland tumours, whilst this changes in both these markers were detected when ZOL was administered following DOX treatment. However, the effect on the bone microvasculature was not investigated [132].

Regarding the effect of ZOL on the microvasculature in bone, there are few studies reported in the current literature, but they reflect the alteration on the shape of the

microvessels that has been described in this chapter. Soki and colleagues reported that ZOL treatment modifies the microvasculature network in bone of immunocompetent young and adult male mice. These vessels appeared fragmented and more numerous but the total volume of vasculature in bone was not altered by the administration twice weekly for 4 weeks of 200µg/kg of the anti-resorptive drug [119]. Data published in 2017 by Ubellacker and colleagues indicated modification of the microvasculature network in bone in response to ZOL; vessels appeared to have lost the characteristic sinusoidal pattern and Endomucin⁺ vessels were shorter after administration of a single dose of ZOL in young (6/7-weeks old) animals [134].

The anti-angiogenic effect of bisphosphonates, and in particular ZOL, has been reported also from clinical data and it has been suggested that this could possibly increase the anti-tumour action of ZOL both through the inhibition of bone-resorbing osteoclasts and the anti-angiogenic effects, resulting in a reduction of tumour growth [127]. The anti-tumour effect of ZOL treatment has been extensively studied, both *in vitro*, *in vivo* and in the clinical settings [120]. Although treatment with ZOL has been reported to reduce the tumour burden both inside and outside the bone microenvironment, a combination therapy with repeated dosing of DOX and ZOL was much more effective in tumour bearing mice [126], [127], [131], [132]. When treating ER⁺ tumours, ZOL administration has not been shown to be effective in the reduction of the tumour growth in soft tissue, however it reduced the dissemination of tumour cells to bone and the development of bone metastasis in an *in vivo* model [231]. Although, due to the cytotoxic effect of the lipophilic dye used in this chapter, it was not possible to compare the number of tumour cells located in the bone marrow, in groups of animals receiving the vehicle control or ZOL, an *in vivo* study performed in our laboratory demonstrated that for triple negative breast cancer cells ZOL administration did not alter the overall number of cells in the bone, but their location within the bone marrow was altered quantified by two-photon microscopy [118]. In similar study of prostate cancer bone metastasis, Wang and colleagues described that ZOL administration prevent tumour growth but did not affect the overall number of cancer cells homing to the bone microenvironment [242]. Since tumour growth in bone is prevented or slowed down without detecting changes in the overall number of

cancer cells seeding in the fertile bone microenvironment, could indicate that tumour cells remain dormant in the bone for longer period of time. As described in chapter 4, Thrombospondin-1 is one of the molecules suggested to support tumour cells dormancy [35] and in the *in vivo* study presented in this Chapter the level of TSP-1 in bone appeared to be increased by ZOL treatment in young animals.

One peculiarity of the anti-tumour effect of ZOL treatment is that it has been shown to have a differential effect between pre- and post-menopausal status. Animals mimicking the post-menopausal (ovariectomy) status benefit from ZOL administration compared to animals mimicking the pre-menopausal (sham) status. It has been shown that ZOL prevented tumour growth in ovariectomised animals despite disseminated tumour cells were detected in the tumour microenvironment [243]. The variance in the success of ZOL treatment in the early stages of breast cancer was also identified in the clinical trial AZURE, where it has been reported that patients with established menopause showed improvement in the disease-free and overall survival compared to patients in pre-menopausal settings [146], [147], [244]. An important point highlighted by the AZURE trial was that there were no differences in response between ER+ and ER- tumours, indicating that the microenvironment plays a key role. The mechanisms driving these differential effects remain to be established. To elucidate to what extent the bone microenvironment components are involved, an interesting clinical trial, ZOLMENO, is ongoing which will compare the bone microenvironment in pre- and post-menopausal breast cancer patient before and after a single dose of ZOL.

Taken together, the data presented in this chapter describe the differentials effect of ZOL on the bone microenvironment of young and mature animal models. ZOL treatment modifies the bone structure of young animals to a greater extent, while the organisation of the microvasculature network of the bone microenvironment is altered in the mature animals. Further investigation is needed to better understand why the beneficial effect of ZOL treatment in early breast cancer is restricted to women with established menopause.

The data presented in the current Chapter suggests that changes in the perivascular niche is a promising research area to pursue to improve the knowledge on the potential mechanisms of action and may identify how the anti-resorptive drug has

differential response, with the ultimately aim of improving therapies for breast cancer bone metastasis by targeting multiple components of the metastatic niche.

Chapter 6

Therapeutic modification of the microvasculature and its effect on the bone metastatic niche

6.1 Summary

Angiogenesis is a fundamental process required for the development and progression of tumours and therefore pathways involved in regulating angiogenesis have been explored as targets in the development of new anti-tumour therapies. Anti-VEGF therapies, such as anti-VEGF antibodies (e.g. Bevacizumab) VEGF tyrosine kinase receptor inhibitors (Cabozantinib and Cediranib), have proven successful in the treatment of a range of solid tumours, including breast cancer. Cediranib in particular is one promising candidate drug for the treatment of breast cancer and it is the focus of multiple clinical studies investigating its potential therapeutic effect in different stages of cancer development. Currently, research is focusing also on the upstream the VEGF pathway targeting HIF-1 α . Deferoxamine mesylate (DFM) is an iron chelator that has been shown to be an effective HIF-1 α enhancer.

The anti- and pro-angiogenic effect of these drugs has been extensively evaluated both *in vitro* and *in vivo*, however their actions on multiple components of the bone marrow microenvironment have not been fully elucidated. It is known that angiogenesis and osteogenesis are tightly associated and the hypothesis to be tested in this chapter is that pharmacological induced decrease (Cediranib) or increase (Deferoxamine mesylate) of the microvascular activity resulted in a modification of the bone structure, in particular in the trabecular region of bone where breast cancer cells preferentially home.

6.2 Introduction

The microenvironment in which metastasis occur is complex containing multiple cell populations involved in the maintenance of the dormancy of DTC or in the progression of overt tumours. Currently several therapies strategies are available for the treatment of advanced breast cancer, hormone receptor positive cancers usually receive endocrine treatments while in the case of oestrogen-negative receptor (or when endocrine treatments has failed) chemotherapy is the most common option, bisphosphonates have proved to be effective in both ER+ and ER- breast cancers [112], [245]. Increasingly interest in other possible targets in the microenvironment has led to the development of anti-angiogenic therapies, including the anti-VEGF (Bevacizumab) and VEGF tyrosine kinase receptor inhibitor (Cabozantinib and Cediranib) [111], [246]. The FDA approval for Bevacizumab was revoked for the treatment of breast cancer patients due to its side effects while Cabozantinib and Cediranib are being evaluated in multiple clinical trials investigating the response to the agents both alone or in combination with other therapies for the treatment of breast cancer (see table 1.2).

Cediranib has been shown to be a promising therapeutic agent for the treatment of breast cancer. Experimental *in vivo* studies reported that the VEGF tyrosine kinase receptor inhibitor even at small doses (0.75mg/kg/daily) is effective in the treatment of subcutaneous tumours of different cancers such as prostate, breast, ovary, lung, colon [168]. Moreover, several studies reported the highly potent anti-angiogenic effect that Cediranib has on the tumour microenvironment [168], [171], [173], [174]. Clinical trials and *in vivo* studies investigating the effects of progression or reducing growth rate of overt tumours and the changes that these drugs cause on the established tumour microenvironment and in most cases subcutaneous models are used. As previously mentioned, tumour cells interact with the surrounding microenvironment and this cross-talk influences the tumour growth, therefore it is important to investigate whether the response to drugs is reflected by a change in several components of the niche. In chapter 4 it is described how changes in bone structure as well as the microvasculature forms a bone microenvironment that promotes tumour growth (young animals) or support dormancy (mature animals). In

this chapter, Cediranib was used in *in vivo* models to investigate whether the anti-angiogenic effect identified in the tumour is also reflected in the bone microenvironment, prior to the injection of breast cancer cells and subsequently if any modulation resulted in a modification of the pattern of homing of tumour cells in bone. The microvascular activity was also increased by administration of Deferoxamine mesylate (DFM) to investigate whether changes in the bone microvasculature alter other components of the niche, such as the bone and extracellular matrix, and the homing of breast cancer cells to bone. This drug is commonly used as an iron chelator but it has the ability to expand the vascular network through enhancement of hypoxia inducible factor 1 alpha (Hif-1 α), recently described both *in vivo* and *in vitro* [97], [184], [185]. Seeing that angiogenesis and osteogenesis are tightly connected it is not surprising that the pro-angiogenic effect of DFM is reflected in a modification of the bone structure in several animal models [97], [186]–[192]. DFM has also been reported to increase the number of HSCs homing to the bone marrow after transplantation [196]. Furthermore, enhanced invasion and migration of breast cancer cells has been demonstrated after *in vitro* treatment with DFM [194], [195]. In the current chapter it was investigated whether treatment with Cediranib or DFM in our animal model would alter the bone and microvascular components of the niche as reported in literature and whether this potential change affects the homing of breast cancer cells to bone.

6.3 Aims

The aim of this chapter was to test the hypothesis that:

Therapeutic modification of the perivascular niche resulted in modification of the bone component and ultimately in alteration of the homing of breast cancer cells to bone.

This will be tested by the following objectives that will characterise the effect of Cediranib (reducing microvascular activity) or Deferoxamine mesylate (increasing microvascular activity) on:

- Bone structure and number of osteoprogenitors
- Bone microvasculature structure and content of different vessel sub-types
- Expression of dormancy-supporting Thrombospondin
- Breast cancer bone colonisation

6.4 Materials and methods

Summary of the methods used in this chapter is found in table 6.1 below and methods not described in the next section can be found in the Materials and Methods chapter of this thesis.

Table 6.1 Summary of material and methods of Chapter 6

Method	Analysis	Equipment
Two-photon microscopy	<ul style="list-style-type: none"> • Number of tumour cells homing to the bone microenvironment • Location of tumour cells within the bone marrow • Distance to the nearest bone surface • Distance to the nearest cancer cell 	<ul style="list-style-type: none"> • Two-photon Zeiss LSM510 NLO • Chameleon 900nm (bone structure) • HeNe 543 (Vybrant-CM-Dil) • Hene 633 (Vybrant-DiD) • Volocity 3D Image Analysis software
Micro Computed Tomography	<ul style="list-style-type: none"> • Trabecular bone volume (BV/TV %) • Trabecular number (Tb. N. in mm⁻¹) • Trabecular thickness (Tb. Th. In mm) 	<ul style="list-style-type: none"> • SkyScan 1272 scanner • NRecon software • CTAn software
Toluidine Blue staining	<ul style="list-style-type: none"> • Area of the extracellular matrix rich in proteoglycan – growth plate 	<ul style="list-style-type: none"> • OM-AFHM advanced histomorphometry microscope • Aperio ImageScope software
Osterix/Endomucin immunofluorescent staining	<ul style="list-style-type: none"> • Area of bone marrow expressing Osterix • Number of osteoprogenitors in the bone marrow 	<ul style="list-style-type: none"> • Zeiss LSM880 AiryScan Confocal microscope • ImageJ software
Endomucin immunofluorescent staining	<ul style="list-style-type: none"> • Area of bone marrow occupied by H- and L-vessels • Number of H- and L-vessels • Average length of H- and L-vessels 	<ul style="list-style-type: none"> • Leica AF6000 inverted fluorescence microscope • Zeiss LSM880 AiryScan Confocal microscope • Aperio ImageScope software
CD31/Endomucin immunofluorescent staining	<ul style="list-style-type: none"> • Area of bone marrow expressing CD31 • Area of bone marrow expressing Endomucin • Percentage of Endomucin vessels expressing also CD31 • Number of CD31⁺ vessels • Average length of CD31⁺ vessels 	<ul style="list-style-type: none"> • Zeiss LSM880 AiryScan Confocal microscope • ImageJ software • Aperio ImageScope software
CD34/Endomucin immunofluorescent staining	<ul style="list-style-type: none"> • Area of bone marrow expressing CD34 • Area of bone marrow expressing Endomucin • Percentage of Endomucin vessels expressing also CD34 • Number of CD34⁺ vessels • Average length of CD34⁺ vessels 	<ul style="list-style-type: none"> • Zeiss LSM880 AiryScan Confocal microscope • ImageJ software • Aperio ImageScope software
TSP-1/Endomucin immunofluorescent staining	<ul style="list-style-type: none"> • Area of bone marrow expressing TSP-1 • Number of Megakaryocytes (expressing TSP-1) 	<ul style="list-style-type: none"> • Zeiss LSM880 AiryScan Confocal microscope • ImageJ software • Aperio ImageScope software

6.4.1 *In vivo* studies

Animal studies were performed in accordance with local guidelines and with Home Office approval under the project licence 70/8964 held by Professor Nicola Brown, University of Sheffield, UK.

To investigate the effect of the reduction of microvascular activity of the bone microenvironment, 6-week old female BALB/c nude received 3mg/kg/daily (5 days/week) of VEGF tyrosine-kinase inhibitor Cediranib through oral gavage while control animals were administered with the control 1% Tween-80 (made in PBS)(n=10/group). On day 21, 5 animals/group were culled and hind limbs collected for *ex vivo* analyses. The remaining 5 animals/group were injected i.c. with 0.5×10^5 MDA-MB-231-NW1-Luc2 breast cancer cells labelled with the lipophilic dye Vybrant-CM-Dil. After seven days animals were culled and hind limbs collected (figure 6.1).

To detect whether increased microvascular activity would modify the bone microenvironment, 6-week old female BALB/c nude were injected i.p daily (5 days/week) with 15mg/ml (100 μ l) of Deferoxamine mesylate (DFM) or PBS control (n=13/group). On day 21, 3 animals/group were culled and hind limbs were collected to check the effect of DFM on the bone structure by μ CT. No changes were detected, therefore the animals were treated for additional three weeks with either DFM or PBS and on day 42, 5 animals/group were culled and hind limbs collected for *ex vivo* analyses. The remaining 5 animals/group were injected i.c. with 0.5×10^5 MDA-MB-231-NW1-Luc2 breast cancer cells labelled with the lipophilic dye Vybrant-CM-Dil. After seven days animals were culled and hind limbs collected for analyses of tumour cells homing to bone (figure 6.1).

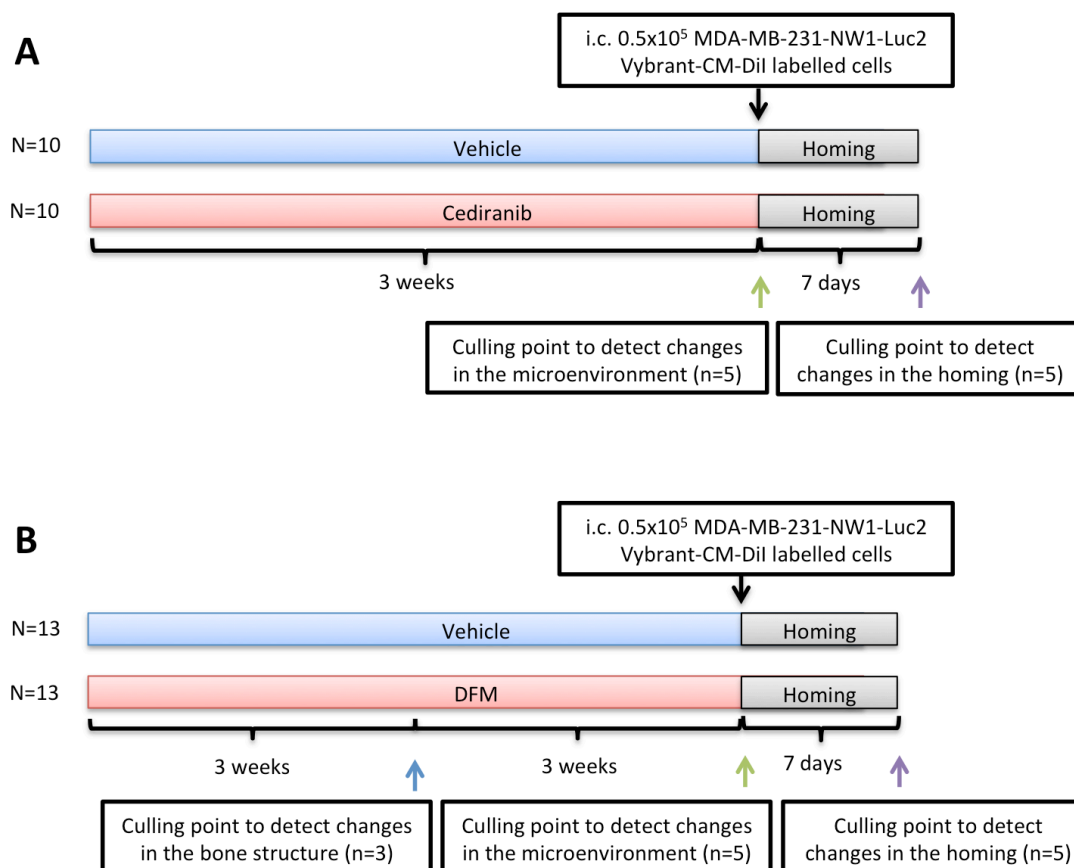


Figure 6.1 Outline of the in vivo studies evaluating the effect of Cediranib and DFM on the bone microenvironment

5 days/week) or vehicle control. After three weeks of treatment 5 mice/group were culled to detect the effect of Cediranib on bone microenvironment while the remaining 5 mice/group were injected i.c. with 0.5×10^5 MDA-MB-231-NW1-Luc2 cells labelled with Vybrant-CM-Dil). Animals were culled seven days after the injection and tibiae and femora were collected for *ex-vivo* analysis. B) 6-week old female BALB/c nude mice were injected i.p. with 15mg/ml (100 μ l) of Deferoxamine mesylate (DFM) or PBS control 5 days/week for three weeks (n=13/group). After three weeks of treatment 3 mice/group were culled to detect the effect of DFM on bone structure. Since no difference was detected, animals were treated for an additional three weeks. After the six weeks of treatment 5 mice/group were culled to investigate the effect of DFM on the bone microenvironment while the remaining 5 mice/group were injected i.c. with 0.5×10^5 MDA-MB-231-NW1-Luc2 cells labelled with Vybrant-CM-Dil). Animals were culled seven days after the injection and tibiae and femora were collected for *ex-vivo* analysis.

6.4.2 Processing of bone samples

On the day of cull hind limbs were dissected, muscle tissue surrounding the bones was carefully removed and femora and tibiae separated.

Left femora were snap frozen in liquid nitrogen and processed as explained in section 2.10.1 to perform two-photon microscopy analyses, left tibiae were fixed in 4% PFA followed by decalcification in 0.5M EDTA/0.5% PFA for histological analyses (see section 2.9.1) and right legs (both femur and tibia) were fixed in 4% PFA for 4hr, decalcified in 0.5M EDTA for 48hr, embedded in gelatine and stored at -80°C until immunofluorescent staining was performed (see section 2.9.2).

6.4.3 Two-photon microscopy

Two-photon microscopy was used to visualise tumour cells seeded in the bone microenvironment. The upright two-photon microscope Zeiss LSM510 NLO was used to image the exposed surface of the bone marrow of calcified femora using second harmonic generation to detect the bone structure (Chameleon laser, 900nm) and HeNe laser (543nm) to visualise Vybrant-CM-DiL labelled breast cancer cells within the bone marrow. A tile scan of 2104µm x 2525µm and 70µm depth was captured.

Three-dimensional images of the bones scanned, were reconstructed and analysed using Volocity 3D Image Analysis software. The parameters analysed were the number of tumour cells and their distance to the nearest bone surface and to the nearest cancer cell. The quantifications were all performed in two different ROIs, the trabecular region of the bone and the growth plate area (see section 2.10).

6.4.4 µCT

During the incubation time in 4% PFA, tibiae were scanned using the SkyScan 1272 to detect changes in the bone structure caused by the drug administered. NRecon software was used to reconstruct the images captured with the SkyScan and the VOI was manually drawn using CTAn. Trabecular bone volume (expressed as bone volume per tissue volume, BV/TV in %), trabecular number (Tb.N in mm⁻¹) and trabecular thickness were measured in 1mm of bone length (growth plate used as the reference point and 0.5mm offset)(see section 2.11).

6.4.5 Toluidine Blue staining

To identify any alteration in the extracellular matrix in the growth plate area, toluidine staining was performed on histological sections of two non-consecutive levels of paraffin embedded tibiae. Dewaxed and hydrated bone slides were incubated for 3min at ambient temperature with the toluidine blue solution and rinsed under running water followed by dehydration and cover slipping.

Proteoglycan-rich areas were quantified by manually drawing the area of interest using Aperio ImageScope software. Any trabecular bone not connected with the epiphysis and the cortical, bone were excluded from the analysis (see section 2.14.1).

6.4.6 Immunofluorescent staining

Gelatine embedded 30 μ m sections of tibia were stained with antibodies against Osterix, Endomucin, CD31, CD34 and TSP-1 using the protocol for immunofluorescent staining described in section 2.13.

Aperio ImageScope software was used to quantify the number and length of Endomucin⁺, CD31⁺ and CD34⁺ vessels while ImageJ software was used to measure the overall expression of the Osterix, Endomucin, CD31, CD34 and TSP-1, the percentage of Endomucin⁺ vessels positive both for CD31 or CD34 and the number of osteoprogenitors (Osterix⁺) and megakaryocytes (TSP-1⁺) (see section 2.14.2-4).

6.4.7 Statistical analysis

Statistical analyses were performed using GraphPad Prism software (versions 6.0 and 7.0). T-test and Two-way ANOVA with Tukey post test were used as stated in each figure legend and *p*-value of <0.05 was considered significant.

6.5 Results

Traditional treatments for bone metastasis mostly target the bone component on the microenvironment and in particular the osteoclast population. Currently, researchers are focusing their attention on characterisation of the multiple components of the metastatic niche and this increased knowledge may allow the development of therapies targeting other cell types, such as osteoblasts, endothelial cells, immune cells. However, it is still not clear whether modifications of one of the overlap niches will alter the cell populations in the other niche(s). In this chapter I investigated the response of the microenvironment and the subsequent homing of breast cancer cell to bone in response to therapies targeting microvascular activity; either reduced activity by Cediranib or increased activity with Deferoxamine mesylate (DFM).

6.5.1 Cediranib treatment to decrease the microvascular activity

Even though Cediranib has been suggested to have a direct anti-tumour effect and to significantly reduce the presence of the vasculature within tumours [168], [171], [173], [174], little is known about the effect of this drug on the components of the niche. The alterations of the bone microenvironment caused by administration of Cediranib are described in the following sections.

6.5.1.1 Effect of Cediranib on bone structure

To assess whether the administration of Cediranib affected the bone structure, animals were treated daily (5 days/week) for three weeks by oral gavage with 3mg/kg of Cediranib or vehicle control, culled and the tibiae collected for μ CT analyses (n=3 control and n=5 Cediranib).

The first parameter analysed was the trabecular bone volume. Administration of the VEGF inhibitor at this dose did not affect the trabecular bone of treated animals compared to the controls ($p=0.6085$) (figure 6.2). Trabecular thickness and trabecular number were also not altered by drug administration ($p=0.8376$ and $p=0.3285$, respectively, figure 6.2).

These results show that, at the dosage used in this *in vivo* study, Cediranib treatment did not modify the calcified bone structure of the tibia, the bone most frequently colonised by tumour cells.

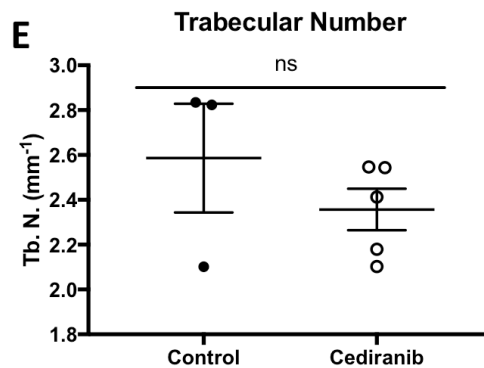
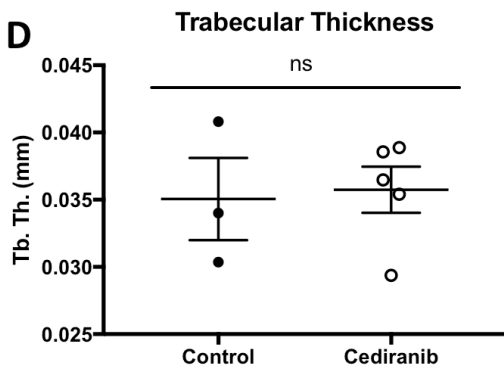
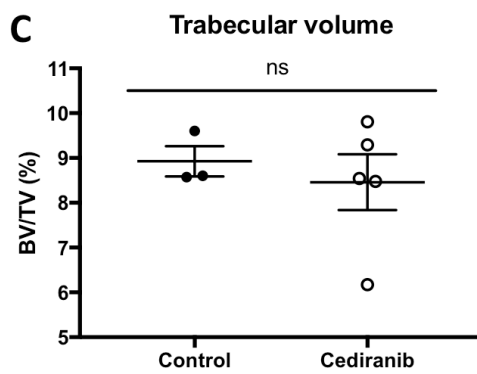
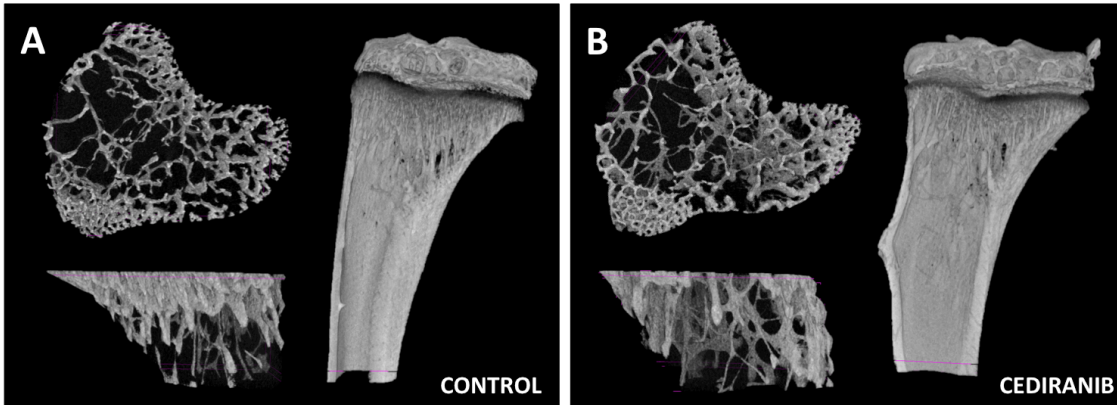


Figure 6.2 Effect of a Cediranib treatment on bone structure

Three-dimensional reconstruction of the trabecular bone analysed and the open cross section of the entire bone scanned. (A) Tibia of animals receiving vehicle control and (B) Cediranib. (C) Quantification of the trabecular bone volume after Cediranib treatment. (D) Trabecular thickness and (E) trabecular number. Graphs show Mean \pm SEM ($n=5$ animals/group, 3 bones analysed control and 5 bones analysed Cediranib), Student t-test, ns is not-significant.

6.5.1.1.1 Changes in the extracellular matrix

It has been reported that repeated oral administration (28 days) of Cediranib causes an expansion of the extracellular matrix of the epiphysis area of the bone when administered in rats at a dose of 5mg/kg/day [168].

To detect whether the dose used in the *in vivo* study here described (3mg/kg 5 days/week for 3 weeks) altered content of the extracellular matrix of the growth plate area, histological sections of tibiae were stained with Toluidine blue (n=4 control and n=5 Cediranib). The area of the proteoglycan-rich matrix was measured using Aperio ImageScope software; trabecular bone not connected with the epiphysis and cortical bone were excluded by the analysis.

As shown in figure 6.3, Cediranib treatment did not alter the area of the epiphysis proteoglycan-rich matrix compared to the vehicle control ($p=0.3969$).

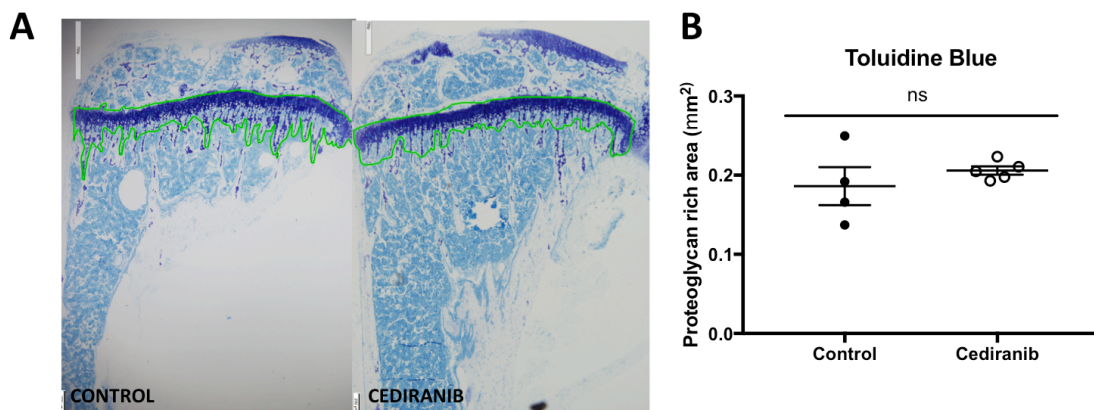


Figure 6.3 Visualisation of the proteoglycan-rich area of bone

(A) Extracellular matrix visualised with Toluidine Blue staining of histological sections of tibiae areas rich in of proteoglycan of the epiphysis and the trabecular bone directly connected to it (green line). Fragments of disconnected bone and cortical bone were excluded from the analysis. (B) Quantification of the proteoglycan rich area. Graph shows mean \pm SEM n=5 animals/group, 4 bones analysed control and 5 bones analysed Cediranib), Student t-test, ns is non-significant. Scale bar 250 μ m and 100 μ m.

6.5.1.1.2 Effect of Cediranib on the osteoprogenitor population

To investigate whether the treatment with Cediranib causes an alteration in the number of osteoprogenitors in the bone marrow, 30 μ m thick gelatine embedded tibia sections were stained with antibodies against Endomucin and Osterix (figure 6.4).

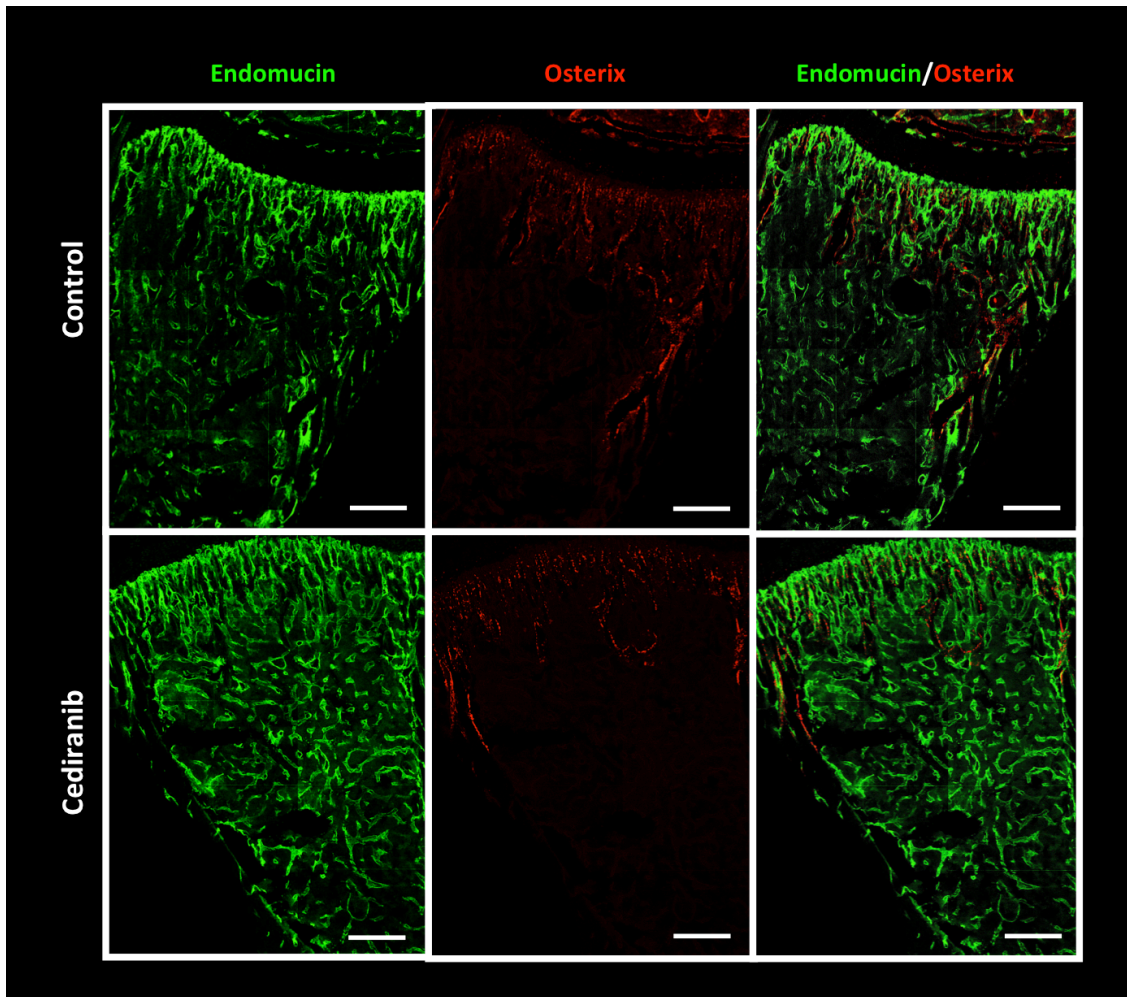


Figure 6.4 Representative image of the effect of Cediranib treatment on Osterix+ cells

Immunofluorescent staining against Osterix and Endomucin performed on 30 μ m tibia section of animals receiving vehicle control or Cediranib treatment for three weeks. Green=Endomucin, red=Osterix and yellow=Endomucin and Osterix. Scale bar 200 μ m.

The images were captured with Zeiss LSM880 AiryScan Confocal microscope and an area of approximately 2.6mm^2 was imaged for both groups (2.58 ± 0.04 and 2.67 ± 0.21 control and Cediranib respectively, $p=0.7184$, $n=3/\text{group}$)(figure 6.5). Within this area the overall expression of Osterix was measured with ImageJ software, Cediranib caused a slightly reduction of the overall expression of Osterix even though this change did not reach statistical significance ($p=0.0746$)(figure 6.5). No differences were detected in the overall number and number of Osterix⁺ cells/ mm^2 between the two groups analysed, $p=0.2355$ and $p=0.8711$ respectively (figure 6.5).

Taken together, this data show that 3mg/kg 5 days/week for 3 weeks of Cediranib does not affect the presence of Osterix⁺ progenitors in the bone marrow.

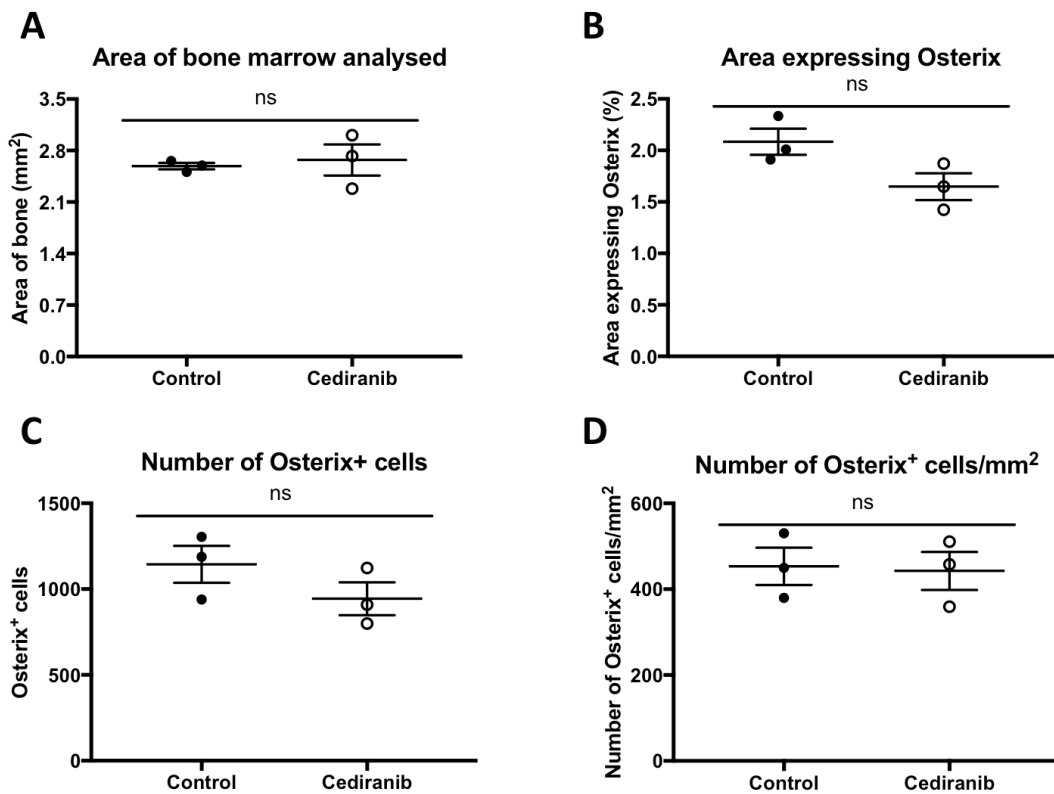


Figure 6.5 Quantifications of the effect of Cediranib treatment on Osterix expression

(A) Area of bone marrow analysed. (B) Percentage area of bone marrow expressing Osterix. (C) Overall number of Osterix⁺ cells and (D) Osterix⁺ cells/ mm^2 . Graphs show mean \pm SEM ($n=5$ animals, 3 bones analysed/group), Student t-test, ns is not-significant.

6.5.1.2 Effect of Cediranib treatment on bone microvasculature

Cediranib is a VEGF-tyrosine kinase inhibitor and it has been shown to reduce the microvascular activity and the number of vessels in tumours [168], [171], [173], [174]. To my knowledge this is the first study investigating the effect of Cediranib on the bone microvasculature to determine if this drug modifies the different vessels sub-types in the absence of tumour.

6.5.1.2.1 Endomucin⁺ vessels

To observe whether Cediranib treatment changed the extensive microvascular network of the bone microenvironment, gelatine sections of tibia were stained with the immunofluorescent protocol described in section 2.13 with an antibody against the endothelial marker Endomucin.

Zeiss LSM880 AiryScan Confocal microscope was used to image the bones and Aperio ImageScope was used to quantify the number of H- and L-vessels, their length and the area of bone marrow occupied by the different vessel sub-type. The total area of bone marrow analysed was approximately 2.7mm^2 (2.67 ± 0.13 and 2.79 ± 0.06 control and Cediranib respectively, $p=0.4678$, $n=3/\text{group}$)(figure 6.6). In the area analysed, Endomucin⁺ vessels can be divided in two different vessel sub-types, H- and L-vessels. The first type of vessels (H-vessels) has a characteristic column-like shape and its located in the metaphysis of bones while the second type of vessels (L-vessels) is more sinusoidal and is found towards the diaphysis of long bones. The first analysis performed on the Endomucin stained section was to determine if Cediranib treatment caused an alteration in the area of bone marrow occupied by the two vessel sub-types. In the area of bone marrow analysed, there was an even distribution of H- and L-vessels in the control group (48.90 ± 4.44 and 51.1 ± 4.437 , $p=0.7443$) while animals treated with cediranib display a slight increment in the portion of bone occupied by the L-vessel sub-type (44.61 ± 3.06 and 55.39 ± 3.06 , $p=0.0675$). However, when comparing between treatment groups there was no statistical difference in the proportion of bone occupied by H- ($p=0.4705$) and L-vessels ($p=0.4705$)(figure 6.6).

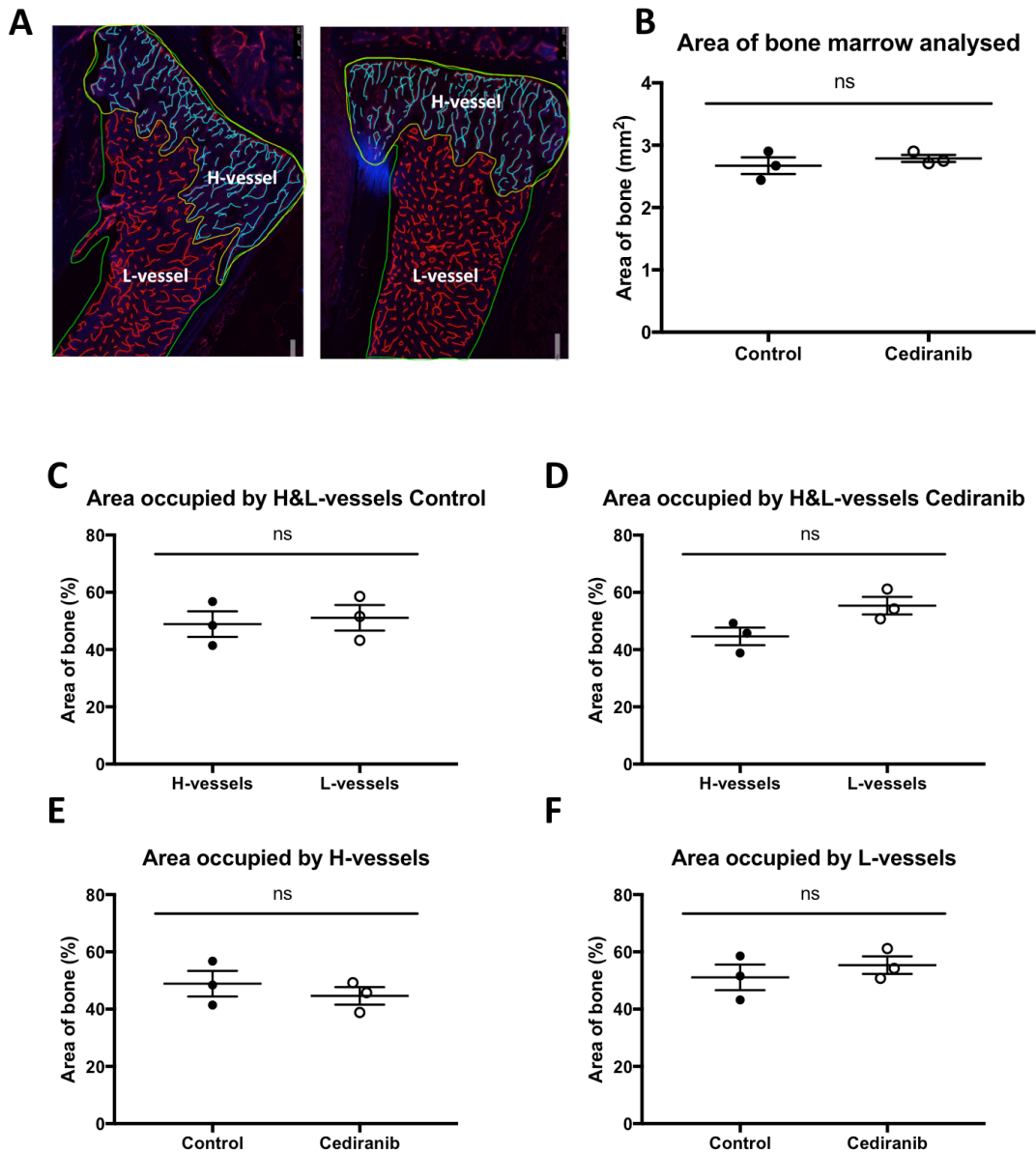


Figure 6.6 Quantification of immunofluorescent staining against Endomucin

A) Representative images of the total area of bone marrow analysed (green), H-vessels (blue) and L-vessels (red) manually tracked with Aperio ImageScope software. Area of bone marrow analysed is drawn in green and its quantification is shown in (B). (C) and (D) show the percentage of area of bones occupied by H- and L-vessels in control and Cediranib treated animals respectively. (E) and (F) show the area of bones occupied by H- and L-vessels in the different groups. Graphs show mean \pm SEM (n=5 animals, 3 bones analysed/group), Student t-test, ns is not-significant.

The second parameter analysed was the number of vessels within the area of bone marrow analysed. As expected, Cediranib treatment caused a significant reduction in the total number of vessels/mm² compared to the control group ($p=0.0378$)(figure 6.7). However, when analysed separately, the number of H- and L-vessel/mm² of the total area of bone marrow analysed was not significantly different between the treatments group ($p=0.2671$ and $p=0.4096$ respectively)(figure 6.6). The number of H-vessels normalised to the area of bone marrow that they occupy was not affected by the Cediranib treatment ($p=0.2193$) while this analysis performed on the L-vessel sub-type revealed a decrease in the number of these vessels compared to the control ($p=0.0222$)(figure 6.7). In tibiae from the control animals there was a significantly higher number of L-vessels compared to H-vessels ($p=0.0012$), but this pattern was lost in animals treated with Cediranib, resulting in a more even distribution of the two vessel sub-types ($p=0.2977$)(figure 6.8). Interestingly, administration of Cediranib resulted in an elongation of the H-vessels compared to controls ($p=0.0344$) while the average length of L-vessels was unchanged ($p=0.3821$)(figure 6.8).

Taken together, the data presented here describe how treatment with the VEGF-tyrosine kinase inhibitor affects the microvasculature in bone. Cediranib increases the area of bone marrow occupied by L-vessels. Moreover, the TKI induces a reduction in the number of vessels, but it increases the average length of column-like vessels (H) compared to controls.

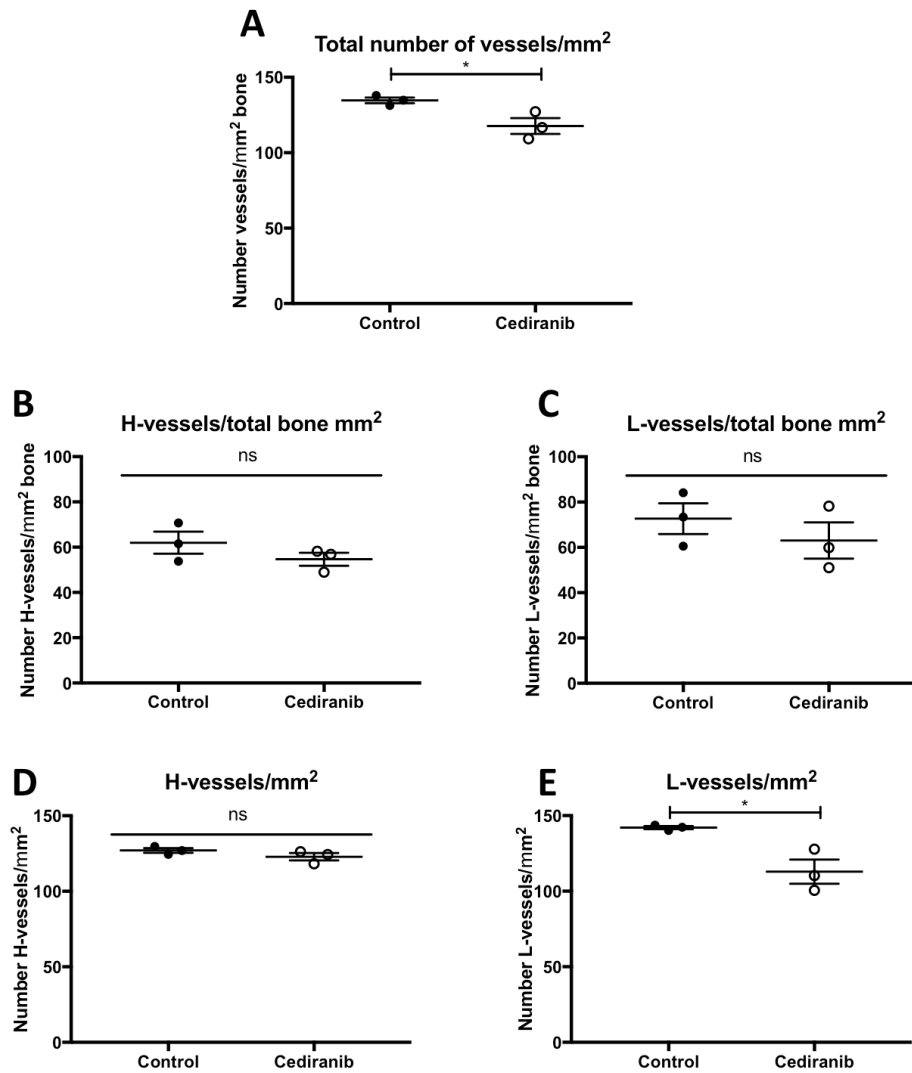


Figure 6.7 Number of vessels quantified in bone marrow

A) Total number of vessels counted in both groups. (B) and (C) show the number of H- and L-vessels/mm² of total area of bone. (D) and (E) show the number H- and L-vessels/mm² of the area occupied by the different vessel sub-types. Graphs show mean \pm SEM (n=5 animals, 3 bones analysed/group), Student t-test, * $p < 0.05$ and ns is not-significant.

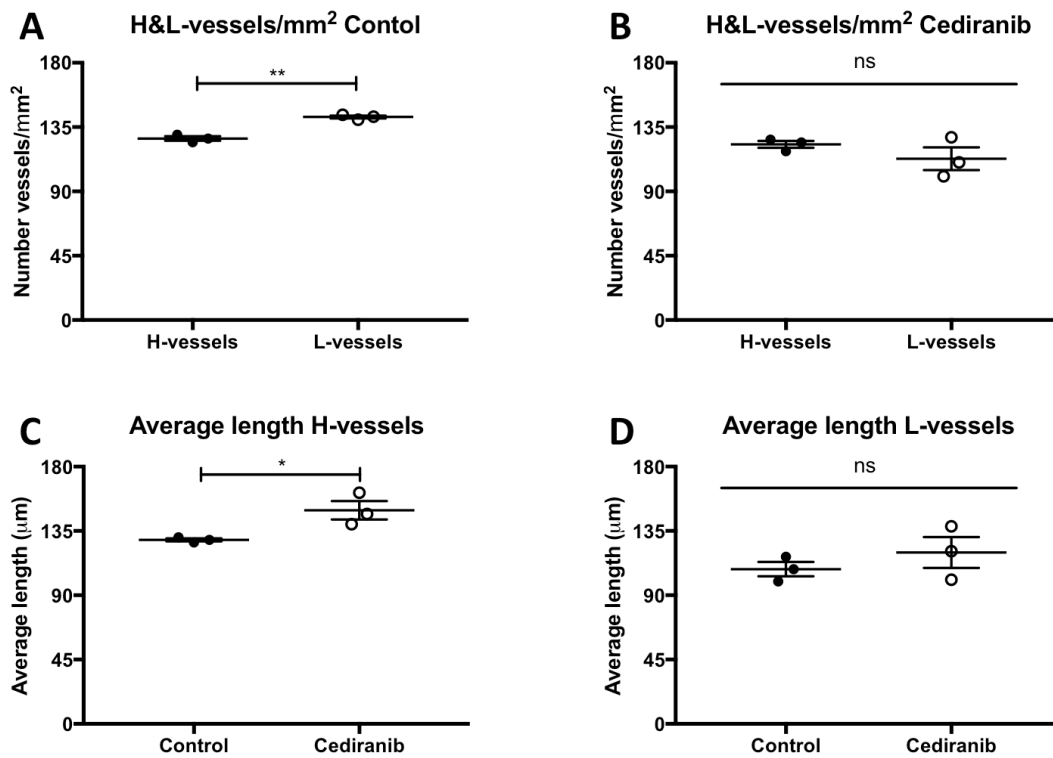


Figure 6.8 Number of H- and L-vessels in different groups and their length

(A) and (B) show the number of H and L- vessels/mm² in control and Cediranib group respectively. (C) and (D) show the length of H- and L- vessels between different groups. Graphs show mean \pm SEM (n=5 animals, 3 bones analysed/group), Student t-test, * $p < 0.05$, ** $p < 0.01$ and ns is not-significant.

6.5.1.2.2 CD31⁺ vessels

To define whether the treatment with Cediranib would result in a change in the established microvasculature present in the bone microenvironment, bone sections were stained with antibodies against Endomucin and CD31 (see section 2.13) and imaged with Zeiss LSM880 AiryScan Confocal microscope (figure 6.9).

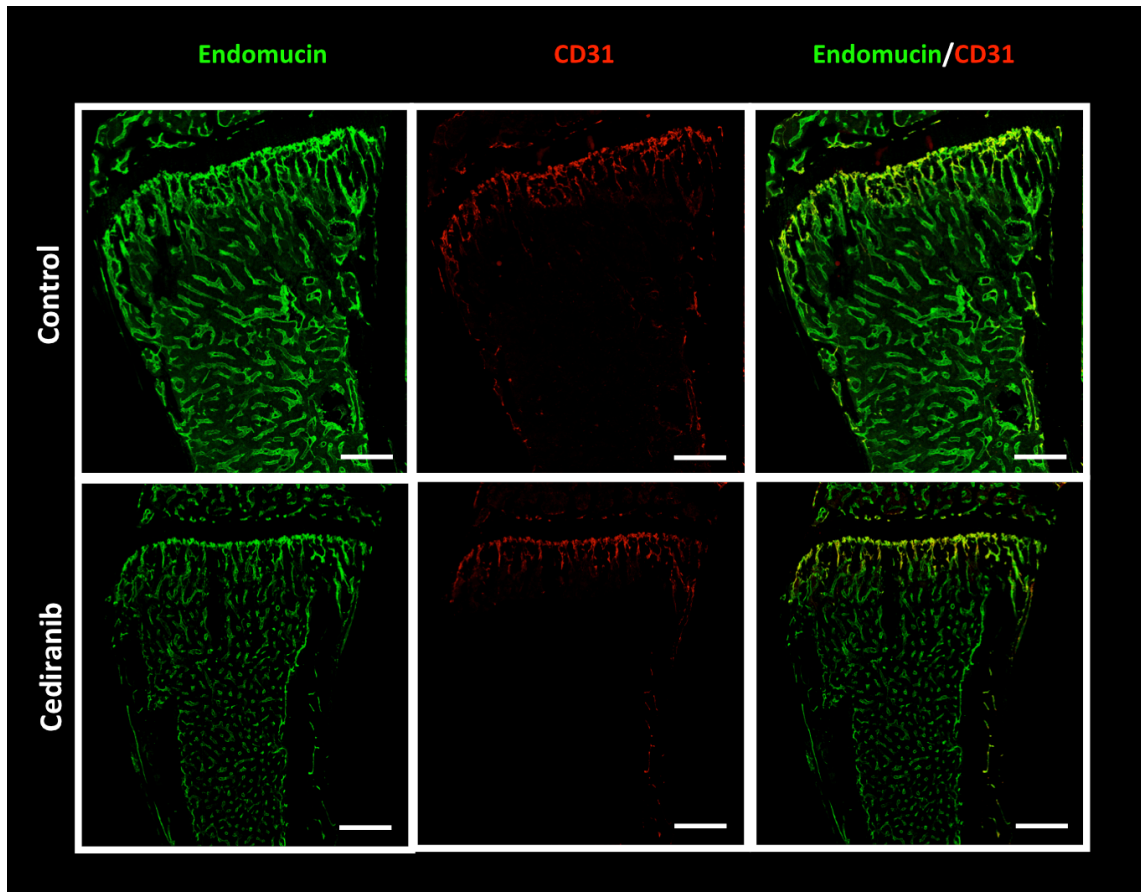


Figure 6.9 Representative image of the effect of Cediranib treatment on CD31⁺ vessels

Immunofluorescent staining against CD31 and Endomucin performed on 30 μ m tibia section from animals receiving vehicle control or Cediranib treatment for three weeks. Green=Endomucin, red=CD31 and yellow=Endomucin and CD31. Scale bar 200 μ m.

An area of approximately 2.5mm^2 was imaged and analysed with ImageJ and Aperio ImageScope software (2.407 ± 0.0968 and 2.540 ± 0.2751 control and Cediranib respectively, $p=0.4678$, $n=3/\text{group}$)(figure 6.10). Animals treated with Cediranib had a significant reduction in the expression of Endomucin compared to controls ($p=0.0208$), while no difference was detected in the expression of CD31 ($p=0.1038$) and in the percentage of Endomucin⁺CD31⁺ between the two groups ($p=0.4209$)(figure 6.10). Furthermore, the administration of the drug did not change the number of CD31⁺ vessels/ mm^2 of total bone or CD31⁺ vessels/ mm^2 of bone occupied by this vessel subtype ($p=0.6468$ and $p=0.3225$ respectively)(figure 6.11). As well as the number, the average length of the established vessels was not modified by the treatment with Cediranib ($p=0.1315$)(figure 6.11).

These results show that the established vasculature (positive for the endothelial marker CD31⁺) was not altered in its overall expression and structure by treatment with Cediranib.

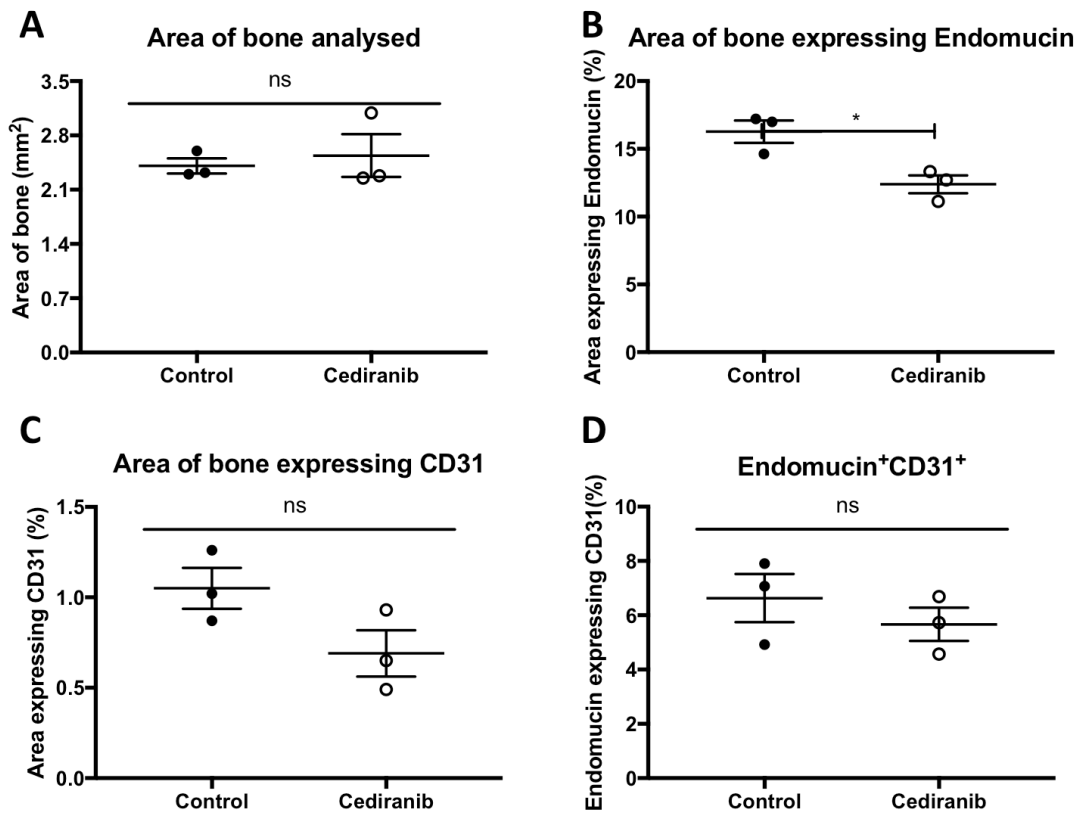


Figure 6.10 Quantification of immunofluorescent staining against CD31

A) Area of bone marrow analysed in the two different groups. B) Shows the overall expression of Endomucin while (C) is the expression of CD31. (D) Percentage of Endomucin⁺ vessels that are also expressing CD31 in the different groups (H). Graphs show mean \pm SEM (n=5 animals, 3 bones analysed/group), Student t-test, * p <0.05 and ns is not-significant.

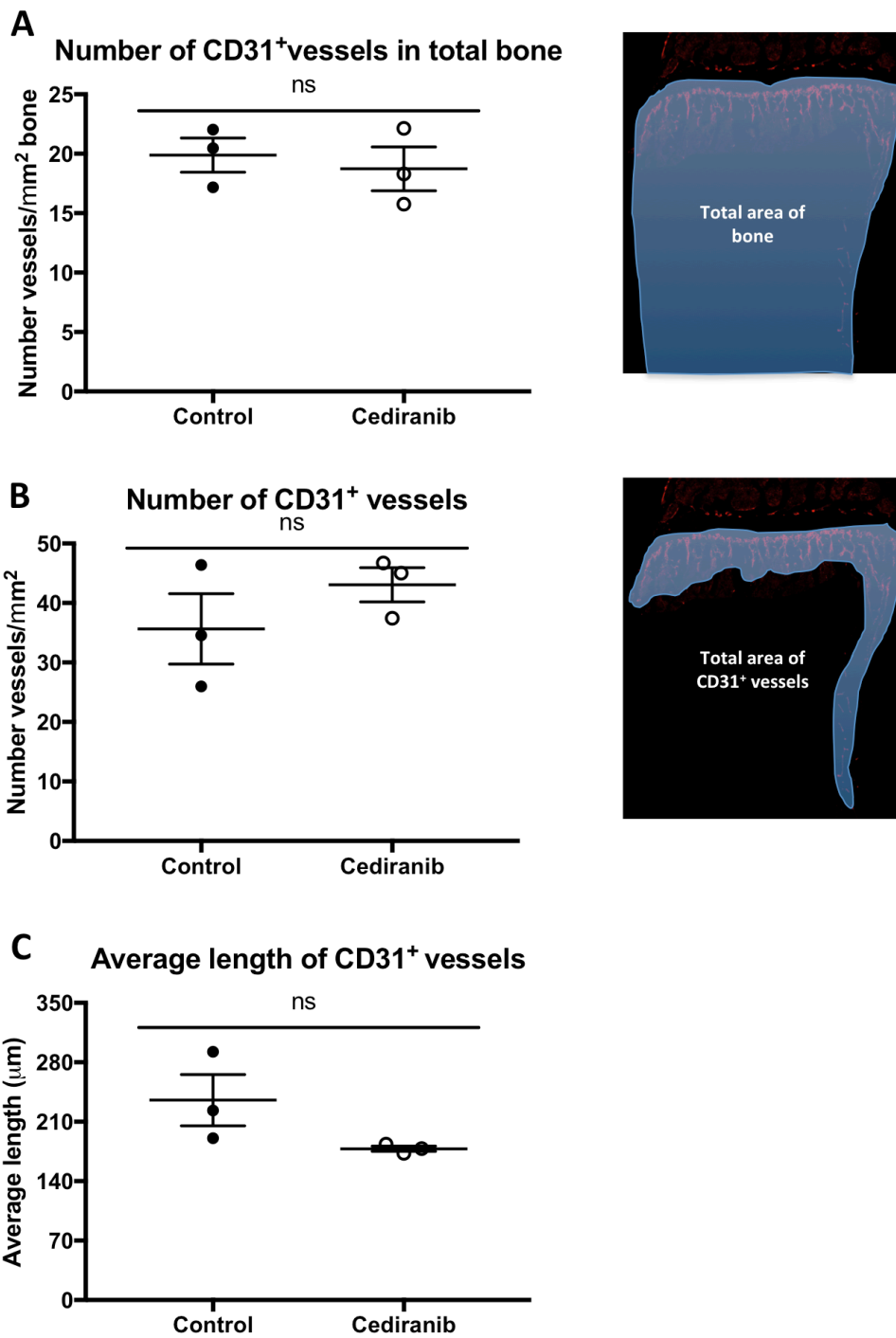


Figure 6.11 Number and average length of CD31⁺ vessels

A) Show the number of CD31⁺ vessels/mm² of total bone and illustration of the area considered for this analysis. (B) Show the number of CD31⁺ vessels/mm² of area occupied by the vessel sub- and illustration of the area considered for this analysis. (C) Displays the average length of CD31⁺ vessels. Graphs show mean ± SEM (n=5 animals, 3 bones analysed/group), Student t-test, ns is not-significant.

6.5.1.2.3 CD34⁺ vessels

One important component of the perivascular niche is the newly formed vessels, which are CD34⁺. To investigate if Cediranib caused an alteration in the structure of the neo vessels immunofluorescent staining, using antibodies against both Endomucin and CD34 was performed on three non-consecutive gelatine embedded sections tibia (n=3 tibia/group)(figure 6.12), as described in section 2.14.

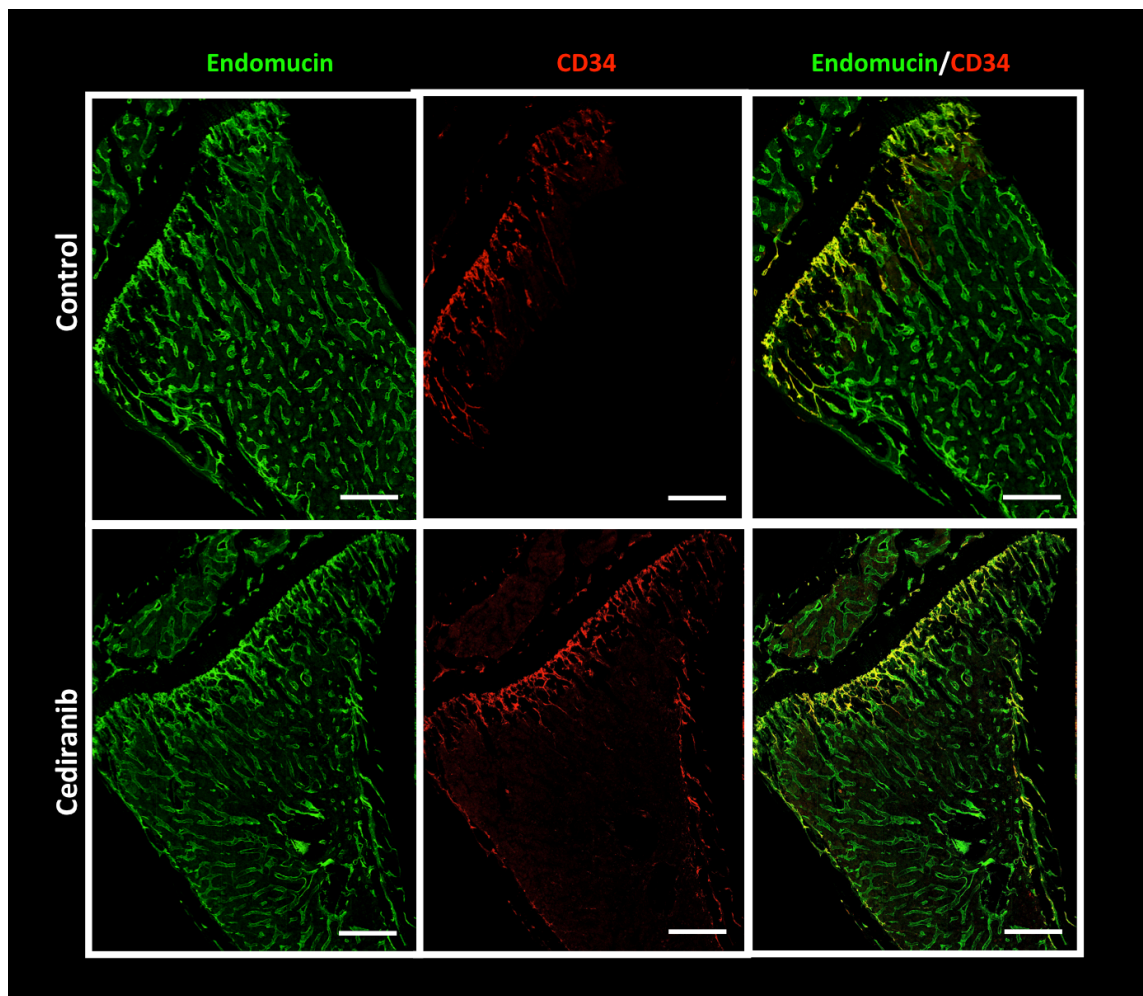


Figure 6.12 Representative image of the effect of Cediranib treatment on CD34⁺ vessels

Immunofluorescent staining against CD34 and Endomucin performed on 30 μ m tibia sections from animals receiving vehicle control or Cediranib treatment for three weeks. Green=Endomucin, red=CD34 and yellow=Endomucin and CD34. Scale bar 200 μ m.

ImageJ and Aperio ImageScope software were used to analyse the area of bone marrow captured with Zeiss LSM880 AiryScan Confocal microscope. The area of bone marrow varied between the bones analysed but no statistical difference was detected when comparing to the Cediranib to the control group (2.62 ± 0.13 and 2.09 ± 0.61 control and Cediranib respectively, $p=0.4678$, $n=3/\text{group}$)(figure 6.13). Endomucin expression was similar in both treatment groups ($p=0.4331$) whereas the CD34 expression was significantly higher in the Cediranib group compared to the control ($p=0.0377$)(figure 6.13). However, there was no difference in the presence of Endomucin⁺CD34⁺ vessels between the groups analysed ($p=0.6902$)(figure 6.13). As shown in figure 6.14, there was a trend towards an increase in the number of CD34⁺vessels/mm² in the total bone and the number of CD34⁺vessels/mm² in the area occupied by this vessel sub-type of the Cediranib group, none of these trends reached the statistical significance when compared to controls ($p=0.1983$ and $p=0.1987$ respectively). As for the CD31⁺vessels, there was no difference detected between the average lengths of the CD34⁺vessels of the two treatment groups ($p=0.4162$)(figure 6.14).

Surprisingly, treatment with Cediranib had only marginal effect on newly formed vasculature in bone. The only parameter that was modified by Cediranib treatment was the overall expression of CD34. It was expected that vascular activity in animals treated with the VEGF-tyrosine kinase inhibitor should be reduced, while in this *in vivo* study the opposite result was obtained, with a small increase in the newly formed vascular network in treated animals.

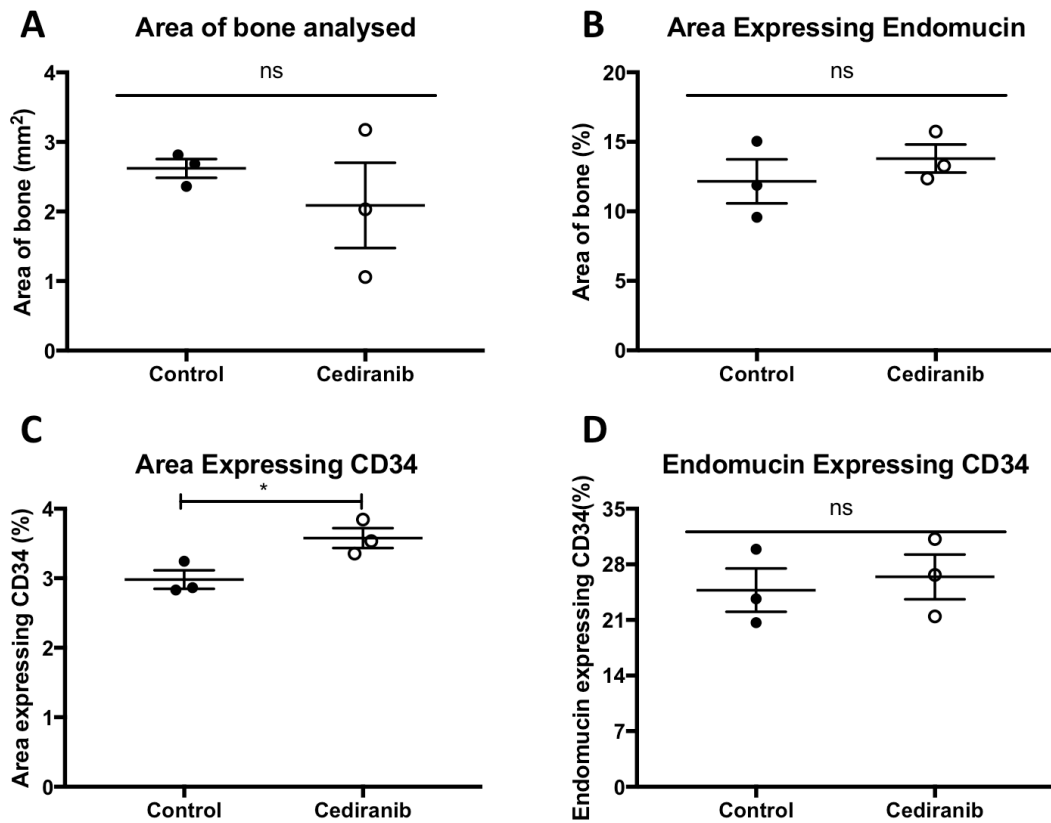


Figure 6. 13 Quantification of immunofluorescent staining against CD34

A) Area of bone marrow analysed in the two different groups. B) Shows the overall expression of Endomucin while (C) is the expression of CD34. (D) Percentage of Endomucin⁺ vessels that are also expressing CD34 in the different groups (H). Graphs show mean \pm SEM (n=5 animals, 3 bones analysed/group), Student t-test, * $p < 0.05$ and ns is not-significant.

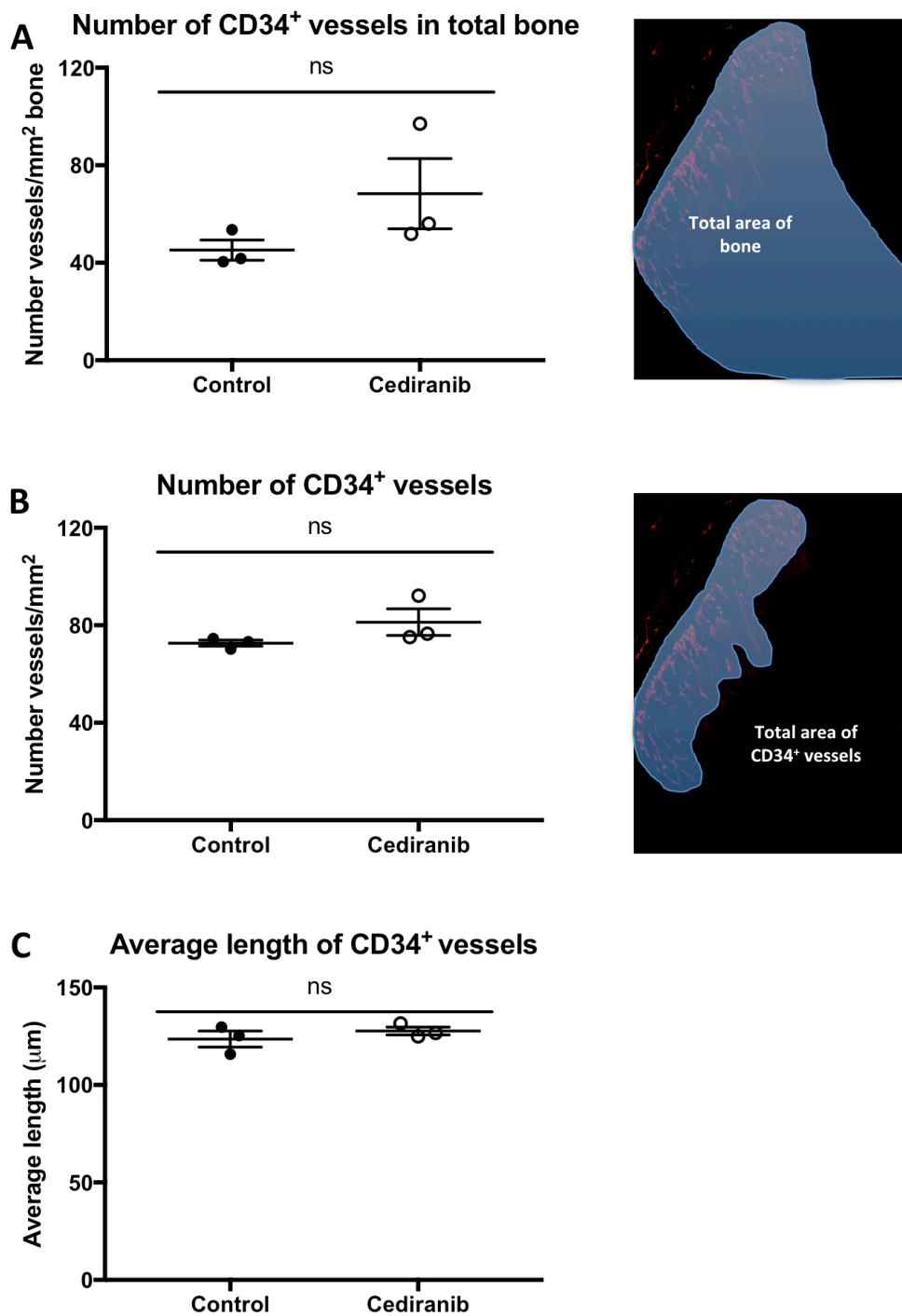


Figure 6.14 Number and average length of CD34⁺ vessels

A) Number of CD34⁺ vessels/mm² of total bone and illustration of the area considered for this analysis. (B) Number of CD34⁺ vessels/mm² of area occupied by the vessel sub- and illustration of the area considered for this analysis. (C) Displays the average length of CD34⁺ vessels. Graphs show mean \pm SEM (n=5 animals, 3 bones analysed/group), Student t-test, ns is not-significant.

6.5.1.3 Effect of Cediranib treatment on TSP-1 expression

TSP-1 has been suggested to be involved in the support of dormancy of breast cancer cells, as outlined in Chapter 4. To investigate whether treatment with Cediranib influences the expression of TSP-1 and/or the number of megakaryocytes in the bone microenvironment, immunofluorescent protocol against TSP-1 was performed on 30 μ m sections of gelatine embedded tibia (n=3/group)(figure 6.15).

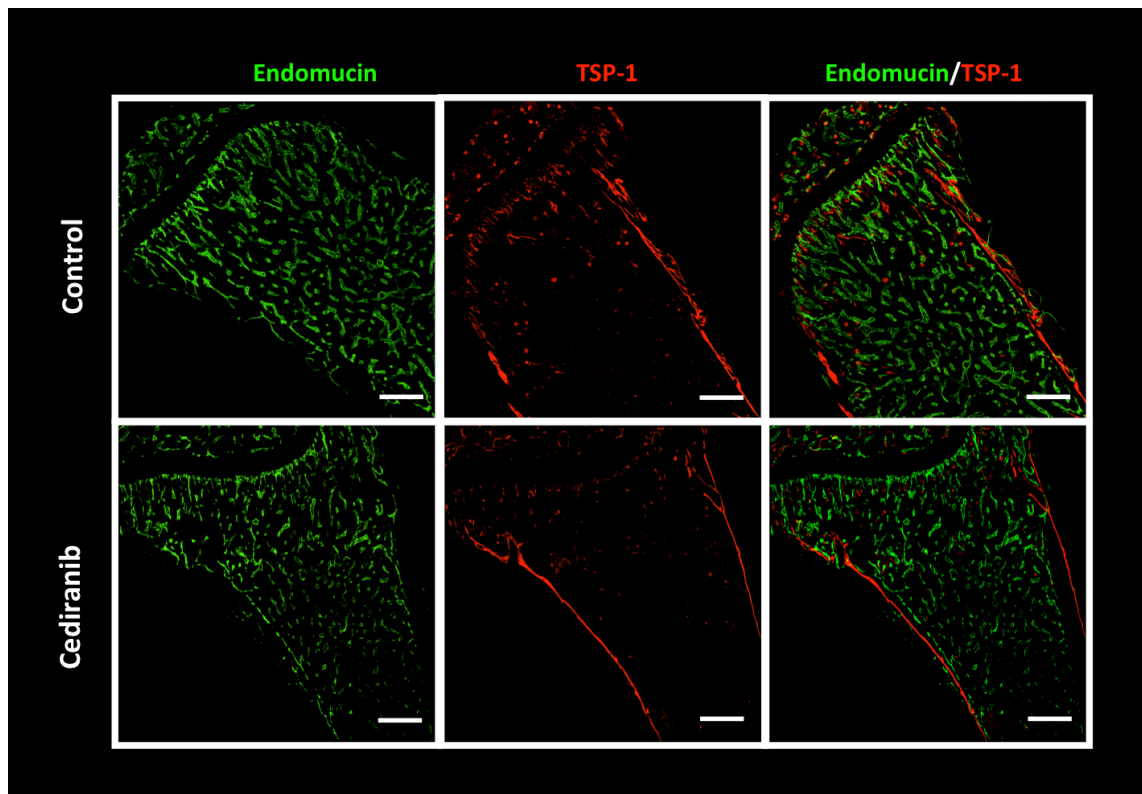


Figure 6.15 Representative image of the effect of Cediranib treatment on TSP-1 expression

Immunofluorescent staining against TSP-1 and Endomucin performed on 30 μ m tibia sections from animals receiving vehicle control or Cediranib treatment for three weeks. Green=Endomucin and red=TSP-1. Scale bar 200 μ m.

As shown in figure 6.16, there was no difference in the size of the area of bone marrow analysed between the two treatment groups ($2.65 \pm 0.13 \text{ mm}^2$ and $2.89 \pm 0.19 \text{ mm}^2$ control and Cediranib respectively, $p=0.3527$, $n=3/\text{group}$)(figure 6.16). Interestingly, Cediranib treatment reduced the overall expression of TSP-1 in the area of bone microenvironment analysed ($p=0.0364$) while the number of megakaryocytes/ mm^2 was not altered ($p=0.1434$)(figure 6.16).

Taken together, these data demonstrated that Cediranib treatment reduces the intensity of expression of the dormancy-supporting TSP-1 without modifying the number of megakaryocytes counted within the bone marrow.

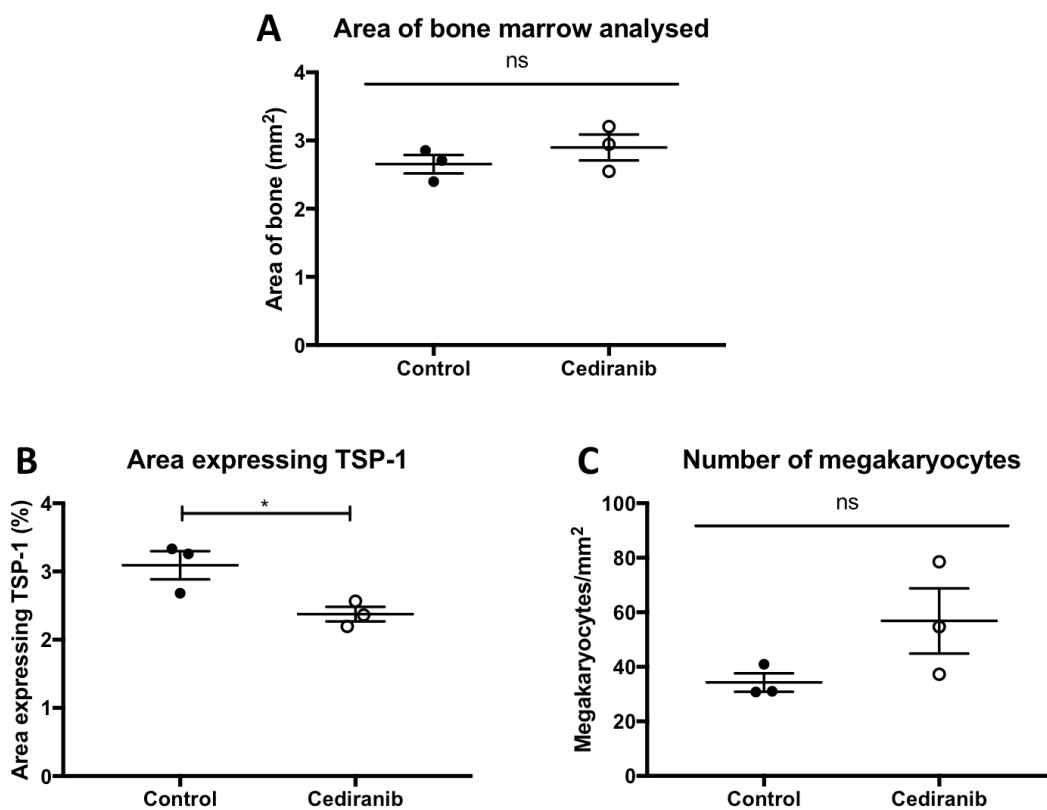


Figure 6.16 Quantification of the effect of Cediranib treatment on TSP-1 expression

(A) Area of bone marrow analysed. (B) Percentage area of bone marrow expressing TSP-1. (C) Number of Megakaryocytes/ mm^2 . Graphs show mean \pm SEM ($n=5$ animals, 3 bones analysed/group), Student t-test, * $p<0.05$ and ns is not-significant.

6.5.1.4 Effect of Cediranib treatment on breast cancer cell homing to bone

An ultimate aim of this chapter was to determine whether Cediranib treatment affected the metastatic niche in bone to an extent that modified breast cancer cell colonisation of the bone microenvironment. To achieve this, MDA-MB-231-NW1-Luc2 cells labelled with the lipophilic dye Vybrant-CM-Dil were injected i.c. into BALB/c nude mice which had previously treated for three weeks (5 days/week) with 3mg/kg of Cediranib or vehicle control. Femora were collected 7 days after tumour cell injection and analysed by two-photon microscopy to map the number and location of breast cancer cells within the bone microenvironment.

The analyses with Volocity 3D Image software were performed in two different ROIs, the trabecular region of bone (ROI1) and growth plate area (ROI2)(n=6 control and n=7 Cediranib). No difference was detected in ROI1 ($p=0.2593$) or in ROI2 ($p=0.7172$) between the treatment groups (figure 6.17). Irrespective of treatment and ROI quantified, breast cancer cells located in close proximity to the bone surface ($36.17\pm 8.266\mu\text{m}$ and $45.9\pm 5.38\mu\text{m}$ $p=0.3315$ ROI1, $34.39\pm 14.06\mu\text{m}$ and $16.77\pm 8.642\mu\text{m}$ $p=0.3759$ ROI2, control and Cediranib respectively)(figure 6.17). Distances to the nearest tumour cells were quantified only in ROI1 as statistical analyses were not possible in ROI2 due to the low number of femora containing cancer cells in this area of bone. Breast cancer cells in ROI1 locate far away from other tumour cells (385.8 ± 122.5 vs. 254.3 ± 42.25 , control vs. Cediranib respectively) and no difference was observed between treatment groups ($p=0.2731$)(figure 6.17). Irrespective of treatment, tumour cells locate closer to the bone surface than to other cancer cells ($p=0.0017$ control and $p=0.0391$ Cediranib)(figure 6.17).

Taken together these data show that Cediranib treatment does not alter the pattern of homing of breast cancer cells to bone, resulting in a preferential homing and in close proximity to the trabecular region of the bone when compared to the growth plate.

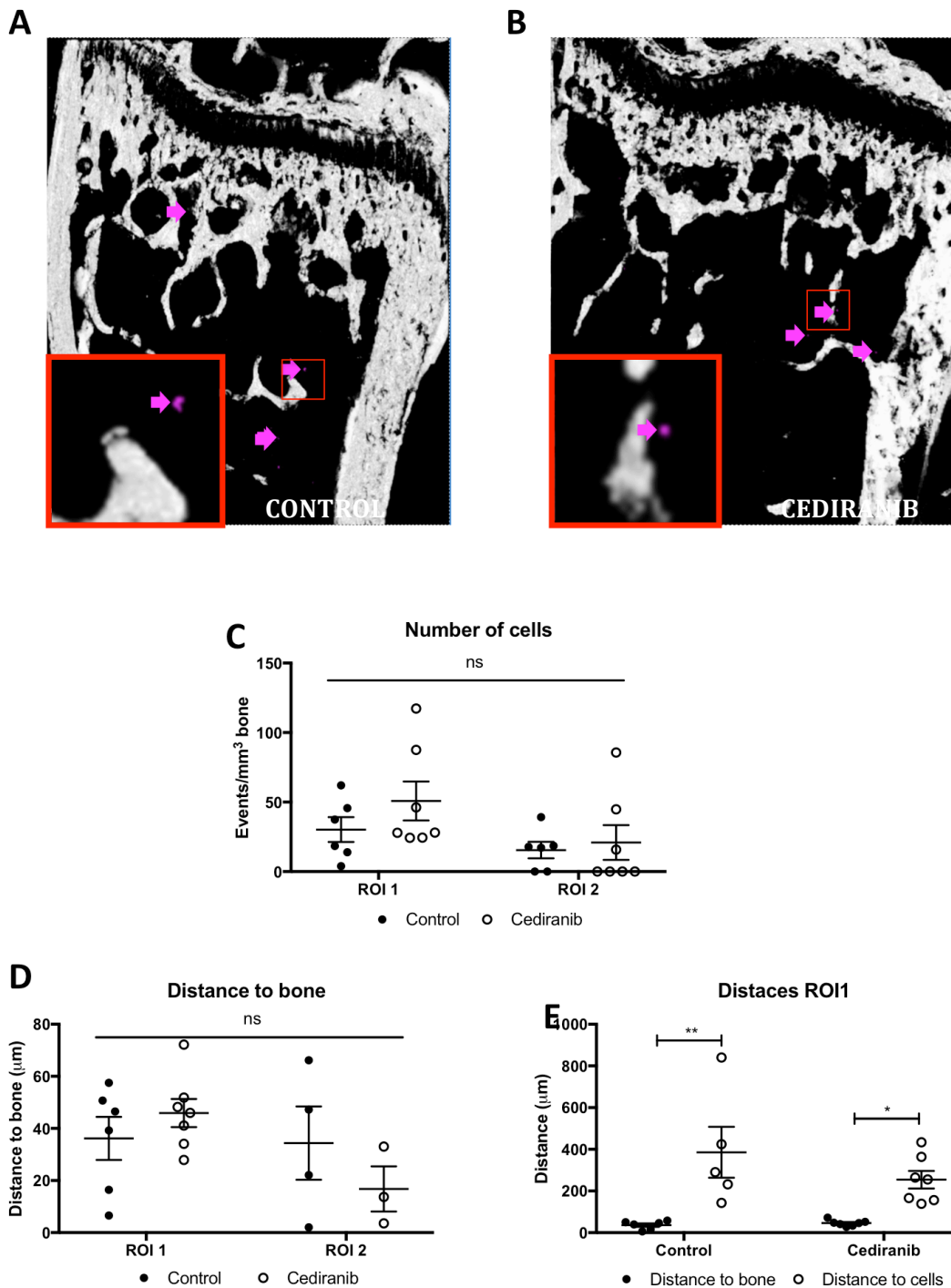


Figure 6.17 Homing of breast cancer cells in animals treated with Cediranib

Example images of two-photon scans of (A) control and (B) Cediranib treated animals showing bone (white) and Vybrant-CM-Dil⁺ cells (pink and pink arrows). C) Graph shows the number of MDA-MB-231-NW1-Luc2 cells detected in the two groups. (D) Distances of the tumour cells to the nearest bone surface. (E) Distances to the nearest bone surface and the nearest tumour cell in ROI1. Graphs show Mean ± SEM (n=5 animals/group, 6 bones analysed control and 7 bones analysed cediranib), Two-way ANOVA and Tukey post test, * $p < 0.05$, ** $p \leq 0.005$ and ns is not-significant.

6.5.2 Deferoxamine mesylate treatment to increase the microvascular activity

DFM increases either the angiogenic and/or osteogenic processes in a wide range of animal models [97], [186]–[190], [192], [193]. The treatment efficacy on the bone microvasculature has been quantified using qPCR [97] or μ CT following vascular perfusion [187], [189], [190], [193] but quantitative analyses on the structure of the vessels have not been previously reported. Moreover, the implications of these changes on the homing of breast cancer cell to bone have not yet been elucidated. Therefore, studies described in the following sections aimed to fill this gap in our current knowledge.

6.5.2.1 Effect of DFM on bone structure

It has been reported that DFM treatment affects both bone mass and osteoprogenitor numbers in bones of aged mice (approximately 40-week old), reversing the reduction of these two components, due to the ageing process [97].

To test whether treatment with DFM modified the bone structure of young animals, 6-week old BALB/c nude mice received 15mg/ml (100 μ l) of DFM daily for 5 days/week for 3 weeks (n=3/group) and tibiae were collected to perform μ CT analyses as described in section 2.11.

A three week course of treatment with this dose of DFM was not sufficient to induce changes in the bone structure of young mice. There were no differences in the trabecular bone volume ($p=0.7035$), trabecular thickness ($p=0.5602$) or trabecular number ($p=0.8788$) of animals treated with DFM compared to the control. Animals were therefore treated with DFM for additional three weeks (n=10/group) (figure 6.18).

Surprisingly, at the end of the six weeks of administration of DFM, no changes were detected in the bone structure of treated animals compared to controls ($p=0.6816$ trabecular bone volume, $p=0.2867$ trabecular thickness and $p=0.4242$ trabecular number)(figure 6.19).

Results described in this section show that treatment with 15mg/ml (100 μ l) of DMF daily for 5 days/week for 3 or 6 weeks does not affect the structure of the bone of young animals.

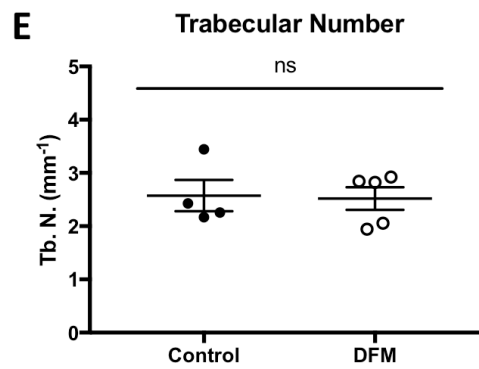
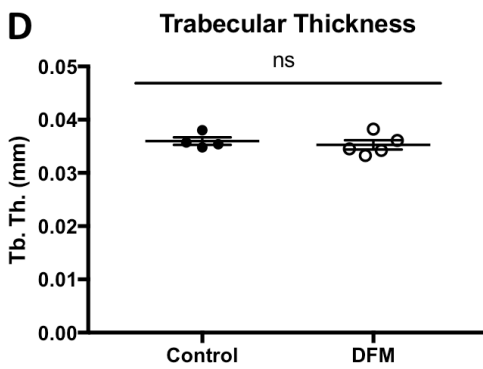
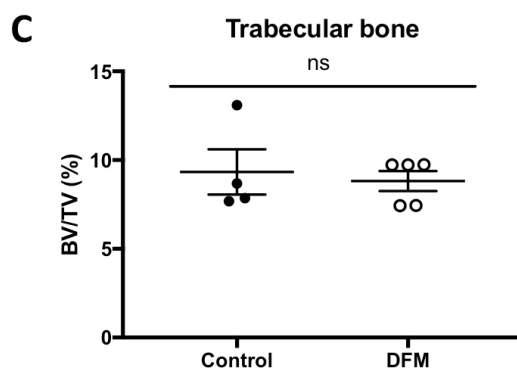
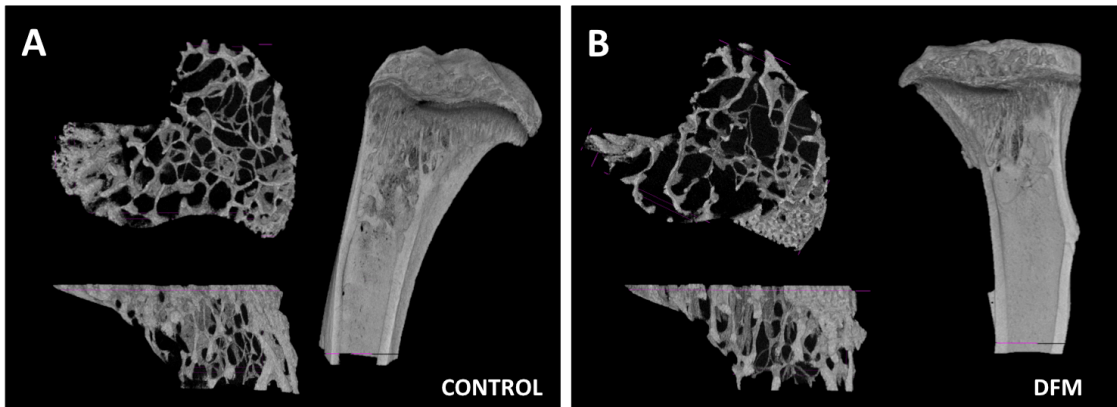


Figure 6.18 Effect of 3 weeks of DFM treatment on bone structure

Three-dimensional reconstruction of the trabecular bone analysed and the open cross section of the entire bone scanned. Tibia of animals receiving (A) vehicle control and (B) DFM. (C) Quantification of the trabecular bone volume after Cediranib treatment. (D) Trabecular thickness and (E) trabecular number. Graphs show Mean \pm SEM (n=3 animals/group, 4 bones analysed control and 5 bones analysed DFM), Student t-test, ns is not-significant.

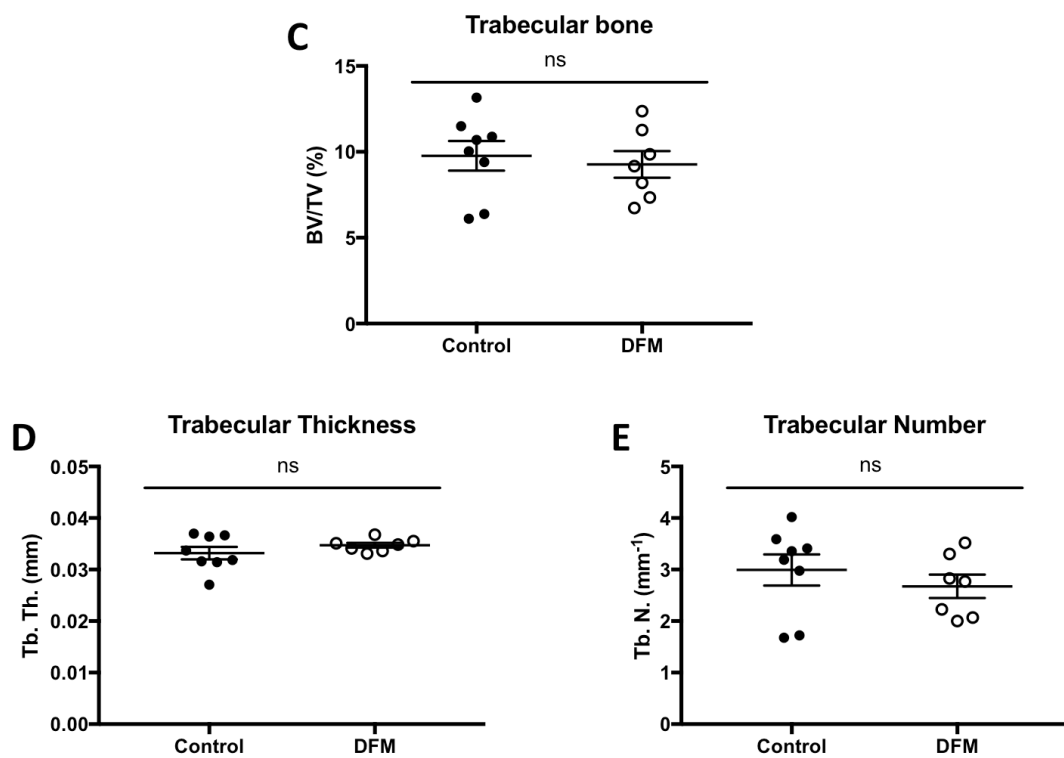
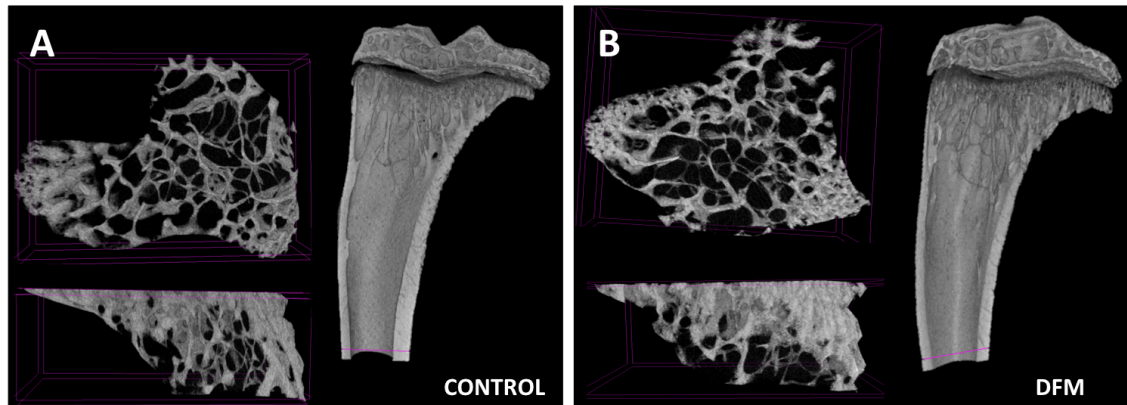


Figure 6.19 Effect of 6 weeks of DFM treatment on bone structure

Three-dimensional reconstruction of the trabecular bone analysed and the open cross section of the entire bone scanned. Tibia of animals receiving (A) vehicle control and (B) DFM. (C) Quantification of the trabecular bone volume after Cediranib treatment. (D) Trabecular thickness and (E) trabecular number. Graphs show Mean \pm SEM (n=5 animals/group, 8 bones analysed control and 7 bones analysed DFM), Student t-test, ns is not-significant.

6.5.2.1.1 Changes in the extracellular matrix

To detect whether DFM treatment modified the extracellular matrix rich area of the epiphysis, Toluidine blue staining was performed on histological sections of tibia as described in section 2.12.4.

There was no difference in the area of the proteoglycan rich region between treatment groups ($p=0.5214$)(figure 6.20).

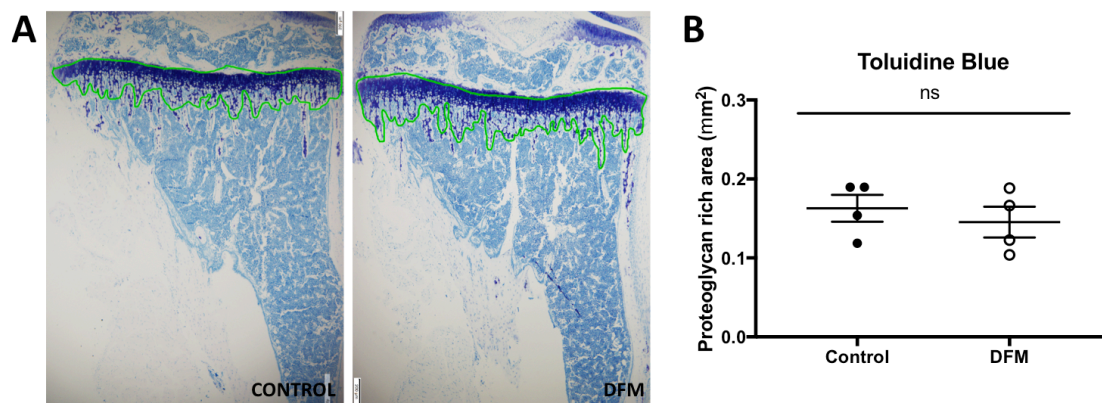


Figure 6.20 Visualisation of the proteoglycan-rich area of bone

(A) Extracellular matrix visualised with Toluidine Blue staining of histological sections of tibiae; area rich in proteoglycan of the epiphysis and the trabecular bone directly connected to it (green line). Fragments of bone disconnected and cortical bone were excluded from the analysis. (B) Quantification of the proteoglycan rich area (n=5 animals and 4 bones analysed/group). Graph shows mean \pm SEM, Student t-test, ns is non-significant. Scale bar 250 μ m.

6.5.2.1.2 Effect of DFM on the osteoprogenitor population

When aged mice (approximately 70-week old) are treated with DFM in addition to an increase in bone volume, the number of osteoprogenitors also increase [97]. To detect whether such changes occur also in young animals, 30µm thick gelatine embedded tibiae section were stained Endomucin and Osterix using the immunofluorescent protocol described in section 2.14 (figure 6.21).

Zeiss AiryScan confocal microscopy was used to image the bone marrow area of the bones stained ($2.553 \pm 0.0778 \text{mm}^2$ control and $2.206 \pm 0.1556 \text{mm}^2$ DFM, $p=0.1168$) and ImageJ was used to quantify the expression of Osterix in the samples analysed ($n=3/\text{group}$). The overall expression of Osterix in the area of bone marrow analysed was not affected by the DFM treatment ($p=0.4380$)(figure 6.21). Likewise, no changes were observed between treatment groups in the overall number of Osterix⁺ cells ($p=0.3033$) or in the number of Osterix⁺ cells/ mm^2 ($p=0.4788$)(figure 6.21).

Data here presented indicate that expression of Osterix in our animal model is not affected by treatment with DFM.

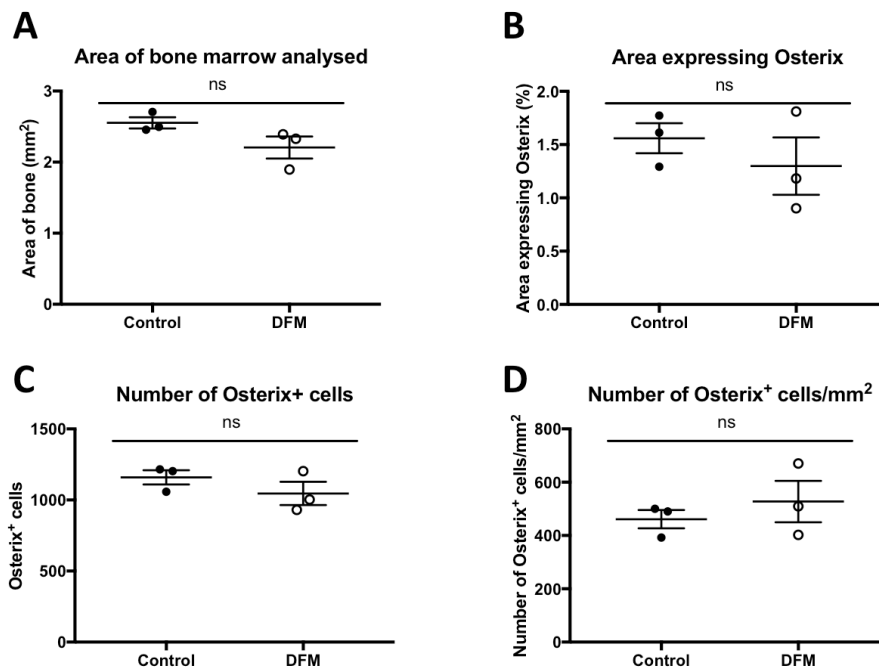
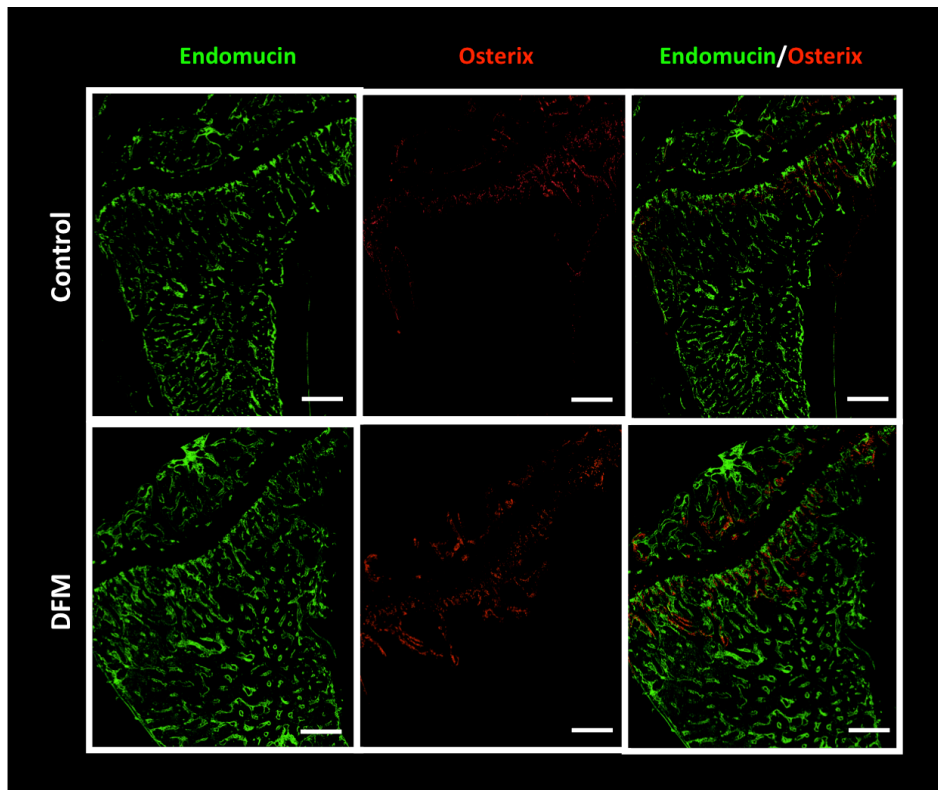


Figure 6.21 Effect of DFM treatment on Osterix⁺ cells

Immunofluorescent staining against Osterix and Endomucin performed on 30 μ m tibia section of animals receiving vehicle control or DFM treatment for three weeks. Green=Endomucin and red=Osterix (A) Area of bone marrow analysed. (B) Percentage area of bone marrow expressing Osterix. (C) Overall number of Osterix⁺ cells and (D) Osterix⁺ cells/mm². Graphs show mean \pm SEM (n=5 animals and 3 bones analysed/group), Student t-test, ns is not-significant. Scale bar 200 μ m.

6.5.2.2 Effect of DFM treatment on bone microvasculature

6.5.2.2.1 Endomucin⁺ vessels

Endomucin is an endothelial marker expressed in the microvasculature of the entire bone marrow. Changes in the percentage of expression of this marker have been studied using the immunofluorescent protocol described in section 2.13. Images were captured using the Zeiss AiryScan confocal microscope and Aperio ImageScope used to quantify the number of H- and L-vessels, their length and the portion of bone marrow area occupied by these different vessel sub-types.

The area of bone marrow analysed was $2.341 \pm 0.0712 \text{mm}^2$ control and $2.194 \pm 0.185 \text{mm}^2$ for the DFM group ($p=0.4986$)(figure 6.22). Interestingly, in animals treated with DFM there appears to be a reorganisation of the microvascular network, resulting in a increase in the area of bone marrow occupied by H-vessels and a reduction in the area occupied by L-vessels compared to the controls, but this trend did not reach statistical significance ($p=0.0957$ and $p=0.0976$ for H- and L-vessels respectively)(figure 6.22).

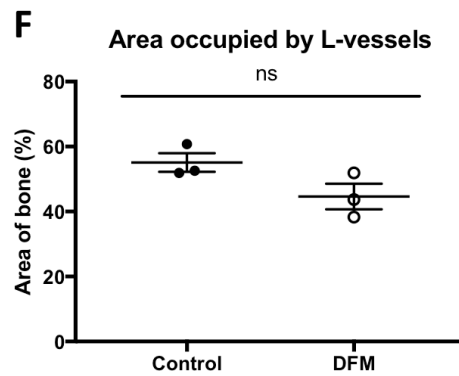
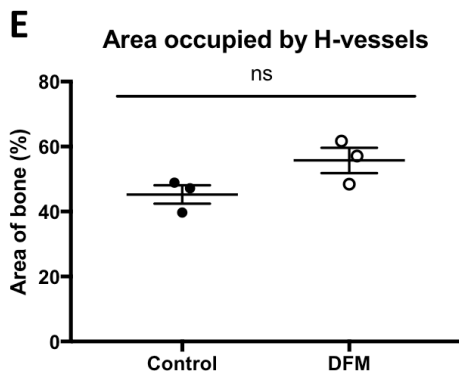
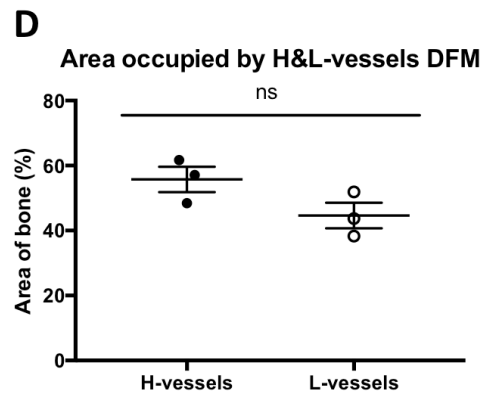
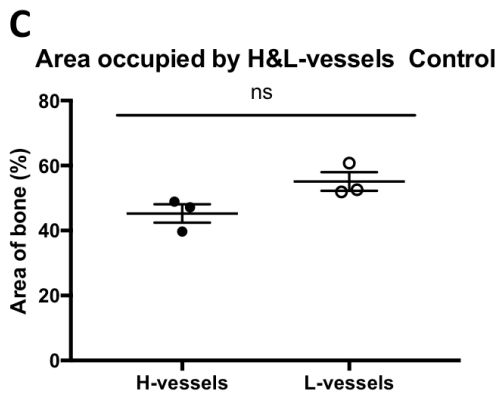
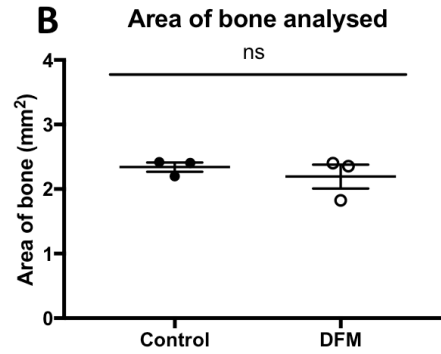
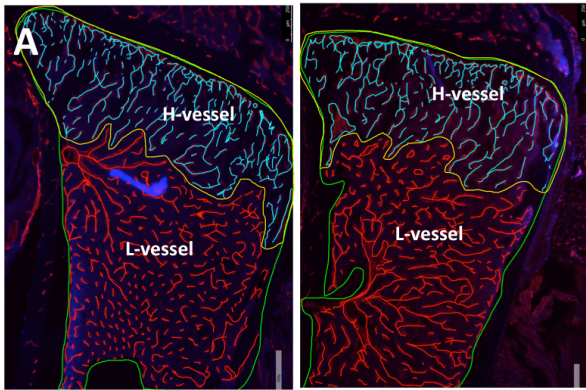


Figure 6.22 Quantification of immunofluorescent staining against Endomucin after treatment with DFM

vessels (red) manually tracked with Aperio ImageScope software. Area of bone marrow analysed is drawn in green and its quantification is shown in (B). (C) and (D) show the percentage area of bones occupied by H- and L-vessels in control and DFM treated animals respectively. (E) and (F) show the percentage area of bones occupied by H- and L-vessels in the different groups. Graphs show mean \pm SEM (n=5 animals and 3 bones analysed/group), Student t-test, ns is not-significant.

The total number of vessels/mm² of bone was not affected by DFM treatment ($p=0.3838$). Surprisingly, the changes in the organisation of the vascular network did not alter the total number of vessels/mm² or the number of H- and L-vessels/mm² in the total bone analysed ($p=0.8233$ and $p=0.4199$ respectively)(figure 6.23). However, the ratio between H- and L-vessels in animals treated with DFM was altered, control animals had a significant higher number of L-vessels than H-vessels ($p=0.0235$) while treated animals lost this characteristic, exhibiting a more even distribution of the two vessels sub-types ($p=0.1653$)(figure 6.23). The characteristic higher number of L-vessels compared to H-vessels was restored when the vessel sub-types were normalised to the area of bone marrow that they covered, with no difference observed between treatment groups in the number of H- and L-vessels/mm² of bone marrow area occupied by the vessel sub-type ($p=0.1298$ and $p=0.5076$ respectively)(figure 6.23). Irrespective of treatments L-vessels/mm² were more abundant than H-vessels/mm² ($p=0.0073$ control and $p=0.0070$ DFM)(figure 6.24).

No differences were detected between DFM treated and control animals in the average vessel length (μm) of the vessels analysed ($p=0.6356$ control and $p=0.52936$ DFM)(figure 6.24).

Taken together these results shows that DFM treatment only marginally modifies bone the microvasculature. The H-vessels, characteristic of the bone metaphysis, appears to be extended towards the bone diaphysis area in DFM treated animals compared to controls. Surprisingly, this change altered the ratio between H- and L-vessel number of the total bone analysed, loosing the characteristic ratio in favour of L-vessels when compared to H-vessels.

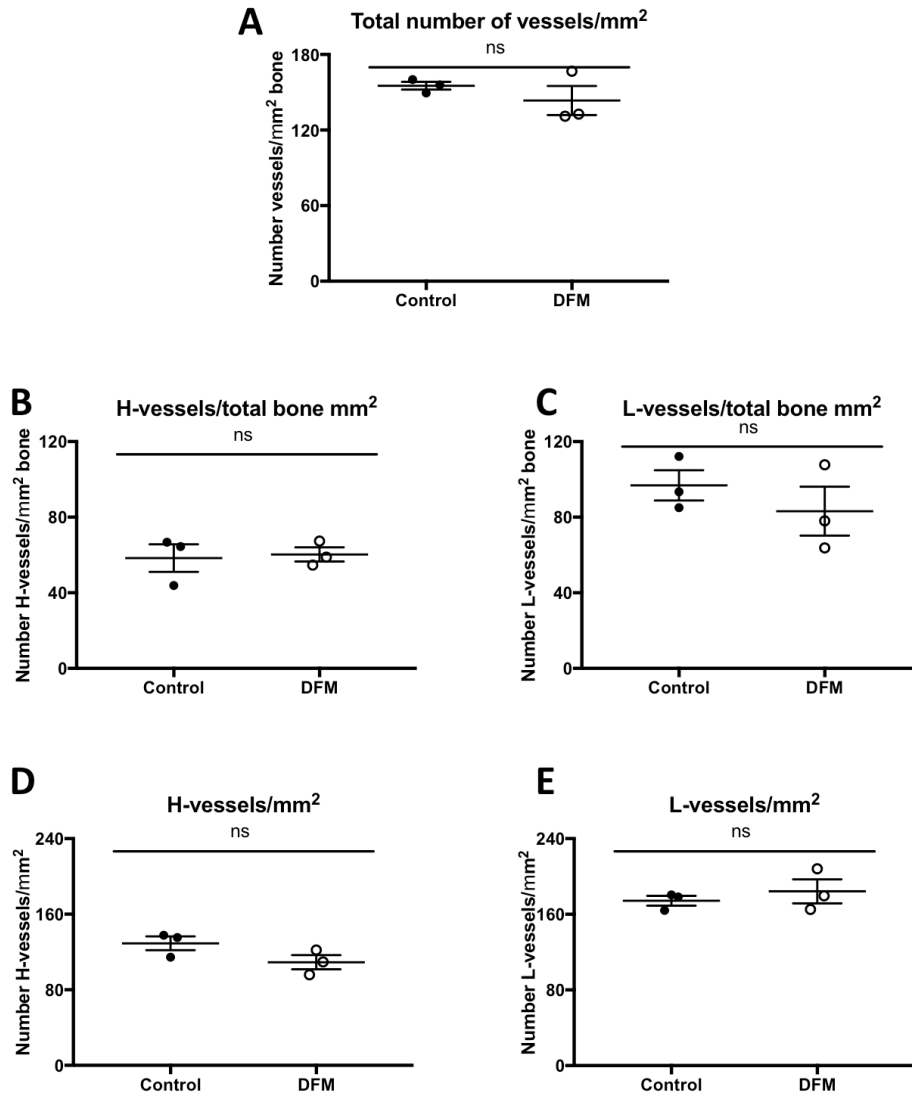


Figure 6.23 Number of vessels quantified in bone marrow after DFM treatment

A) Total number of vessels counted in both groups. (B) and (C) show the number of H- and L-vessels/mm² of total area of bone analysed. (D) and (E) show the number H- and L-vessels/mm² of the area occupied by the different vessel sub-types. Graphs show mean \pm SEM (n=5 animals and 3 bones analysed/group), Student t-test, * $p < 0.05$ and ns is not-significant.

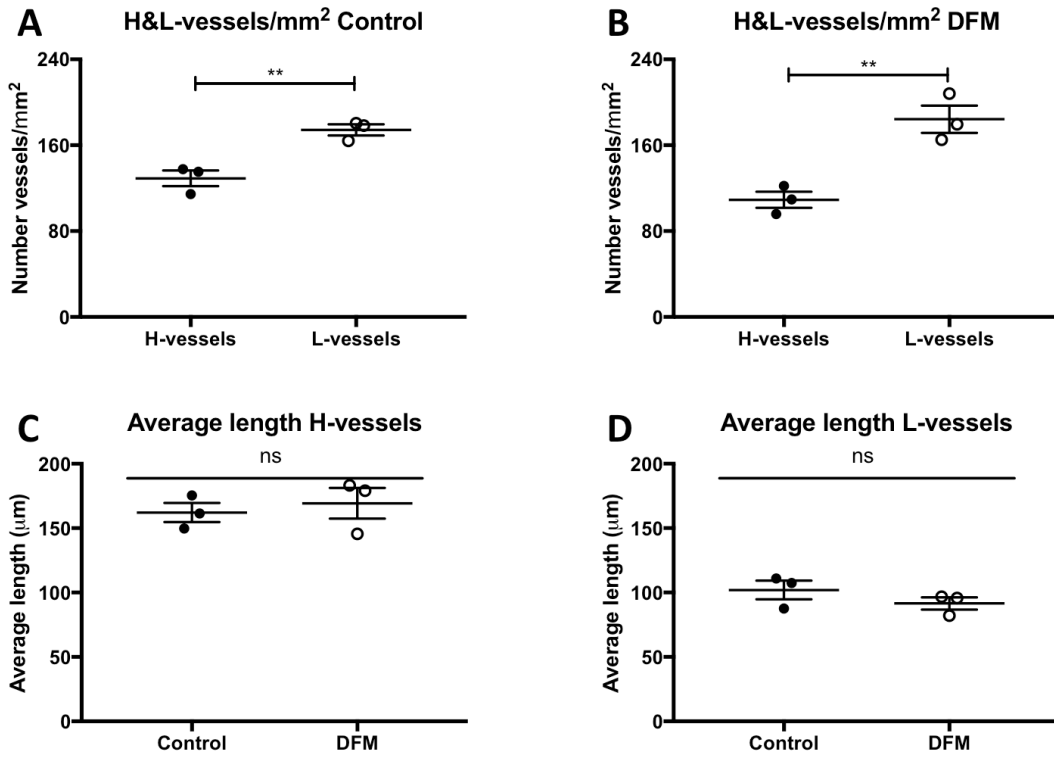


Figure 6.24 Number of H- and L-vessels in different groups and their length

(A) and (B) show the number of H and L- vessels/mm² bone area analysed in control and DFM groups respectively. (C) and (D) show the length of H- and L- vessels between the different groups. Graphs show mean \pm SEM (n=5 animals and 3 bones analysed/group), Student t-test, ** $p < 0.01$ and ns is not-significant.

6.5.2.2.2 CD31⁺ vessels

The HIF-1 α enhancer DFM has been reported to increase the area of established vasculature in aged mice [97]. To visualise modification of the microvascular network and perform quantitative analyses on these changes, 30 μ m thick section of gelatine embedded tibiae were stained with specific antibodies against both Endomucin and CD31 and analysed using the resultant immunofluorescence (figure 6.25).

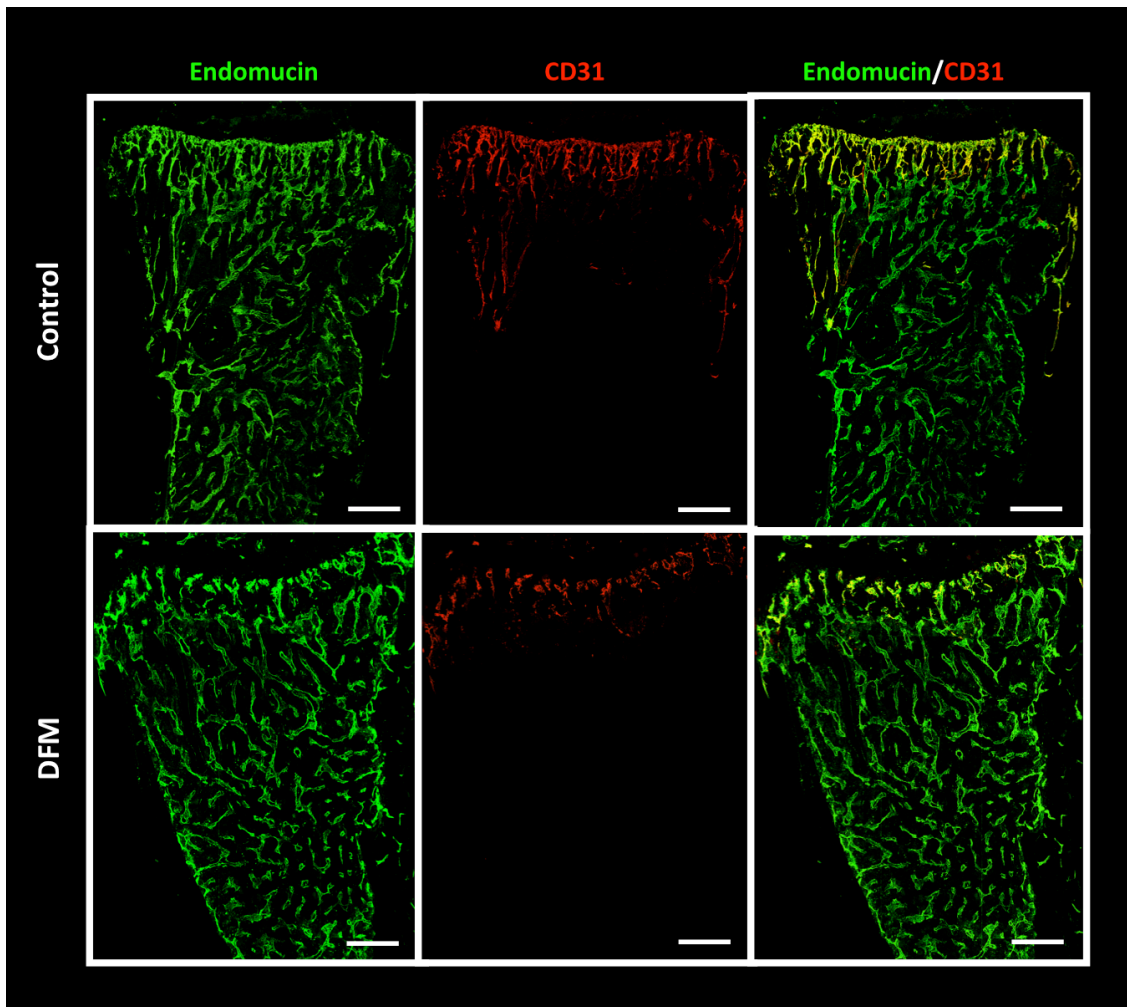


Figure 6.25 Representative image of the effect of DFM treatment on CD31⁺ vessels

Immunofluorescent staining against CD31 and Endomucin performed on 30 μ m tibia section of animals receiving vehicle control or DFM treatment for three weeks. Green=Endomucin, red=CD31 and yellow=Endomucin and CD31. Scale bar 200 μ m.

An area of approximately 2.5mm^2 (2.68 ± 0.11 control and 2.44 ± 0.34 DFM, $p=0.5396$) was imaged using Zeiss AiryScan confocal microscopy and analyses were performed using ImageJ and Aperio ImageScope software. Within the area analysed, no difference was detected in the overall expression of the endothelial cell marker Endomucin between treatment groups ($p=0.3121$)(figure 6.26). As expected, the overall percentage expression of CD31 and Endomucin⁺CD31⁺ vasculature were significantly increased by treatment with DFM ($p=0.0055$ and $p=0.0018$, respectively)(figure 6.26). The number of CD31⁺ vessels in the total area of bone analysed was significantly increased after administration of DFM compared to control ($p=0.0392$). However when the number of vessels/ mm^2 was normalised to the area occupied by this vessel sub-type this was not significant ($p=0.2789$)(figure 6.27). In contrast, the average length of the CD31⁺ vessels was significantly reduced in DFM treated animals compared to controls ($p=0.0282$)(figure 6.27).

In summary, DFM treatment alters the overall expression of CD31 and Endomucin⁺CD31⁺ vasculature. The increased number of CD31⁺ vessels counted within the bone marrow were significantly shorter compared to the control group and had not been quantified in previous studies.

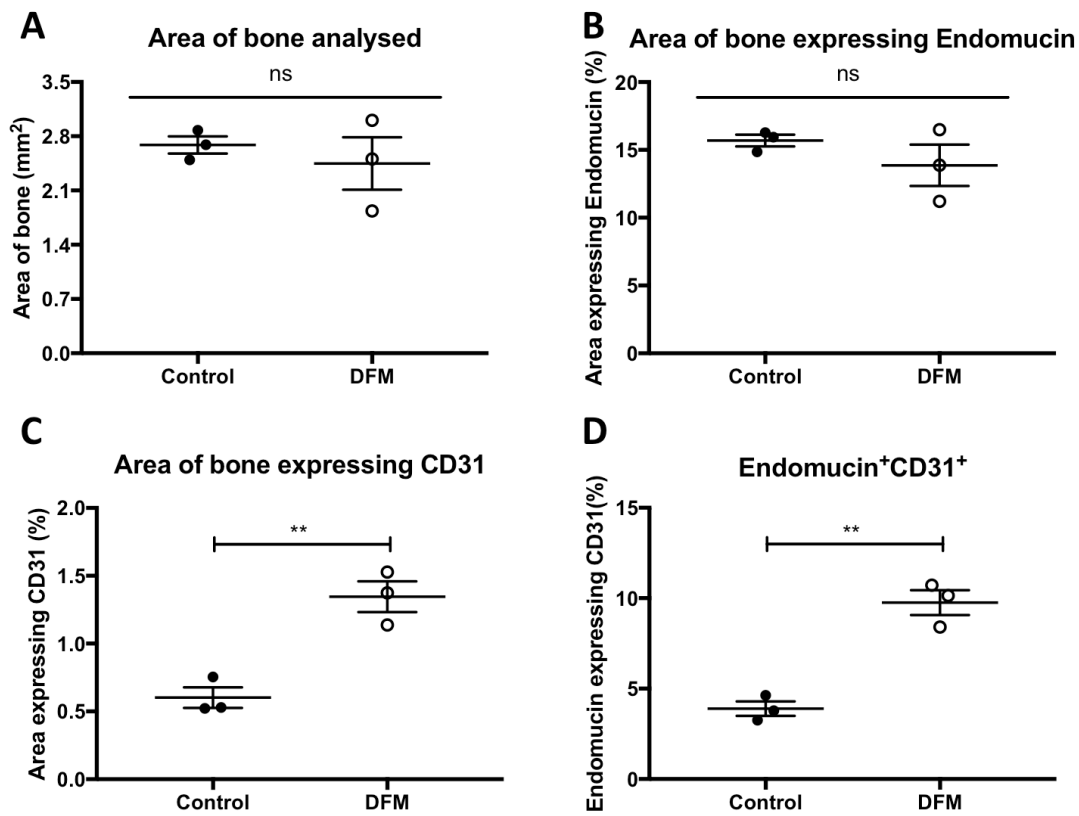


Figure 6.26 Quantification of immunofluorescent staining against CD31

A) Area of bone marrow analysed in the two different groups. B) Shows the overall expression of Endomucin while (C) is the expression of CD31⁺ vessels. (D) Percentage of Endomucin⁺ vessels that also express CD31 in the different groups (H). Graphs show mean \pm SEM (n=5 animals and 3 bones analysed/group), Student t-test, ** $p < 0.01$ and ns is not-significant.

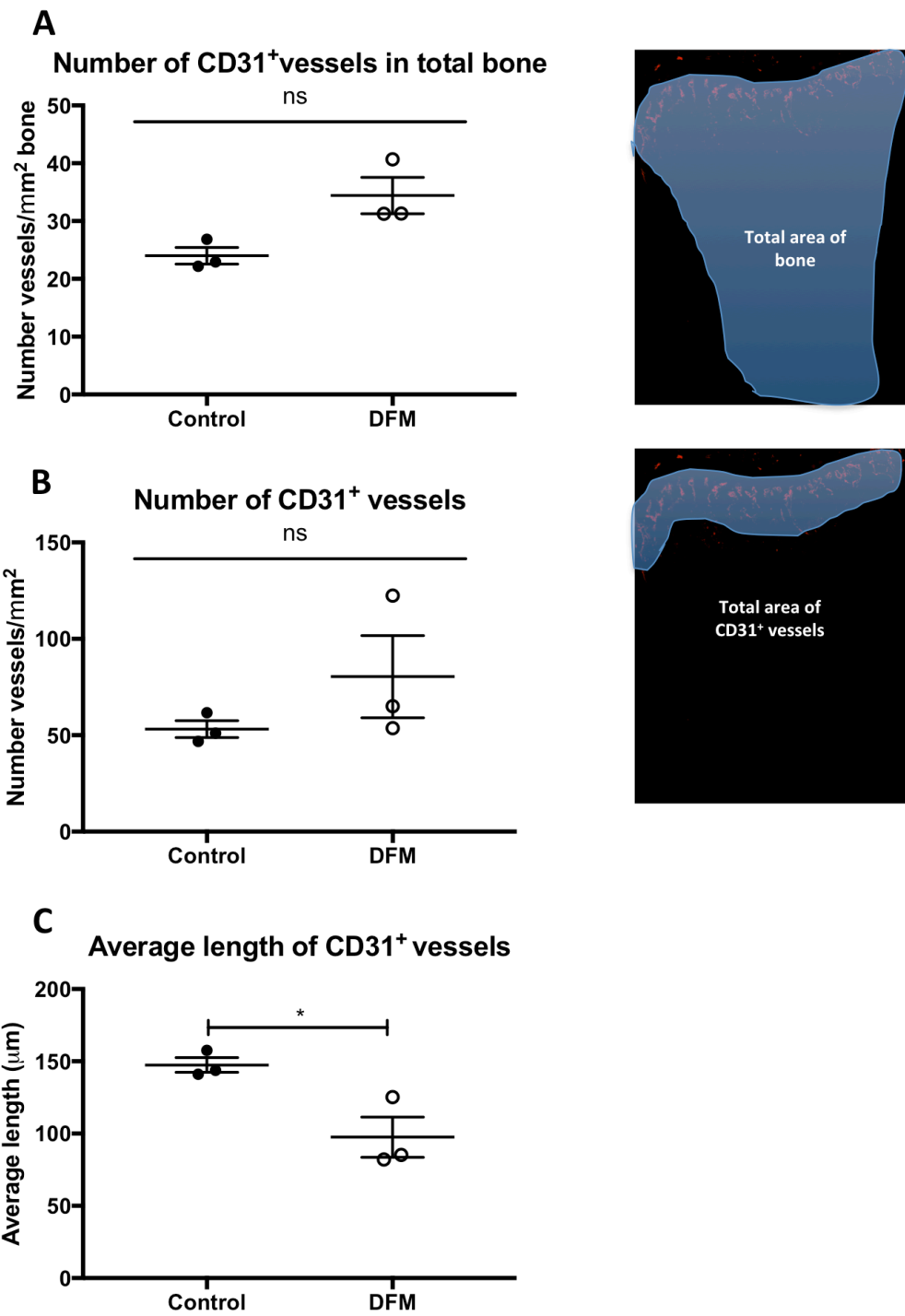


Figure 6.27 Number and average length of CD31⁺ vessels after treatment with DFM

A) Shows the number of CD31⁺ vessels/mm² of total bone and illustration of the area used for this analysis. (B) Show the number of CD31⁺ vessels/mm² of area occupied by the vessels and an image of the area used for this analysis. (C) Displays the average length of CD31⁺ vessels. Graphs show mean ± SEM (n=5 animals and 3 bones analysed/group), Student t-test, ns is not-significant.

6.5.2.2.3 CD34⁺ vessels

To investigate whether treatment with DFM modified the development of new vasculature, tibia sections were stained with antibodies against Endomucin and CD34 using the protocol described in section 2.13 (figure 6.28).

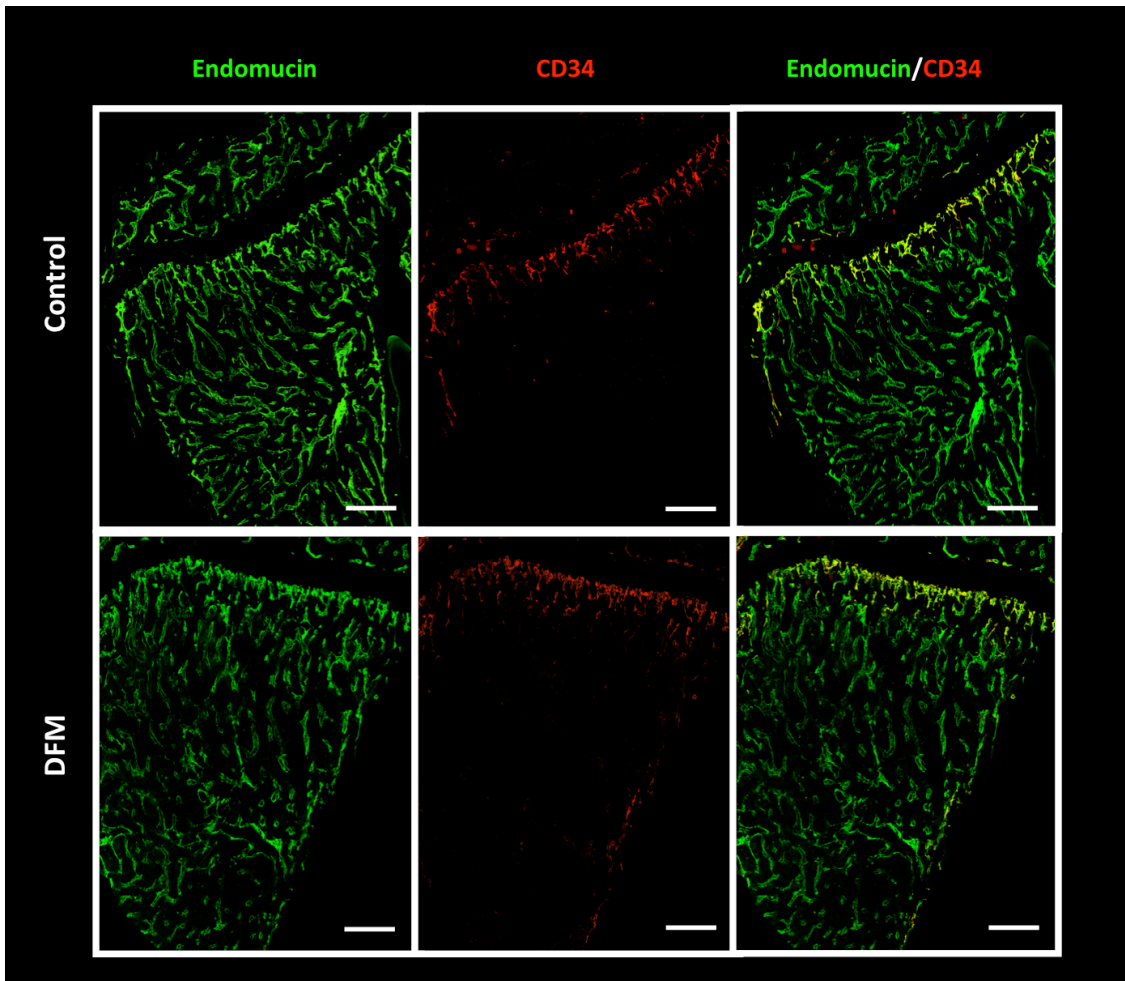


Figure 6.28 Representative image of the effect of DFM treatment on CD34⁺ vessels

Immunofluorescent staining against CD34 and Endomucin performed on 30 μ m tibia sections from animals receiving vehicle control or DFM treatment for three weeks. Green=Endomucin, red=CD34 and yellow=Endomucin and CD34. Scale bar 200 μ m.

A Zeiss AiryScan confocal microscope was used to image the bone marrow area of the stained samples ($2.023 \pm 0.3207 \text{ mm}^2$ control and $2.311 \pm 0.1479 \text{ mm}^2$ DFM, $p=0.4615$), within this area no difference was detected in the overall percentage expression of Endomucin between treatment groups ($p=0.2876$)(figure 6.29). As anticipated, the overall percentage expression of CD34 in animals treated with DFM was increased compared to control, but this did not reach statistical significance ($p=0.0679$). Moreover, DFM administration caused a significant increase in the percentage of Endomucin⁺CD34⁺ vasculature ($p=0.0005$)(figure 6.29).

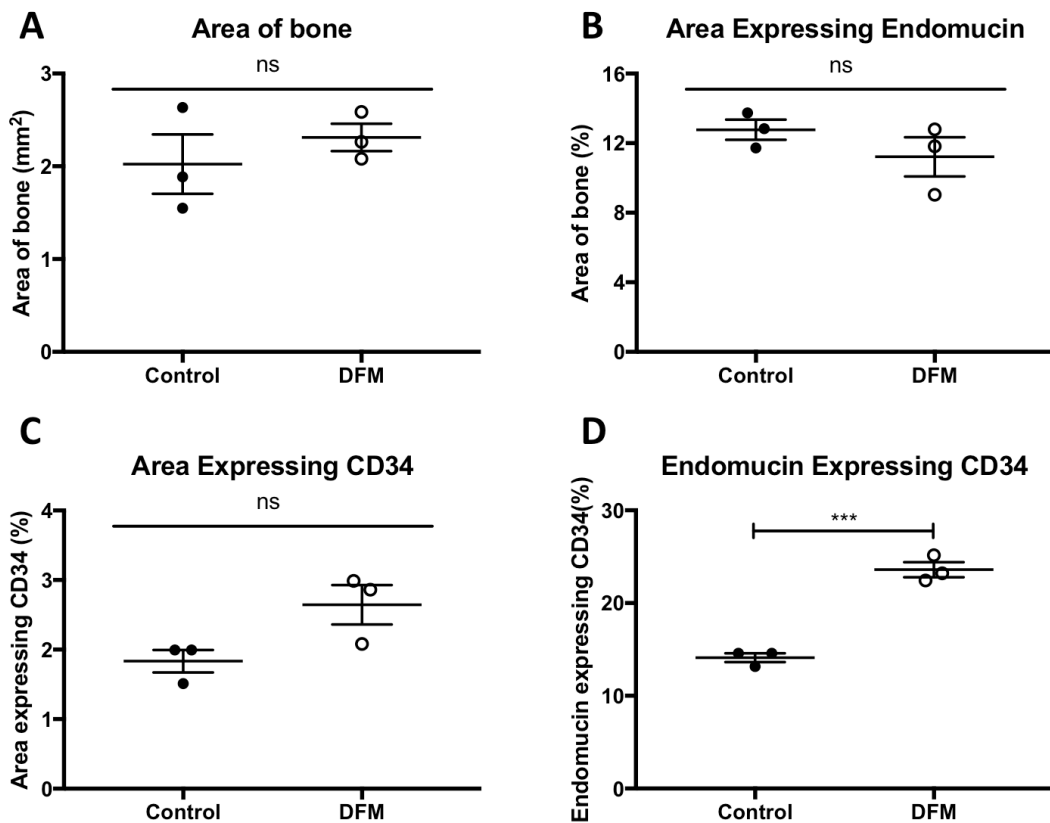


Figure 6.29 Quantification of immunofluorescent staining against CD34

A) Area of bone marrow analysed in the two different groups. B) Overall expression of Endomucin while (C) is the expression of CD34. (D) Percentage of Endomucin⁺ vessels that are also expressing CD34 in the different groups (H). Graphs show mean \pm SEM (n=5 animals and 3 bones analysed/group), Student t-test, *** $p < 0.001$ and ns is not-significant.

To examine whether the increase of percentage expression of CD34 was due to a change in the number of CD34⁺ vessels or in their structure, the number and length of this vessel sub-type were measured by manually tracking using Aperio ImageScope software. DFM treatment did not affect the number of CD34⁺ vessels/mm² of the total surface of bone ($p=0.2584$). However, when the number of CD34⁺ vessels/mm² was quantified only in the area occupied by these vessels there was a significant increase compared to controls ($p=0.0270$)(figure 6.30). Furthermore, the more abundant CD34⁺ vessels appeared shorter in the animals receiving DFM compared to the vehicle control, but this trend did not reach statistical significance ($p=0.0837$)(figure 6.30).

The results presented in this section describe the effect of DFM treatment on newly formed vasculature in bone as identified by CD34. DFM not only increase the overall percentage expression of CD34 but also affected the number of CD34⁺ vessels detected in the bone microenvironment. However, the increased number of CD34⁺ vessels appeared shorter after administration of DFM when compared to control.

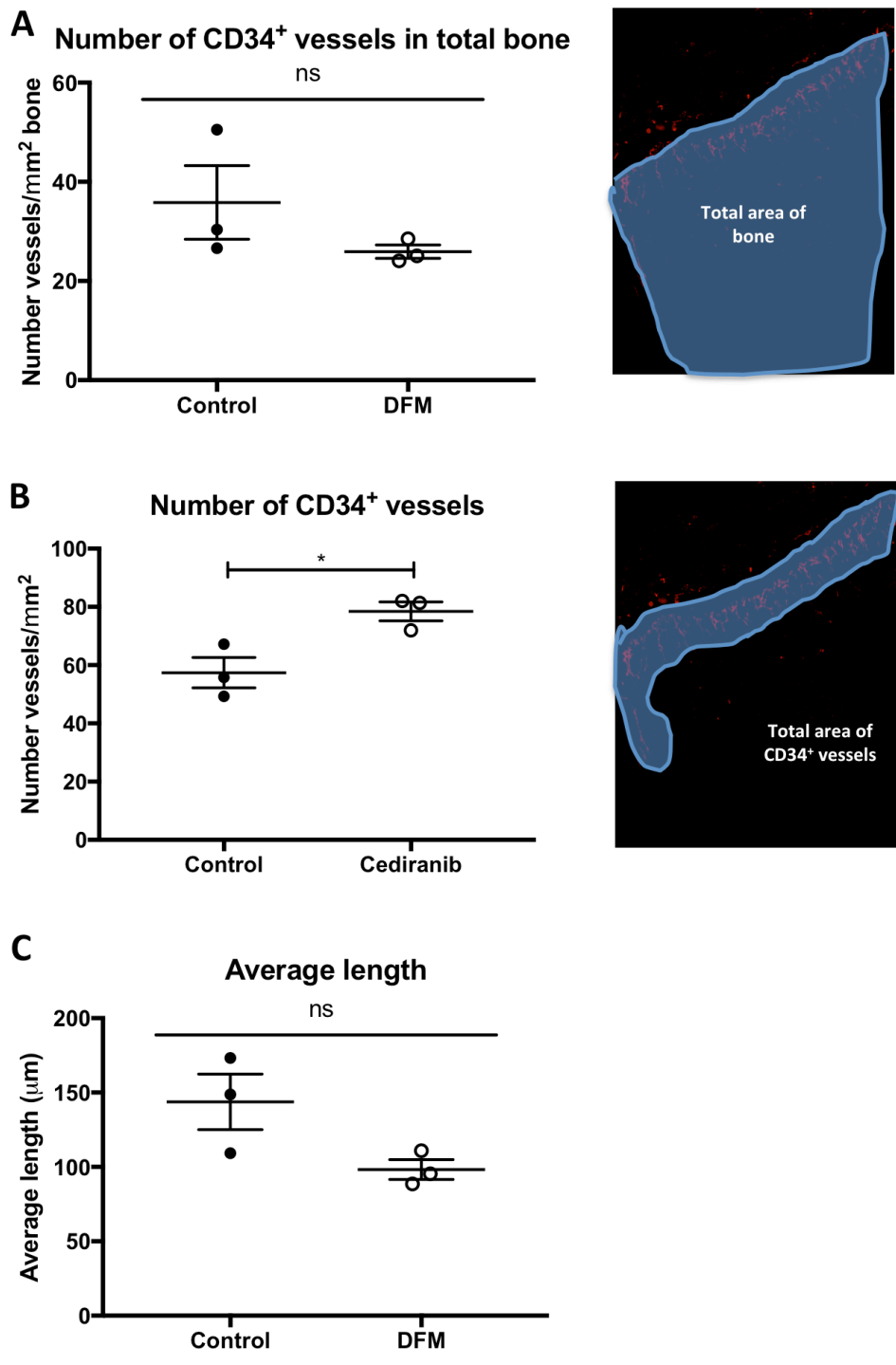


Figure 6.30 Number and average length of CD34⁺ vessels after treatment with DFM

A) Shows the number of CD34⁺ vessels/mm² of total bone and illustration of the area used for analysis. (B) Show the number of CD34⁺ vessels/mm² of area occupied by the vessel sub-type and illustration of the area used for this analysis. (C) Displays the average length of CD34⁺ vessels. Graphs show mean ± SEM (n=5 animals and 3 bones analysed/group), Student t-test, *p<0.05 and ns is not-significant.

6.5.2.3 Effect of DFM treatment on TSP-1 expression

A high expression of TSP-1 and high number of megakaryocytes are detected in a dormancy-supporting microenvironment [35], [110]. Sections of tibia were stained with an antibody against TSP-1 to evaluate the effect of DFM treatment on TSP-1 expression in regions surrounding the microvasculature and in megakaryocytes (figure 6.31).

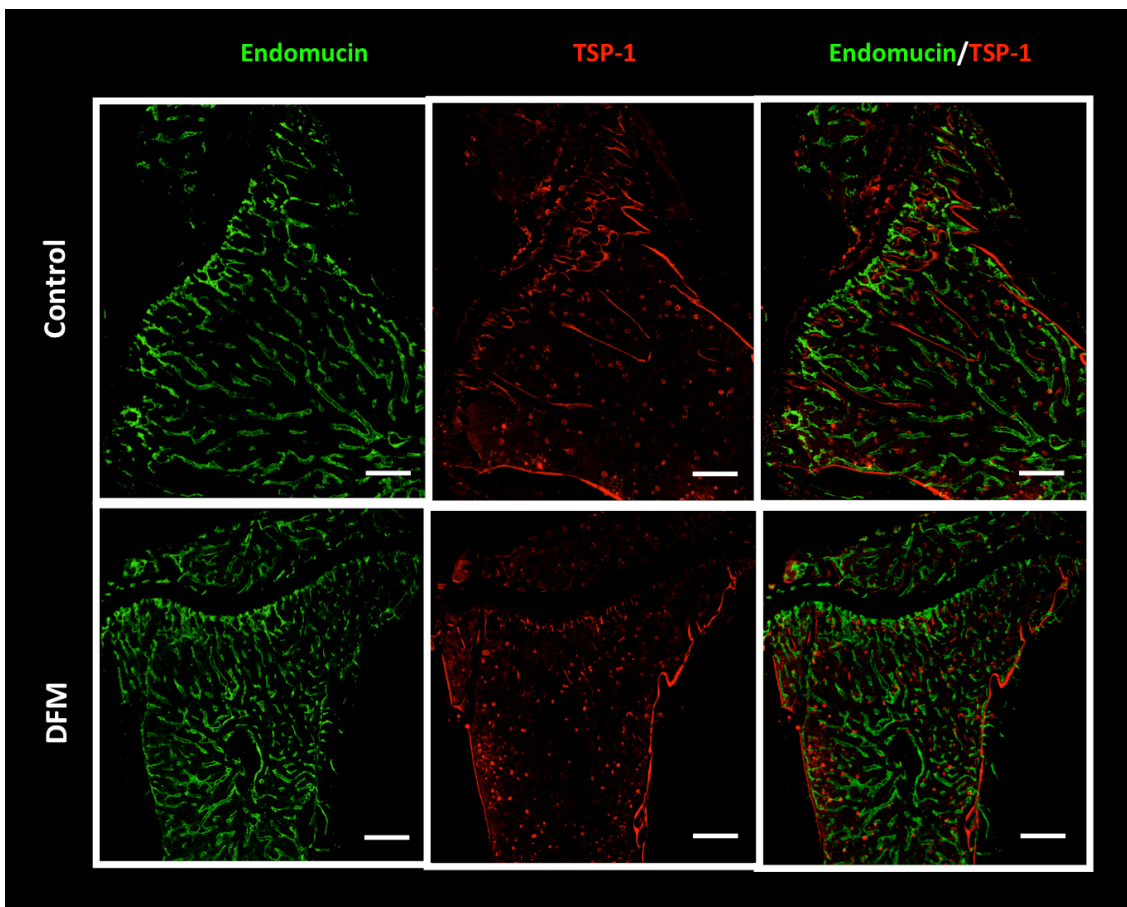


Figure 6.31 Effect of DFM treatment on TSP-1 expression

Immunofluorescent staining against TSP-1 (red) and Endomucin (green) performed on 30 μ m tibia section of animals receiving vehicle control or DFM treatment for three weeks. Scale bar 200 μ m.

The area imaged with Zeiss AiryScan confocal microscope was similar between treatment groups ($p=0.6321$, $2.52\pm 0.33\text{mm}^2$ and $2.35\pm 0.12\text{mm}^2$ control and DFM, respectively). In this area of bone marrow analysed, no changes were observed in the overall percentage expression of TSP-1 ($p=0.9070$) or in the number of megakaryocytes/ mm^2 ($p=0.4005$)(figure 6.32).

These results suggest that the DFM treatment schedule used in this study does not influence the overall expression of the dormancy-supporting marker TSP-1 and the number of megakaryocytes present in the bone microenvironment.

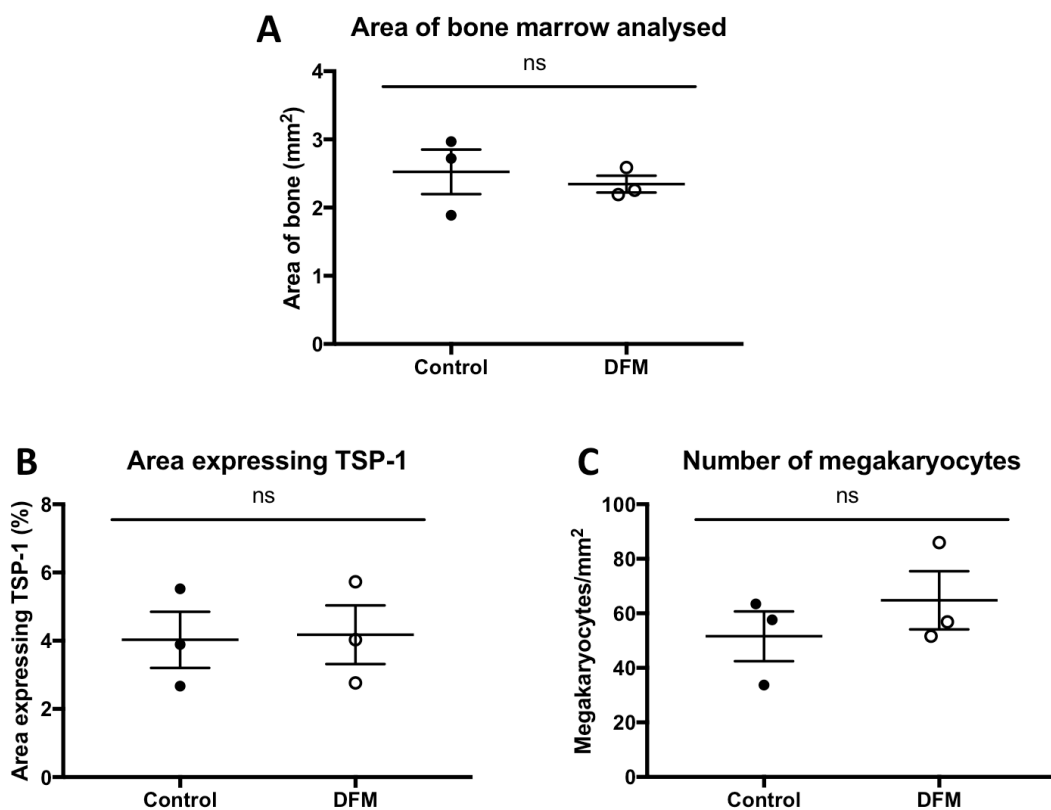


Figure 6.32 Quantification of the effect of DFM treatment on TSP-1 expression

(A) Area of bone marrow analysed. (B) Percentage area of bone marrow expressing TSP=1. (C) Number of Megakaryocytes/ mm^2 . Graphs show mean \pm SEM ($n=5$ animals and 3 bones analysed/group), Student t-test, ns is not-significant.

6.5.2.4 Effect of DFM treatment on breast cancer cell homing to bone

To assess whether the changes in the microvasculature caused by administration of DFM resulted in alteration of the homing of breast cancer cells to bone, BALB/c nude mice treated for six weeks with i.p injection (5 days/week) with 15mg/ml (100µl) of DFM or PBS control were injected i.c. with 0.5×10^5 MDA-MB-231-NW1-Luc2 breast cancer cells labelled with the lipophilic dye Vybrant-CM-Dil and seven days later, femora were collected for two-photon microscopy. Specimens were prepared and analysed as described in section 2.10.

The number of tumour cells homing to the trabecular region of bone (ROI1) or growth plate area (ROI2) was not influenced by the treatment with DFM ($p=0.6557$ and $p=0.6332$ respectively) (figure 6.33). Furthermore, the preferential pattern of homing towards ROI1 compared to ROI2 was maintained in both treatment groups, but did not reach significance level (80.38 ± 18.9 and 33.34 ± 18.45 cells/mm³ ROI1 and ROI2, $p=0.1052$ control; 68.93 ± 14.87 and 49.74 ± 29.03 cells/mm³ ROI1 and ROI2, $p=0.5724$ DFM)(figure 6.33). Irrespective of the area of bone colonised and treatment received, breast cancer cells located in close proximity to the nearest bone surface. The average distance to the nearest bone surface in ROI1 was $39.04 \pm 11.03 \mu\text{m}$ in the control animals and $36.62 \pm 4.98 \mu\text{m}$ in DFM treated ($p=0.8564$) and these values reduced even more in ROI2 with $2.08 \pm 1.09 \mu\text{m}$ and $6.14 \pm 4.69 \mu\text{m}$ for control and DFM respectively ($p=0.5023$)(figure 6.33). As expected, tumour cells colonising the bone microenvironment did not home close to other cancer cells ($134.5 \pm 9.24 \mu\text{m}$ control and $254.1 \pm 87.66 \mu\text{m}$ DFM, $p=0.2117$ ROI; $206.10 \pm 112.90 \mu\text{m}$ control and $46.22 \pm 40.59 \mu\text{m}$ DFM, $p=0.3615$ ROI2)(figure 6.33).

Taken together, the data indicate that DFM does not affect the pattern of homing of breast cancer cells to bone. Irrespective of treatment, tumour cells prefer to locate in the trabecular region of bone compared to the growth plate area and they locate in close proximity to the bone surface and maintain a clear distance from the nearest cancer cell.

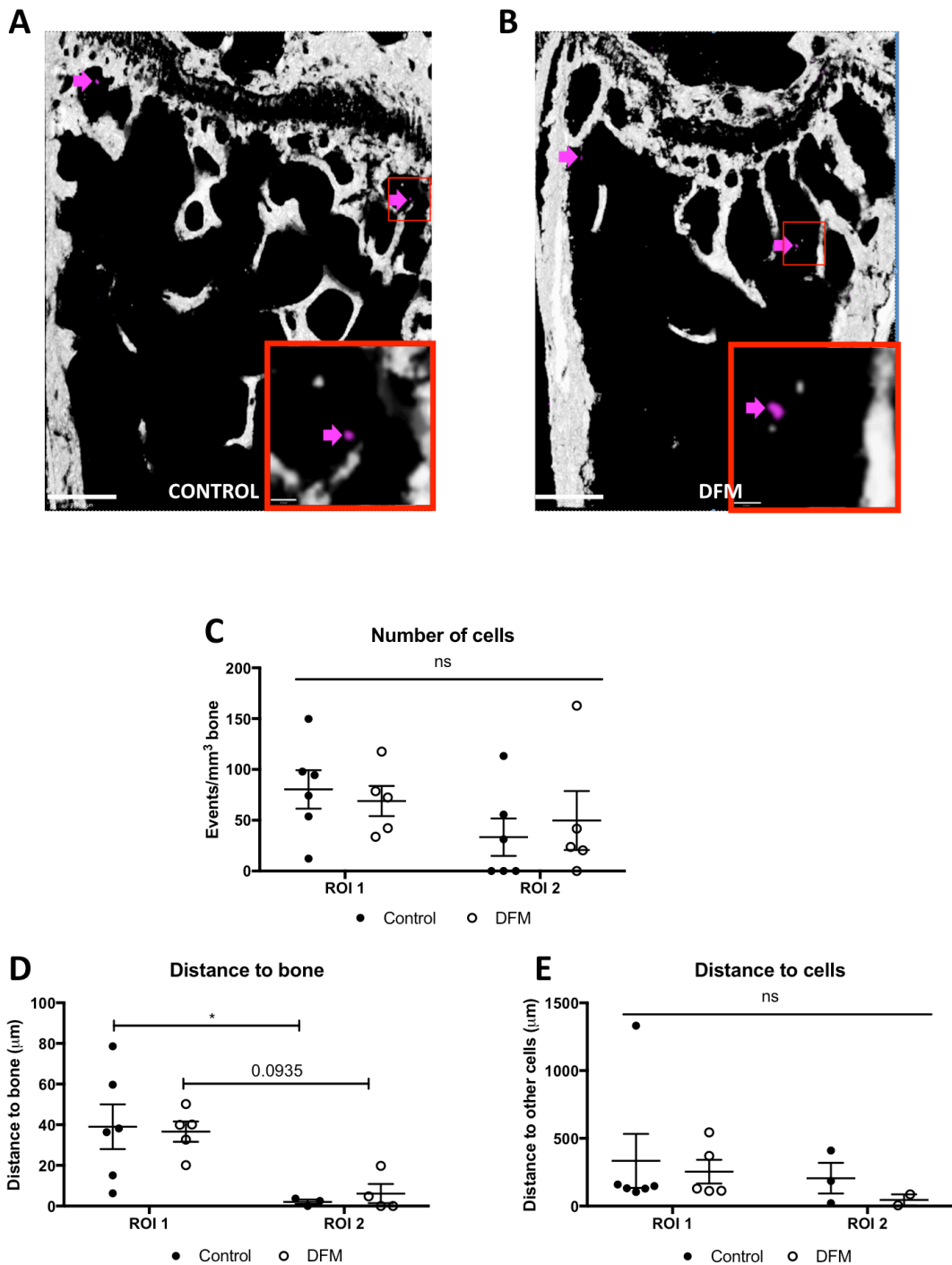


Figure 6.33 Homing of breast cancer cells in animals treated with DFM

(A) and (B) are examples of two-photon scans of control and DFM treated animals showing bone (white) and Vybrant-CM-Dil⁺ cells (pink and pink arrows). (C) Graph shows the number of MDA-MB-231-NW1-Luc2 cells detected in the two groups at both ROIa. (D) Distances of the tumour cells to the nearest bone surface. (E) Distances to the nearest bone surface and the nearest tumour cell in ROI1. Graphs show Mean \pm SEM (n=5 animals/group, 6 bones analysed control and 5 bones analysed DFM), Two-way ANOVA and Tukey post test, * $p < 0.05$ and ns is not-significant.

6.6 Discussion

The main aim of this chapter was to investigate whether alteration of the microvascular activity using pharmacological agents would result in changes in the bone microenvironment and/or in the homing of breast cancer cells to bone. I found that the microvascular activity in bone was reduced by administration of Cediranib and increased by treatment with DFM, as would have been predicted from previous studies.

Components of the bone microenvironment investigated in this chapter were the bone structure (trabecular bone volume, trabecular thickness and trabecular number) analysed by μ CT, the proteoglycan-rich extracellular matrix assessed by Toluidine blue staining and osteroprogenitor number investigated by immunofluorescent staining. Immunofluorescent protocols were also used to determine the effects on different vessel sub-types (Endomucin⁺, CD31⁺ and CD34⁺ vessels) and on the expression of the dormancy supporting molecule TSP-1. The number and location of Vybrant-CM-Dil labelled breast cancer cells homing to the bone microenvironment were analysed by two-photon microscopy.

Cediranib treatment did not alter the bone components of the niche and has only a marginal effect on the microvascular network, consequently it was expected to not observe a change in the pattern of homing of breast cancer cells to bone. No modification of bone structure was observed in animals treated with DFM, while several changes were detected in the microvasculature of these animals. Even though one important component of the metastatic niche was altered by the administration of DFM (the perivascular niche), this modification did not affect the characteristic pattern of homing of tumour cells to bone. However, this change could potentially influence the later stages of metastasis development.

The efficacy of Cediranib as pan-VEGF tyrosine kinase inhibitor has been broadly studied [168], [247], [248], showing an anti-tumour effect against a range of tumours [168]–[170], [249]. Wedge and colleagues reported that a dose of 0.75mg/kg/day for 21 days, treatment starting when tumours were 0.2cm³ was effective in inhibiting subcutaneous tumour growth in xenograft models of lung, colon, ovary, prostate and breast cancer. Moreover between 91-100% tumour growth inhibition across the

different tumours analysed, was achieved by increasing the dosage to 6mg/kg/day [168]. The anti-tumour effect of Cediranib was coupled with a dramatic reduction in the tumour-associated vasculature reflecting the *in vitro* studies of inhibition of vessel sprouting following treatment with Cediranib [168].

In the clinical setting Cediranib has been shown to be well tolerated and to have anti-tumour effects, reducing the growth of solid tumour both as monotherapy or in combination with other treatments [165], [176]–[178], [250], [251]. Some of these clinical trials are focused on the treatment of different sub-types of breast cancer, locally advanced and inflammatory [165], hormone-sensitive [176] and triple-negative breast cancer [178]. The effect on breast cancer varied in the different clinical studies; limited activity was observed in triple-negative breast cancer patients treated with a combination of Cediranib and the PARP inhibitor Olaparib [178], while an increase in progression free survival was registered for patients with hormone-sensitive breast cancer treated with Cediranib and Fulvestrant [176]. The clinical data on hormone-sensitive breast cancer reflect what was reported from previous *in vivo* studies [252]. Cediranib inhibited the progression of MCF-7 implanted mammary fat pad tumours and the efficacy of the drug was increased in tumour developed from MCF-7 cells overexpressing VEGF [252].

Even though the anti-angiogenic and anti-tumour action of Cediranib has been widely studied, little is known about the effect of this drug outside the tumour microenvironment. It is known that VEGF signalling is important for the coupling of angiogenesis and osteogenesis [253] therefore, it was not surprising that treatment with Cediranib resulted in an expansion of the hypertrophic chondrocyte zone of the growth plate area of long bones in rats [168]. This effect was observed with a range of doses (1.5–6mg/kg/day) with the treatment being used for 28 days. The animal model used in the study presented in this chapter received a dose of 3mg/kg 5 days/week for 21 days and no effect was seen on the bone structure (μ CT), osteoprogenitors presence (immunofluorescent staining against Osterix) or growth plate extension (toluidine blue staining). The difference between the data reported in the literature and my study may be due to the shorter period of administration of Cediranib and that the dosing was not continuous for the 21 days of treatment (5 days/week).

Furthermore, I only used a small number of animals in this study that resulted in variable data, which could be another reason accounting for the discrepancy between data found in literature and the results here described.

There is also little known about the effect of Cediranib on the microvasculature network in bone. The few published studies consider the vasculature mainly in the context of prostate cancer bone metastasis. It has been shown that daily gavage of 5mg/kg of Cediranib treatment reduced the intraosseous growth and associated bone response of platelet-derived growth factor D (PDGF D) overexpressing prostate cancer cells injected intratibially in 5-week old SCID mice, and this effect was enhanced when administered in combination with docetaxel [254]. An *in vivo* model of prostate cancer bone and brain metastasis showed an increase in overall survival after the treatment with 6 mg/kg/daily for 5 weeks of Cediranib, while this result was not achieved using the agent as a preventive treatment [171]. Beneficial effect of Cediranib on prostate cancer bone metastasis has also been recorded in the clinical setting where Cediranib administered as monotherapy increased the progression-free survival [251]. Moreover, bone metastasis were inhibited in both the preventive and the treatment (for 3 weeks) settings using Cediranib (6mg/kg/day), while brain metastasis were inhibited only with continuous dosing [171]. These data suggest that treatment with Cediranib, maintains the dormant state of tumour cells that reach the bone microenvironment even after the end of the treatment. This is in contrast with the lower level of TSP-1 detected in treated animals in our study, however it was in line with the two-photon microscopy results indicating that pre-treatment with Cediranib does not alter the number of breast cancer cells reaching the bone microenvironment. Further investigations are required to understand the fate of the tumour cells located in the bone metastatic niches. Another aspect that needs clarification is the increase expression of CD34 in animals treated with Cediranib compared to controls, but this data can not be compared to any other data found in literature because vascular density has mostly be reported in the tumour microenvironment or tumour bearing animals and not in a non-tumour bearing model.

The HIF-1 α enhancer Deferoxamine mesylate (DFM) is used in the clinical setting as an iron chelator in the case of iron overdose due to multiple blood transfusions or genetic

condition such as thalassemia and aluminium toxicity in people in dialysis. HIF-1 α is involved in physiological and pathological angiogenesis, such as wound healing and tumour angiogenesis [255], [256]. For this reason DFM has been studied in the pre-clinical settings for its pro-angiogenic properties. *In vitro* studies showed that treatment with 0-100 μ M DFM significantly increased the tubule formation by CD34-positive cells isolated from the bone marrow of 6- to 8-week-old male nude mice [184], human aortic endothelial cells [185] and human umbilical vein endothelial cells [257]. Moreover, this pro-angiogenic property has also been reported *in vivo*; DFM has been tested for its efficacy to restore blood flow after hind limb ischemia in mice [184], [185] and for wound healing properties in diabetic rats [257]. Angiogenesis and osteogenesis are tightly coupled processes, therefore the action of DFM on the bone structure has also been investigated. Kusumbe and colleagues reported that treatment with DFM 15mg/ml/mouse every other day for 4-6 weeks in aged mice resulted in an expansion of H-vessels and an increase in bone volume [97], [221]. Li *et al.* showed that administration of DFM activated HIF and the downstream expression of VEGF was amplified, leading to increased angiogenesis and bone repair of steroid-induced osteonecrosis in the femoral head of rabbits [186]. Donneys and colleagues reported the dual action of DFM as a pro-angiogenic and osteogenic drug using a rat *in vivo* model of mandibular distraction. Treatment with DFM resulted in an increased bone volume measured by μ CT and an improved vascular response visualised with injection of Microfil [193]. Moreover, the mandibular fracture model was used also to detect the effect of DFM on the osteocytes after radiotherapy, and these *in vivo* studies determined that DFM had the ability to reverse the anti-angiogenic effects of radiation [190], [192].

The data reported in this Chapter are in agreement with the literature. The animals treated with DFM had an increased expression of the CD31 (mature) and CD34 (immature, proliferating) endothelial markers and the H-vessel network was expanded compared to that of the control animals [97]. However, in our animal model no difference in the bone structure or osteoprogenitor number was detected between the two groups. Matsumoto and colleagues reported that administering DFM to mitigate the reduction of osteogenesis caused by unloading, successfully stimulated

the bone microvasculature but this effect was not associated with a complete restoration of the bone structure [187], suggesting that this was due to an inadequate dosage of DFM. In my *in vivo* study the lack of modification of the bone structure could be in part due to the dose used or to the low number of samples analysed.

It has been shown that treatment with 5-100 μ M of DFM for 7 days induced apoptosis and arrested the growth of tumour-associated macrophages, mesenchymal stromal cells [258], and acute myeloid leukaemia cells [259]. *In vivo* DFM treatment showed an increase in the survival and decrease in tumour size of acute myeloid leukaemia models, however Duarte and colleagues observed higher number of HSCs in the trabecular region of bone of treated mice and an improvement of HSCs homing to the bone marrow [196]. The increased homing of HSCs to the bone niche should be taken into consideration in the treatment of breast cancer patients since the mechanism of homing of breast cancer cells is thought to be similar to the one utilised by the HSCs. Moreover, *in vitro* studies reported an enhanced DFM-mediated migration and invasion in MDA-MB-231 breast cancer cells [194]. The pre-treatment setting used in my *in vivo* study did not alter the homing of cancer cells to bone compared to the control animals, but further analyses are needed to understand whether continuous administration of DFM could increase the tumour cells able to seed in the bone microenvironment or modify the tumour progression.

Collectively, my data did not show substantial changes in either the bone or the microvasculature structure. Moreover, these analyses were focused on changes caused by the pharmaceutical agent on the capillaries network, alteration of arteries and veins have not been investigated. Further analyses are needed to understand whether treatment with these drugs would be beneficial in the treatment of metastatic breast cancer.

Chapter 7

Discussion

7.1 Discussion

Advanced breast cancer is associated with high mortality and development of secondary disease. Breast cancer preferentially colonises the skeleton, resulting in a considerable decrease in patient quality of life. To date, treatments are focused on the latest stages of bone metastasis when there are already established lesions and therapeutic interventions are only palliative. The metastatic process consists of several steps, which are all influenced by the cross talk between cancer cells and different components of the bone microenvironment. Thus, a better understanding of the response of the microenvironment to the therapeutic approaches may improve the treatments for the secondary disease. It has become clear that, when arriving in bone, breast cancer cells locate in a putative metastatic niche, which is thought to comprise of the overlapping HSCs, endosteal, and perivascular niches [34], [39]–[41]. Interactions of the components of these niches and tumour cells have therefore been increasingly investigated for the development of new therapeutic treatments that target both cancer cells and the microenvironment. Current standard of care for breast cancer bone metastasis involves the use of anti-resorptive agents, such as Zoledronic acid (ZOL), moreover novel agents, such as TKI inhibitors (i.e. Cediranib), are achieving promising results in pre-clinical and clinical settings indicating that targeting the tumour microvasculature could be an effective approach. A better understanding of the early stages of the metastatic process would allow the development of therapies targeting the DTCs in bone before the establishment of cancer-induced bone disease, thus improving the patients' quality of life and overall survival.

Work presented in this thesis has utilised *in vivo* models and novel methodologies to (i) investigate the homing of breast cancer cells to bone, (ii) characterise the microenvironment in which tumour cells seed and (iii) determine the response of both the microenvironment and the homing of breast cancer cells to therapeutic agents.

Homing of breast cancer cells to the bone microenvironment

The recent technological advances both in cell labelling and imaging allows research to focus investigations on the early steps of bone colonisation [25]. Two-photon microscopy has been used to visualise single tumour cells colonizing the bone in myeloma [260], prostate cancer [24], [26] and breast cancer [118] models, however the majority of published studies focus only on one cancer cell line and one route of injection. The work presented in Chapter 3 of this thesis represents a more comprehensive investigation involving several breast cancer cell lines and route of injections. Wang *et al.* described the homing of prostate cancer cells to the bone microenvironment indicating that Vybrant-DiD labelled PC3 cells colonise the osteoblast-rich area of the bone with a preferential pattern of homing towards the lateral bone surface [26]. The current investigations did not discriminate between the lateral and medial sides of the bone to allow the determination of whether breast cancer cells locate in area where both osteoblasts and vessels reside, with the latter component of the metastatic niche being equally present on both sides of the bone. Therefore, the regions of interested were divided into the trabecular bone region (ROI1) rich in osteoblasts, osteoclasts and vessels, and the growth plate area (ROI2) consisting principally of chondrocytes and extracellular matrix with no vascularisation.

As hypothesized, breast cancer cells were mainly located in ROI1 compared to ROI2, irrespective of ER status, route of injection or lipophilic membrane dye used to label the cells. Intriguingly, only a small number (<100 cells/bone) of the breast cancer cells injected in the animal models (1×10^5 /mouse) could be detected the bone microenvironment. Valkenburg *et al.* using the intracardiac route of administration 1×10^6 MDA-MB-231 cells to immunocompromised mice, harvested the bone marrow 3 and 5 days post injection [261]. Bone marrow was centrifugated and red blood cells lysed, marrow solution was then washed in PBS and resuspended in a solution containing 3×10^6 cells. Samples were later stained with an antibody against human leukocyte antigen (HLA) and the number of cells positive for this marker was counted using an automatic slide scanner. The results obtained from day 3 post injection were comparable with those presented in Chapter 3 using the two-photon microscopy technology with <50 breast cancer cells detected. At 5 days post injection

approximately 500 MDA-MB-231 cells/ 3×10^6 bone marrow cells were detected; this value is considerably higher than I observed, however still indicates that only a small number of the tumour cells injected (1×10^6) home to and survives in the bone microenvironment [261]. It has been shown in several studies that the presence of high number of DTC in bone marrow aspirates is associated with a poor prognosis in breast cancer [262]–[265]. However the study of sufficient numbers of patients samples is not always achievable therefore to improve the knowledge of the early steps of the metastatic process model systems are required.

Previous work has highlighted that tumour cells and HSCs may use the same mechanism(s) to home to bone and are thought to localise to the same region of bone. Moreover, a theory has been proposed that assumes the presence of a niche(s) which has the capacity to retain HSCs, their progenitors and other cells compatible with that specific microenvironmental niche, including tumour cells [16], [26], [36], [78], [79]. This hypothesis of the ‘equivalent’ niche, introduces the concept of cellular competition for the limited space available within the niche [41], [165]. Shiozawa and colleagues elegantly demonstrated that prostate cancer cells locate in the same niche(s) occupied by HSCs. In their experiments, treatment with the CXCR4 antagonist AMD3100 resulted in a mobilization of HSCs in the circulation, and in a higher number of prostate cancer cells (detected by PCR) homing to the bone marrow [36]. Others studies have quantified the homing of prostate cancer cells to bone after treatment with AMD3100 using two-photon microscopy, but did not detect any changes in the number of cancer cells in the bone microenvironment between treatment and control groups [26]. Price *et al.* used *intra-vital* microscopy to detect the homing of ER+ve and ER-ve breast cancer cells to the calvaria of immunocompromised mice after treatment with ADM3100, with no differences identified between treatment groups. However, the parameter measured was ‘bone trafficking’ rather than true cancer cell homing since the images were taken immediately after injection of the cancer cells, and not following seeding in the bone marrow [266]. The use of calvarial bone marrow as site of homing was probably chosen due to the deep-tissue imaging limitation of the *intra-vital* microscopy; however overt metastasis rarely develop in calvaria in preclinical models, in contrast to the long bones, a common metastatic site in both preclinical

models and patients. To my knowledge the work described in Chapter 3, represents the first time that cancer cells competition for the HSC niche, after treatment with AMD3100, has been studied in long bones in a xenograft model of breast cancer. The modification of the bone marrow using AMD3100 resulted in a higher number of breast cancer cells successfully homing to the bone marrow compared with the control group, supporting the theory of an 'equivalent niche' [41], [165] and competition for the space in the niche(s) between HSCs and tumour cells as suggested by Shiozawa [36].

Simply arriving in bone is not sufficient for tumour cells to result in overt secondary tumour [2], [16], [205], [206], [214], [217]. Once tumour cells reach the bone microenvironment, they have to interact with the microenvironment in order to both receive and respond to signals which enable their survival and proliferation [87], [218]. Despite the two-photon microscopy allowing high resolution imaging, this is not sufficiently sensitive to visualise the components of the bone microenvironment likely to play a key role in the fate of the tumour cells seeded in the bone marrow. Hence, in Chapters 4-6 of this thesis I combined the two-photon microscopy with fluorescence microscopy and histology to allow enhanced visualisation of the components of the bone microenvironment, with a particular focus of characterisation of the perivascular niche, which has been less well described.

Characterisation of the metastatic niche in young and mature mice

Previous studies have highlighted that is the condition of the microenvironment where tumour cells seed and will determine whether the DTC present in bone will develop into overt metastasis [101]. In a previous study from our laboratory no differences in the number of breast cancer cells homing to the bones of young (6-week old) or mature mice (16-week old) were identified, however young animals developed a significantly higher number of tumours in bone indicating that the fertile microenvironment into which the breast cancer cells located was a key player in the progression of the metastatic disease [101]. Thus, in Chapter 4 of this thesis I have characterised the bone microenvironment of both young and mature murine models.

In younger animals, bone turnover is higher when compared to mature animals, resulting in a less dense mature trabecular structure in mature mice accompanied by a

reduced number of osteoprogenitors (Osterix⁺ cells). Osteoprogenitors are located in close proximity to the trabeculae in the metaphysis of tibiae, an area of bone that is particularly well vascularised, reinforcing the concept that osteogenesis and angiogenesis are closely coupled [88], [97], [221], [232], [267]. Visualisation of the three-dimensional structure of the bone marrow microvasculature and the surrounding cellular component was challenging, until an innovative methodology was described by Kusumbe and colleagues in 2014 [97]. This new technique allows imaging of thick sections (30µm) of decalcified bones, which are only fixed for a short period of time (4h) and do not require antigen retrieval methodologies likely to damage the tissue. Even though, Kusumbe *et al.* described the structural organization of the microvasculature, particularly H- and L-vessels in the bone marrow, their loss during the ageing process and changes in the osteoprogenitors numbers in detail, the analyses were largely qualitative with only partial quantification performed using flow cytometry or qPCR [97]. Using an optimised version of Kusumbe's protocol allowing use of the equipment available at the University of Sheffield, I was able to visualise the complex network of the bone marrow microvasculature and for the first time quantify the differences in the structure of the vessels, the area of bone occupied and the number and length, in young and mature mice. Moreover, in my work I used CD31 and Endomucin to quantify mature likely quiescent vessels in addition to identifying changes in the newly formed microvasculature positive for the marker CD34, that has not been previously described.

Previous *in vivo* work observed that the microvasculature not only plays a role in the delivery of oxygen and nutrients but also in the homing of HSCs and DTCs; intriguingly after bone marrow transplantation, hematopoietic stem cells progenitors locate in the trabecular region of bone where the vascular and endosteal niches are overlapping [98], [99]. *In vitro* studies have demonstrated that breast cancer cells locate in close proximity to the vessels, furthermore it has been observed that the tumour cells that home next to the established microvasculature remain in the dormant state while cells seeded in the vicinity of a sprouting microvasculature undergo proliferation. Moreover, this study reported that different state of the microvasculature development (i.e. quiescent vs. sprouting) influences the expression of the inhibitory Thrombospondin

(TSP-1) or growth promoting (periostin and TGF- β 1) signalling [35]. Moreover, a further study performed IHC on microarrays containing core biopsy from 100 breast cancer patients and observed that TSP-1 expression was low in invasive breast cancer with increased expression in adjacent and normal tissue [268]. In the current study TSP-1 expression was higher in the dormancy supporting (mature) compared to the tumour-promoting (young) animal model, supporting the role for TSP-1 as key regulator of tumour cell dormancy.

TSP-1 is highly expressed in areas surrounding the established vessels but this molecule is also expressed by megakaryocytes. Megakaryocytes have been shown to maintain HSC quiescence and promote their expansion following chemotherapy via the secretion of platelet factor 4 (PF4) [108], [269]. Furthermore, it has been shown in *in vitro* studies that osteoclast formation and activity is inhibited by co-culture with megakaryocytes, however further investigations are required to determine the mechanism(s) involved in this inhibition [270]. Given the high level of expression TSP-1, the regulation of HSC dormancy and the inhibitory action on osteoclast activity, it is not surprising that *in vivo* studies using genetically engineered mice lacking in megakaryocytes, developed a bigger burden of metastases, suggesting that megakaryocytes may have a protective role against metastases, even though the potential mechanism(s) of action has not been fully elucidated [110]. In my study I detected a higher number of megakaryocytes in the bone marrow of mature compared to young animals, which may also be involved in the maintenance of DTC dormancy in the bone marrow.

By using confocal microscopy I visualised single tumour cells in close proximity of different vessel sub-types in the bone marrow, an area where TSP-1 is highly expressed and there are megakaryocytes. However, due to the low number of cells homing to bone and the inadequate equipment available, it was not possible to perform quantitative analyses. To better understand the interaction between cancer cells and the components of the surrounding niche, it would be interesting to establish the location of single tumour cells in relation to the vessel sub-types present in the bone microenvironment, the TSP-1 expressing region and the megakaryocytes. This challenging task requires access to a confocal microscope capable of imaging the entire

surface of the bone (tile scan), and allows penetrate deep into the tissue, to obtain the three-dimensional structure of the components analysed (z-stack) with multiple colour detectors.

Effect of ZOL on the bone microvasculature structure

Although Bisphosphonates (BPs), in particular Zoledronic acid (ZOL), are the standard treatment of care in metastatic breast cancer, comprehensive data on the effect of the anti-resorptive agents on components of the bone other than osteoclasts and osteoblasts, including the bone microvasculature are not available. This is somewhat surprising in light of the close association between osteogenesis and angiogenesis [97]. The anti-angiogenic response to ZOL was reported by Wood *et al.* in 2002; the anti-resorptive agent caused a reduction in the proliferation of HUVEC cells *in vitro* (0.3-30 μ M for 24h), *ex vivo* exposure for 24h to 50 μ M ZOL induced a reduction in angiogenesis of rat aortic ring and *in vivo* chicken egg chorioallantoic membrane angiogenesis was reduced with 100 μ M of ZOL and with complete inhibition using 1mM ZOL [136]. Misso and colleagues observed that ZOL administration (0.31-160 μ M) for 24h inhibited the tubule formation of HUVEC cells in a dose-dependent manner *in vitro*, moreover they also showed that *in vivo* administration of 100 μ M of ZOL reduced the formation of vessels in matrigel plugs and ZOL treatment (20 μ g/mouse trice/week for 3 weeks) significantly reduced the number of newly formed vessels CD34⁺ in xenograft model of breast cancer [135]. Furthermore, *in vitro* administration of ZOL at low concentration (1-5 μ M) inhibited the differentiation of endothelial progenitors, caused their apoptosis at higher doses (>10 μ M), inhibited tubule formation at a dose as little as 1 μ M and reduced the expression of VEGFR-2 [137]. Moreover, the ZOL-induced reduction of VEGF has also been reported in the clinical setting; 26 patients with solid tumour and bone metastasis received 1mg/week of ZOL for 4 weeks and then continued with 4 cycles of the standard dosing regime (4mg every 28 days). This repeated administration of low doses of ZOL resulted in a significant reduction of circulating VEGF, 7 days after the first treatment and this effect persisted even at the last time point analysed [138]. All these data indicate that ZOL has a direct effect on the angiogenesis process, which results in an indirect anti-tumour effect.

Given the data suggesting an anti-angiogenic effect and the fact that ZOL is used to treat skeletal disease, it seems somewhat surprising that the effect on the bone microvasculature has not been extensively investigated. This may be due to the difficulties in obtaining patient samples and, until recently, it has been challenging to visualise the bone microvasculature even in pre-clinical settings. Soki *et al.* investigated the changes in the bone microvasculature in response to ZOL by injecting radiopaque silicone rubber agent Microfil™ followed by μ CT analysis and reported that administration twice weekly for 4 weeks of 200 μ g/kg ZOL, resulted in a higher number of shorter vessels in bone of immunocompetent young (4-week old) and mature male mice (16-week old), however the total bone volume occupied by the microvasculature was not altered by the anti-resorptive drug [119]. Although visualising the three-dimensional microvasculature structure is feasible using Microfil™, this technique does not allow the discrimination between different vessel sub-types. Therefore, in Chapter 5 of this thesis, I have investigated the effect of a single dose of ZOL on young (6-week old) and mature animals (12-week old), focusing in particular on the effect of the anti-resorptive drug on the capillary components of bone microvasculature using confocal microscopy. Using immunofluorescent protocols I observed that, irrespective of age, the vessel sub-types positive for the markers CD31 (mature and quiescent) and CD34 (immature) were not affected by ZOL treatment. In contrast, the organisation of Endomucin⁺ vessels in 12-week old animals was altered resulting in fragmented and more numerous vessels, as observed by Soki and colleagues [119]. Given that the greater effect on the bone structure were observed in young animals and that osteogenesis and angiogenesis are tightly coupled, it was expected that greater changes in the microvasculature of young animals would be detected and not in the mature animals. The reason there is a differential effect in the two ages analysed is not clear, however it somewhat reflects the effect of ZOL on pre- and post-menopausal women with early breast cancer. Ottewell and colleagues used pre-clinical models to assess the effect of ZOL treatment in animals that mimicked pre- (sham operated 12-week old mice) and post-menopausal status (ovarectomised (OVX) 12-week old mice). MDA-MB-231 breast cancer cells were injected in the left ventricle of mature animals and the ZOL treatment (100 μ g/kg once a week) commenced four days after tumour cell

inoculation, when there were no metastases established. OVX increased tumour growth in bone, and which was inhibited by ZOL administration. ZOL treatment was not effective in preventing the development of overt bone metastasis of sham-operated animals [216]. Intriguingly, a differential response to ZOL treatment was recorded also in the clinical setting. A meta-analysis performed by the Early Breast Cancer Trials Collaborative Group (EBCTCG) collected the results from 26 randomised trials involving 18,766 women and showed that treatment with bisphosphonates (BPs) had a beneficial effect only in postmenopausal women. The clinical outcomes for the overall population (pre- and post-menopausal) was often 'borderline' beneficial, however in post-menopausal women, BP treatment improved the time until the first overall recurrence, recurrence in bone, distant recurrence at any site and breast cancer mortality [145].

In my study, detecting changes in the homing of breast cancer cells in animals treated with ZOL was not possible due to technical limitations, however it has been shown that a single dose of ZOL (100 µg/kg) alters the pattern of seeding of breast cancer cells to bone. Previous *in vivo* study from our laboratory found that the overall number of cancer cells homing to bone was not affected by ZOL but were evenly distributed between the growth plate and the trabecular region of bone, losing their preferential pattern of seeding [118]. I observed that tumour cells located in close proximity to the microvasculature in bone and the fact that the vessels were fragmented after ZOL treatment could potentially explain why the tumour cells switch their homing towards the growth plate rather than homing to the trabecular bone.

Therapeutic modification of the microvasculature and its effect on the bone metastatic niche

Targeting angiogenesis to inhibit tumour growth and progression is a well-accepted concept. After the ground breaking observation of Folkman and colleagues in the 1970s [150], several approaches targeting the angiogenic process have been developed [151]–[153], [159]–[161]. Novel tyrosine kinase inhibitors (TKI) such as Cediranib have shown promising results with their anti-angiogenic and anti-tumour efficacy [164]–[170], [247], however only little is known about effects on the bone microenvironment. Previous work reported an alteration in structure of the growth

plate area in rats treated with the TKI daily for 28 days [168]. Yin and colleagues observed a reduction in metastatic growth in bone with the administration of Cediranib in both treatment and preventative settings [171]. The work presented in Chapter 6 of this thesis investigates for the first time, the effect of this TKI on the bone microvasculature. Given that the osteoblastic and perivascular niches are tightly coupled and breast cancer cells home in close proximity to vessels and bone surface, I tested the ability of two agents to modulate the microvasculature *in vivo*, cediranib to decrease the angiogenic process and DFM to increase it, and detect any changes in the bone structure and in the homing of breast cancer cells to the modified microenvironment. In my study the bone structure was not altered and the effect of cediranib on the bone microvasculature was marginal, the treatment resulted in longer H-vessels and fewer L-vessels when compared to the control animals. Since these changes did not cause major alterations of the bone metastatic niche, this likely explains why no differences in the homing of breast cancer cells to bone was observed. The marginal effect obtained could have been due to the dose used, furthermore, due to the invasiveness of the gavage administration and the fact that technical support was not available during the weekend, the TKI was administered 5 days/week rather than 7days/week used in other studies. Further experiments using different dose ranges and timing of administration are required to better understand the effect of cediranib on the bone microenvironment. In clinical trials, cediranib is mostly tested as part of combination therapy, rather than as single agent, and this should be tested in our pre-clinical model. Moreover, the data showed in Chapter 6 reports a decreased expression of the dormancy-supporting molecule TSP-1, this could indicate that tumour cells arriving in bone could proliferate and result in a higher rate of overt metastasis when receiving Cediranib. Thus, a tumour growth study is needed to understand this aspect of TKI treatment.

In Chapter 6 of this thesis I have also used Deferoxamine mesylate (DFM) to investigate whether the expansion of the perivascular niche increased the homing of breast cancer cells to bone *in vivo*. This iron chelator has been shown to increase the angiogenesis in response to hindlimb ischemia [184], [185] and the pro-angiogenic effect of DFM is accompanied by an increase of the bone mass in various animal

models [97], [186]–[192]. Deciding on the dose to use in my *in vivo* study was quite challenging since most studies in literature used rats [187], [189], [190], [192] and/or use the *in vivo* models to detect the healing property of the drugs while we were trying to manipulate the microenvironment without any previous alteration of the bone structure such as fracture, ischemia or loading. Kusumbe and colleagues used DFM on naïve mice and described that the administration of 15mg/ml per mouse every other day for 4-6 weeks altered both the bone structure and the microvasculature of aged mice (60-65 weeks old) [97]. Although in my work I used a comparable dose to Kusumbe's study (animals treated 5days/week for 6 weeks with 15mg/ml DFM) no changes in the bone structure were detected, while the expression of both CD31 and CD34 were increased in animals treated with DFM, however these vessels appeared shorter than in control animals. Also the homing of breast cancer cells to bone was not altered, indicating that a marginal change in the microvasculature was insufficient to modify the early steps of breast cancer bone colonisation. A different range of doses and older mice should be used in the future to detect if DFM cause an enhanced expansion of the perivascular niche and consequently the homing of breast cancer cells to bone is affected by this alteration of the niche.

7.2 Future work

Listed below is the proposed future work to follow-up the work presented in this thesis:

- Establish protocols to visualise other components of the perivascular niche (e.g. PDGFR β ⁺ mesenchymal cells, arteries and veins)
- Investigate whether, within the trabecular region of bone (ROI1), breast cancer cells locate in proximity to a particular vessel sub-type and establish whether there are differences dependent on sub-types of breast cancer
- Perform quantitative analysis on the location of cancer cells in relation to the bone microvasculature
- Obtain histological sample from clinical trials/patients to explore whether DTC locate in the immediacy of endosteal and vascular niche(s)
- Investigate the effect of modulating the microvascular activity using different dose ranges of Cediranib and DFM, different animal models (i.e. older/younger animals, immunocompetent mice) and consider both ER+ve and -ve breast cancer subtypes
- Assess whether the treatment with Cediranib and DFM affects the development of metastasis from disseminated tumour cells or inhibit/promote the growth of established micro-metastasis
- Determine the response of the bone microenvironment to Cediranib in combination with other therapies (i.e. bisphosphonates, chemotherapy, PARP inhibitors etc.)
- Establish the effect of increasing/decreasing the microvascular activity on the dissemination of tumour cells in the presence of a primary tumour

7.3 Conclusion

The work presented in this thesis provide the first detailed characterisation of the homing of several sub-types of breast cancer cells administered with different routes of injections to the bone microenvironment, visualisation of several components of the perivascular niche that contribute to the fate of the DTC in bone, short term effects of ZOL treatment in the bone microenvironment of both young and mature animal

models and effects in bone of agents targeting the microvasculature. I demonstrate that irrespective of ER/HER status and route of administration, breast cancer cells prefer to locate in the trabecular region of bone compared to the growth plate area. Moreover, I have shown that mobilization of HSCs in the circulation results in the homing of more breast cancer cell to the niche(s), suggesting that tumour cells and HSCs compete for the space available in the bone marrow niche(s). It has been shown that the homing of tumour cells to the bone microenvironment does not change between young and mature animal models, however young animals are more likely to develop overt metastasis compared to mature animals. In this thesis I have therefore characterised the bone structure and microvasculature of these two animal models, highlighting the differences between the tumour-promoting (young) and the dormancy-supporting (mature) animal models. Bisphosphonates, in particular ZOL, are the standard of care in bone metastatic cancer, however it has been shown that the administration of ZOL at the early stages of breast cancer is beneficial only for post-menopausal women. My work contributes to the characterisation of the effect of ZOL treatment on the bone microenvironment in young and mature animals, in particular I have investigated the alteration on the bone microvasculature that could be involved in the differential response of pre- or post-menopausal patients. I have also examined the response of the bone microenvironment to agents targeting the angiogenic process.

Further work is required to elucidate the function of the perivascular niche on the metastatic process and the mechanism(s) of cross-talk between different components of the niche(s). However, the work presented here suggests that breast cancer cells home to particular regions of bone where the HSCs, endosteal and perivascular niches overlap and that new therapeutic approaches should take into consideration the interconnection between niche(s) to target in a more effective way the metastatic disease.

References

- [1] H. Pan, R. Gray, J. Braybrooke, C. Davies, C. Taylor, P. McGale, R. Peto, K. I. Pritchard, J. Bergh, M. Dowsett, and D. F. Hayes, "20-Year Risks of Breast-Cancer Recurrence after Stopping Endocrine Therapy at 5 Yearfile:///Users/gloriaallocca/Desktop/JCI39104.pdf", *N. Engl. J. Med.*, vol. 377, no. 19, pp. 1836–1846, 2017.
- [2] R. E. Coleman and R. D. Rubens, "The clinical course of bone metastases from breast cancer," *Br. J. Cancer*, vol. 55, no. 1, pp. 61–66, 1987.
- [3] C. L. Chaffer and R. A. Weinberg, "A perspective on cancer cell metastasis," *Science (80- .)*, vol. 331, no. 6024, pp. 1559–1564, 2011.
- [4] M. C. Green, J. L. Murray, and G. N. Hortobagyi, "Angiogenesis and Antiangiogenic Therapy With Thalidomide in Multiple Myeloma," *Cancer Treat. Rev.*, vol. 26, no. 1, pp. 269–286, 2000.
- [5] R. E. Coleman, "Clinical features of metastatic bone disease and risk of skeletal morbidity.," *Clin. Cancer Res.*, vol. 12, no. 20 Pt 2, p. 6243s–6249s, 2006.
- [6] R. Kalluri and R. a Weinberg, "Review series The basics of epithelial-mesenchymal transition.," *J. Clin. Invest.*, vol. 119, no. 6, pp. 1420–1428, 2009.
- [7] J. a Aguirre-Ghiso, "Models, mechanisms and clinical evidence for cancer dormancy.," *Nat. Rev. Cancer*, vol. 7, no. 11, pp. 834–46, Nov. 2007.
- [8] L. Gelao, C. Criscitiello, L. Fumagalli, M. Locatelli, S. Manunta, A. Esposito, I. Minchella, A. Goldhirsch, and G. Curigliano, "Tumour dormancy and clinical implications in breast cancer.," *Ecancermedalscience*, vol. 7, p. 320, Jan. 2013.
- [9] S.-M. Käkönen and G. R. Mundy, "Mechanisms of osteolytic bone metastases in breast carcinoma.," *Cancer*, vol. 97, no. 3 Suppl, pp. 834–9, Feb. 2003.
- [10] L. R. Patel, D. F. Camacho, Y. Shiozawa, K. J. Pienta, and R. S. Taichman, "Mechanisms of cancer cell metastasis to the bone: a multistep process," *Future Oncology*, vol. 7, no. 11, pp. 1285–1297, 2011.
- [11] S. Paget, "The distribution of secondary growths in cancer of the breast. 1889.," *Cancer Metastasis Rev.*, vol. 8, no. 2, pp. 98–101, 1989.
- [12] R. Faccio, "Immune regulation of the tumor/bone vicious cycle.," *Ann. N. Y. Acad. Sci.*, vol. 1237, pp. 71–8, Nov. 2011.
- [13] L. C. Hofbauer, T. Rachner, and S. K. Singh, "Fatal attraction: why breast cancer cells home to bone.," *Breast Cancer Res.*, vol. 10, no. 1, p. 101, Jan. 2008.
- [14] L. a Kingsley, P. G. J. Fournier, J. M. Chirgwin, and T. a Guise, "Molecular biology of bone metastasis.," *Mol. Cancer Ther.*, vol. 6, no. 10, pp. 2609–17, Oct. 2007.
- [15] T. A. Guise, "The vicious cycle of bone metastases," *j musculoskel neuron interact*, vol. 2, no. August, pp. 570–572, 2002.
- [16] A. Mishra, Y. Shiozawa, K. J. Pienta, and R. S. Taichman, "Homing of cancer cells to the bone.," *Cancer Microenviron.*, vol. 4, no. 3, pp. 221–35, Dec. 2011.

- [17] K. Pantel and C. Alix-Panabières, "Bone marrow as a reservoir for disseminated tumor cells: a special source for liquid biopsy in cancer patients," *Bonekey Rep.*, vol. 3, no. September, pp. 1–6, 2014.
- [18] C. Schindlbeck, U. Andergassen, J. Jueckstock, B. Rack, W. Janni, and U. Jeschke, "Disseminated and circulating tumor cells in bone marrow and blood of breast cancer patients: properties, enrichment, and potential targets," *J. Cancer Res. Clin. Oncol.*, vol. 142, no. 9, pp. 1883–1895, 2016.
- [19] M. Guba, G. Cernaianu, G. Koehl, E. K. Geissler, K. W. Jauch, M. Anthuber, W. Falk, and M. Steinbauer, "A primary tumor promotes dormancy of solitary tumor cells before inhibiting angiogenesis," *Cancer Res.*, vol. 61, no. 14, pp. 5575–5579, 2001.
- [20] K. J. Luzzi, I. C. MacDonald, E. E. Schmidt, N. Kerkvliet, V. L. Morris, a F. Chambers, and a C. Groom, "Multistep nature of metastatic inefficiency: dormancy of solitary cells after successful extravasation and limited survival of early micrometastases.," *Am. J. Pathol.*, vol. 153, no. 3, pp. 865–873, 1998.
- [21] G. N. Naumov, I. C. MacDonald, a F. Chambers, and a C. Groom, "Solitary cancer cells as a possible source of tumour dormancy?," *Semin. Cancer Biol.*, vol. 11, no. 4, pp. 271–6, Aug. 2001.
- [22] S. Pece, D. Tosoni, S. Confalonieri, G. Mazzarol, M. Vecchi, S. Ronzoni, L. Bernard, G. Viale, P. G. Pelicci, and P. P. Di Fiore, "Biological and molecular heterogeneity of breast cancers correlates with their cancer stem cell content.," *Cell*, vol. 140, no. 1, pp. 62–73, Jan. 2010.
- [23] W. Janni, F. D. Vogl, G. Wiedswang, M. Synnestvedt, T. Fehm, J. Jückstock, E. Borgen, B. Rack, S. Braun, H. Sommer, E. Solomayer, K. Pantel, J. Nesland, K. Friese, and B. Naume, "Persistence of disseminated tumor cells in the bone marrow of breast cancer patients predicts increased risk for relapse--a European pooled analysis.," *Clin. Cancer Res.*, vol. 17, no. 9, pp. 2967–76, May 2011.
- [24] N. Wang, F. E. Docherty, H. K. Brown, K. J. Reeves, C. A. Fowles, M. Lawson, P. D. Ottewell, I. Holen, P. I. Croucher, and C. L. Eaton, "Mitotic quiescence, but not unique 'stemness', marks the phenotype of bone metastasis-initiating cells in prostate cancer," *researchgate.net*.
- [25] G. Allocca, A. P. Kusumbe, S. K. Ramasamy, and N. Wang, "Confocal/two-photon microscopy in studying colonisation of cancer cells in bone using xenograft mouse models," *BoneKEy Rep*, vol. 5, Dec. 2016.
- [26] N. Wang, F. E. Docherty, H. K. Brown, K. J. Reeves, A. C. Fowles, P. D. Ottewell, T. N. Dear, I. Holen, P. I. Croucher, and C. L. Eaton, "Prostate Cancer Cells Preferentially Home to Osteoblast-rich Areas in the Early Stages of Bone Metastasis: Evidence From In Vivo Models.," *J. Bone Miner. Res.*, vol. 29, no. 12, pp. 2688–96, Dec. 2014.
- [27] Y. Shiozawa, B. Nie, K. J. Pienta, T. M. Morgan, and R. S. Taichman, "Cancer stem cells and their role in metastasis.," *Pharmacol. Ther.*, vol. 138, no. 2, pp. 285–93, May 2013.
- [28] T. R. Shiozawa Y, Pienta KJ, "Hematopoietic Stem Cell Niche Is a Potential Therapeutic Target for Bone Metastatic Tumors," *Clin. Cancer Res.*, vol. 17, no. 17, p. 5553–8., 2011.
- [29] S. W. Z. Olechnowicz and C. M. Edwards, "Contributions of the host microenvironment

- to cancer-induced bone disease," *Cancer Res.*, vol. 74, no. 6, pp. 1625–1631, 2014.
- [30] M. Esposito and Y. Kang, "Targeting tumor-stromal interactions in bone metastasis.," *Pharmacol. Ther.*, vol. 141, no. 2, pp. 222–33, Feb. 2014.
- [31] C. Kan, G. Vargas, F. Le Pape, and P. Clézardin, "Cancer cell colonisation in the bone microenvironment," *Int. J. Mol. Sci.*, vol. 17, no. 10, 2016.
- [32] K. N. Weilbaecher, T. A. Guise, and L. K. McCauley, "Cancer to bone: A fatal attraction," *Nat. Rev. Cancer*, vol. 11, no. 6, pp. 411–425, 2011.
- [33] L. Li and R. Bhatia, "Stem cell quiescence.," *Clin. Cancer Res.*, vol. 17, no. 15, pp. 4936–41, 2011.
- [34] H. Wang, P. Zhang, L. Liu, and L. Zou, "Hierarchical organization and regulation of the hematopoietic stem cell osteoblastic niche.," *Crit. Rev. Oncol. Hematol.*, vol. 85, no. 1, pp. 1–8, Jan. 2013.
- [35] C. M. Ghajar, H. Peinado, H. Mori, I. R. Matei, K. J. Evason, H. Brazier, D. Almeida, A. Koller, K. a Hajjar, D. Y. R. Stainier, E. I. Chen, D. Lyden, and M. J. Bissell, "The perivascular niche regulates breast tumour dormancy.," *Nat. Cell Biol.*, vol. 15, no. 7, pp. 807–17, Jul. 2013.
- [36] Y. Shiozawa, E. A. Pedersen, A. M. Havens, Y. Jung, A. Mishra, J. Joseph, J. K. Kim, L. R. Patel, C. Ying, A. M. Ziegler, and others, "Human prostate cancer metastases target the hematopoietic stem cell niche to establish footholds in mouse bone marrow," *J. Clin. Invest.*, vol. 121, no. 4, pp. 1298–1312, 2011.
- [37] G. A. Rodan, "Introduction to bone biology," *Bone*, vol. 13, pp. S3–S6, 1992.
- [38] R. N. Kaplan, B. Psaila, and D. Lyden, "Bone marrow cells in the 'pre-metastatic niche': Within bone and beyond," *Cancer Metastasis Rev.*, vol. 25, no. 4, pp. 521–529, 2006.
- [39] D. S. Krause, D. T. Scadden, and F. I. Preffer, "The hematopoietic stem cell niche-home for friend and foe?," *Cytom. Part B Clin. Cytom.*, vol. 84B, no. 1, pp. 7–20, 2013.
- [40] K. Neiva, Y.-X. Sun, and R. S. Taichman, "The role of osteoblasts in regulating hematopoietic stem cell activity and tumor metastasis.," *Brazilian J. Med. Biol. Res.*, vol. 38, no. 10, pp. 1449–54, 2005.
- [41] F. Ugarte and E. C. Forsberg, "Haematopoietic stem cell niches: new insights inspire new questions.," *EMBO J.*, vol. 32, no. 19, pp. 2535–47, Oct. 2013.
- [42] Z. S. Templeton, W. R. Lie, W. Wang, Y. Rosenberg-Hasson, R. V. Alluri, J. S. Tamaresis, M. H. Bachmann, K. Lee, W. J. Maloney, C. H. Contag, and B. L. King, "Breast Cancer Cell Colonization of the Human Bone Marrow Adipose Tissue Niche," *Neoplasia*, vol. 17, no. 12, pp. 849–861, 2015.
- [43] E. V. Morris and C. M. Edwards, "Bone marrow adipose tissue: A new player in cancer metastasis to bone," *Front. Endocrinol. (Lausanne)*, vol. 7, no. JUL, pp. 1–7, 2016.
- [44] T. L. Rogers and I. Holen, "Tumour macrophages as potential targets of bisphosphonates," *J. Transl. Med.*, vol. 9, no. 1, p. 177, 2011.
- [45] J. W. Pollard, "Opinion: Tumour-educated macrophages promote tumour progression

and metastasis," *Nat. Rev. Cancer*, vol. 4, no. 1, pp. 71–78, 2004.

- [46] K. M. Bussard, L. Mutkus, K. Stumpf, C. Gomez-Manzano, and F. C. Marini, "Tumor-associated stromal cells as key contributors to the tumor microenvironment," *Breast Cancer Res.*, vol. 18, no. 1, pp. 1–11, 2016.
- [47] T. R. Cox, R. M. H. Rumney, E. M. Schoof, L. Perryman, A. M. Høye, A. Agrawal, D. Bird, N. A. Latif, H. Forrest, H. R. Evans, I. D. Huggins, G. Lang, R. Linding, A. Gartland, and J. T. Erler, "The hypoxic cancer secretome induces pre-metastatic bone lesions through lysyl oxidase," *Nature*, vol. 522, pp. 106–110, 2015.
- [48] H. K. Brown, P. D. Ottewill, C. a Evans, and I. Holen, "Location matters: osteoblast and osteoclast distribution is modified by the presence and proximity to breast cancer cells in vivo.," *Clin. Exp. Metastasis*, vol. 29, no. 8, pp. 927–38, Dec. 2012.
- [49] J. J. Trentin, "Determination of bone marrow stem cell differentiation by stromal hemopoietic inductive microenvironments (HIM).," *Am. J. Pathol.*, vol. 65, no. 3, pp. 621–628, 1971.
- [50] R. Schofield, "The relationship between the spleen colony-forming cell and the haemopoietic stem cell.," *Blood Cells*, vol. 4, no. 1–2, pp. 7–25, Jan. 1978.
- [51] M. J. Kiel and S. J. Morrison, "Uncertainty in the niches that maintain haematopoietic stem cells.," *Nat. Rev. Immunol.*, vol. 8, no. 4, pp. 290–301, Apr. 2008.
- [52] R. S. Taichman, "Human osteoblasts support hematopoiesis through the production of granulocyte colony-stimulating factor," *J. Exp. Med.*, vol. 179, no. 5, pp. 1677–1682, 1994.
- [53] R. S. Taichman and S. G. Emerson, "The role of osteoblasts in the hematopoietic microenvironment," *Stem Cells*, vol. 16, no. 1, pp. 7–15, 1998.
- [54] B. R. S. Taichman, M. J. Reilly, and S. G. full. pd. Emerson, "Human Osteoblasts Support Human Hematopoietic Progenitor Cells in In Vitro Bone Marrow Cultures," vol. 87, no. 2, pp. 518–524, 1996.
- [55] L. M. Calvi, G. B. Adams, K. W. Weibrecht, J. M. Weber, D. P. Olson, M. C. Knight, R. P. Martin, E. Schipani, P. Divieti, F. R. Bringhurst, L. A. Milner, H. M. Kronenberg, and D. T. Scadden, "Osteoblastic cells regulate the haematopoietic stem cell niche.," *Nature*, vol. 425, no. 6960, pp. 841–846, 2003.
- [56] J. Weber and L. Calvi, "Notch signaling and the bone marrow hematopoietic stem cell niche," *Bone*, vol. 46, no. 2, pp. 281–285, 2010.
- [57] D. Li, "The Notch ligand Jagged1 as a target for anti-tumor therapy," *Front. Oncol.*, vol. 4, no. September, pp. 1–13, 2014.
- [58] H. Yoshihara, F. Arai, K. Hosokawa, T. Hagiwara, K. Takubo, Y. Nakamura, Y. Gomei, H. Iwasaki, S. Matsuoka, K. Miyamoto, H. Miyazaki, T. Takahashi, and T. Suda, "Thrombopoietin/MPL Signaling Regulates Hematopoietic Stem Cell Quiescence and Interaction with the Osteoblastic Niche," *Cell Stem Cell*, vol. 1, no. 6, pp. 685–697, 2007.
- [59] F. Arai and T. Suda, "Quiescent stem cells in the niche," *StemBook*, vol. 3474, pp. 1–11, 2008.

- [60] H. E. Fleming, V. Janzen, C. Lo Celso, J. Guo, K. M. Leahy, and M. Henry, "Wnt signaling in the niche enforces hematopoietic stem cell quiescence and is necessary to preserve self-renewal in vivo," *Cell Stem Cell.*, vol. 2, no. 3, pp. 274–283, 2008.
- [61] S. Nilsson and H. Johnston, "Osteopontin, a key component of the hematopoietic stem cell niche and regulator of primitive hematopoietic progenitor cells," *Blood*, vol. 106, no. 4, pp. 1232–1239, 2005.
- [62] C. H. Kim and H. E. Broxmeyer, "hematopoietic progenitor cells : differential activity of ligands of CCR7 , CXCR3 , or CXCR4 in chemotaxis vs . suppression of progenitor proliferation Abstract : Chemokines induce chemotaxis of hema- CXC chemokine receptor , CXCR3 , in addition to a," vol. 66, no. September, pp. 455–461, 1999.
- [63] A. Aiuti, M. Taviani, A. Cipponi, F. Ficara, E. Zappone, J. Hoxie, B. Peault, and C. Bordignon, "Expression of CXCR4, the receptor for stromal cell-derived factor-1 on fetal and adult human lymphohematopoietic progenitors," *Eur. J. Immunol.*, vol. 29, no. 6, pp. 1823–1831, 1999.
- [64] H. E. Broxmeyer, C. M. Orschell, D. W. Clapp, G. Hangoc, S. Cooper, P. A. Plett, W. C. Liles, X. Li, B. Graham-Evans, T. B. Campbell, G. Calandra, G. Bridger, D. C. Dale, and E. F. Srouf, "Rapid mobilization of murine and human hematopoietic stem and progenitor cells with AMD3100, a CXCR4 antagonist," *J. Exp. Med.*, vol. 201, no. 8, pp. 1307–1318, 2005.
- [65] C. Martin, G. J. Bridger, and S. M. Rankin, "Structural analogues of AMD3100 mobilise haematopoietic progenitor cells from bone marrow in vivo according to their ability to inhibit CXCL12 binding to CXCR4 in vitro.," *Br. J. Haematol.*, vol. 134, no. 3, pp. 326–9, Aug. 2006.
- [66] R. S. Taichman, C. Cooper, E. T. Keller, K. J. Pienta, N. S. Taichman, and L. K. Mccauley, "Use of the Stromal Cell-derived Factor-1 / CXCR4 Pathway in Prostate Cancer Metastasis to Bone 1," *Cancer Res.*, vol. 62, pp. 1832–1837, 2002.
- [67] C. Nombela-Arrieta, G. Pivarnik, B. Winkel, K. J. Canty, B. Harley, J. E. Mahoney, S.-Y. Park, J. Lu, A. Protopopov, and L. E. Silberstein, "Quantitative imaging of hematopoietic stem and progenitor cell localization and hypoxic status in the bone marrow microenvironment," *Nat. Cell Biol.*, vol. 15, no. 5, pp. 533–543, 2013.
- [68] F. Arai, A. Hirao, M. Ohmura, H. Sato, S. Matsuoka, K. Takubo, K. Ito, G. Y. Koh, and T. Suda, "Tie2/angiopoietin-1 signaling regulates hematopoietic stem cell quiescence in the bone marrow niche," *Cell*, vol. 118, no. 2, pp. 149–161, 2004.
- [69] A. Horner, S. Bord, A. W. Kelsall, N. Coleman, and J. E. Compston, "Tie2 ligands angiopoietin-1 and angiopoietin-2 are coexpressed with vascular endothelial cell growth factor in growing human bone," *Bone*, vol. 28, no. 1, pp. 65–71, 2001.
- [70] Y. M. Ikushima, F. Arai, Y. Nakamura, K. Hosokawa, Y. Kubota, M. Hirashima, H. Toyama, and T. Suda, "Enhanced Angpt1/Tie2 signaling affects the differentiation and long-term repopulation ability of hematopoietic stem cells," *Biochem. Biophys. Res. Commun.*, vol. 430, no. 1, pp. 20–25, 2013.
- [71] A. Hirao, F. Arai, and T. Suda, "Regulation of cell cycle in hematopoietic stem cells by the niche.," *Cell Cycle*, vol. 3, no. December, pp. 1481–1483, 2004.

- [72] S. C. Lin, Y. C. Lee, G. Yu, C. J. Cheng, X. Zhou, K. Chu, M. Murshed, N. T. Le, L. Baseler, J. ichi Abe, K. Fujiwara, B. deCrombrughe, C. J. Logothetis, G. E. Gallick, L. Y. Yu-Lee, S. N. Maity, and S. H. Lin, "Endothelial-to-Osteoblast Conversion Generates Osteoblastic Metastasis of Prostate Cancer," *Dev. Cell*, vol. 41, no. 5, p. 467–480.e3, 2017.
- [73] K. M. Bussard, N. Okita, N. Sharkey, T. Neuberger, A. Webb, and A. M. Mastro, "Localization of osteoblast inflammatory cytokines MCP-1 and VEGF to the matrix of the trabecula of the femur, a target area for metastatic breast cancer cell colonization," *Clin. Exp. Metastasis*, vol. 27, no. 5, pp. 331–340, May 2010.
- [74] J. Tombran-Tink and C. J. Barnstable, "Osteoblasts and osteoclasts express PEDF, VEGF-A isoforms, and VEGF receptors: Possible mediators of angiogenesis and matrix remodeling in the bone," *Biochem. Biophys. Res. Commun.*, vol. 316, no. 2, pp. 573–579, 2004.
- [75] J. M. Kanczler, "Osteogenesis and Angiogenesis : the Potential for Engineering," pp. 100–114, 2008.
- [76] S. Y. Heazlewood, A. Oteiza, H. Cao, and S. K. Nilsson, "Analyzing hematopoietic stem cell homing, lodgment, and engraftment to better understand the bone marrow niche," *Ann. N. Y. Acad. Sci.*, vol. 1310, no. 1, pp. 119–128, 2014.
- [77] S. K. Nilsson, H. M. Johnston, and J. a Coverdale, "Spatial localization of transplanted hemopoietic stem cells : inferences for the localization of stem cell niches Spatial localization of transplanted hemopoietic stem cells : inferences for the localization of stem cell niches," vol. 97, no. 8, pp. 2293–2299, 2014.
- [78] S. M. Cabarcas, L. A. Mathews, and W. L. Farrar, "The cancer stem cell niche-there goes the neighborhood?," *Int. J. Cancer*, vol. 129, no. 10, pp. 2315–2327, 2011.
- [79] M. L. Burness and D. A. Sipkins, "The stem cell niche in health and malignancy," *Semin. Cancer Biol.*, vol. 20, no. 2, pp. 107–115, 2010.
- [80] T. Sugiyama, H. Kohara, M. Noda, and T. Nagasawa, "Maintenance of the Hematopoietic Stem Cell Pool by CXCL12-CXCR4 Chemokine Signaling in Bone Marrow Stromal Cell Niches," *Immunity*, vol. 25, no. 6, pp. 977–988, 2006.
- [81] a Müller, B. Homey, H. Soto, N. Ge, D. Catron, M. E. Buchanan, T. McClanahan, E. Murphy, W. Yuan, S. N. Wagner, J. L. Barrera, a Mohar, E. Verástegui, and a Zlotnik, "Involvement of chemokine receptors in breast cancer metastasis.," *Nature*, vol. 410, no. 6824, pp. 50–56, 2001.
- [82] M. C. P. Smith, K. E. Luker, J. R. Garbow, J. L. Prior, E. Jackson, D. Piwnica-Worms, and G. D. Luker, "CXCR4 Regulates Growth of Both Primary and Metastatic Breast Cancer," *Cancer Res.*, vol. 64, no. 23, pp. 8604–8612, 2004.
- [83] C. Xu, H. Zhao, H. Chen, and Q. Yao, "CXCR4 in breast cancer: Oncogenic role and therapeutic targeting," *Drug Des. Devel. Ther.*, vol. 9, pp. 4953–4964, 2015.
- [84] F. Andre, W. Xia, R. Conforti, Y. Wei, T. Boulet, G. Tomasic, M. Spielmann, M. Zoubir, N. Berrada, R. Arriagada, G. N. Hortobagyi, M.-C. Hung, L. Pusztai, S. Delalogue, S. Michiels, and M. Cristofanilli, "CXCR4 Expression in Early Breast Cancer and Risk of Distant Recurrence," *Oncologist*, vol. 14, no. 12, pp. 1182–1188, 2009.
- [85] N. Cabioglu, a Sahin, M. Doucet, E. Yavuz, a Igci, O. Y. E, E. Aktas, S. Bilgic, B. Kiran, G.

- Deniz, and J. E. Price, "Chemokine receptor CXCR4 expression in breast cancer as a potential predictive marker of isolated tumor cells in bone marrow," *Clin Exp Metastasis*, vol. 22, no. 1, pp. 39–46, 2005.
- [86] H. J. Donahue, M. M. Saunders, Z. Li, A. M. Mastro, C. V. Gay, and D. R. Welch, "A potential role for gap junctions in breast cancer metastasis to bone.," *J. Musculoskelet. Neuronal Interact.*, vol. 3, no. 2, pp. 156–161, 2003.
- [87] H. Wang, C. Yu, X. Gao, T. Welte, A. M. Muscarella, L. Tian, H. Zhao, Z. Zhao, S. Du, J. Tao, B. Lee, T. F. Westbrook, S. T. C. Wong, X. Jin, J. M. Rosen, C. K. Osborne, and X. H.-F. Zhang, "The Osteogenic Niche Promotes Early-Stage Bone Colonization of Disseminated Breast Cancer Cells," *Cancer Cell*, vol. 27, no. 2, pp. 193–210, Jan. 2015.
- [88] P. Bianco, "Bone and the hematopoietic niche : a tale of two stem cells," *Blood*, vol. 117, no. 20, pp. 5281–5289, 2011.
- [89] I. G. Winkler, N. a Sims, A. R. Pettit, V. Barbier, B. Nowlan, F. Helwani, I. J. Poulton, N. Van Rooijen, K. A. Alexander, L. J. Raggatt, and J. P. Lévesque, "Bone marrow macrophages maintain hematopoietic stem cell (HSC) niches and their depletion mobilizes HSCs," *Blood*, vol. 116, no. 23, pp. 4815–4828, 2010.
- [90] M. Dominici, V. Rasini, R. Bussolari, X. Chen, T. J. Hofmann, C. Spano, D. Bernabei, E. Veronesi, F. Bertoni, P. Paolucci, P. Conte, M. Edwin, W. Dc, and E. M. Horwitz, "Restoration and reversible expansion of the osteoblastic hematopoietic stem cell niche after marrow radioablation Restoration and reversible expansion of the osteoblastic hematopoietic stem cell niche after marrow radioablation," vol. 114, no. 11, pp. 2333–2343, 2011.
- [91] Y. Zheng, S.-O. Chow, K. Boernert, D. Basel, A. Mikuscheva, S. Kim, C. Fong-Yee, T. Trivedi, F. Buttgerit, R. L. Sutherland, C. R. Dunstan, H. Zhou, and M. J. Seibel, "Direct crosstalk between cancer and osteoblast lineage cells fuels metastatic growth in bone via auto-amplification of IL-6 and RANKL signaling pathways.," *J. Bone Miner. Res.*, vol. 29, no. 9, pp. 1938–49, Sep. 2014.
- [92] M. Kinder, E. Chislock, K. M. Bussard, L. Shuman, and A. M. Mastro, "Metastatic breast cancer induces an osteoblast inflammatory response.," *Exp. Cell Res.*, vol. 314, no. 1, pp. 173–83, Jan. 2008.
- [93] M. Rajski, B. Vogel, F. Baty, C. Rochlitz, and M. Buess, "Global gene expression analysis of the interaction between cancer cells and osteoblasts to predict bone metastasis in breast cancer," *PLoS One*, vol. 7, no. 1, 2012.
- [94] K. Fizazi, J. Yang, S. Peleg, C. R. Sikes, E. L. Kreimann, D. Daliani, M. Olive, K. a. Raymond, T. J. Janus, C. J. Logothetis, G. Karsenty, and N. M. Navone, "Prostate cancer cells-osteoblast interaction shifts expression of growth/survival-related genes in prostate cancer and reduces expression of osteoprotegerin in osteoblasts," *Clin. Cancer Res.*, vol. 9, no. 7, pp. 2587–2597, 2003.
- [95] T. Bellido, R. L. Jilka, B. F. Boyce, G. Girasole, H. Broxmeyer, S. A. Dalrymple, R. Murray, and S. C. Manolagas, "Regulation of interleukin-6, osteoclastogenesis, and bone mass by androgens: The role of the androgen receptor," *J. Clin. Invest.*, vol. 95, no. 6, pp. 2886–2895, 1995.
- [96] K. M. Bussard, C. V. Gay, and A. M. Mastro, "The bone microenvironment in metastasis;

what is special about bone?," *Cancer Metastasis Rev.*, vol. 27, no. 1, pp. 41–55, 2008.

- [97] A. P. Kusumbe, S. K. Ramasamy, and R. H. Adams, "Coupling of angiogenesis and osteogenesis by a specific vessel subtype in bone.," *Nature*, vol. 507, no. 7492, pp. 323–8, Mar. 2014.
- [98] S. L. Ellis, J. Grassinger, A. Jones, J. Borg, T. Camenisch, D. Haylock, I. Bertoncello, and S. K. Nilsson, "The relationship between bone, hemopoietic stem cells, and vasculature.," *Blood*, vol. 118, no. 6, pp. 1516–1524, 2011.
- [99] Y. Jiang, B. Halvard, T. Ulyanova, K. Chang, and T. Papayannopoulou, "On the adaptation of endosteal stem cell niche function in response to stress," *Blood*, vol. 114, no. 18, pp. 3773–3782, 2009.
- [100] H. P. Gerber and N. Ferrara, "Angiogenesis and bone growth," *Trends Cardiovasc. Med.*, vol. 10, no. 5, pp. 223–228, 2000.
- [101] N. Wang, K. J. Reeves, H. K. Brown, A. C. M. Fowles, F. E. Docherty, P. D. Ottewell, P. I. Croucher, I. Holen, and C. L. Eaton, "The frequency of osteolytic bone metastasis is determined by conditions of the soil , not the number of seeds ; evidence from in vivo models of breast and prostate cancer," *J. Exp. Clin. Cancer Res.*, pp. 1–12, 2015.
- [102] P. L. Doan and J. P. Chute, "The vascular niche: home for normal and malignant hematopoietic stem cells.," *Leukemia*, vol. 26, no. 1, pp. 54–62, Jan. 2012.
- [103] S. Rafii, F. Shapiro, R. Pettengell, B. Ferris, R. L. Nachman, M. A. Moore, and A. S. Asch, "Human bone marrow microvascular endothelial cells support long-term proliferation and differentiation of myeloid and megakaryocytic progenitors.," *Blood*, vol. 86, no. 9, pp. 3353–63, 1995.
- [104] B. Heissig, K. Hattori, S. Dias, M. Friedrich, B. Ferris, N. R. Hackett, R. G. Crystal, P. Besmer, D. Lyden, M. A. S. Moore, W. Zena, and S. Rafii, "Recruitment of Stem and Progenitor Cells from the Bone Marrow Niche Requires MMP-9 Mediated Release of Kit-Ligand," *Cell*, vol. 109, no. 5, pp. 625–637, 2002.
- [105] S. T. Avezilla, K. Hattori, B. Heissig, R. Tejada, F. Liao, K. Shido, D. K. Jin, S. Dias, F. Zhang, T. E. Hartman, N. R. Hackett, R. G. Crystal, L. Witte, D. J. Hicklin, P. Bohlen, D. Eaton, D. Lyden, F. De Sauvage, and S. Rafii, "Chemokine-mediated interaction of hematopoietic progenitors with the bone marrow vascular niche is required for thrombopoiesis," *Nat. Med.*, vol. 10, no. 1, pp. 64–71, 2004.
- [106] A. P. Kusumbe, "Vascular niches for disseminated tumour cells in bone," *J. Bone Oncol.*, vol. 5, no. 3, pp. 112–116, 2016.
- [107] S. M. Weis and D. a Cheresch, "A wake-up call for hibernating tumour cells.," *Nat. Cell Biol. Biol.*, vol. 15, no. 7, pp. 721–3, Jul. 2013.
- [108] I. Bruns, D. Lucas, S. Pinho, J. Ahmed, M. P. Lambert, Y. Kunisaki, S. Christoph, L. Schiff, M. Poncz, A. B. Frenette, and P. S. Frenette, "Megakaryocytes regulate hematopoietic stem cell quiescence via Cxcl4 secretion," vol. 20, no. 11, pp. 1315–1320, 2014.
- [109] R. Catena, N. Bhattacharya, T. El Rayes, S. Wang, H. Choi, D. Gao, S. Ryu, N. Joshi, D. Bielenberg, S. B. Lee, S. A. Haukaas, K. Gravdal, O. J. Halvorsen, L. A., Aklsen6, R. S. Watnick, and V. Mittal, "Bone marrow-derived Gr1+ cells can generate a

- metastasis- resistant microenvironment via induced secretion of thrombospondin-1," vol. 5, no. 3, pp. 578–589, 2013.
- [110] W. Jackson, D. M. Sosnoski, S. E. Ohanessian, P. Chandler, A. Mobley, K. D. Meisel, and A. M. Mastro, "Role of megakaryocytes in breast cancer metastasis to bone," *Cancer Res.*, vol. 77, no. 8, pp. 1942–1954, 2017.
- [111] S. Sousa and P. Clézardin, "Bone-Targeted Therapies in Cancer-Induced Bone Disease," *Calcif. Tissue Int.*, vol. 102, no. 2, pp. 227–250, 2018.
- [112] M. S. Aapro and R. E. Coleman, "Bone health management in patients with breast cancer: Current standards and emerging strategies," *Breast*, vol. 21, no. 1, pp. 8–19, 2012.
- [113] G. R. Mundy, "Metastasis to bone: causes, consequences and therapeutic opportunities.," *Nat. Rev. Cancer*, vol. 2, no. 8, pp. 584–593, 2002.
- [114] P. J. Masarachia, M. Weinreb, R. Balena, and G. A. Rodan, "Comparison of the distribution of 3H-alendronate and 3H-etidronate in rat and mouse bones," *Bone*, vol. 19, no. 3, pp. 281–290, 1996.
- [115] L. Widler, K. A. Jaeggi, M. Glatt, K. Müller, R. Bachmann, M. Bisping, A. R. Born, R. Cortesi, G. Guiglia, H. Jeker, R. Klein, U. Ramseier, J. Schmid, G. Schreiber, Y. Seltenmeyer, and J. R. Green, "Highly potent geminal bisphosphonates. From pamidronate disodium (Aredia) to zoledronic acid (Zometa)," *J. Med. Chem.*, vol. 45, no. 17, pp. 3721–3738, 2002.
- [116] M. J. Rogers, "New Insights Into the Molecular Mechanisms of Action of Bisphosphonates," *Curr. Pharm. Des.*, vol. 9, no. 32, pp. 2643–2658, 2003.
- [117] A. J. Roelofs, K. Thompson, S. Gordon, M. J. Rogers, Boyce, Roodman, Suva, Coleman, Weilbaecher, Bruland, Vessella, and Lipton, "Molecular mechanisms of action of bisphosphonates: Current status," *Clin. Cancer Res.*, vol. 12, no. 20 PART 2, pp. 6222–6231, 2006.
- [118] M.-T. Haider, I. Holen, T. N. Dear, K. Hunter, and H. K. Brown, "Modifying the osteoblastic niche with zoledronic acid in vivo-potential implications for breast cancer bone metastasis.," *Bone*, vol. 66, pp. 240–50, Sep. 2014.
- [119] F. N. Soki, X. Li, J. Berry, A. Koh, B. P. Sinder, X. Qian, K. M. Kozloff, R. S. Taichman, and L. K. Mccauley, "The Effects of Zoledronic Acid in the Bone and Vasculature Support of Hematopoietic Stem Cell Niches," vol. 114, no. 1, pp. 67–78, 2013.
- [120] P. Clézardin, F. H. Ebetino, and P. G. J. Fournier, "Bisphosphonates and cancer-induced bone disease: Beyond their antiresorptive activity," *Cancer Res.*, vol. 65, no. 12, pp. 4971–4974, 2005.
- [121] H. L. Neville-Webbe, I. Holen, and R. E. Coleman, "The anti-tumour activity of bisphosphonates," *Cancer Treat. Rev.*, vol. 28, no. 6, pp. 305–319, 2002.
- [122] O. Fromigue, L. Lagneaux, and J. J. Body, "Bisphosphonates induce breast cancer cell death in vitro.," *J. Bone Miner. Res.*, vol. 15, no. 11, pp. 2211–21, 2000.
- [123] R. Verdijk, H. R. Franke, F. Wolbers, and I. Vermes, "Differential effects of bisphosphonates on breast cancer cell lines," *Cancer Lett.*, vol. 246, no. 1–2, pp. 308–

312, 2007.

- [124] J. E. Brown, S. P. Ellis, J. E. Lester, S. Gutcher, T. Khanna, O. P. Purohit, E. McCloskey, and R. E. Coleman, "Prolonged efficacy of a single dose of the bisphosphonate zoledronic acid," *Clin. Cancer Res.*, vol. 13, no. 18, pp. 5406–5410, 2007.
- [125] T. Chen, J. Berenson, V. R. R. Swift, a Gilchick, S. Goodin, P. LoRusso, P. Ma, C. Ravera, F. Deckert, H. Schran, S. J, and a Skerjanec, "Pharmacokinetics and pharmacodynamics of zoledronic acid in cancer patients with bone metastases," *J. Clin. Pharmacol.*, vol. 42, p. 1228, 2002.
- [126] H. K. Brown, P. D. Ottewell, C. a. Evans, R. E. Coleman, and I. Holen, "A single administration of combination therapy inhibits breast tumour progress bone and modifies both osteoblasts and osteoclasts," *J. Bone Oncol.*, vol. 1, no. 2, pp. 47–56, 2012.
- [127] M. C. Winter, I. Holen, and R. E. Coleman, "Exploring the anti-tumour activity of bisphosphonates in early breast cancer," *Cancer Treat. Rev.*, vol. 34, no. 5, pp. 453–475, 2008.
- [128] P. D. Ottewell, N. Wang, J. Meek, C. A. Fowles, P. I. Croucher, C. L. Eaton, and I. Holen, "Castration-induced bone loss triggers growth of disseminated prostate cancer cells in bone," 2014.
- [129] O. Peyruchaud, B. Winding, I. Pécheur, C. M. Serre, P. Delmas, and P. Clézardin, "Early detection of bone metastases in a murine model using fluorescent human breast cancer cells: application to the use of the bisphosphonate zoledronic acid in the treatment of osteolytic lesions.," *J Bone Min. Res.*, vol. 16, no. 11, pp. 2027–34, 2001.
- [130] E. F. Solomayer, G. Gebauer, P. Hirnle, W. Janni, H. J. Lück, S. Becker, J. Huober, B. Krämer, B. Wackwitz, D. Wallwiener, and T. Fehm, "Influence of zoledronic acid on disseminated tumor cells in primary breast cancer patients," *Ann. Oncol.*, vol. 23, no. 9, pp. 2271–2277, 2012.
- [131] P. D. Ottewell, H. Mönkkönen, M. Jones, D. V Lefley, R. E. Coleman, and I. Holen, "Antitumor Effects of Doxorubicin Followed by Zoledronic Acid in a Mouse Model of Breast Cancer," *J. Natl. cancer Inst.*, pp. 1167–1178, 2008.
- [132] P. D. Ottewell, H. K. Brown, M. Jones, T. L. Rogers, S. S. Cross, N. J. Brown, R. E. Coleman, and I. Holen, "Combination therapy inhibits development and progression of mammary tumours in immunocompetent mice," *Breast Cancer Res. Treat.*, vol. 133, no. 2, pp. 523–536, 2012.
- [133] T. L. Rogers, N. Wind, R. Hughes, F. Nutter, H. K. Brown, I. Vasiliadou, P. D. Ottewell, and I. Holen, "Macrophages as potential targets for zoledronic acid outside the skeleton—evidence from in vitro and in vivo models," *Cell. Oncol.*, vol. 36, no. 6, pp. 505–514, 2013.
- [134] J. M. Ubellacker, M. T. Haider, M. J. DeCristo, G. Allocca, N. J. Brown, D. P. Silver, I. Holen, and S. S. McAllister, "Zoledronic acid alters hematopoiesis and generates breast tumor-suppressive bone marrow cells," *Breast Cancer Res.*, vol. 19, no. 1, pp. 1–15, 2017.
- [135] G. Misso, M. Porru, A. Stoppacciaro, M. Castellano, F. De Cicco, C. Leonetti, D. Santini,

- and M. Caraglia, "Evaluation of the in vitro and in vivo antiangiogenic effects of denosumab and zoledronic acid," *Cancer Biol. Ther.*, vol. 13, no. 14, pp. 1491–1500, 2012.
- [136] J. Wood, K. Bonjean, S. Ruetz, A. Bellahcène, L. Devy, J. M. Foidart, V. Castronovo, and J. R. Green, "Novel antiangiogenic effects of the bisphosphonate compound zoledronic acid," *J. Pharmacol. Exp. Ther.*, vol. 302, no. 3, pp. 1055–61, 2002.
- [137] J. Yamada, N. H. Tsuno, J. Kitayama, T. Tsuchiya, S. Yoneyama, M. Asakage, Y. Okaji, Y. Shuno, T. Nishikawa, J. Tanaka, K. Takahashi, and H. Nagawa, "Anti-Angiogenic Property of Zoledronic Acid by Inhibition of Endothelial Progenitor Cell Differentiation," *J. Surg. Res.*, vol. 151, no. 1, pp. 115–120, 2009.
- [138] D. Santini, B. Vincenzi, S. Galluzzo, F. Battistoni, L. Rocci, O. Venditti, G. Schiavon, S. Angeletti, F. Uzzalli, M. Caraglia, G. Dicuonzo, and G. Tonini, "Repeated intermittent low-dose therapy with zoledronic acid induces an early, sustained, and long-lasting decrease of peripheral vascular endothelial growth factor levels in cancer patients," *Clin. Cancer Res.*, vol. 13, no. 15, pp. 4482–4486, 2007.
- [139] R. Coleman, M. Gnant, G. Morgan, and P. Clezardin, "Effects of bone-targeted agents on cancer progression and mortality," *J. Natl. Cancer Inst.*, vol. 104, no. 14, pp. 1059–1067, 2012.
- [140] L. J. Diel, A. Jaschke, E. F. Solomayer, C. Gollan, G. Bastert, C. Sohn, and F. Schuetz, "Adjuvant oral clodronate improves the overall survival of primary breast cancer patients with micrometastases to the bone marrow - A long-term follow-up," *Ann. Oncol.*, vol. 19, no. 12, pp. 2007–2011, 2008.
- [141] R. Coleman, D. Cameron, D. Dodwell, R. Bell, C. Wilson, E. Rathbone, M. Keane, M. Gil, R. Burkinshaw, R. Grieve, P. Barrett-Lee, D. Ritchie, V. Liversedge, S. Hinsley, and H. Marshall, "Adjuvant zoledronic acid in patients with early breast cancer: Final efficacy analysis of the AZURE (BIG 01/04) randomised open-label phase 3 trial," *Lancet Oncol.*, vol. 15, no. 9, pp. 997–1006, 2014.
- [142] R. E. Coleman, H. Marshall, D. Cameron, D. Dodwell, R. Burkinshaw, M. Keane, M. Gil, S. J. Houston, R. J. Grieve, P. J. Barrett-Lee, D. Ritchie, J. Pugh, C. Gaunt, U. Rea, J. Peterson, C. Davies, V. Hiley, W. Gregory, and R. Bell, "Breast-Cancer Adjuvant Therapy with Zoledronic Acid," *N. Engl. J. Med.*, vol. 365, no. 15, pp. 1396–1405, 2011.
- [143] R. Coleman, R. De Boer, H. Eidtmann, A. Llombart, N. Davidson, P. Neven, G. Von Minckwitz, H. P. Sleeboom, J. Forbes, C. Barrios, A. Frassoldati, I. Campbell, O. Pajja, N. Martin, A. Modi, and N. Bundred, "Zoledronic acid (zoledronate) for postmenopausal women with early breast cancer receiving adjuvant letrozole (ZO-FAST study): Final 60-month results," *Ann. Oncol.*, vol. 24, no. 2, pp. 398–405, 2013.
- [144] M. Gnant and H. Eidtmann, "The anti-tumor effect of bisphosphonates ABCSG-12, ZO-FAST and more ...," *Crit. Rev. Oncol. Hematol.*, vol. 74, no. SUPPL. 1, pp. S2–S6, 2010.
- [145] R. Coleman, R. Gray, T. Powles, A. Paterson, M. Gnant, J. Bergh, K. I. Pritchard, J. Bliss, D. Cameron, R. Bradley, H. Pan, R. Peto, T. Powles, J. Burrett, M. Clarke, C. Davies, F. Duane, V. Evans, L. Gettins, J. Godwin, H. Liu, P. McGale, E. Mackinnon, T. McHugh, S. James, P. Morris, S. Read, C. Taylor, Y. Wang, Z. Wang, S. Anderson, I. Diel, J. Gralow, G. von Minckwitz, V. Moebus, R. Bartsch, P. Dubsy, C. Fesl, H. Fohler, R. Greil, R. Jakesz, A. Lang, G. Luschin-Ebengreuth, C. Marth, B. Mlineritsch, H. Samonigg, C. F. Singer, G. G.

Steger, H. Stoger, I. Olivotto, J. Ragaz, P. Christiansen, B. Ejlertsen, M. Ewertz, M. B. Jensen, S. Moller, H. T. Mouridsen, W. Eiermann, J. Hilfrich, W. Jonat, M. Kaufmann, R. Kreienberg, M. Schumacher, J. U. Blohmer, S. D. Costa, H. Eidtmann, B. Gerber, C. Jackisch, S. Loibl, U. Dafni, C. Markopoulos, C. Blomqvist, T. Saarto, J. H. Ahn, K. H. Jung, F. Perrone, G. Bass, A. Brown, J. Bryant, J. Costantino, J. Dignam, B. Fisher, C. Geyer, E. P. Mamounas, S. Paik, C. Redmond, S. Swain, L. Wickerham, N. Wolmark, P. Hadji, R. Hern, M. Dowsett, A. Makris, M. Parton, K. Pennert, I. E. Smith, J. R. Yarnold, G. Clack, C. Van Poznak, T. Safra, R. Bell, D. Dodwell, S. Hinsley, H. C. Marshall, E. Solomayer, T. Fehm, J. Lester, M. C. Winter, J. M. Horsman, R. Aft, A. M. Brufsky, H. A. Llombart, E. Perez, J. N. Ingle, V. J. Suman, K. Pritchard, K. Albain, R. Arriagada, W. Barlow, E. Bergsten-Nordstrom, F. Boccardo, M. Buyse, A. Coates, C. Correa, J. Cuzick, N. Davidson, A. Di Leo, J. Forbes, R. Gelber, L. Gianni, A. Goldhirsch, D. Hayes, C. Hill, J. Ingle, W. Janni, M. Martin, L. Norton, Y. Ohashi, M. Piccart, L. Pierce, V. Raina, P. Ravdin, J. Robertson, E. Rutgers, J. Sparano, G. Viale, X. Wang, T. Whelan, N. Wilcken, E. Winer, and W. Wood, "Adjuvant bisphosphonate treatment in early breast cancer: Meta-analyses of individual patient data from randomised trials," *Lancet*, vol. 386, no. 10001, pp. 1353–1361, 2015.

- [146] R. E. Coleman, "Adjuvant bone-targeted therapy to prevent metastasis: Lessons from the AZURE study," *Curr. Opin. Support. Palliat. Care*, vol. 6, no. 3, pp. 322–329, 2012.
- [147] P. Hadji, R. Coleman, M. Gnant, and J. R. Green, "The impact of menopause on bone, zoledronic acid, and implications for breast cancer growth and metastasis," *Ann. Oncol.*, vol. 23, no. 11, pp. 2782–2790, 2012.
- [148] P. D. Ottewell, N. Wang, H. K. Brown, K. J. Reeves, C. A. Fowles, P. I. Croucher, C. L. Eaton, and I. Holen, "Zoledronic Acid Has Differential Antitumor Activity in the Pre- and Postmenopausal Bone Microenvironment In Vivo," *Clin. Cancer Res.*, vol. 20, no. 11, pp. 2922–2932, 2014.
- [149] P. D. Ottewell, N. Wang, H. K. Brown, C. A. Fowles, P. I. Croucher, C. L. Eaton, and I. Holen, "OPG-Fc inhibits ovariectomy-induced growth of disseminated breast cancer cells in bone," *Int. J. Cancer*, vol. 137, no. 4, pp. 968–977, 2015.
- [150] J. Folkman, "Tumor Angiogenesis Factor Tumor Angiogenesis Factor," no. AUGUST, pp. 2109–2113, 1974.
- [151] J. Folkman, "Angiogenesis: an organizing principle for drug discovery?," *Nat. Rev. Drug Discov.*, vol. 6, no. 4, pp. 273–86, 2007.
- [152] N. Ferrara, "Vascular endothelial growth factor as a target for anticancer therapy.," *Oncologist*, vol. 9 Suppl 1, no. Supplement 1, pp. 2–10, 2004.
- [153] N. Ferrara, "Vascular endothelial growth factor: Basic science and clinical progress," *Endocr. Rev.*, vol. 25, no. 4, pp. 581–611, 2004.
- [154] L. G. Presta, H. Chen, S. J. O'Connor, V. Chisholm, Y. G. Meng, L. Krummen, M. Winkler, and N. Ferrara, "Humanization of an Anti-Vascular Endothelial Growth Factor Monoclonal Antibody for the Therapy of Solid Tumors and Other Disorders," *Cancer Res.*, vol. 57, no. 20, pp. 4593–4599, 1997.
- [155] H. Gerber and N. Ferrara, "Pharmacology and Pharmacodynamics of Bevacizumab as Monotherapy or in Combination with Cytotoxic Therapy in Preclinical Studies Pharmacology and Pharmacodynamics of Bevacizumab as Monotherapy or in

Combination with Cytotoxic Therapy in Preclinical Studies,” no. 3, pp. 671–680, 2005.

- [156] G. M. Keating, “Bevacizumab: A review of its use in advanced cancer,” *Drugs*, vol. 74, no. 16, pp. 1891–1925, 2014.
- [157] L. Manso, F. Moreno, R. Marquez, B. Castelo, A. Arcediano, M. Arroyo, A. I. Ballesteros, I. Calvo, M. J. Echarri, S. Enrech, A. Gomez, R. Gonzalez Del Val, E. Lopez-Miranda, M. Martin-Angulo, N. Martinez-Janez, C. Olier, and P. Zamora, “Use of bevacizumab as a first-line treatment for metastatic breast cancer.,” *Curr. Oncol.*, vol. 22, no. 2, pp. e51-60, 2015.
- [158] Editorial, “Difficult decisions.,” *Nat. Med.*, vol. 17, no. 8, p. 901, 2011.
- [159] K. C. Aalders, K. Tryfonidis, E. Senkus, and F. Cardoso, “Anti-angiogenic treatment in breast cancer: Facts, successes, failures and future perspectives,” *Cancer Treat. Rev.*, vol. 53, pp. 98–110, 2017.
- [160] R. J. Young and M. W. R. Reed, “Anti-angiogenic Therapy: Concept to Clinic,” *Microcirculation*, vol. 19, no. 2, pp. 115–125, 2012.
- [161] K. M. Cook and W. D. Figg, *Angiogenesis Inhibitors- Current Strategies and Future Prospects*, vol. 60, no. 4. 2010.
- [162] K. J. Gotink and H. M. W. Verheul, “Anti-angiogenic tyrosine kinase inhibitors: what is their mechanism of action?,” *Angiogenesis*, vol. 13, no. 1, pp. 1–14, 2010.
- [163] S. R. Brave, K. Ratcliffe, Z. Wilson, N. H. James, S. Ashton, A. Wainwright, J. Kendrew, P. Dudley, N. Broadbent, G. Sproat, S. Taylor, C. Barnes, J. C. Silva, C. L. Farnsworth, L. Hennequin, D. J. Ogilvie, J. M. Jurgensmeier, M. Shibuya, S. R. Wedge, and S. T. Barry, “Assessing the Activity of Cediranib, a VEGFR-2/3 Tyrosine Kinase Inhibitor, against VEGFR-1 and Members of the Structurally Related PDGFR Family,” *Mol. Cancer Ther.*, vol. 10, no. 5, pp. 861–873, 2011.
- [164] C. A. Heckman, T. Holopainen, M. Wirzenius, S. Keskitalo, M. Jeltsch, S. Ylä-Herttuala, S. R. Wedge, J. M. Jürgensmeier, and K. Alitalo, “The tyrosine kinase inhibitor cediranib blocks ligand-induced vascular endothelial growth factor receptor-3 activity and lymphangiogenesis,” *Cancer Res.*, vol. 68, no. 12, pp. 4754–4762, 2008.
- [165] N. Denduluri, A. R. Tan, J. Walshe, A. Berman, S. X. Yang, C. K. Chow, and S. M. Swain, “A pilot study to evaluate the vascular endothelial growth factor receptor tyrosine kinase inhibitor AZD2171 and chemotherapy in locally advanced and inflammatory breast cancer,” *Clin. Breast Cancer*, vol. 6, no. 5, pp. 460–463, 2005.
- [166] O. Martinho, R. Silva-Oliveira, V. Miranda-Gonçalves, and C. Clara, “In Vitro and In Vivo Analysis of RTK Inhibitor Efficacy and Identification of Its Novel Targets in Glioblastomas,” *Transl. Oncol.*, vol. 6, no. 2, pp. 187–196, 2013.
- [167] A. L. R. Bordinhão, A. F. Evangelista, R. J. S. Oliveira, T. Macedo, H. C. Silveira, R. M. Reis, and M. M. Marques, “MicroRNA profiling in human breast cancer cell lines exposed to the anti-neoplastic drug cediranib,” *Oncol. Rep.*, vol. 36, no. 6, pp. 3197–3206, 2016.
- [168] S. R. . R. e Wedge, J. . Kendrew, L. F. . F. Hennequin, P. J. . J. Valentine, S. T. . T. Barry, S. R. . R. Brave, N. R. . R. Smith, N. H. . H. James, M. . Dukes, J. O. . O. Curwen, R. . Chester, J. A. . A. Jackson, S. J. . J. Boffey, L. L. . L. Kilburn, S. . Barnett, G. H. P. . H. Richmond, P. F. . F. Wadsworth, M. . Walker, A. L. . L. Bigley, S. T. . T. Taylor, L. . Cooper, S. . Beck, J. M.

- Jürgensmeier, D. J. . J. Ogilvie, J. M. . Jürgensmeier, and D. J. . J. Ogilvie, "AZD2171: a highly potent, orally bioavailable, vascular endothelial growth factor receptor-2 tyrosine kinase inhibitor for the treatment of cancer," *Cancer Res.*, vol. 65, no. 0008–5472 (Print), pp. 4389–4400, 2005.
- [169] M. Medinger, N. Esser, U. Zirrgiebel, A. Ryan, J. M. Jürgensmeier, and J. Dreves, "Antitumor and antiangiogenic activity of cediranib in a preclinical model of renal cell carcinoma," *Anticancer Res.*, vol. 29, no. 12, pp. 5065–5076, 2009.
- [170] D. P. Bradley, J. J. Tessier, T. Lacey, M. Scott, J. M. Jürgensmeier, R. Odedra, J. Mills, L. Kilburn, and S. R. Wedge, "Examining the acute effects of cediranib (RECENTIN, AZD2171) treatment in tumor models: a dynamic contrast-enhanced MRI study using gadopentate," *Magn. Reson. Imaging*, vol. 27, no. 3, pp. 377–384, 2009.
- [171] J. J. Yin, L. Zhang, J. Munasinghe, R. I. Linnoila, and K. Kelly, "Cediranib/AZD2171 inhibits bone and brain metastasis in a preclinical model of advanced prostate cancer," *Cancer Res.*, vol. 70, no. 21, pp. 8662–8673, 2010.
- [172] J. K. R. Boulton, G. Box, M. Vinci, L. Perryman, S. A. Eccles, C. Jones, and S. P. Robinson, "Evaluation of the Response of Intracranial Xenografts to VEGF Signaling Inhibition Using Multiparametric MRI," *Neoplasia (United States)*, vol. 19, no. 9, pp. 684–694, 2017.
- [173] A. Decio, G. Taraboletti, V. Patton, R. Alzani, P. Perego, R. Fruscio, J. M. Jürgensmeier, R. Giavazzi, and D. Belotti, "Vascular endothelial growth factor c promotes ovarian carcinoma progression through paracrine and autocrine mechanisms.," *Am. J. Pathol.*, vol. 184, no. 4, pp. 1050–61, 2014.
- [174] F. Gomez-Rivera, A. A. Santillan-Gomez, M. N. Younes, S. Kim, D. Fooshee, M. Zhao, S. A. Jasser, and J. N. Myers, "The tyrosine kinase inhibitor, AZD2171, inhibits vascular endothelial growth factor receptor signaling and growth of anaplastic thyroid cancer in an orthotopic nude mouse model," *Clin. Cancer Res.*, vol. 13, no. 1078–0432 (Print), pp. 4519–4527, 2007.
- [175] M. A. Becker, T. Farzan, S. C. Harrington, J. W. Krempski, S. J. Weroha, X. Hou, K. R. Kalli, T. W. Wong, and P. Haluska, "Dual HER/VEGF Receptor Targeting Inhibits In Vivo Ovarian Cancer Tumor Growth," *Mol. Cancer Ther.*, vol. 12, no. 12, pp. 2909–2916, 2013.
- [176] D. M. Hyams, A. Chan, C. De Oliveira, R. Snyder, J. Vinholes, M. W. Audeh, V. M. Alencar, J. Lombard, B. Mookerjee, J. Xu, K. Brown, and P. Klein, "Cediranib in combination with fulvestrant in hormone-sensitive metastatic breast cancer: A randomized Phase II study," *Invest. New Drugs*, vol. 31, no. 5, pp. 1345–1354, 2013.
- [177] T. Trarbach, B. Schultheis, T. C. Gauler, V. Schneider, D. Strumberg, W. E. E. Eberhardt, S. Le Scouiller, M. Marotti, K. H. Brown, and J. Dreves, "Phase I open-label study of cediranib, an oral inhibitor of VEGF signalling, in combination with the oral Src inhibitor saracatinib in patients with advanced solid tumours," *Invest. New Drugs*, vol. 30, no. 5, pp. 1962–1971, 2012.
- [178] J. Liu, S. Tolane, and M. Birrer, "A Phase 1 trial of the PARP inhibitor olaparib (AZD2281) in combination with the anti-angiogenic cediranib (AZD2171) in recurrent epithelial ovarian or triple-," *Eur. J. ...*, vol. 49, no. 14, pp. 2972–2978, 2013.

- [179] P. M. Hoff, A. Hochhaus, B. C. Pestalozzi, N. C. Tebbutt, J. Li, T. W. Kim, K. D. Koynov, G. Kurteva, T. Pintér, Y. Cheng, B. Van Eyll, L. Pike, A. Fielding, J. D. Robertson, and M. P. Saunders, "Cediranib plus FOLFOX/CAPOX versus placebo plus FOLFOX/CAPOX in patients with previously untreated metastatic colorectal cancer: A randomized, double-blind, phase III study (HORIZON II)," *J. Clin. Oncol.*, vol. 30, no. 29, pp. 3596–3603, 2012.
- [180] T. T. Batchelor, P. Mulholland, B. Neyns, L. B. Nabors, M. Campone, A. Wick, W. Mason, T. Mikkelsen, S. Phuphanich, L. S. Ashby, J. DeGroot, R. Gattamaneni, L. Cher, M. Rosenthal, F. Payer, J. M. Jürgensmeier, R. K. Jain, A. G. Sorensen, J. Xu, Q. Liu, and M. Van Den Bent, "Phase III randomized trial comparing the efficacy of cediranib as monotherapy, and in combination with lomustine, versus lomustine alone in patients with recurrent glioblastoma," *J. Clin. Oncol.*, vol. 31, no. 26, pp. 3212–3218, 2013.
- [181] G. N. Masoud and W. Li, "HIF-1 α pathway: Role, regulation and intervention for cancer therapy," *Acta Pharm. Sin. B*, vol. 5, no. 5, pp. 378–389, 2015.
- [182] R. Kant, A. Bali, N. Singh, and A. S. Jaggi, "Prolyl 4 hydroxylase: A critical target in the pathophysiology of diseases," *Korean J. Physiol. Pharmacol.*, vol. 17, no. 2, pp. 111–120, 2013.
- [183] K. L. Gorres and R. T. Raines, *Prolyl 4-Hydroxylase*, vol. 45, no. 2. 2010.
- [184] Z. Du, T. Zan, X. Huang, L. Sheng, H. Li, H. Li, and Q. Li, "Dfo enhances the targeting of CD34-positive cells and improves neovascularization," *Cell Transplant.*, vol. 24, no. 11, pp. 2353–2366, 2015.
- [185] Y. Ikeda, S. Tajima, S. Yoshida, N. Yamano, Y. Kihira, K. Ishizawa, K. I. Aihara, S. Tomita, K. Tsuchiya, and T. Tamaki, "Deferoxamine promotes angiogenesis via the activation of vascular endothelial cell function," *Atherosclerosis*, vol. 215, no. 2, pp. 339–347, 2011.
- [186] J. Li, L. Fan, Z. Yu, X. Dang, and K. Wang, "The effect of deferoxamine on angiogenesis and bone repair in steroid-induced osteonecrosis of rabbit femoral heads," *Exp Biol Med*, pp. 273–280, 2014.
- [187] T. Matsumoto and S. Sato, "Stimulating angiogenesis mitigates the unloading-induced reduction in osteogenesis in early-stage bone repair in rats," *Physiol. Rep.*, vol. 3, no. 3, pp. e12335–e12335, 2015.
- [188] Z. Xu, W. Sun, Y. Li, S. Ling, C. Zhao, G. Zhong, D. Zhao, J. Song, H. Song, J. Li, L. You, G. Nie, Y. Chang, and Y. Li, "The regulation of iron metabolism by hepcidin contributes to unloading-induced bone loss," *Bone*, vol. 94, pp. 152–161, 2017.
- [189] R. Stewart, J. Goldstein, A. Eberhardt, T.-M. G. Chu, and and Shawn Gilbert, "Increasing Vascularity to Improve Healing of a Segmental Defect of the Rat Femur Rena," vol. 25, no. 8, pp. 472–476, 2011.
- [190] A. S. Farberga, X. L. Jinga, L. A. Monsona, A. Donneysa, C. N.Tchanque-Fossuoa, and and S. R. B. Sagar S. Deshpandea, "Deferoxamine reverses radiation induced hypovascularity during bone regeneration & repair in the murine mandible," *Computer (Long. Beach. Calif.)*, vol. 144, no. 5, pp. 724–732, 2008.
- [191] U. Baschant, M. Rauner, E. Bulycheva, H. Weidner, A. Roetto, U. Platzbecker, and L. C. Hofbauer, "Wnt5a is a key target for the pro-osteogenic effects of iron chelation on osteoblast progenitors," *Haematologica*, vol. 1013324, pp. 1499–1507, 2016.

- [192] A. Donneys, N. S. Nelson, E. E. Page, S. S. Deshpande, P. A. Felice, C. N. T. Fossuo, J. P. Spiegel, S. R. Buchman, and S. Carolina, "Targeting angiogenesis as a therapeutic means to reinforce osteocyte survival and prevent nonunions in the aftermath of radiotherapy," vol. 37, no. 9, pp. 1261–1267, 2015.
- [193] A. Donneys, A. S. Farberg, C. N. T.- Fossuo, and S. R. B. Sagar S. Deshpande, "Deferoxamine Enhances the Vascular Response of Bone Regeneration in Mandibular Distraction Osteogenesis," vol. 27, no. 6, pp. 316–324, 2015.
- [194] Y. Liu, Y. Cui, M. Shi, Q. Zhang, Q. Wang, and X. Chen, "Deferoxamine promotes MDA-MB-231 cell migration and invasion through increased ros-dependent HIF-1a accumulation," *Cell. Physiol. Biochem.*, vol. 33, no. 4, pp. 1036–1046, 2014.
- [195] P. Liu, K. He, H. Song, Z. Ma, W. Yin, and L. X. Xu, "Deferoxamine-induced increase in the intracellular iron levels in highly aggressive breast cancer cells leads to increased cell migration by enhancing TNF-a-dependent NF-kB signaling and TGF-b signaling," *J. Inorg. Biochem.*, vol. 160, pp. 40–48, 2016.
- [196] D. Duarte, E. D. Hawkins, O. Akinduro, H. Ang, K. De Filippo, I. Y. Kong, M. Haltalli, N. Ruivo, L. Straszowski, S. J. Vervoort, C. McLean, T. S. Weber, R. Khorshed, C. Pirillo, A. Wei, S. K. Ramasamy, A. P. Kusumbe, K. Duffy, R. H. Adams, L. E. Purton, L. M. Carlin, and C. Lo Celso, "Inhibition of Endosteal Vascular Niche Remodeling Rescues Hematopoietic Stem Cell Loss in AML," *Cell Stem Cell*, vol. 22, no. 1, p. 64–77.e6, 2018.
- [197] R. Cailleau, R. Young, M. Olive, and W. J. Reeves, "Breast Tumor Cell Lines From Pleural Effusions," *J Natl Cancer Inst*, vol. 53, no. 3, pp. 661–674, 1974.
- [198] F. Nutter, I. Holen, H. K. Brown, S. S. Cross, C. Alyson Evans, M. Walker, R. E. Coleman, J. A. Westbrook, P. J. Selby, J. E. Brown, and P. D. Ottewell, "Different molecular profiles are associated with breast cancer cell homing compared with colonisation of bone: Evidence using a novel bone-seeking cell line," *Endocr. Relat. Cancer*, vol. 21, no. 2, pp. 327–341, 2014.
- [199] H. D. Soule, J. Vazquez, a. Long, S. Albert, and M. Brennan, "A Human Cell Line From a Pleural Effusion Derived From a Breast Carcinoma," *J Natl Cancer Inst*, vol. 51, no. 5, pp. 1409–1416, 1973.
- [200] I. Keydar, L. Chen, S. Karby, F. R. Weiss, J. Delarea, M. Radu, S. Chaitcik, and H. J. Brenner, "Establishment and characterization of a cell line of human breast carcinoma origin," *Eur. J. Cancer*, vol. 15, no. 5, pp. 659–670, 1979.
- [201] P. Horan and S. Slezak, "Stable cell membrane labelling," *Nature*, vol. 340, pp. 167–8, 1989.
- [202] B. S. Huang, P. Law, K. Francis, B. O. Palsson, and A. D. Ho, "Symmetry of Initial Cell Divisions Among Primitive Hematopoietic Progenitors," *Blood*, pp. 2595–2605, 1999.
- [203] B. S. M. Lanzkron, M. I. Collector, and S. J. Sharkis, "Hematopoietic Stem Cell Tracking In Vivo: A Comparison of Short-Term and Long-Term Repopulating Cells," *Blood*, no. 93, pp. 1916–1922, 1999.
- [204] S. Pece, D. Tosoni, S. Confalonieri, G. Mazzarol, M. Vecchi, S. Ronzoni, L. Bernard, G. Viale, P. G. Pelicci, and P. P. Di Fiore, "Biological and molecular heterogeneity of breast cancers correlates with their cancer stem cell content.," *Cell*, vol. 140, no. 1, pp. 62–73,

Jan. 2010.

- [205] A. Fantozzi and G. Christofori, "Mouse models of breast cancer metastasis.," *Breast Cancer Res.*, vol. 8, no. 4, p. 212, Jan. 2006.
- [206] K. Pantel and R. H. Brakenhoff, "Dissecting the metastatic cascade.," *Nat. Rev. Cancer*, vol. 4, no. 6, pp. 448–56, Jun. 2004.
- [207] J. L. Townson and A. F. Chambers, "Dormancy of Solitary Metastatic Cells," *Cell Cycle*, vol. 5, no. 16, pp. 1744–1750, Oct. 2014.
- [208] S. S. McAllister and R. a. Weinberg, "The tumour-induced systemic environment as a critical regulator of cancer progression and metastasis," *Nat. Cell Biol.*, vol. 16, no. 8, pp. 717–727, Aug. 2014.
- [209] M. Guba, G. Cernaianu, G. Koehl, E. K. Geissler, K. Jauch, M. Anthuber, W. Falk, and M. Steinbauer, "A Primary Tumor Promotes Dormancy of Solitary Tumor Cells before Inhibiting Angiogenesis A Primary Tumor Promotes Dormancy of Solitary Tumor Cells before," *Cancer Res.*, vol. 61, no. 14, pp. 5575–5579, 2001.
- [210] G. N. Naumov, I. C. MacDonald, P. M. Weinmeister, N. Kerkvliet, K. V. Nadkarni, S. M. Wilson, V. L. Morris, A. C. Groom, and A. F. Chambers, "Persistence of solitary mammary carcinoma cells in a secondary site: A possible contributor to dormancy," *Cancer Res.*, vol. 62, no. 7, pp. 2162–2168, 2002.
- [211] Y. Shiozawa, a M. Havens, K. J. Pienta, and R. S. Taichman, "The bone marrow niche: habitat to hematopoietic and mesenchymal stem cells, and unwitting host to molecular parasites.," *Leukemia*, vol. 22, no. 5, pp. 941–50, May 2008.
- [212] B. S. Guerrouahen, I. Al-Hijji, and A. R. Tabrizi, "Osteoblastic and vascular endothelial niches, their control on normal hematopoietic stem cells, and their consequences on the development of leukemia.," *Stem Cells Int.*, vol. 2011, p. 375857, Jan. 2011.
- [213] L. E. Purton, D. T. Scadden, and S. Vincent, "The hematopoietic stem cell niche," *StemBook*, pp. 1–14, 2008.
- [214] N. Ribelles, A. Santonja, B. Pajares, C. Ll acer, and E. Alba, "The seed and soil hypothesis revisited: current state of knowledge of inherited genes on prognosis in breast cancer.," *Cancer Treat. Rev.*, vol. 40, no. 2, pp. 293–9, Mar. 2014.
- [215] N. Wang, F. E. Docherty, H. K. Brown, K. J. Reeves, C. A. Fowles, M. Lawson, P. D. Ottewell, I. Holen, P. I. Croucher, and C. L. Eaton, "Mitotic quiescence, but not unique 'stemness', marks the phenotype of bone metastasis-initiating cells in prostate cancer," *FASEB J.*, vol. Epublished, 2015.
- [216] P. D. Ottewell, N. Wang, H. K. Brown, K. J. Reeves, C. A. Fowles, P. I. Croucher, C. L. Eaton, and I. Holen, "Zoledronic acid has differential antitumor activity in the pre- and postmenopausal bone microenvironment in vivo.," *Clin. Cancer Res.*, vol. 20, no. 11, pp. 2922–32, Jun. 2014.
- [217] J. Massagu e and A. C. Obenauf, "Metastatic colonization by circulating tumour cells," *Nature*, vol. 529, no. 7586, pp. 298–306, Jan. 2016.
- [218] P. a Phadke, R. R. Mercer, J. F. Harms, Y. Jia, A. R. Frost, J. L. Jewell, K. M. Bussard, S. Nelson, C. Moore, J. C. Kappes, C. V Gay, A. M. Mastro, and D. R. Welch, "Kinetics of

metastatic breast cancer cell trafficking in bone.," *Clin. Cancer Res.*, vol. 12, no. 5, pp. 1431–40, Mar. 2006.

- [219] D. Bhattacharya, A. Czechowicz, A. G. L. Ooi, D. J. Rossi, D. Bryder, and I. L. Weissman, "Niche recycling through division-independent egress of hematopoietic stem cells.," *J. Exp. Med.*, vol. 206, no. 12, pp. 2837–50, Nov. 2009.
- [220] A. Czechowicz, D. Kraft, I. L. Weissman, and D. Bhattacharya, "Efficient transplantation via antibody-based clearance of hematopoietic stem cell niches.," *Science (80-.)*, vol. 318, no. 5854, pp. 1296–9, Nov. 2007.
- [221] A. P. Kusumbe, S. K. Ramasamy, T. Itkin, M. A. Mäe, U. H. Langen, C. Betsholtz, T. Lapidot, and R. H. Adams, "Age-dependent modulation of vascular niches for haematopoietic stem cells," *Nature*, vol. 532, no. 7599, pp. 380–384, 2016.
- [222] J. Adjo Aka and S.-X. Lin, "Comparison of Functional Proteomic Analyses of Human Breast Cancer Cell Lines T47D and MCF7," *PLoS One*, vol. 7, no. 2, p. e31532, 2012.
- [223] D. M. Sosnoski, R. J. Norgard, C. D. Grove, S. J. Foster, and A. M. Mastro, "Dormancy and growth of metastatic breast cancer cells in a bone-like microenvironment.," *Clin. Exp. Metastasis*, vol. 32, no. 4, pp. 335–344, Mar. 2015.
- [224] T. A. Guise, "Breast cancer bone metastases: It's all about the neighborhood," *Cell*, vol. 154, no. 5. 2013.
- [225] P. I. Croucher, M. M. McDonald, and T. J. Martin, "Bone metastasis: The importance of the neighbourhood," *Nat. Rev. Cancer*, vol. 16, no. 6, pp. 373–386, 2016.
- [226] A. Aiuti, M. Tavian, and A. Cipponi, "Expression of CXCR4, the receptor for stromal cell-derived factor-1 on fetal and adult human lymphohematopoietic progenitors," *Eur. J. Immunol.*, vol. 29, pp. 1823–1831, 1999.
- [227] Y. Shiozawa, J. E. Berry, M. R. Eber, Y. Jung, K. Yumoto, F. C. Cackowski, H. J. Yoon, P. Parsana, R. Mehra, J. Wang, S. McGee, E. Lee, S. Nagrath, K. J. Pienta, R. S. Taichman, Y. Shiozawa, J. E. Berry, M. R. Eber, Y. Jung, K. Yumoto, F. C. Cackowski, H. J. Yoon, P. Parsana, R. Mehra, J. Wang, S. McGee, E. Lee, S. Nagrath, K. J. Pienta, and R. S. Taichman, "The marrow niche controls the cancer stem cell phenotype of disseminated prostate cancer," *Oncotarget*, vol. 7, no. 27, pp. 41217–41232, 2016.
- [228] K. M. Bussard, D. J. Venzon, and A. M. Mastro, "Osteoblasts are a major source of inflammatory cytokines in the tumor microenvironment of bone metastatic breast cancer.," *J. Cell. Biochem.*, vol. 111, no. 5, pp. 1138–48, Dec. 2010.
- [229] D. W. Dempster, "Tethering Formation to Resorption: Reversal Revisited," *J. Bone Miner. Res.*, vol. 32, no. 7, pp. 1389–1390, 2017.
- [230] T. Guise, "Examining the metastatic niche: targeting the microenvironment.," *Semin. Oncol.*, vol. 37 Suppl 2, no. 5, pp. S2-14, Oct. 2010.
- [231] I. Holen, M. Walker, F. Nutter, A. Fowles, C. A. Evans, C. L. Eaton, and P. D. Ottewell, "Oestrogen receptor positive breast cancer metastasis to bone: inhibition by targeting the bone microenvironment in vivo," *Clin. Exp. Metastasis*, vol. 33, no. 3, pp. 211–224, 2016.
- [232] K. K. Sivaraj and R. H. Adams, "Blood vessel formation and function in bone,"

Development, vol. 143, no. 15, pp. 2706–2715, 2016.

- [233] C. Sun, J. Li, B. Wang, J. Shangguan, M. Figini, N. Shang, L. Pan, and Z. Zhang, “Tumor angiogenesis and bone metastasis - Correlation in invasive breast carcinoma,” *J. Immunol. Methods*, vol. 452, no. September 2017, pp. 46–52, 2018.
- [234] E. Keyhani, A. Muhammadnejad, F. Behjati, F. Sirati, F. Khodadadi, M. Karimlou, F. a Moghaddam, and R. Pazhoomand, “Angiogenesis markers in breast cancer - potentially useful tools for priority setting of anti-angiogenic agents,” *Asian Pac. J. Cancer Prev.*, vol. 14, no. 12, pp. 7651–6, 2013.
- [235] X. Zhou, X. Liu, G. Fan, S. Wu, J. Zhao, and X. Shi, “Expression of Matrix Metalloproteinase-9 and CD34 in Giant Cell Tumor of Bone,” *Orthop. Surg.*, vol. 8, no. 2, pp. 220–225, 2016.
- [236] S. K. Ramasamy, A. P. Kusumbe, M. Schiller, D. Zeuschner, M. G. Bixel, C. Milia, J. Gamrekeshvili, A. Limbourg, A. Medvinsky, M. M. Santoro, F. P. Limbourg, and R. H. Adams, “Blood flow controls bone vascular function and osteogenesis,” *Nat. Commun.*, vol. 7, pp. 1–13, 2016.
- [237] G. Yang, C. Sau, W. Lai, J. Cichon, and W. Li, “HHS Public Access,” vol. 344, no. 6188, pp. 1173–1178, 2015.
- [238] R. J. Thomas, T. a. Guise, J. J. Yin, J. Elliott, N. J. Horwood, T. J. Martin, and M. T. Gillespie, “Breast cancer cells interact with osteoblasts to support osteoclast formation,” *Endocrinology*, vol. 140, no. 10, pp. 4451–4458, 1999.
- [239] C. Wilson, R. Bell, S. Hinsley, H. Marshall, J. Brown, D. Cameron, D. Dodwell, and R. Coleman, “Adjuvant zoledronic acid reduces fractures in breast cancer patients; an AZURE (BIG 01/04) study,” *Eur. J. Cancer*, vol. 94, pp. 70–78, 2018.
- [240] K. Nakashima, X. Zhou, and G. K. et Al., “The novel zinc fingercontaining transcription factor Osterix is required for osteoblast 12 BioMed Research International differentiation and bone formation,” *Cell*, vol. 108, pp. 17–29, 2002.
- [241] M. M. L. Deckers, E. R. Van Beek, G. Van Der Pluijm, A. Wetterwald, L. Van Der Wee-Pals, M. G. Cecchini, S. E. Papapoulos, and C. W. G. M. Löwik, “Dissociation of angiogenesis and osteoclastogenesis during endochondral bone formation in neonatal mice,” *J. Bone Miner. Res.*, vol. 17, no. 6, pp. 998–1007, 2002.
- [242] P. D. Ottewell, N. Wang, J. Meek, C. A. Fowles, P. I. Croucher, C. L. Eaton, and I. Holen, “Castration-induced bone loss triggers growth of disseminated prostate cancer cells in bone,” *Endocrine-Related Cancer*, vol. 21, no. 5, pp. 769–781, 2014.
- [243] P. D. Ottewell, N. Wang, H. K. Brown, K. Reeves, A. Fowles, P. Croucher, C. Eaton, and I. Holen, “Zoledronic acid has differential anti-tumour activity in the pre-and post-menopausal bone microenvironment in vivo,” *Clin. Cancer Res.*, vol. i, no. 11, p. clincanres. 1246.2013, 2014.
- [244] R. E. Coleman, M. C. Winter, D. Cameron, R. Bell, D. Dodwell, M. M. Keane, M. Gil, D. Ritchie, J. L. Passos-Coelho, D. Wheatley, R. Burkinshaw, S. J. Marshall, and H. Thorpe, “The effects of adding zoledronic acid to neoadjuvant chemotherapy on tumour response: Exploratory evidence for direct anti-tumour activity in breast cancer,” *Br. J. Cancer*, vol. 102, no. 7, pp. 1099–1105, 2010.

- [245] M. Aapro, S. Monfardini, A. Jirillo, and U. Basso, "Management of primary and advanced breast cancer in older unfit patients (medical treatment)," *Cancer Treat. Rev.*, vol. 35, no. 6, pp. 503–508, 2009.
- [246] N. S. Vasudev and A. R. Reynolds, "Anti-angiogenic therapy for cancer: current progress, unresolved questions and future directions.," *Angiogenesis*, vol. 17, no. 3, pp. 471–94, Jul. 2014.
- [247] S. R. Brave, K. Ratcliffe, Z. Wilson, N. H. James, S. Ashton, A. Wainwright, J. Kendrew, P. Dudley, N. Broadbent, G. Sproat, S. Taylor, C. Barnes, J. C. Silva, C. L. Farnsworth, L. Hennequin, D. J. Ogilvie, J. M. Jürgensmeier, M. Shibuya, S. R. Wedge, and S. T. Barry, "Assessing the activity of cediranib, a VEGFR-2/3 tyrosine kinase inhibitor, against VEGFR-1 and members of the structurally related PDGFR family.," *Mol. Cancer Ther.*, vol. 10, no. 5, pp. 861–73, 2011.
- [248] D. Mukhopadhyay, B. Knebelmann, H. T. Cohen, S. Ananth, and V. P. Sukhatme, "The von Hippel-Lindau tumor suppressor gene product interacts with Sp1 to repress vascular endothelial growth factor promoter activity," *Mol Cell Biol*, vol. 17, no. 9, pp. 5629–5639, 1997.
- [249] P. R. Wachsberger, Y. R. Lawrence, Y. Liu, B. Daroczi, X. Xu, and A. P. Dicker, "Epidermal growth factor receptor expression modulates antitumor efficacy of vandetanib or cediranib combined with radiotherapy in human glioblastoma xenografts," *Int. J. Radiat. Oncol. Biol. Phys.*, vol. 82, no. 1, pp. 483–491, 2012.
- [250] J. Dreves, P. Siegert, M. Medinger, K. Mross, R. Strecker, U. Zirrgiebel, J. Harder, H. Blum, J. Robertson, J. M. Jürgensmeier, T. A. Puchalski, H. Young, O. Saunders, and C. Unger, "Phase I clinical study of AZD2171, an oral vascular endothelial growth factor signaling inhibitor, in patients with advanced solid tumors," *J. Clin. Oncol.*, vol. 25, no. 21, pp. 3045–3054, 2007.
- [251] W. L. Dahut, R. A. Madan, J. J. Karakunnel, D. Adelberg, J. L. Gulley, I. B. Turkbey, C. H. Chau, S. D. Spencer, M. Mulquin, J. Wright, H. L. Parnes, S. M. Steinberg, P. L. Choyke, and W. D. Figg, "Phase II clinical trial of cediranib in patients with metastatic castration-resistant prostate cancer," *BJU Int.*, vol. 111, no. 8, pp. 1269–1280, 2013.
- [252] K. D. Miller, M. Miller, S. Mehrotra, B. Agarwal, B. H. Mock, Q. H. Zheng, S. Badve, G. D. Hutchins, and G. W. Sledge, "A physiologic imaging pilot study of breast cancer treated with AZD2171," *Clin. Cancer Res.*, vol. 12, no. 1, pp. 281–288, 2006.
- [253] C. E. Clarkin and L. C. Gerstenfeld, "VEGF and bone cell signalling: An essential vessel for communication?," *Cell Biochem. Funct.*, vol. 31, no. 1, pp. 1–11, 2013.
- [254] A. J. Najy, Y. S. Jung, J. J. Won, M. K. Conley-Iacomb, C. J. Kim, E. Heath, M. L. Cher, R. D. Bonfil, and H. C. Kim, "Cediranib Inhibits both the Intraosseous Growth of PDGF D-Positive Prostate Cancer Cells and the Associated Bone Reaction," vol. 72, no. 12, pp. 1328–1338, 2012.
- [255] C. W. Pugh and P. J. Ratcliffe, "Regulation of angiogenesis by hypoxia: Role of the HIF system," *Nat. Med.*, vol. 9, no. 6, pp. 677–684, 2003.
- [256] N. Tang, L. Wang, J. Esko, F. J. Giordano, Y. Huang, H. P. Gerber, N. Ferrara, and R. S. Johnson, "Loss of HIF-1 α in endothelial cells disrupts a hypoxia-driven VEGF autocrine loop necessary for tumorigenesis," *Cancer Cell*, vol. 6, no. 5, pp. 485–495, 2004.

- [257] Z. Hou, C. Nie, Z. Si, and Y. Ma, "Deferoxamine enhances neovascularization and accelerates wound healing in diabetic rats via the accumulation of hypoxia-inducible factor-1 α ," *Diabetes Res. Clin. Pract.*, vol. 101, no. 1, pp. 62–71, 2013.
- [258] G. Wang, G. Shen, and T. Yin, "In vitro assessment of deferoxamine on mesenchymal stromal cells from tumor and bone marrow," *Environ. Toxicol. Pharmacol.*, vol. 49, pp. 58–64, 2017.
- [259] C. Callens, S. Coulon, J. Naudin, I. Radford-Weiss, N. Boissel, E. Raffoux, P. H. M. Wang, S. Agarwal, H. Tamouza, E. Paubelle, V. Asnafi, J.-A. Ribeil, P. Dessen, D. Canioni, O. Chandesris, M. T. Rubio, C. Beaumont, M. Benhamou, H. Dombret, E. Macintyre, R. C. Monteiro, I. C. Moura, and O. Hermine, "Targeting iron homeostasis induces cellular differentiation and synergizes with differentiating agents in acute myeloid leukemia," *J. Exp. Med.*, vol. 207, no. 4, pp. 731–750, 2010.
- [260] M. A. Lawson, M. M. McDonald, N. Kovacic, W. H. Khoo, R. L. Terry, J. Down, W. Kaplan, J. Paton-Hough, C. Fellows, J. A. Pettitt, T. N. Dear, E. Van Valckenborgh, P. A. Baldock, M. J. Rogers, C. L. Eaton, K. Vanderkerken, A. R. Pettit, J. M. W. Quinn, A. C. W. Zannettino, T. G. Phan, and P. I. Croucher, "Osteoclasts control reactivation of dormant myeloma cells by remodelling the endosteal niche," *Nat. Commun.*, vol. 6, no. May, pp. 1–15, 2015.
- [261] K. C. Valkenburg, S. R. Amend, J. E. Verdone, E. E. Van Der, J. R. Hernandez, M. A. Gorin, and K. J. Pienta, "A simple selection-free method for detecting disseminated tumor cells (DTCs) in murine bone marrow," vol. 7, no. 43, pp. 1–10, 2016.
- [262] A. D. Hartkopf, D. Stefanescu, M. Wallwiener, M. Hahn, S. Becker, E. F. Solomayer, T. N. Fehm, S. Y. Brucker, and F. A. Taran, "Tumor cell dissemination to the bone marrow and blood is associated with poor outcome in patients with metastatic breast cancer," *Breast Cancer Res. Treat.*, vol. 147, no. 2, pp. 345–351, 2014.
- [263] M. Banys, N. Krawczyk, and T. Fehm, "The role and clinical relevance of disseminated tumor cells in breast cancer," *Cancers (Basel)*, vol. 6, no. 1, pp. 143–152, 2014.
- [264] M. Balic, H. Lin, L. Young, D. Hawes, A. Giuliano, G. McNamara, R. H. Datar, and R. J. Cote, "Most early disseminated cancer cells detected in bone marrow of breast cancer patients have a putative breast cancer stem cell phenotype," *Clin. Cancer Res.*, vol. 12, no. 19, pp. 5615–5621, 2006.
- [265] F. C. Bidard, A. Vincent-Salomon, S. Gomme, C. Nos, Y. De Rycke, J. P. Thiery, B. Sigal-Zafrani, L. Mignot, X. Sastre-Garau, and J. Y. Pierga, "Disseminated tumor cells of breast cancer patients: A strong prognostic factor for distant and local relapse," *Clin. Cancer Res.*, vol. 14, no. 11, pp. 3306–3311, 2008.
- [266] T. T. Price, M. L. Burness, A. Sivan, M. J. Warner, R. Cheng, C. H. Lee, L. Olivere, K. Comatas, J. Magnani, H. K. Lyster, Q. Cheng, C. M. McCall, and D. A. Sipkins, "Dormant breast cancer micrometastases reside in specific bone marrow niches that regulate their transit to and from bone," *Sci. Transl. Med.*, vol. 8, no. 340, pp. 1–12, 2016.
- [267] A. Grosso, M. G. Burger, A. Lunger, D. J. Schaefer, A. Banfi, and N. Di Maggio, "It Takes Two to Tango: Coupling of Angiogenesis and Osteogenesis for Bone Regeneration," *Front. Bioeng. Biotechnol.*, vol. 5, no. November, pp. 1–7, 2017.
- [268] B. Lopes-bastos, L. Jin, F. Ruge, S. Owen, A. Sanders, C. Cogle, J. Chester, W. G. Jiang,

and J. Cai, "Association of breast carcinoma growth with a non-canonical axis of IFN γ / IDO1 / TSP1," vol. 1, no. 49, pp. 85024–85039, 2017.

- [269] S. K. Ramasamy, A. P. Kusumbe, T. Itkin, S. Gur-Cohen, T. Lapidot, and R. H. Adams, "Regulation of Hematopoiesis and Osteogenesis by Blood Vessel–Derived Signals," *Annu. Rev. Cell Dev. Biol.*, vol. 32, no. 1, pp. 649–675, 2016.
- [270] C. A. Beeton, S. Bord, D. Ireland, and J. E. Compston, "Osteoclast formation and bone resorption are inhibited by megakaryocytes," *Bone*, vol. 39, no. 5, pp. 985–990, 2006.